博士論文

Doctorate Thesis

Microscopic view of intermolecular interaction for CO chemisorbed on Pt(111)

(吸着分子間相互作用に関する微視的考察：
Pt(111)上に化学吸着した CO)

Department of Advanced Materials Science
Graduate School of Frontier Sciences
The University of Tokyo

Hyun Jin Yang

東京大学大学院 新領域創成科学研究科 物質系専攻

梁　賢眞

Thesis

Microscopic view of intermolecular interaction for CO chemisorbed on Pt(111)

吸着分子間相互作用に関する微視的考察：
Pt(111)上に化学吸着した CO

A Thesis Submitted to the University of Tokyo
for the Degree of Doctor of Science

By Hyun Jin Yang

Department of Advanced Materials Science
Graduate School of Frontier Sciences
The University of Tokyo

March, 2014

Supervised by Professor Maki Kawai

사랑하고, 사랑하고, 사랑하고 사랑하는

아빠와, 엄마 그리고 언니에게

Contents

List of Figures

List of Tables

Abbreviations

STM	Scanning tunneling microscopy
STS	Scanning tunneling spectroscopy
STM-IETS	STM inelastic electron tunneling spectroscopy
STM-AS	STM action spectroscopy
HREELS	High-resolution electron energy loss spectroscopy
IRAS	Infra-red reflection-absorption spectroscopy
LEED	Low-energy electron diffraction
HAS	Helium atom scattering
XPS	X-ray photoelectron spectroscopy
UPS	Ultraviolet photoelectron spectroscopy
IPS	Inverse photoemission spectroscopy
2PPE	Two-photon photoelectron spectroscopy
XAS	X-ray absorption spectroscopy
PES	Potential energy surface
HT	Hindered translation
HR	Hindered rotation
RC	Reaction coordinate
TPD	Temperature-programmed desorption
DFT	Density functional theory
DOS	Density of states
LDOS	Local density of states
ESDIAD	Electron-stimulated desorption in ion angular distribution
NEXAFS	Near-edge x-ray absorption fine structure
UHV	Ultra high vacuum
FFT	Fast Fourier transform

MO	Molecular orbital
HOMO	Highest occupied molecular orbital
LUMO	Lowest unoccupied molecular orbital
RT	Room temperature
FWHM	Full width of half maximum
SFG	Sum frequency generation

Symbols

I_T	Tunneling current
V_S	Sample bias voltage
E_{ads}	Adsorption energy
θ	Surface coverage
ϕ	Work function
E_F	Fermi energy

Physical Constants

Avogadro constant	N_A	$=$	$6.022\,1367 \times 10^{23}\ \mathrm{mol}^{-1}$
Proton charge	e	$=$	$1.602\,177\,33 \times 10^{-19}\ \mathrm{C}$
Boltzmann constant	k_B	$=$	$8.617\,373 \times 10^{-5}\ \mathrm{eV}$
Planck constant	$\hbar$	$=$	$1.054\,572\,66 \times 10^{-34}\ \mathrm{J \cdot s}$
Permittivity of vacuum	ε_0	$=$	$8.854\,187\,816 \times 10^{-12}\ \mathrm{C^2 \cdot J^{-1} \cdot m^{-1}}$

Chapter 1

Introduction

The main topic of my dissertation is the investigation of CO chemisorbed on Pt(111) surface by means of scanning tunneling microscopy and relevant spectroscopies, including the analysis and the interpretation of real-space observation and microscopic dynamic behavior to investigate the intermolecular interaction of CO chemisorbed on Pt(111) surface. As one of the most extensively studied system in the surface science due to fundamental as well as practical importance, many researchers have worked on the CO on Pt(111) from the beginning of modern surface science. Prior to describe my investigation, I would like to introduce the basic frame to understand a chemisorption system, and preceding results specifically dealing with CO on Pt(111).

1.1 Motivation, objective & outline of this thesis

The term "adsorption" describes a process where a molecule or atom (an adsorbate) approaches and sticks to a surface (an adsorbent). In particular,"chemisorption" means the formation of a chemical bond between the adsorbate and the adsorbent, which is the rehybridization of the electronic state of the adsorbate and the adsorbent to gain a specific amount of energy, which is adsorption energy (E_{ads}).

Consider a small molecule and a closed-packed surface, a carbon monoxide (CO) molecule and Pt(111) surface. If a CO molecule approaches the surface, the molecule and

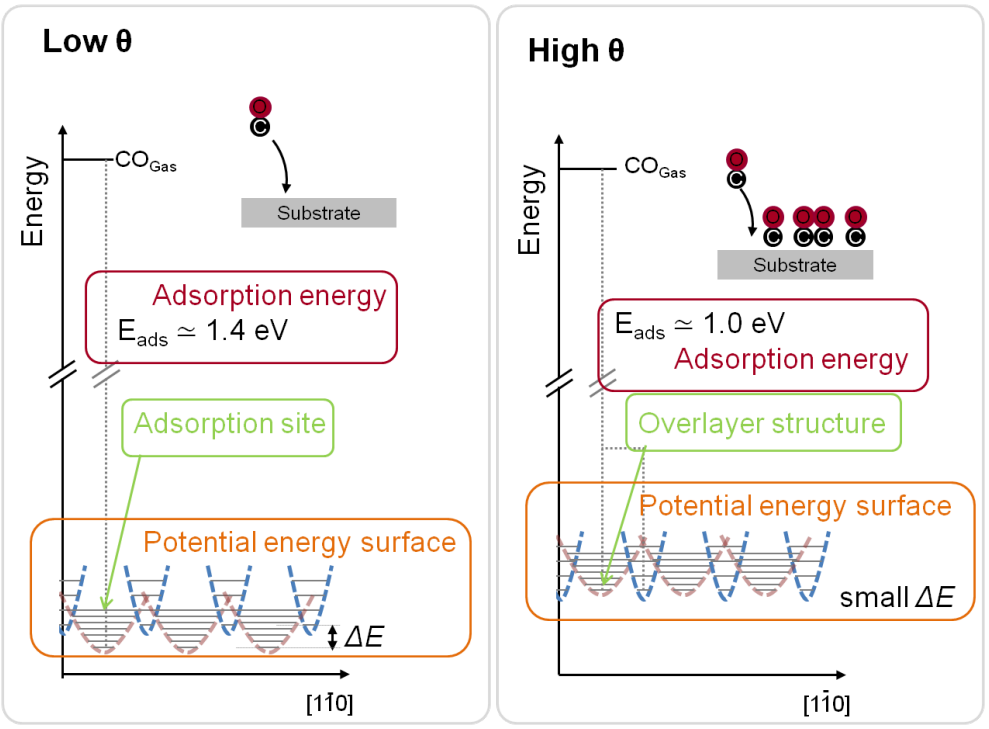

FIGURE 1.1: Comparison of adsorption scheme for low coverage(a) and high coverage(b)

surface atom of Pt(111) forms a chemical bond, by rehybridizing their electronic states. This bond formation is an exothermic process, to emit the *adsorption energy* (E_{ads}) approximately 1.4 eV.[1] Precisely, the adsorbed molecule feels three available *adsorption site* on the surface, namely ontop, bridge and hollow site, and the nature of chemical bonds between the adsorbate and surface atom differs according to the adsorption site. The energy difference between adsorption sites forms a basis for contruction of a *potential energy surface* which influences lateral motions of the adsorbate, namely *diffusion*.

If the number of adsorbate increases, then the intermolecular interaction between the adsorbates begins to modify all the circumstances. For example with CO on Pt(111), the *adsorption energy decreases* down to 1.0 eV[1], the adsorbates form specific *overlayer structures* according to the number of adsorbates, and the relative position of each adsorption site in terms of energy (potential energy surface) changes to allow occupation of multiple adsorption site, followed by the change in *the diffusion process* of adsorbates.

The total energy of the adsorbate-adsorbent (CO on Pt(111)) system can be described as follows:

$$E_{\text{Total}} = N_{\text{Ontop}} \times E_{\text{ads, Ontop}} + N_{\text{Bridge}} \times E_{\text{ads, Bridge}} + \sum \textbf{Interaction energy},$$

where the interaction energy accounts for the intermolecular interaction between adsorbates. This interaction energy is a key factor to describe the adsorption system, to explain the change of adsorption energy, overlayer structures, and diffusion dynamics depending on the surface coverage. Thus the ultimate understanding of chemisorption system consists of two interactions, namely the adsorbate-adsorbent interaction, and inter-adsorbate interaction. Since the beginning of the surface science, the development of experimental tools and the theoretical interpretation of the experimental results aim the understanding of those interactions. However, the inter-adsorbate interaction is less studied than the adsorbate-substrate interaction, probably due to the difficulty in characterization.

Scanning tunneling microscopy, developed by Binnig, Rohrer, Gerber and Weibel at IBM laboratory[2, 3], has become a powerful tool for measuring the topography and electronic structure of a solid surface with atomic resolution, enabling atom- or molecule-resolved observation of overlayer structures. The real-space observation of individual adsorbates allows the precise investigation of local arrangement in overlayer structures, which is not available in other surface spectroscopic tools due to averaging. This dissertation aims the investigation of interactions in an adsorption system, CO chemisorbed on Pt(111), mainly focusing on the intermolecular interaction by means of real space observation using STM under ultra-high vacuum (UHV) environment and cryogenic temperature (4.7 K).

The organization of chapters in this dissertation is as follows : Chapter 1 provides a general introduction regarding CO chemisorbed on Pt(111), including the importance of CO both in fundamental and practical aspects, and summary of previous results and ambiguities. The methodologies used in my investigation is introduced in Chapter 2. Chapter 3 through 5 includes the main contents of this dissertation. Chapter 3 deals with the isolated

molecules on Pt(111) for appearance of CO according to the adsorption site, and the electronic structure in unoccupied energy range. Chapter 4 presents the overlayer structure as a function of the surface coverage from randomly scattered molecules, the $(\sqrt{3} \times \sqrt{3})$R30° structures, to c$(4 \times 2)$ domain. These overlayer structures are discussed in terms of the intermolecular interactions for ontop CO-ontop CO interaction ($(\sqrt{3} \times \sqrt{3})$R30° islands) and ontop CO-bridge CO interaction in bridge-vacant c(4×2) domain. Chapter 5 describes the motion of bridge CO inside the overlayer structure, induced by injection of tunneling electrons. Finally, conclusion and further perspectives are summarized in Chapter 6.

1.2 CO chemisorbed on Pt(111)

For the objective to investigate adsorbate-adsorbent as well as inter-adsorbate interaction, there are numerous model adsorption system in the field of surface science. Among the numerous adsorption system, I chose CO chemisorbed on Pt(111) as my model system of real-space investigation using STM. In this section, I will describe why I chose CO on Pt(111).

1.2.1 Carbon monoxide, and CO on Pt(111)

In a practical aspect, both CO and platinum is one of the most important molecules / materials in the field of catalysis. Platinum is well known as the "all-round" catalyst, where the very first catalysis in history was the discovery of the platinum surface-catalyzed reaction of H_2 and O_2 in 1823 by Dobereiner.[4] Not only for the historical perspective, platinum is widely used as a catalyst over wide arnge of applications: automotive, fossil-fuel refining and production of chemicals.

Carbon monoxide (CO) has two aspect in practical catalysis; one is as a reactant, and the other is as a reagent which poisons the catalytic activity of transition metal catalysts. CO is one of side product of the combustion process inside automobiles, and the conversion of CO to CO_2 by oxidation is an important process to remove the toxicity of

exhaust gas. This CO oxidation reaction on Pt(111) is also the representative surface chemical reaction with Langmuir-Hinshelwood mechanism which involves the activation of both reactants by adsorption.

On the other hand, the reduction of catalytic activity due to adsorption of CO, is one of the main drawbacks in the practical aspect. As a representative example, the activation barrier of CO oxidation reaction without pre-adsorbed CO is approximately 100 kJ/mol, but CO adsorption multiplies the activation energy barrier energy as twice of without CO adsorption, which is so-called "'CO poisoning".[5] Therefore, CO poisoning of Pt catalyst is a hot issue in hydrogen extraction in fuel cells, even only 100 ppm of CO in the anode reduces the power output of the fuel cell to 25 %, when it is compared to the power output obtained without CO. [6] To deal with the critical reduction of catalytic activity, the basic understanding of CO adsorption on the surface of platinum is important.

In fundamental aspect, CO is one of the representative hetero-diatomic molecules; even its molecular orbital is discussed in a physical chemistry textbook.[7] Not only in physical chemistry, but also in inorganic chemistry the main topics in coordination chemistry are CO-complexes. CO is undoubtedly one of the most-studied molecular adsorbates, in the electronic structural point of view. CO adsorption on transition metal surface shows some fascinating complexities. In terms of adsorption geometry, CO almost invariably bonds the C atom to the metal surface. However, the adsorption symmetry (adsorption site) varies depending on the substrate materials, the crystalographic face, and the surface coverages, as adopting one-fold (ontop), two-fold (bridge) or three-fold or four-fold(hollow) coordination sites on the surfaces. For example, CO sits the ontop site of Ni(100), while it occupies the bridge site in Ni(110) and hollow site of Ni(111). In terms of adsorption site and its energetics, one interesting aspect of CO on Pt(111) is the occupation of multiple adsorption site as a function of the surface coverage. In this point of view, CO on Pt(111) would provide information how the intermolecular interaction modifies the adsorption energetics, and the bonding structures.

In this point of view, I adopted the CO on Pt(111) as the model system to observe in microscopic scale with scanning tunneling microscopy. From the following section, I will

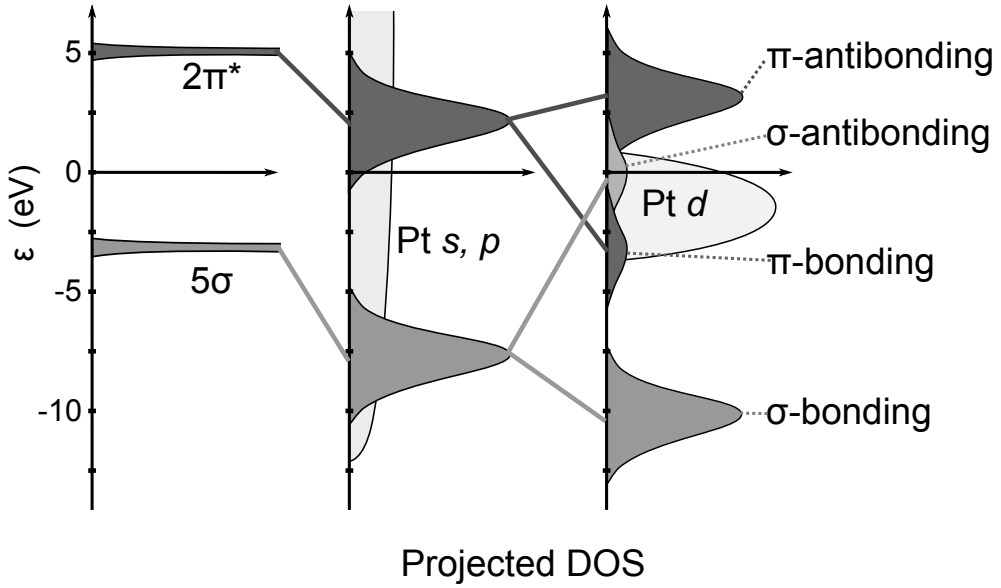

FIGURE 1.2: Schematic illustration of two-step model for CO adsorption on a transition metal. Adapted from reference [8], redrawn for clearance. Reuse permission is granted from Springer.

begin the introduction of basic aspects of CO chemisorption on Pt(111).

1.2.2 Theoretical basis to understand CO on Pt(111)

The beginning of understanding chemisorption system would be how the adsorbate and adsorbent interact to form a chemical bond. A chemical bond is the result of rehybridization of electronic states, many preceding studies have been tried to understand the electronic structures.

The most accepted theoretical picture of CO on transition metals is given by Hammer et al.[9] The essential idea is schematically presented in Figure 1.2, that the discrete molecular orbitals of CO, $2\pi^*$ for the lowest unoccupied molecular orbital (LUMO) and 5σ for the highest occupied molecular orbital (HOMO), broaden and are renormalized by interaction with metal *sp* continuum. At the same time, the interaction between the metal *d* band and broadened MOs splits the bonding, and antibonding orbitals.

The adsorption energy of CO is only 10 % of molecular dissociation energy, and this value can be interpreted as a weak molecule-surface interaction upon chemisorption, i.e. small amount of MO modification compared to the free molecules. The contribution

of molecular orbitals is conventionally described with the Blyholder model[10], which assumes symmetry-matched hybridization between MOs of CO and metal orbitals, i.e. theσ-type hybridized orbitals with HOMO of CO (5σ) and π-type hybridization with LUMO of CO($2\pi^*$). This model leads to charge-transfer scheme as charge donation into the metal which is compensated by a back-donation into the molecular $2\pi^*$. In this frontier-orbital scheme, the π bonding significantly weakens the C–O bonding through backdonation to antibonding orbital($2\pi^*$), which correctly predicts the decrease of C-O stretch mode frequency as the coordination number of adsorption site increases.

However the original paper by Blyholder[10] only considers π-system, while the σ orbitals are assumed to be unchanged. Moreover, consideration of only frontier orbital neglects the contribution of non-frontier orbitals such as 1π orbital. The alternative model of conventional Blyholder model has been suggested by Nilsson et al.[11], which considers mixed π orbitals and mixed σ orbitals for interpretation of x-ray emission spectroscopy measured from N_2 adsorbed on Ni(100). This model could successfully explain the result of X-ray emission spectroscopy measured on the CO chemisorbed on Ni(100), and Cu(100). [12, 13] This orbital mixing scheme was also supported by electron emission spectra obtained by thermal collisions of He*($2\,^3S$) metastable atoms with CO on Ni(100) and Ni(111).[14] The characteristic of this model is that the mixed σ bonding makes the molecule and substrate repulsive, and the mixed π bonding attracts the molecule and the substrate. [15]

In the following section, I will briefly introduce the preceding studies of CO on Pt(111). There are numerous references regarding CO on Pt(111), and sometimes they are not consistent each other. The discrepancies and ambiguities will be also discussed in addition to the result of previous results.

1.3 CO chemisorbed on Pt(111): Preceding results

CO chemisorbed on Pt(111) is one of well studied systems with accepted knowledges as follows: (a) the carbon atom facing the adsorbent atom, oxygen faces to the

vacuum, (b) the primary adsorption site is ontop site, and bridge site starts to be occupied with increasing the surface coverage, (c) the molecular axis of adsorbed CO is perpendicular to the surface for both ontop and bridge-occupied CO. In this section, the previous results of CO chemisorbed on Pt(111) will be briefly summarized, mainly focused on the surface-coverage(θ, the ratio of adsorbate over surface atom, for Pt(111) surface : 1.58×10^{15} molecules/ cm^2) dependency.

1.3.1 Adsorption energy, adsorption site & overlayer structures

Figure 1.3 shows a graphical summary of preceding results in terms of the adsorption sites, intermolecular interaction and overlayer structures according to the surface coverage.

Adsorption sites and the adsorption energy

The first step to understand the adsorption is finding the place where the molecule sits, and the energy gained with the adsorption. Many studies revealed the adsorption energy to be estimated from 1 eV to 2 eV at low coverage limit, according to the surface condition (polycrystalline ribbon, the population of surface defects, number of steps, and so on) and research groups. Generally accepted adsorption energy for CO on Pt(111) surface at the low coverage limit is about 1.4 eV as shown in Figure 1.3, which is the adsorption energy obtained by Ertl et al. by adsorption isotherm.[1] The adsorption energy monotonically decreases with increasing surface coverage, indicating repulsive intermolecular interaction among CO molecules. The monotonic decrease of adsorption energy was also suggested from the coverage-dependent temperature-programmed desorption (TPD), which showed the decrease of peak desorption temperature with increasing coverage.[16, 17] The decrease of adsorption energy calculated from TPD does not show enough resolution to discuss detailed coverage-dependent feature, while adsorption energy obtained by direct calorimetric measurement showed detailed structures near 0.3 ML[18] which is not observed by other references.

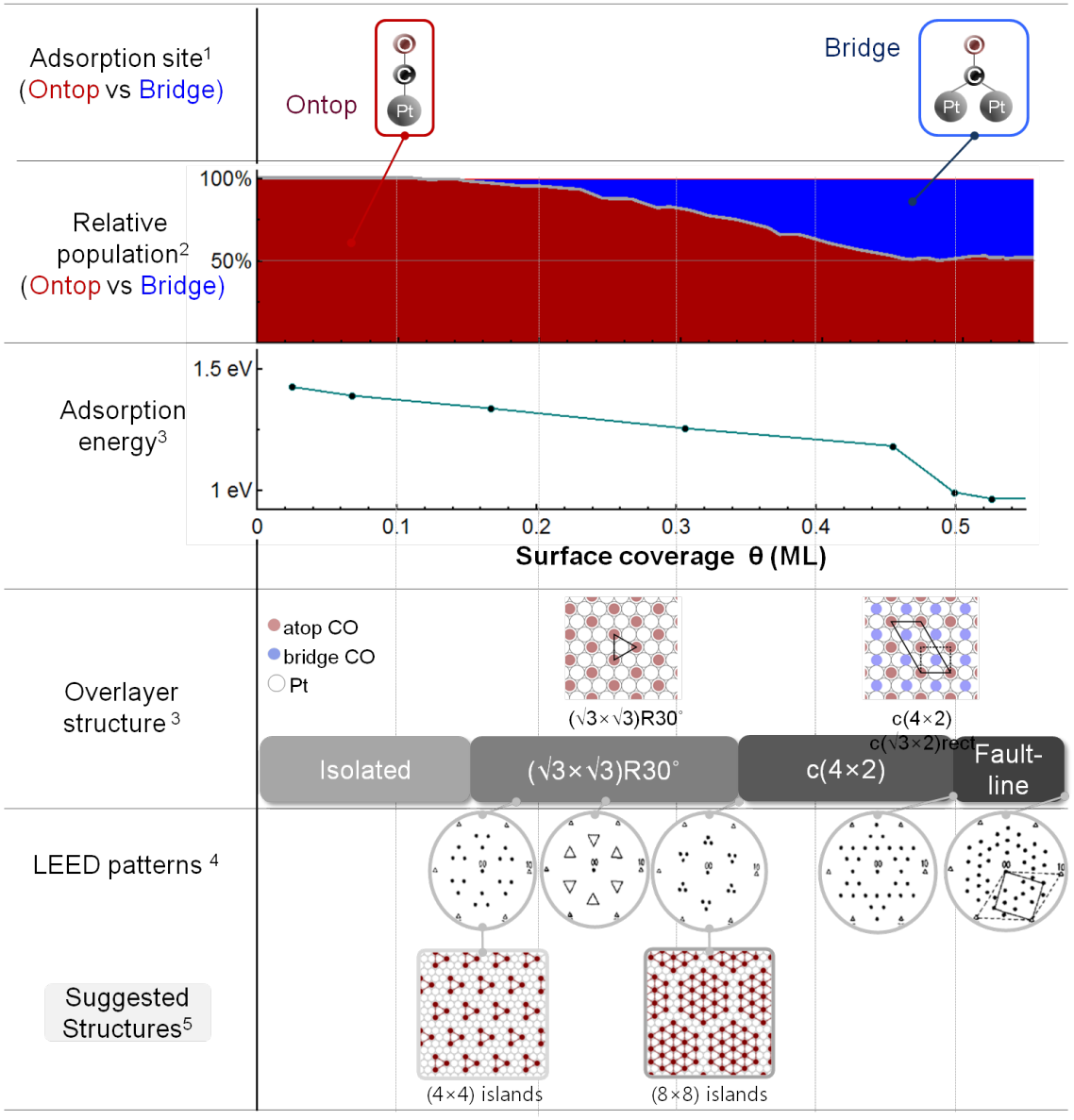

FIGURE 1.3: Summary of adsorption energy, adsorption site & overlayer structures according to the surface coverage. 1 from [19], 2 from [24], 3 from [1], 4 from [16], 5 from [25]. The models for LEED patterns are used from [16] under reprint permission from Elsevier, copyright 1982.

Coverage-dependent occupation of two adsorption site

Regarding the adsorption site, the ontop adsorption at low coverage, and bridge-site occupation from a certain increased surface coverage has been widely accepted for decades from the result of electron energy loss spectroscopy (EELS)[19] as well as infrared reflection-absorption spectroscopy(IRAS)[20], by showing 260 mV of C–O stretch frequency at low exposure, while 230 mV peak appeared from increased coverage. The discrimination between two adsorption sites, the estimation of threshold coverage for bridge-site occupation, and the determination of relative population between ontop and bridge site have been done with those vibrational spectroscopies (IRAS[21] and high-resolution EELS,[22, 23]) as well as high-resolution X-ray photoelectron spectroscopy(XPS)[24].

Regarding the threshold coverage of bridge occupation, many research groups showed the consistent result to show threshold coverage at 0.17 ML $\sim$ 0.19 ML since Steininger et al.[16, 22–24, 26], while Bradshaw's group kept insisted that the bridge band appears from 0.3 ML of the threshold surface coverage.[25, 27]. The reason why Bradshaw's group did not observe the bridge-bands may come from the lower sensitivity of IRAS compared to the sensitivity of EELS due to the smaller excitation cross-section, as well as smaller cross-section for bridge CO than ontop CO. Later (1989) Malik and Trenary could observe the bridge band less than 0.25 ML of surface coverage by means of IRAS with enhanced sensitivity.[26] The estimation of relative population of each adsorption site could be done by calibrating the area of each peak at 0.5 ML and the desorbed amount of total CO. From this analysis, partial coverage according to the adsorption site can be obtained. The relative population of ontop and bridge CO presented in Figure 1.3 is re-estimated from the partial coverage obtained experimentally at 100 K. The estimation of partial coverage at a specific temperature allows the estimation of adsorption energy difference ΔE between the adsorption site, by fitting the population onto a theoretical model. Schweizer et al. used the lattice-gas model approach to account the occupation probability according to the adsorption site, to estimate coverage-dependent adsorption energy difference.[21]. Other approach to construct the model was assuming a potential energy surface according to the adsorption site and the thermal equilibrium between two adsorption site at the corresponding temperature.[22–24]

Coverage-dependent overlayer structures

The most well-known overlayer structure is undoubtedly c(4×2) at 0.5 ML observed by low energy electron diffraction (LEED).[1] Ertl et al. interpreted the c(4×2) arrangement with highly coordinated hollow sites, but Froitzheim et al.[19] suggested the combination of ontop and bridge CO, and Hopster et al.[28] clearly showed the ontop-bridge combination for the c(4×2) structures by correlating C–O stretch frequency in EELS and LEED pattern. The scheme of c(4×2) domain is shown in the 4th row of Figure 1.3, composed up of alternating arrangement of ontop and bridge CO with $1 : 1$ ratio. c(4×2) structure can be noted as c(4×2)–2CO, or c$(\sqrt{3} \times 2)$rect structures according to the way to define the unit cell of domain structure. This rectangular domain is a characteristic pattern which appears well from CO adsorbed on various metal surfaces, even with different adsorption sites such as bridge sites (Pd(111)[29] and Ni(111)[30, 31]).

Other than c(4×2) domain, Ertl et al. reported another overlayer structures from faint spots with $(\sqrt{3} \times \sqrt{3})$R30° geometry at 150 K,[1] supported by other reports[28], and detailed analysis using $I - V$ curve from the diffuse spot was also done so far.[32] Faint pattern indicated a substantial disorder at 150 K, probably due to the surface diffusion. Steininger et al. found out the diffuse plot could be developed well-defined detailed structures at lower temperature (100 K) according to the surface coverage, as shown in Figure 1.3.[16] The $(\sqrt{3} \times \sqrt{3})$R30° spots are temperature-sensitive, disappearing if the temperature increases over 150 K. This is also consistent with the previously observed faint $(\sqrt{3} \times \sqrt{3})$R30° patterns.

Regarding the well-defined patterns with $\theta < 0.35$ML shown in Figure 1.3, Tüshaus et al. suggested the real space model, showing small-size island formation with global symmetry (4×4) and (8×8) at $\theta = 0.19$ML and 0.30 ML, respectively.[25] The models of islands are also shown in Figure 1.3.

1.3.2 Vibrational modes & relevant information

Gas-phase CO has only one vibrational degree of freedom as C–O stretch mode at 2143 cm^{-1}. This vibration is fully symmetric, as represented A_1 representation. The adsorption of CO onto a metal surface lowers the symmetry as well as induces decrease in C–O stretch mode frequency. The reduction of symmetry depends on the adsorption site, as the gas phase CO ($C_{\infty\nu}$) is reduced to $C_{6\nu}$ for ontop-adsorbed CO and $C_{2\nu}$ for bridge-adsorbed CO, in the case of adsorption onto close-packed (111) surface. The displacement patterns and corresponding vibrational modes are described in Table 1.1 and Table 1.2.

The degree of change in C–O stretch frequency according to the adsorption site has been qualitatively explained by Blyholder model.[10] According to the Blyholder model, the adsorption onto higher coordination site results in the more π-interaction to inject charges to the antibonding orbital of CO $2\pi^*$, weakening the C–O bonds and consequently lowering the C–O stretch mode frequency. Accordingly the C–O stretch mode frequency is used as an indirect evidence to identify the adsorption site as described in the previous section, for a variety of metals. The general energy region according to the adsorption site lies: near 2100 cm^{-1}($\approx$ 260 meV) for ontop-adsorbed (linear) CO, 1850 $\sim$ 1900 cm^{-1}($\approx$ 230 meV) for bridge-adsorbed CO, $<$ 1800 cm^{-1}(near 220 meV) for hollow-adsorbed CO.[4] These energy range also applies to CO chemisorbed on Pt(111) as described in the previous section, for the adsorption site according to the surface coverage.

The vibrational mode energies provided in Table 1.1 and Table 1.2 are extracted from various experimental techniques. Not only previously mentioned IRAS and HREELS, sum frequency generation(SFG) also shows consistent result for C–O stretch vibration for ontop-adsorbed CO. However up to now SFG detection is mainly limited to the C–O stretch mode of ontop CO, not for bridge band due to limited Raman polarizability compared to ontop CO. The measurement of low-frequency modes, such as M–C stretch mode and hindered modes, is relatively more difficult than the measurement of high-energy C–O stretch mode, so that the measurement of the low frequency modes are available with only limited techniques. So far, the M–C stretch mode and hindered rotation modes for both

TABLE 1.1: Vibrational mode frequency of ontop-adsorbed CO

Scheme			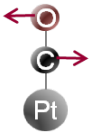	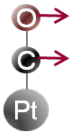
Description	Internal stretch	M-C stretch	Hindered rotation	Hindered translation
Symmetry	A_1	A_1	E	E
Mode	ν_1	ν_2	ν_3	ν_4
Energy	260 meV[a]	58 meV[a]	51 meV[a]	7 meV[b]

[a] from [16] [b] from [33, 34]

TABLE 1.2: Vibrational mode energies of bridge-adsorbed CO in c(4×2) structures

Scheme	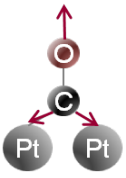	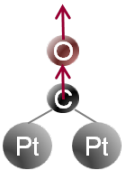	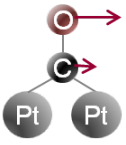	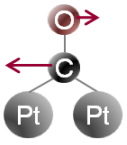	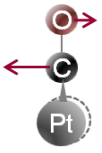	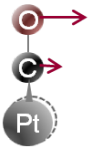
Description	Internal stretch	M-C stretch	Hindered translation	Hindered rotation	Hindered rotation	Hindered translation
Symmetry	A_1	A_1	B_1	B_1	B_2	B_2
Mode	ν_1	ν_2	ν_3	ν_4	ν_5	ν_6
Energy	230 meV[a]	47 meV[a]	38 meV[b] 10 meV[c]	37 meV[d]	44.5 meV[a]	8 meV[c]

[a] from [16] [b] from [21] [c] from [34] [d] from [34], inferred value in conjunction with [35]

ontop and bridge CO could be detected with EELS.[16] Hindered translation modes are the result of helium atom scattering[33, 34].

1.3.3 Electronic structure & theoretical/numerical calculation

The theoretical frame described in Section 1.2.2 is based on the experimentally measured electronic structures of CO adsorbed on Pt(111). The electronically hybridized states, denoted with *tilde* type orbital notation, have been detected using UV photoelectron spectroscopy and inverse photoemission, two photon photoemission spectroscopy, for occupied and unoccupied energy region respectively. Not only for the direct probing of adsorbate states, the work function as a function of the surface coverage, core-level energy change will be briefly discussed.

Energy level of adsorbate orbitals

The schematic model in Figure 1.2 suggests (a) the broadening of CO molecular orbitals by contribution of metal sp band, (b) followed energy level split by contribution of metal d bands. The contribution of CO MO is limited to the frontier orbitals in the model. However, not only the frontier orbitals ($2\pi^*$, 5σ), but also inner orbitals such as 1π and 4σ may contributes to the chemisorption bond formation, according to the symmetry (σ and π) of MO. The orbital symmetry can be separately studied by polarizing the excitation source as shown in Figure 1.4.

I begin with the gas phase ionization energy of CO. The energy level alignment of gas-phase CO is 14.0 eV for 5σ, 17.6 eV for 1π, and 19.7 eV for 4σ.[7] X-ray emission spectra have resulted identical MO order and energy differences, 5σ at 5.9 eV, 1π at 8.7 eV and 4σ at 11.5 eV.[36] CO adsorption on the Pt(111) surface changes the energetic orders as well as the energy levels. The most recent result obtained with high-resolution ultraviolet photoelectron spectroscopy(UPS) is shown in Figure 1.4,[37] which is consistent with preceding observations in terms of energetic position and the order of MO.[38–40]

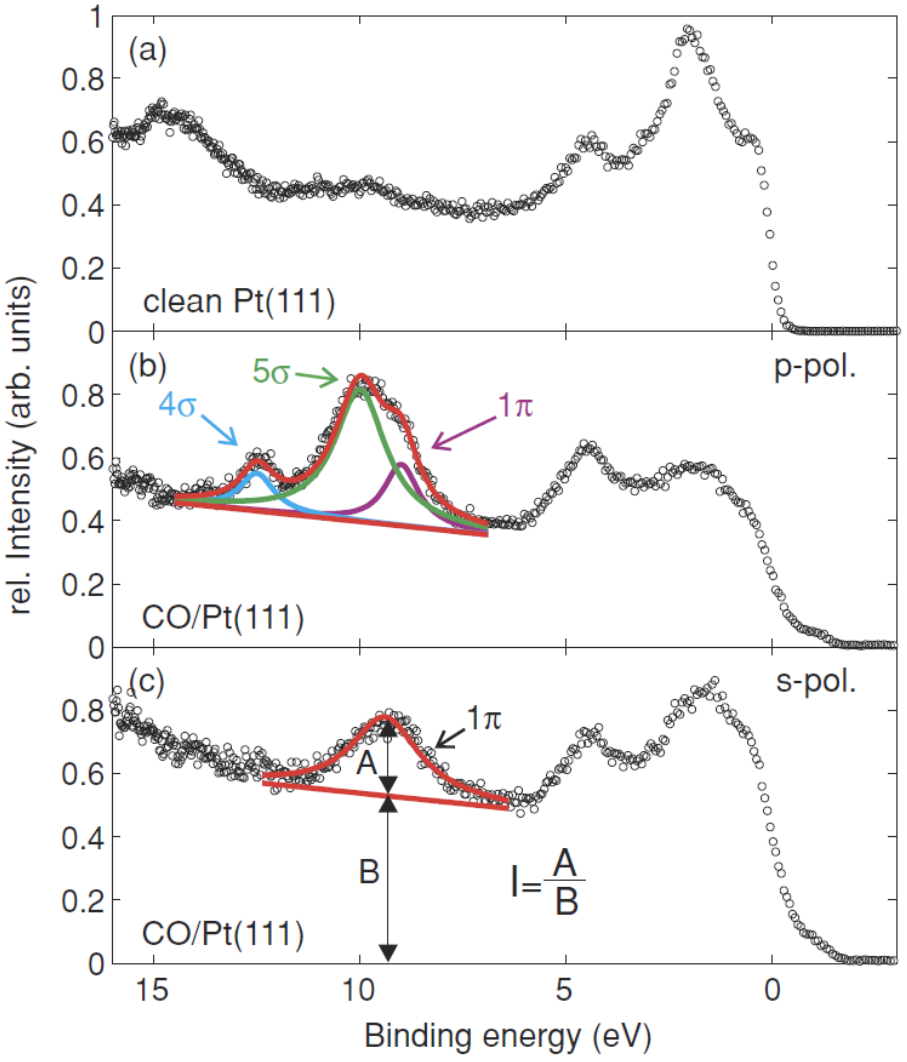

FIGURE 1.4: Electronic structure in occupied energy region: UPS, with photon energy of $h\nu = 32.8\,\text{eV}$. The energetic positions are fitted by Lorentzian profiles, at 9.0 eV, 10.0 eV, and 12.5 eV for 1π, 5σ and 4σ, respectively. Adapted from [37] under a reprint permission, copyright 2011 by the American Physical Society.

In Figure 1.4, the decrease of bare Pt(111) signal near 3 eV is evidence of *d*-electron contribution to the CO chemisorption. The *s*-polarized excitation results in the photoemission from only 1π states (Figure 1.4a), compared to the *p*-polarized light (Figure 1.4b) excites all the occupied orbital regardless of the orbital symmetry. The binding energies of 1π, 5σ and 4σ are measured to be 9.0 eV, 10.0 eV, and 12.5 eV, respectively. Comparing the gas-phase energy, 5σ significantly downshifted by 4 eV, changing the order with 1π orbital. The inversion of order between 1π and 5σ is consistent for chemisorbed CO on various metals. Compared to the binding energy shift of 5σ orbital, the 1π binding energy remains unchanged from the gas phase, implying little contribution to the chemisorption of CO on Pt(111). Small contribution of π symmetry also infers the ontop-adsorption, which the ontop adsorption indicates smaller contribution of π orbital than the bridge site occupation. The energy difference between 4σ and 1π was 3.5 eV which is larger than the difference in gas phase(2.8 eV), which may imply the contribution of 4σ orbital to the chemisorption bond formation.

The experimental studies regarding the unoccupied region is limited in number, compared to the studies on the occupied energy region. There are two preceding reports which is widely accepted, one is by Dose et al. using inverse photo-emission (IPE),[41] and the other is by Anazawa et al. using two-photon photoemission (2PPE).[42] Figure 1.5 shows the result of Anazawa et al., (a) shows the original data and (b) is the spectra with subtraction of bare Pt surface.

Polarization dependence of the 2PPE spectra with bare Pt surface, $\theta = 0.1\,\mathrm{ML}$ and $\theta = 0.5\,\mathrm{ML}$ shows the predominant π-symmetry of the molecular origin. At initial adsorption of CO results in a peak at 4.5 eV above E_F, followed by appearance of a feature at 4.3 eV, and the authors assigned the features according to the adsorption site, as designated with B and T. Distinguished two peaks in 2PPE spectra is in contrast to the inverse photoemission result, which showed only one peak at 4.3 eV above E_F without any coverage dependence. Nonetheless, these features near 4.5 eV are accepted as $2\pi^*$ states, which is the dominant energy level in unoccupied region.

The relative energy position of $2\pi^*$ between ontop and bridge site is explained by

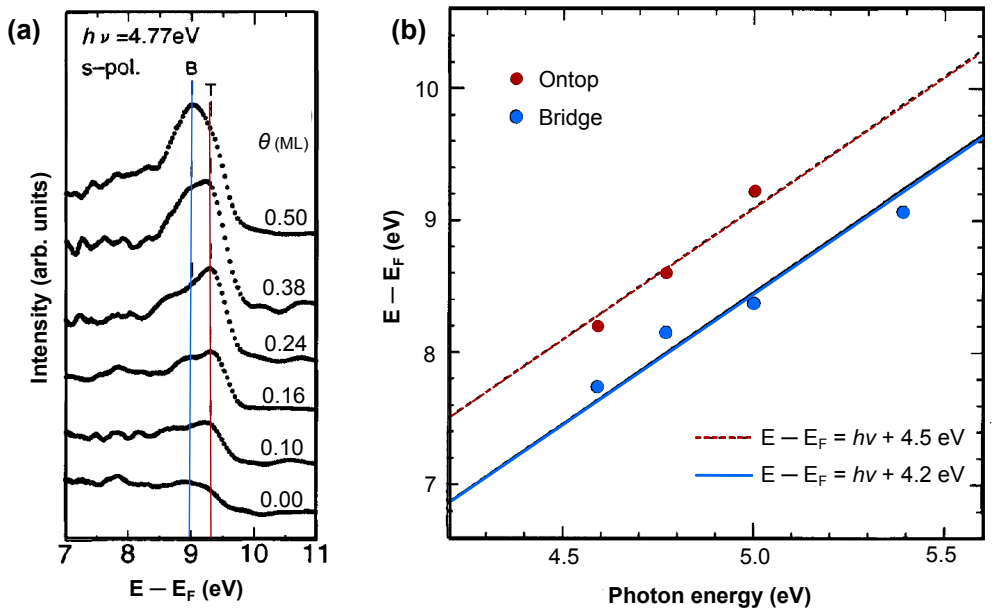

FIGURE 1.5: Electronic structure in unoccupied energy region: two photon photoemission (2PPE). Reprinted from [42], Copyright 1998, with permission from Elsevier.

balance between two interaction strength : the resonance interaction with sp-band and the hybridization with occupied $5d$ state. Considering the adsorption energy difference between ontop and bridge site, one would expect the higher position of $2\pi^*$ for ontop site caused by greater splitting between bonding and the anti-bonding states. However, from the C–O stretch mode frequency, the bridge CO shows lower energy vibration which indicates the stronger binding of CO $2\pi^*$ state with $5d$ state for bridge CO. Thus, the whole adsorption energy is governed by σ-interaction to result more stable ontop adsorption, while the interaction between $2\pi^*$ and metal bands ($5d$ and sp-bands) results in wider splitting to result in the higher energy of $2\pi^*$ state for bridge-occupied CO.[42]

Coverage-dependent work function change

As an extended discussion of rehybridization of electronic states, the work function change ($\Delta\phi$) has been considered to depend on the balance between π-interaction and σ-interaction.[43, 44] The work function change upon CO chemisorption on Pt(111) surface is different from other metals. In contrast to CO adsorbed on Pd(111), Ni(111) and Ru(0001) which show a monotonic increase of work function with increasing surface coverage,[44]

CO chemisorbed on Pt(111) shows decrease at initial adsorption, followed by increase from certain surface coverage, reaches to $\Delta\phi = 0$ at $\theta = 0.5\,\mathrm{ML}$. This phenomenon is consistently observed from various research groups, nonetheless the detail was different each other, such as the surface coverage with minimum work function ($\theta_{\phi_{min}}$), and the value of work function change.[1, 16, 28, 38, 45, 46] The differences in detail may originate from the difference in the way to estimate the surface coverage, and the difference in the experimental condition such as measurement temperature and method of measurements. Ertl et al. and Norton et al. reported the minimum work function appears at $\theta \approx 0.3$ ML, while Steininger et al., Hopster et al. and Poelsema et al. reported the minimum less than 0.2 ML. Most authors correlated the surface coverage with minimum work function as the onset coverage for the bridge-site occupation, leading the implication of different amount and direction of charge transfer according to the adsorption site. Furthermore, Norton et al. reported the reversal of dipole moment from $C^{\delta-} - O^{\delta+}$ to $C^{\delta+} - O^{\delta-}$, though no other evidence has been proposed so far in my best knowledge.

1.4 Intermolecular interaction: Interpretation of coverage-dependence

As described in the beginning of this chapter, the total energy of system is summation over the adsorption energy i.e. CO-metal interaction and the intermolecular interaction between CO molecules. In this section, I will describe preceding interpretation of experimental results of CO chemisorbed on Pt(111), from the viewpoint of lateral intermolecular interaction. For this purpose, I will briefly discuss the types of intermolecular interaction and available origin of them.

1.4.1 Categorization of intermolecular interaction

The most direct measure of intermolecular interaction on a surface is the overlayer structure according to the surface coverage. Schematic correlation between the overlayer structure and intermolecular interaction can be sketched with the interaction energy as

a function of intermolecular distance. The averaged value of intermolecular distance is proportional to the square root of surface coverage (θ). If the interaction energy has a local minimum at a specific intermolecular distance, the overlayer structure will show ordered structures with the specific intermolecular distance. If the interaction is attractive, locally ordered islands will be formed even at low surface coverage. If the interaction is repulsive in relatively short range, the ordered structure with the intermolecular distance of local minimum interaction energy will appear gradually with increasing surface coverage.

The primary origin of intermolecular interaction is electrostatic. The amplitude and the polarity of the interaction energy and the distance-dependence depend on the local charge distribution. The representative attractive interactions, hydrogen bonding and the van der Waals interaction, are also understood in terms of electrostatic interaction. For example, control of island formation through controlling attractive intermolecular interaction with functional groups has been achieved with dehydro[12]benzoannulene(DBA) derivatives,[47] via hydrogen bonding in epoxy group and van der Waals interaction with various length of hydrocarbon chains. On the other hand, if the molecule has a dipole moment as well as forming strong dipole through charge transfer between the adsorbate and a metal surface, the dipole-dipole interaction would work repulsively over a long range. If the strength of adsorbate-metal interaction is not too large, the interaction through substrate would be involved on to the intermediate dipole-dipole interaction. According to the categorization by Persson[48], if the interaction involves the ions of the substrate (ion interaction, or elastic deformation), the intermolecular interaction will appear repulsive, and long-ranged. If the electron of the substrate is involved to the intermolecular interaction, the indirect interaction will appear as oscillatory manner with short-range, except the case which the surface state of metal is involved (long range). If the intermolecular distance decreases enough to overlap the occupied orbitals, it will work as strong repulsive interaction, namely Pauli repulsion.

Focusing on CO chemisorbed on Pt(111), the important parameters of CO chemisorption in terms of intermolecular interactions are (a) internal dipole of CO, (b) interfacial dipole between the molecule and the Pt(111) surface due to the charge transfer. These static dipoles involve the image dipole in the substrate. Because adsorbed CO stands in

perpendicular to the surface, all the dipoles are in perpendicular to the surface. Thus, the electrostatic interaction will be repulsive in a whole with $1/r^3$ distance dependence. At the surface coverage where bridge-occupation is available the detail of interaction may not be simple, due to the different dipole moments according to the adsorption site, as well as the inter-species (ontop and bridge) dipole-dipole interaction.

1.4.2 Interpretation of experimental result in terms of intermolecular interaction

The experimental results regarding CO on Pt(111) are summarized in the previous section. In this subsection, I will briefly summarize interpretation of experimental results in terms of the intermolecular interaction. To describe the total energy of the system with CO-metal interaction and intermolecular interaction among CO molecules, the CO-metal interaction may be described by potential energy surface, and the intermolecular interaction may be described as an additional term which has pair-wise or multi-body interaction according to the intermolecular distance.

CO adsorbed on the Pt(111) surface has two available adsorption sites, therefore, the potential energy surface for CO adsorption also should be constructed as two-site potential energy surface, having two parameters. The two parameters are the adsorption energy difference between two deterministic site(ΔE), and the diffusion barrier height (E_B). In addition, the shape of potential energy surface for each adsorption site is determined by the two frustrated translational frequencies, parallel to the surface. Relative population of each adsorption site has been studied with IRAS[21], time-resolved EELS[22, 23] and high-resolution XPS[24]. The temperature-dependence of relative population gives the cross-section for adsorption-site conversion, which is an entropy factor.

The primary intermolecular interaction is repulsive, as represented in the decrease of peak temperature in temperature-programmed desorption with increasing surface coverage,[1, 16, 27, 38] even with surface coverage less than 0.3 ML. The main origin of the repulsive interaction is considered to be dipole-dipole interaction, as discussed in the previous section.

Only considering the simple repulsive interaction successfully reproduced the formation of c(4×2) domains with Monte Carlo simulation, since Persson's paper.[49] However, the simulation fails to result $(\sqrt{3} \times \sqrt{3})$R30° island structures as suggested by Tüshaus et al. The existence of $(\sqrt{3} \times \sqrt{3})$R30° island structures provoked the trials to introduce attractive interaction by employing Lennard-Jones 6-12 potential [50] or non-monotonic intermolecular interaction[51]. However the introduction of Lennard-Jones model failed to reproduce the heat of adsorption and the mode frequency of ontop CO [50], and the non-monotonic lateral interaction has been beaten by another Monte Carlo simulation study[52].

One interesting approach on the intermolecular interaction paid the attention to the interpretation of linewidth of M-C stretch mode according to the surface coverage.[53] Brako and Brenig included the Pt atoms adjacent to the Pt atom where a CO is adsorbed, assuming that the adjacent Pt atoms are displaced in-plane.[54] According to their calculation, the suggested adsorbate structures by Tüshaus et al. could be explained by the displacement of adjacent Pt atoms. Furthermore, they suggested that the non-monotonic lateral interaction between ontop CO molecules, showing that CO molecules in the same low of Pt lattice has higher interaction energy than CO molecules which are not in the same low.[55]

1.5 Microscopic investigation in real-space using STM

Since the development of STM, the many studies on the surface and adsorbate system were done with STM. A wide range of surface of materials were covered, from various metals and semiconductors, and adsorbed atoms or molecules. And those studies revealed various field of knowledges, such as magnetic properties, surface states and interferences, and intermolecular interactions between surface adsorbates.

1.5.1 STM and its application

The application of STM is not limited to high resolution in imaging, but also includes various spectroscopic information. The operating principle of STM, quantum tunneling, basically involves the density of states(DOS) of the adsorbate-substrate hybridized states, and resultantly the $\mathrm{d}I/\mathrm{d}V$ signal at the local point has been considered to represent the local distribution of electronic states. The spectroscopic information which can be obtained using tunneling is not limited to the electronic structures, but also the chemical information such as vibrations. In this section, I introduce the pioneering studies in this vibrational spectroscopy using STM in a qualitative way. The principle and quantitative frame will be described in Chapter 2.

Inelastic tunneling spectroscopy

Because STM offers very high current density at a very local point, it can be used as an effective electron source for exciting a molecule underneath the tip. Thus, STM is applied as a vibrational spectroscopic tools with two different approach. One is STM-InElastic Tunneling Spectroscopy(STM-IETS), which is a powerful tool for a vibrational spectroscopy in a single molecule level. STM-IETS, which detects the change of total current by inelastic excitation of vibrational modes by taking the second derivative of tunneling current (d^2I/dV^2), was first demonstrated by Stipe et al. in their study of C_2H_2 on Cu(100) as shown in Figure 1.6.[56] Kim et al. utilized STM-IETS to identify the chemical identity of the reactants and products of a chemical reaction by injection of tunneling electron. The target reaction was dehydrogenation of *trans*-2-butene to 1,3-butadiene. In this experiment, the reactant (*trans*-2-butene) and the suspected product (1,3-butadiene) were deposited onto the surface simultaneously, and all IET spectra were taken for (a) *trans*-2-butene, (b) deposited 1,3-butadiene and (c) the reaction product obtained by injection of tunneling electrons. While IET spectrum of trans-2-butene(the reactant) showed the signal of C-H stretch mode, both the molecularly deposited 1,3-butadiene and the reaction product showed similar spectral features without the C-H stretch mode signal. This

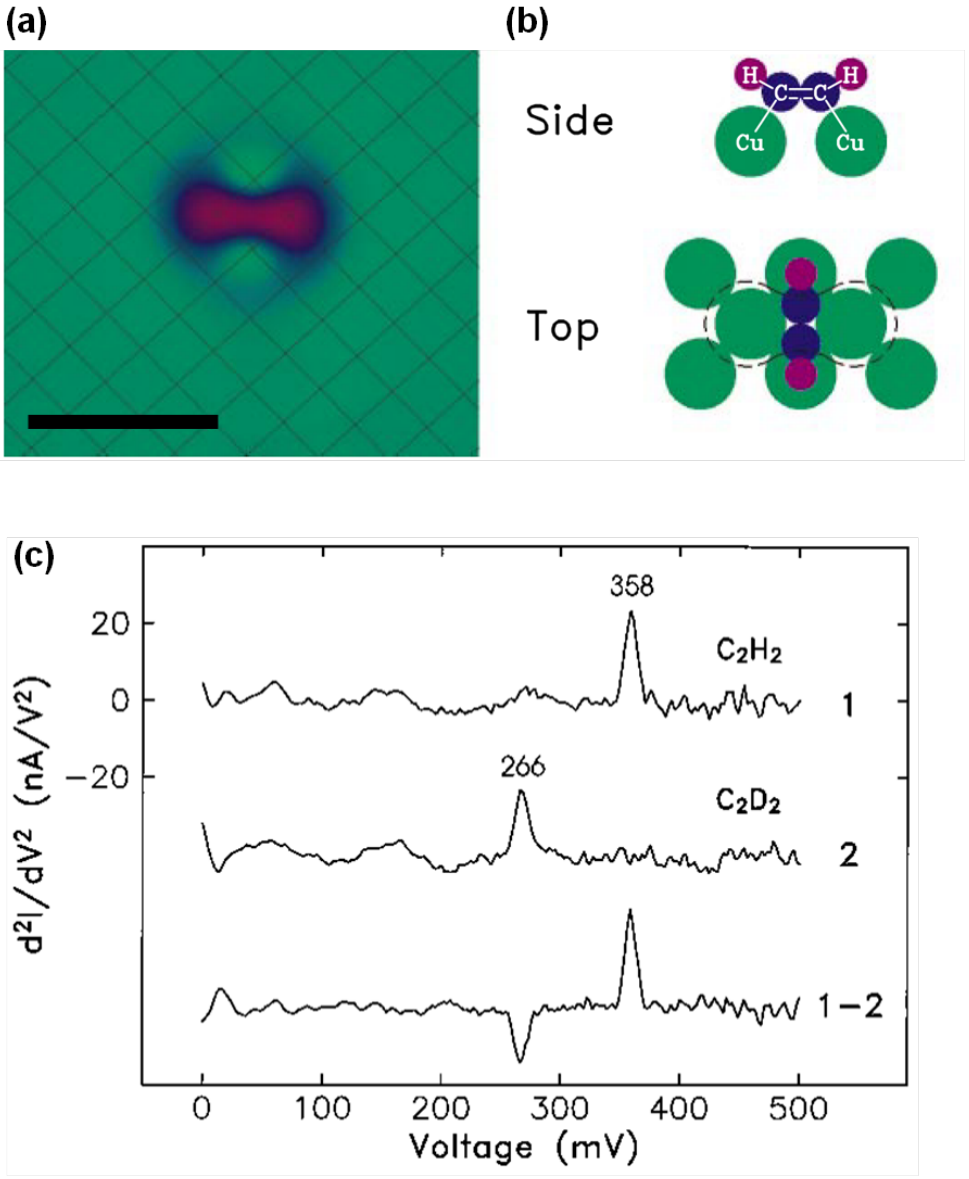

FIGURE 1.6: Inelastic tunneling spectroscopy : C_2H_2 on Cu(110). Adapted from [56], reprinted with permission from AAAS.

comparison provided the evidence for the dehydrogenation reaction from a *trans*-2-butene molecule into a 1,3-butadiene molecule.[57]

STM action spectroscopy

STM-IETS has limitation as a vibrational spectroscopic tool, one limitation is in the detectable vibrational modes due to the propensity rule. Also, STM-IETS scans the bias

with triangular wave, the target molecule need to be stable without any diffusion, reaction, or rotation during the applied bias. However, many molecules experiences surface-dynamic processes as well as reactions by injection of tunneling electrons, which transfers the energy inelastically to excite the reaction coordinate modes. STM-AS is an alternative spectroscopic methodology which can be used to measure the vibrational / electronic spectra of mobile and reactive adsorbates. The very first demonstration of spectroscopic detection of events triggered by tunneling electron was the rotation of acetylene molecule by vibrational excitation, by Stipe et al.[58] Later, similar methodology was extended to the detection of C–O stretch mode from lateral hopping of CO molecules on Pd(110) surface[59], dehydrogenation reaction of *trans*-butene molecule[57], configurational change of *cis*-butene on Pd(110) surface[60], and so on. Among these cases, Sainoo et al. introduced a new concept called "action spectroscopy" (STM-AS) which utilizes vibrationally induced molecular motion and reactions.[60] STM action spectroscopy measures the probability of the corresponding events (motion yield $Y(V)$) over a range of applied bias, to find any threshold bias which shows rapid change in $Y(V)$. In addition to the yield $Y(V)$, another important relationship in action spectroscopy is the number of electron (N)consumed during the process, which is estimated from the power law between the reaction (motion) rate and the amount of current injected.

1.5.2 CO on Pt(111) studied with STM : preceding results

*In spite of the richness of preceding results regarding CO molecules and other single-molecular study, the number of STM studies regarding CO on Pt(111) is small, and most of them are limited in terms of coverage range. Stroscio and Eigler observed two different types of isolated CO molecules at very low coverage, one as protrusion (according to them, 'bump' type) another as sombrero-type which has about half in height compared to the bump-type protrusion(Figure 1.7c and d). They could not determine the adsorption site with atomic resolution, though according to their observation and comparison to the preceding results such as the adsorption energy difference, and so on, they insisted that

*Part of this section is reproduced from my research paper with permission from [63]. Copyright 2013 American Chemical Society.

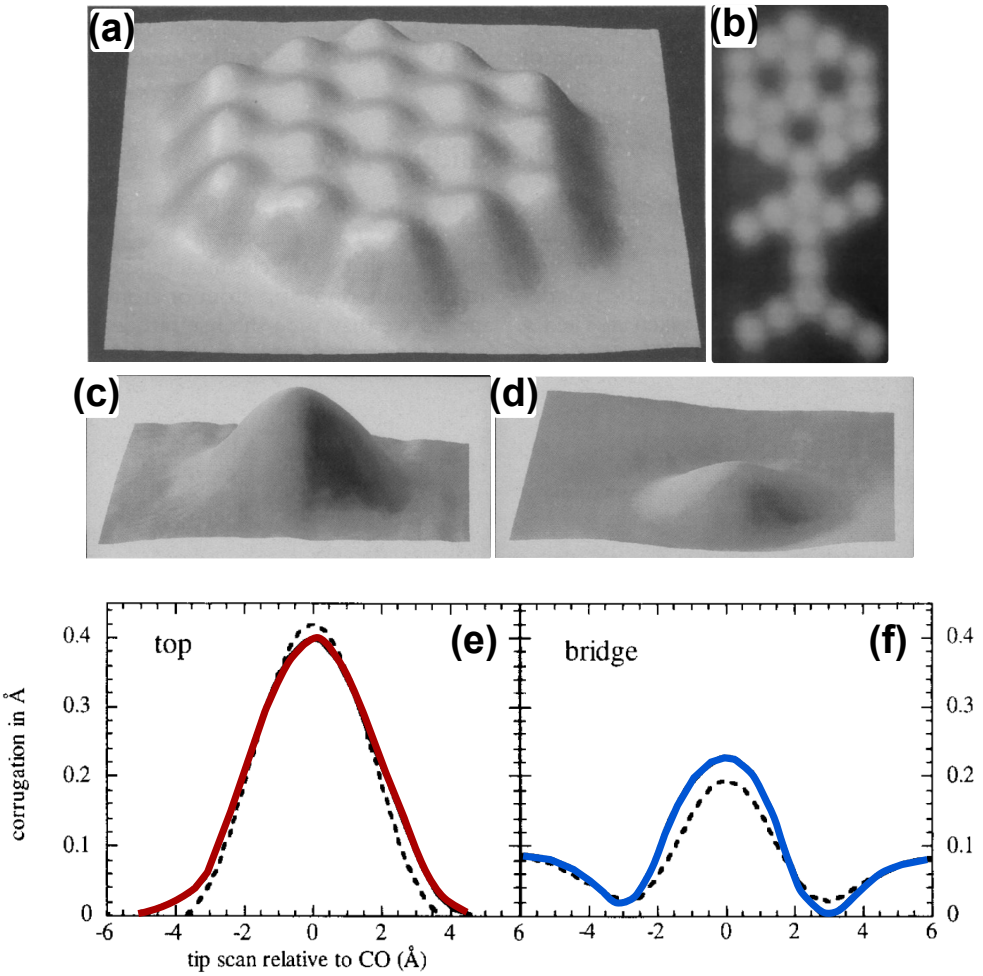

FIGURE 1.7: Result of preceding STM study on isolated CO on Pt(111). (a), (c) and (d) adapted from [?], (b) adapted from [61], (e) and (f) adapted from [62], copyright 1996, with permission from Elsevier.

the bump-type protrusion and sombrero-type protrusion as ontop and bridge CO respectively. Bocquet and Sautet et al. theoretically calculated the STM images of isolated CO on Pt(111) as shown in Figure 1.7e and f, and they successfully reproduce the topography of molecules according to the adsorption site, supporting the observation of Stroscio and Eigler.[62] Stroscio and Eigler also successfully manipulated the CO molecules to fabricate a small $(\sqrt{3} \times \sqrt{3})$R30° island by controlling junction resistance between the molecule and the STM tip, forming local $(\sqrt{3} \times \sqrt{3})$R30° islands of CO molecules(Figure 1.7a) and so-called "molecular man"(Figure 1.7b).[61, 64]

Another category of STM studies of CO on Pt(111) is the observation of $c(4 \times 2)$ domains. Regarding the $c(4 \times 2)$ domain, Song et al.[66](Figure 1.8c and d) and Pedersen

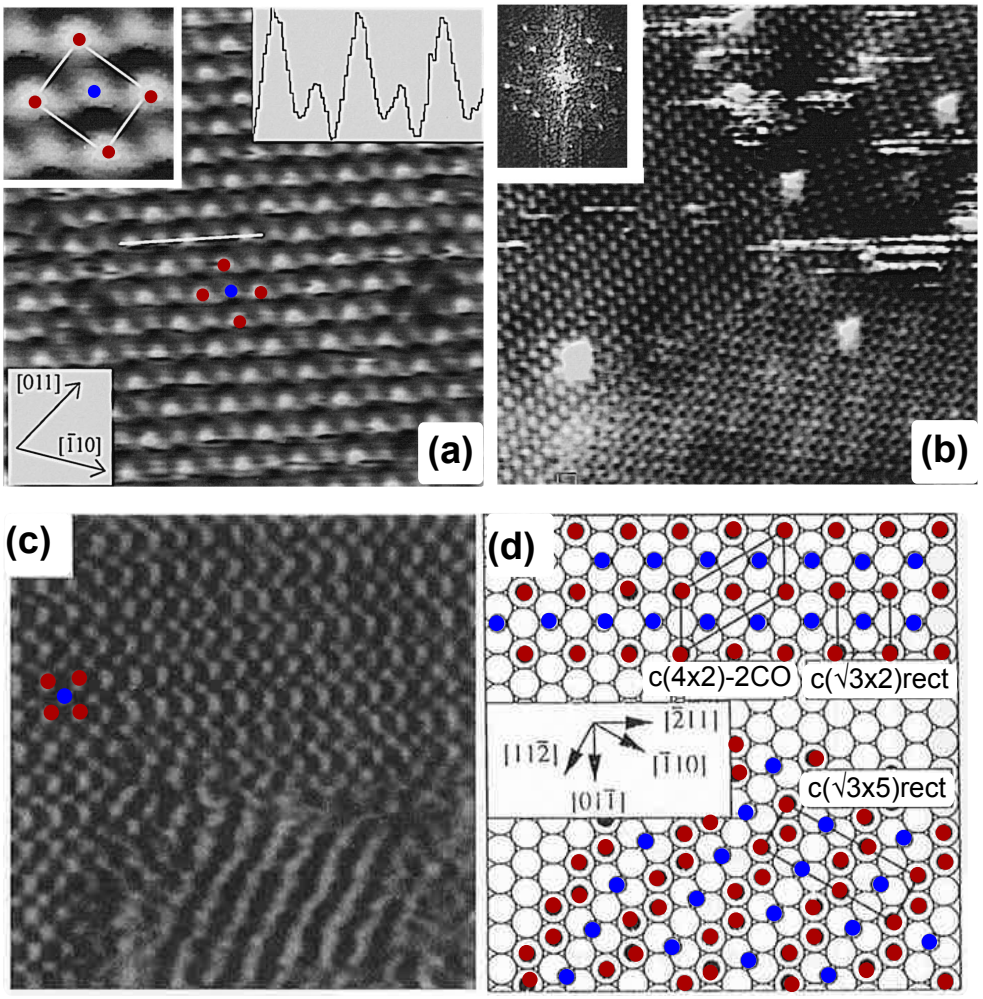

FIGURE 1.8: Results of preceding STM study on $c(4 \times 2)$ structures. (a) and (b) adapted from [65], (c) and (d) adapted from [66]. Copyright (a), (b) 1999 and (c), (d) 1996. Reprinted under permission from Elsevier.

et al.[65](Figure 1.8a and b) independently investigated overlayer structures in the 0.5 ML range, showing the $c(4 \times 2)$ domains with clearly resolved bridge species. So far, neither detailed studies of overlayer structure evolution other than 0.5 ML nor spectroscopic studies with STM such as scanning tunneling spectroscopy (STS), inelastic electron tunneling spectroscopy with STM (STM-IETS) or action spectroscopy have been reported.

References

[1] Ertl, G., Neumann, M. & Streit, K. M. Chemisorption of CO on the Pt(111) surface. *Surf. Sci.* **64**, 393–410 (1977). URL http://www.sciencedirect.com/science/article/pii/0039602877900528.

[2] Binnig, G., Rohrer, H., Gerber, C. & Weibel, E. Surface studies by scanning tunneling microscopy. *Phys. Rev. Lett.* **49**, 57–61 (1982). URL http://link.aps.org/doi/10.1103/PhysRevLett.49.57.

[3] Binnig, G., Rohrer, H., Gerber, C. & Weibel, E. 7×7 reconstruction on Si(111) resolved in real space. *Phys. Rev. Lett.* **50**, 120–123 (1983). URL http://link.aps.org/doi/10.1103/PhysRevLett.50.120.

[4] Somorjai, G. A. & Li, Y. *Introduction to Surface Chemistry and Catalysis* (Wiley, 2010), 2 edn.

[5] Ertl, G. Reactions at surfaces: From atoms to complexity (nobel lecture). *Angew. Chem. Int. Edit.* **47**, 3524–3535 (2008). URL http://onlinelibrary.wiley.com/doi/10.1002/anie.200800480/abstract.

[6] Papageorgopoulos, D. C. & Bruijn, F. A. d. Examining a potential fuel cell poison a voltammetry study of the influence of carbon dioxide on the hydrogen oxidation capability of carbon-supported pt and PtRu anodes. *J. Electrochem. Soc.* **149**, A140–A145 (2002). URL http://jes.ecsdl.org/content/149/2/A140. 00082.

[7] McQuarrie, D. A. & Simon, J. D. *Physical chemistry: a molecular approach* (University Science Books, Sausalito, Calif., 1997). 00603.

[8] Hammer, B., Nielsen, O. H. & Nørskov, J. K. Structure sensitivity in adsorption: CO interaction with stepped and reconstructed pt surfaces. *Catal. Lett.* **46**, 31–35 (1997). URL http://link.springer.com/article/10.1023/A%3A1019073208575.

[9] Hammer, B., Morikawa, Y. & Nørskov, J. K. CO chemisorption at metal surfaces and overlayers. *Phys. Rev. Lett.* **76**, 2141–2144 (1996). URL http://link.aps.org/doi/10.1103/PhysRevLett.76.2141.

[10] Blyholder, G. Molecular orbital view of chemisorbed carbon monoxide. *J. Phys. Chem.* **68**, 2772–2777 (1964). URL http://dx.doi.org/10.1021/j100792a006.

[11] Nilsson, A., Weinelt, M., Wiell, T., Bennich, P., Karis, O., Wassdahl, N., Stöhr, J. & Samant, M. G. An atom-specific look at the surface chemical bond. *Phys. Rev. Lett.* **78**, 2847–2850 (1997). URL http://link.aps.org/doi/10.1103/PhysRevLett.78.2847.

[12] Föhlisch, A., Nyberg, M., Bennich, P., Triguero, L., Hasselström, J., Karis, O., Pettersson, L. G. M. & Nilsson, A. The bonding of CO to metal surfaces. *J. Chem. Phys.* **112**, 1946–1958 (2000). URL http://jcp.aip.org/resource/1/jcpsa6/v112/i4/p1946_s1.

[13] Föhlisch, A., Nyberg, M., Hasselström, J., Karis, O., Pettersson, L. G. M. & Nilsson, A. How carbon monoxide adsorbs in different sites. *Phys. Rev. Lett.* **85**, 3309–3312 (2000). URL http://link.aps.org/doi/10.1103/PhysRevLett.85.3309.

[14] Masuda, S., Suzuki, R., Aoki, M., Morikawa, Y., Kishi, R. & Kawai, M. Spatial electron distribution of CO adsorbed on Ni(100) and Ni(111) surfaces probed by metastable impact electron spectroscopy. *J. Chem. Phys.* **114**, 8546 (2001). URL http://link.aip.org/link/JCPSA6/v114/i19/p8546/s1&Agg=doi. 00019.

[15] Nilsson, A. & Pettersson, L. G. M. Chemical bonding on surfaces probed by x-ray emission spectroscopy and density functional theory. *Surf. Sci. Rep.* **55**, 49–167 (2004). URL http://www.sciencedirect.com/science/article/B6TVY-4D7CGD4-1/2/0076f56169344e76bfa54a02b0846ffe.

[16] Steininger, H., Lehwald, S. & Ibach, H. On the adsorption of CO on Pt(111). *Surf. Sci.* **123**, 264–282 (1982). URL http://www.sciencedirect.com/science/article/pii/0039602882903284.

[17] Shigeishi, R. & King, D. A. Chemisorption of carbon monoxide on platinum {111}: Reflection-absorption infrared spectroscopy. *Surf. Sci.* **58**, 379–396 (1976). URL http://www.sciencedirect.com/science/article/pii/0039602876904775.

[18] Yeo, Y. Y., Vattuone, L. & King, D. A. Calorimetric heats for CO and oxygen adsorption and for the catalytic CO oxidation reaction on Pt(111). *J. Chem. Phys.* **106**, 392–401 (1997). URL http://jcp.aip.org/resource/1/jcpsa6/v106/i1/p392_s1.

[19] Froitzheim, H., Hopster, H., Ibach, H. & Lehwald, S. Adsorption sites of CO on Pt(111). *Appl. Phys.* **13**, 147–151 (1977). URL http://rd.springer.com/article/10.1007%2FBF00882473.

[20] Krebs, H. J. & Lüth, H. Evidence for two different adsorption sites of CO on Pt(111) from infrared reflection spectroscopy. *Appl. Phys.* **14**, 337–342 (1977). URL http://rd.springer.com/article/10.1007%2FBF00883436.

[21] Schweizer, E., Persson, B., Tüshaus, M., Hoge, D. & Bradshaw, A. The potential energy surface, vibrational phase relaxation and the order-disorder transition in the adsorption system Pt{111}-CO. *Surf. Sci.* **213**, 49–89 (1989). URL http://www.sciencedirect.com/science/article/pii/0039602889902525.

[22] Mieher, W. D., Whitman, L. J. & Ho, W. A time resolved electron energy loss spectroscopy study of CO on Pt(111): Adsorption site occupations versus coverage and temperature. *J. Chem. Phys.* **91**, 3228–3239 (1989). URL http://jcp.aip.org/resource/1/jcpsa6/v91/i5/p3228_s1.

[23] Cudok, A., Froitzheim, H. & Schulze, M. Low-temperature adsorption kinetics of CO on Pt(111) derived from nonequilibrium time-resolved electron-energy-loss spectroscopy measurements. *Phys. Rev. B* **47**, 13682–13686 (1993). URL http://link.aps.org/doi/10.1103/PhysRevB.47.13682.

[24] Kinne, M., Fuhrmann, T., Whelan, C. M., Zhu, J. F., Pantförder, J., Probst, M., Held, G., Denecke, R. & Steinrück, H.-P. Kinetic parameters of CO adsorbed on Pt(111) studied by in situ high resolution x-ray photoelectron spectroscopy. *J. Chem. Phys.* **117**, 10852 (2002). URL http://link.aip.org/link/JCPSA6/v117/i23/p10852/s1&Agg=doi.

[25] Tüshaus, M., Schweizer, E., Hollins, P. & Bradshaw, A. Yet another vibrational study of the adsorption system Pt{111}-CO. *J. Electron Spectrosc. Relat. Phenom.* **44**, 305–316 (1987). URL http://www.sciencedirect.com/science/article/pii/0368204887870317.

[26] Malik, I. J. & Trenary, M. Infrared reflection-absorption study of the adsorbate-substrate stretch of CO on Pt(111). *Surf. Sci. Lett.* **214**, L237–L245 (1989). URL http://www.sciencedirect.com/science/article/pii/0167258489900327.

[27] Hayden, B. & Bradshaw, A. The adsorption of CO on Pt(111) studied by infrared reflection-absortion spectroscopy. *Surf. Sci.* **125**, 787–802 (1983). URL http://www.sciencedirect.com/science/article/pii/S0039602883800600.

[28] Hopster, H. & Ibach, H. Adsorption of CO on Pt(111) and Pt 6(111) $\times$ (111) studied by high resolution electron energy loss spectroscopy and thermal desorption spectroscopy. *Surf. Sci.* **77**, 109–117 (1978). URL http://www.sciencedirect.com/science/article/pii/0039602878901644.

[29] Ertl, G. & Koch, J. Adsorption von CO auf einer Palladium(111)-Oberfläche. *Z. Naturforsch.* **25a**, 1906–1911 (1970).

[30] Conrad, H., Ertl, G., Küppers, J. & Latta, E. Adsorption of CO on clean and oxygen covered Ni(111) surfaces. *Surf. Sci.* **57**, 475 – 484 (1976). URL http://www.sciencedirect.com/science/article/pii/0039602876903411.

[31] Campuzano, J. C. & Greenler, R. G. The adsorption sites of CO on ni(111) as determined by infrared reflection-absorption spectroscopy. *Surf. Sci.* **83**, 301–312 (1979). URL http://www.sciencedirect.com/science/article/pii/0039602879904953.

[32] Blackman, G. S., Xu, M. L., Ogletree, D. F., Van Hove, M. A. & Somorjai, G. A. Mix of molecular adsorption sites detected for disordered CO on Pt(111) by diffuse low-energy electron diffraction. *Phys. Rev. Lett.* **61**, 2352–2355 (1988). URL http://link.aps.org/doi/10.1103/PhysRevLett.61.2352.

[33] Lahee, A., Toennies, J. & Wöll, C. Low energy adsorbate vibrational modes observed with inelastic helium atom scattering: CO on Pt(111). *Surf. Sci.* **177**, 371–388 (1986). URL http://www.sciencedirect.com/science/article/pii/0039602886901469.

[34] Graham, A. P. The low-frequency vibrational modes of c(4×2) CO on Pt(111). *J. Chem. Phys.* **109**, 9583 (1998). URL http://link.aip.org/link/JCPSA6/v109/i21/p9583/s1&Agg=doi.

[35] Engström, U. & Ryberg, R. Coupling to dipole-forbidden modes: CO on Pt(111) studied by infrared spectroscopy. *Phys. Rev. Lett.* **78**, 1944 (1997). URL http://link.aps.org/doi/10.1103/PhysRevLett.78.1944.

[36] Skytt, P., Glans, P., Gunnelin, K., Guo, J., Nordgren, J., Luo, Y. & Ågren, H. Role of screening and angular distributions in resonant x-ray emission of co. *Phys. Rev. A* **55**, 134–145 (1997). URL http://link.aps.org/doi/10.1103/PhysRevA.55.134.

[37] Haarlammert, T., Golovin, A. V. & Zacharias, H. 1π resonance of CO on Pt(111) studied by angle-resolved ultraviolet photoelectron spectroscopy. *Phys. Rev. B* **83**, 125435 (2011). URL http://link.aps.org/doi/10.1103/PhysRevB.83.125435.

[38] Norton, P., Goodale, J. & Selkirk, E. Adsorption of CO on Pt(111) studied by photoemission, thermal desorption spectroscopy and high resolution dynamic measurements of work function. *Surf. Sci.* **83**, 189–227 (1979). URL http://www.sciencedirect.com/science/article/pii/0039602879904886.

[39] Trenary, M., Tang, S., Simonson, R. & McFeely, F. An angle-resolved photoemission study of CO chemisorbed on the Pt(111) surface. *Surf. Sci.* **124**, 555–562 (1983). URL http://www.sciencedirect.com/science/article/pii/0039602883908099.

[40] Tsilimis, G., Kutzner, J. & Zacharias, H. Photoemission study of clean and c(4×2)-2CO-covered Pt(111) using high-harmonic radiation. *Appl Phys A* **76**, 743–749 (2003). URL http://link.springer.com/article/10.1007/s00339-002-1496-3. Cited by 0018.

[41] Dose, V., Rogozik, J., Bradshaw, A. & Prince, K. Inverse photoemission from CO co-adsorbed with K on Pt(111). *Surf. Sci.* **179**, 90–100 (1987). URL http://www.sciencedirect.com/science/article/pii/003960288790121X.

[42] Anazawa, T., Kinoshita, I. & Matsumoto, Y. Two-photon photoemission study of CO/Pt(111). *J. Electron Spectrosc. Relat. Phenom.* **88-91**, 585–590 (1998). URL http://www.sciencedirect.com/science/article/pii/S036820489700131X.

[43] Nieuwenhuys, B. Correlation between work function change and degree of electron back-donation in the adsorption of carbon monoxide and nitrogen on group VIII metals. *Surface Science* **105**, 505–516 (1981). URL http://www.sciencedirect.com/science/article/pii/0039602881900157.

[44] Ishi, S.-i., Ohno, Y. & Viswanathan, B. An overview on the electronic and vibrational properties of adsorbed CO. *Surf. Sci.* **161**, 349–372 (1985). URL http://www.sciencedirect.com/science/article/pii/0039602885908155.

[45] Horn, K. & Pritchard, J. Infrared spectra of ordered and disordered overlayers on metals: carbon monoxide on a Pt(111) single crystal surface. *Le Journal de Physique Colloques* **38**, 8 (1977).

[46] Poelsema, B., Palmer, R. L. & Comsa, G. Helium scattering and work function investigation of co adsorption on Pt(111) and vicinal surfaces. *Surf. Sci.* **123**, 152–164 (1982). URL http://www.sciencedirect.com/science/article/pii/0039602882901376.

[47] Kim, J.-H., Tahara, K., Jung, J., De Feyter, S., Tobe, Y., Kim, Y. & Kawai, M. Ordering of molecules with π-conjugated triangular core by switching hydrogen bonding and van der waals interactions. *J. Phys. Chem. C* **116**, 17082–17088 (2012). URL http://dx.doi.org/10.1021/jp3048949.

[48] Persson, B. Ordered structures and phase-transitions in adsorbed layers. *Surf. Sci.e Rep.* **15**, 1–135 (1992). WOS:A1992HW63500001.

[49] Persson, B. Monte-carlo calculations of adsorbate structures. *Solid State Commun.* **70**, 211–214 (1989). URL http://www.sciencedirect.com/science/article/pii/0038109889909769.

[50] FICHTHORN, K., GULARI, E. & ZIFF, R. Monte-carlo simulation of the adsorption of CO on Pt(111) - thermodynamic consideration s for the surface configuration of adsorbed species. *Surf. Sci.* **243**, 273–294 (1991). WOS:A1991FD22500037.

[51] Skelton, D., Wei, D. & Kevan, S. Non-monotonic lateral interactions in CO/Pt(111). *Surf. Sci.* **320**, 77–84 (1994). URL http://www.sciencedirect.com/science/article/pii/0039602894004552.

[52] McEwen, J. S., Payne, S. H., Kreuzer, H. J., Kinne, M., Denecke, R. & Steinruck, H. P. Adsorption and desorption of CO on Pt(111): a comprehensive analysis. *Surf. Sci.* **545**, 47–69 (2003). WOS:000186245700013.

[53] Ryberg, R. Phase transitions in a chemisorbed overlayer studied by infrared spectroscopy: CO on Pt(111). *Phys. Rev. B* **40**, 865–868 (1989). URL http://link.aps.org/doi/10.1103/PhysRevB.40.865.

[54] Brako, R. & Brenig, W. Vibrational linewidth of CO adsorbed on Pt(111). *Surf. Sci.* **336**, 27–36 (1995). URL http://www.sciencedirect.com/science/article/pii/0039602895005153.

[55] Brako, R. & Šokčević, D. Adsorbate interactions of CO chemisorbed on Pt(111). *Surf. Sci.* **401**, L388–L394 (1998). URL http://www.sciencedirect.com/science/article/pii/S0039602898000740.

[56] Stipe, B. C., Rezaei, M. A. & Ho, W. Single-molecule vibrational spectroscopy and microscopy. *Science* **280**, 1732 –1735 (1998). URL http://www.sciencemag.org/content/280/5370/1732.abstract.

[57] Kim, Y., Komeda, T. & Kawai, M. Single-molecule reaction and characterization by vibrational excitation. *Phys. Rev. Lett.* **89**, 126104 (2002). URL http://link.aps.org/doi/10.1103/PhysRevLett.89.126104.

[58] Stipe, B., Rezaei, M. & Ho, W. Coupling of vibrational excitation to the rotational motion of a single adsorbed molecule. *Phys. Rev. Lett.* **81**, 1263–1266 (1998). WOS:000075303600032.

[59] Komeda, T., Kim, Y., Kawai, M., Persson, B. N. J. & Ueba, H. Lateral hopping of molecules induced by excitation of internal vibration mode. *Science* **295**, 2055–2058 (2002). URL http://www.sciencemag.org/content/295/5562/2055.abstract.

[60] Sainoo, Y., Kim, Y., Okawa, T., Komeda, T., Shigekawa, H. & Kawai, M. Excitation of molecular vibrational modes with inelastic scanning tunneling microscopy processes: Examination through action spectra of cis-2-butene on Pd(110). *Phys. Rev. Lett.* **95**, 246102 (2005). URL http://link.aps.org/doi/10.1103/PhysRevLett.95.246102.

[61] Enter the molecular man. *New Scientist* **129**, 20 (1991). 00000.

[62] Bocquet, M.-L. & Sautet, P. STM and chemistry: a qualitative molecular orbital understanding of the image of CO on a pt surface. *Surf. Sci.* **360**, 128–136 (1996). URL http://www.sciencedirect.com/science/article/pii/0039602896005900.

[63] Yang, H. J., Minato, T., Kawai, M. & Kim, Y. STM investigation of CO ordering on Pt(111): From an isolated molecule to high-coverage superstructures. *J. Phys. Chem. C* **117**, 16429–16437 (2013). URL http://dx.doi.org/10.1021/jp404231t.

[64] Stroscio, J. A. & Eigler, D. M. Atomic and molecular manipulation with the scanning tunneling microscope. *Science* **254**, 1319 –1326 (1991). URL http://www.sciencemag.org/content/254/5036/1319.abstract.

[65] Pedersen, M. ., Bocquet, M. L., Sautet, P., Lægsgaard, E., Stensgaard, I. & Besenbacher, F. CO on Pt(111): binding site assignment from the interplay between measured and calculated STM images. *Chem. Phys. Lett.* **299**, 403–409 (1999). URL http://www.sciencedirect.com/science/article/pii/S0009261498013189.

[66] Song, M.-B., Yoshimi, K. & Ito, M. STM observations of bridge-bonded CO on Pt(111) and asymmetric on-top CO on Pt(100). *Chem. Phys. Lett.* **263**, 585–590 (1996). URL `http://www.sciencedirect.com/science/article/pii/S0009261496012304`.

Chapter 2

Methods and techniques

As indicated in the Introduction, this dissertation is focused on the analysis and discussion of real-space observation to investigate the intermolecular interaction of CO chemisorbed on Pt(111) surface. To achieve this purpose I used scanning tunneling microscopy under ultra-high vacuum(UHV) environment under cryogenic temperature. STM is one of the most powerful tools for measuring topography and surface properties in individual atom-level resolution. This chapter will describe the principles and working theory of STM and related spectroscopic tools, and experimental detail.

2.1 Scanning Tunneling Microscopy(STM)

Scanning tunneling microscopy (STM) is based on quantum tunneling behavior, the phenomena that a wavefunction tunnels through a potential barrier which exceeds the energy of wavefunction. The theoretical description of quantum tunneling began from the study of radioactivity, such as alpha decay. Later the electron tunneling was demonstrated in 1960s by Giaver, and this work led to the demonstration of vacuum tunneling in early 1970s,[1] and finally development of scanning tunneling microscopy[2] with a beautiful atomic-resolution image of silicon 7×7 surface structure[3]. STM technology has been expanded for performing in a variety of ambient conditions including air, inert gas, UHV, liquids.

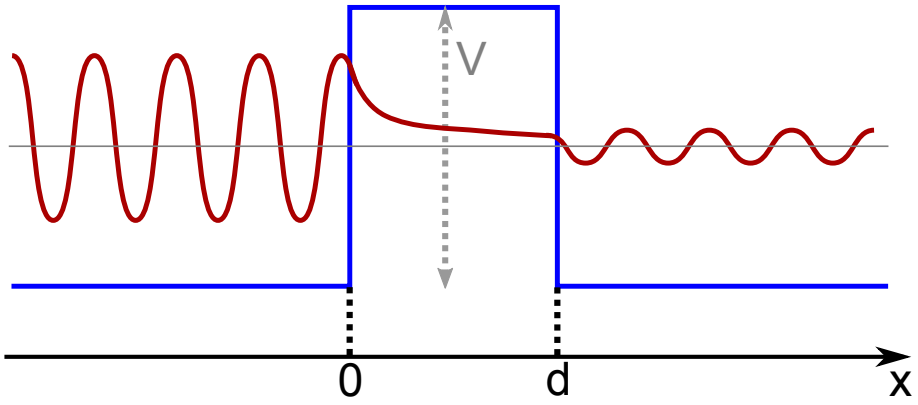

FIGURE 2.1: Schematic diagram of one-dimensional rectangular potential barrier.

2.1.1 Principles and theory of STM

The basic operating principle of STM is quantum tunneling between a sharp metal tip and a sample substrate, when the tip is brought close enough to a conducting surface within a separation of only a few Å range. Oversimplified model of this quantum tunneling is described with the square potential as shown in Figure 2.1.

Time-independent Schrödinger equation with one-dimensional rectangular barrier (Figure 2.1) gives the solutions as form of

$$\psi = e^{\pm \kappa z} \tag{2.1}$$

with the crucial parameter κ

$$\kappa^2 = \frac{2m(V-E)}{\hbar^2}. \tag{2.2}$$

The simplest case in STM is given when V corresponds to the vacuum level, so $V - E$ at Fermi level corresponds to the work function.

If the transmission probability T, or the tunneling current, can be calculated as follows:

$$T = \left\{ 1 + \frac{(e^{\kappa d} - e^{-\kappa d})^2}{16\varepsilon(1-\varepsilon)} \right\}^{-1} \approx 16\varepsilon(1-\varepsilon)e^{-2\kappa d} \tag{2.3}$$

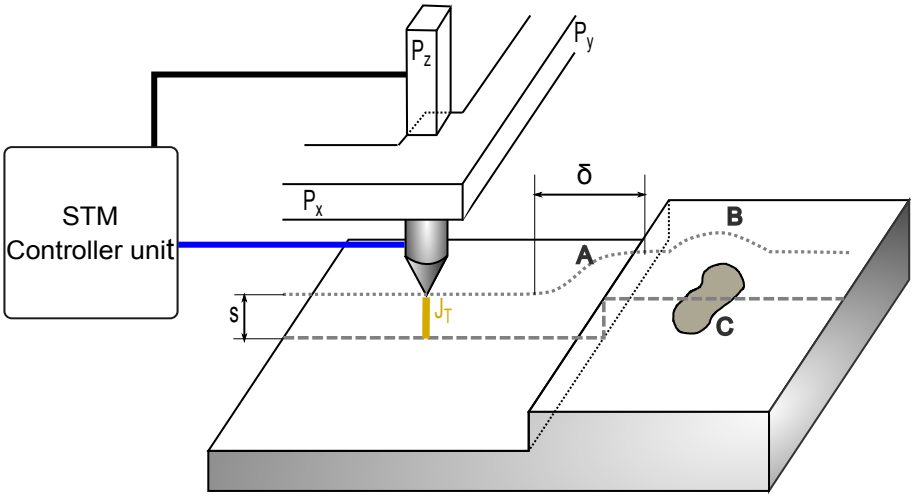

FIGURE 2.2: Principle of operation of the scanning tunneling microscope, re-drawn based on a scheme in [2]. The control unit (CU) applies the appropriate voltage V_P to the piezo-drive P_z to maintain constant tunnel current J_T at bias voltage V_T. The broken line indicate the z displacement in a y scan at (a) a surface step, and (b) a spot C with lower work function.

where $\varepsilon = E/V$, and $\kappa d \gg 1$ is assumed. Therefore, the transmission coefficient T exponentially decays with barrier width d.

The representative scheme of firstly developed STM using this simple principle is shown Figure 2.2. The position of the tip in three dimensions is accurately controlled by piezoelectric drivers. The tip scans two lateral dimensions, while P_z controls the tip height using a feedback circuit to maintain constant current. This is constant current mode, and the constant current yields roughly a constant tip height, the topographic information can be obtained with this operational mode.

2.1.2 Electronic structure of the surface and tip

More precise theoretical consideration of STM begins with first-order time-independent perturbation theory suggested by Bardeen's transfer Hamiltonian,[4] where the tunneling current I can be described as

$$I = \frac{2\pi e}{\hbar} \sum_{\mu,\nu} \{ f(E_\mu)[1 - f(E_\nu + eV_z)] - f(E_\nu + eV_z)[1 - f(E_\mu)] \} \cdot |M_{\mu\nu}|^2 \delta(E_\nu - E_\mu) \quad (2.4)$$

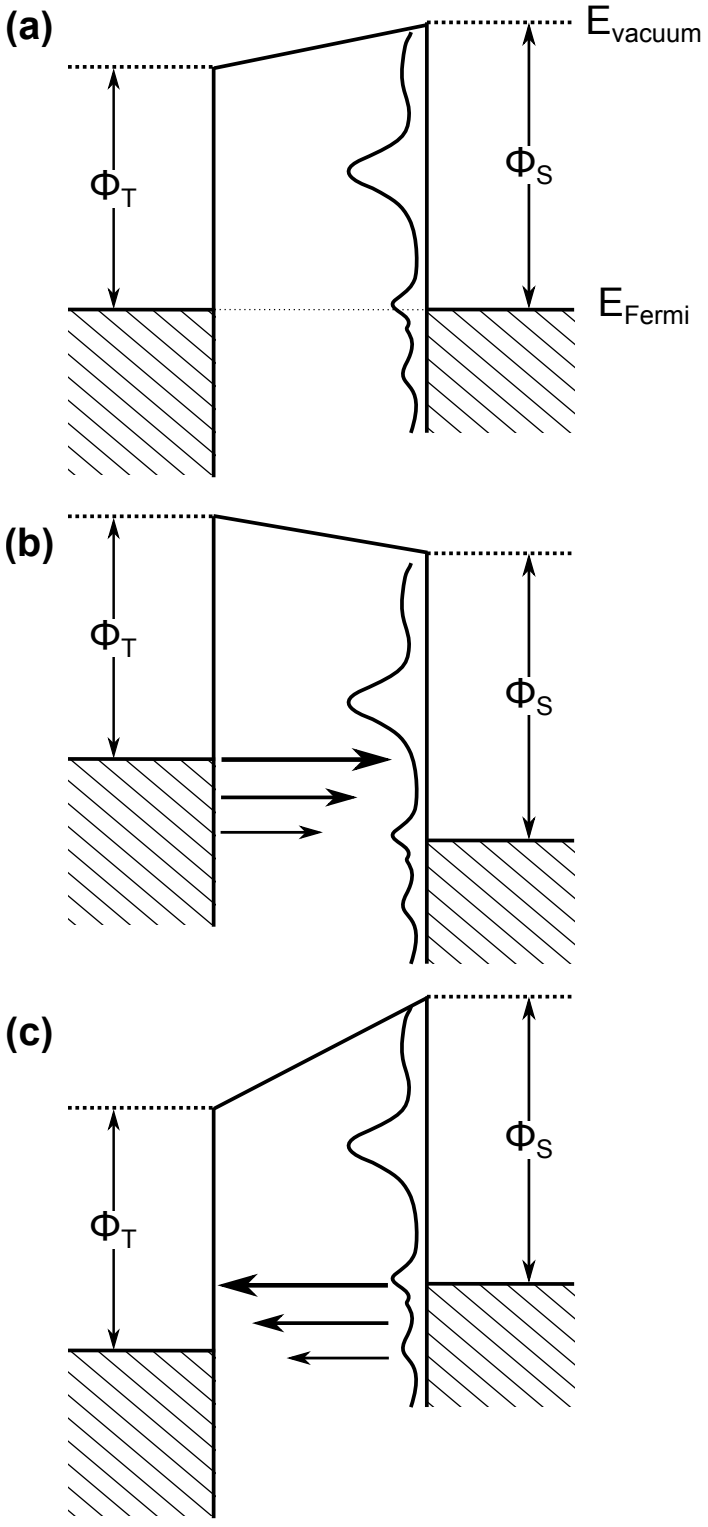

FIGURE 2.3: Energy level diagram between tip(left) and sample(adsorbate+substrate, right) according to the relative energy difference. Tungsten tip ($\phi_T = 4.5\,eV$) and Platinum substrate ($\phi_S = 5.3\,eV$) are qualitatively modeled.

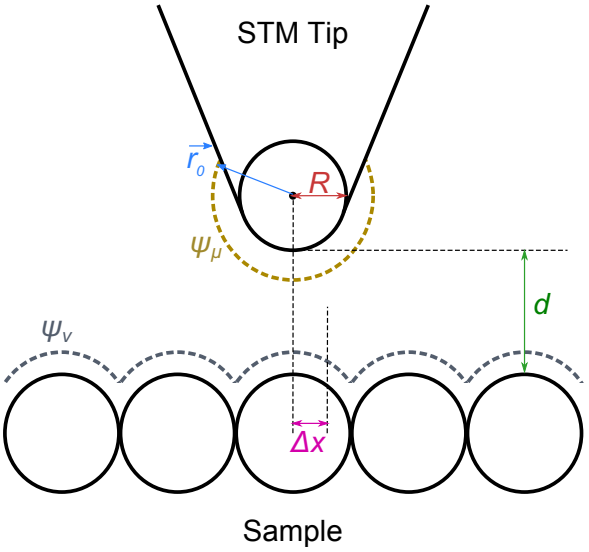

FIGURE 2.4: Schematic configuration and parameters of the tip and the sample in Tersoff-Hamann theory.

where $f(E)$ is the Fermi function, $M_{\mu\nu}$ is the tunneling matrix element between the unperturbed electronic state ψ_μ of the tip and ψ_ν of the sample surface, and E_μ (or E_ν is the energy of the state ψ_μ (or ψ_ν) in the absence of tunneling. The tunneling matrix element $M_{\mu\nu}$ is given as:

$$M_{\mu\nu} = \frac{-\hbar^2}{2m} \int d\vec{S} \cdot (\psi_\mu^* \vec{\nabla} \psi_\nu - \psi_\nu^* \vec{\nabla} \psi_\mu). \tag{2.5}$$

Therefore, precise calculation of tunneling current requires the precise wavefunction of the tip ψ_μ. One simplest model was proposed by Tersoff and Hamann[5, 6] with assuming the tip with a locally spherical symmetry and *s*-type tip wave function, to neglect the angular dependence of tip wavefunction.(Figure 2.4) *In the limits of low temperature and small applied bias voltage*, the tunneling current becomes

$$I = \frac{2\pi e^2 V_z}{\hbar} \sum_{\mu,\nu} |M_{\mu\nu}|^2 \delta(E_\nu - E_F) \cdot \delta(E_\mu - E_F) \tag{2.6}$$

$$\propto V_z \cdot n_t(E_F) \cdot e^{2\kappa R} \cdot \sum_\nu |\psi_\nu(\vec{r_0})|^2 \delta(E_\nu - E_F) \tag{2.7}$$

where $\kappa = (2m\phi)/\hbar$ the decay rate for the wavefunction in the vacuum region, ϕ the effective local potential barrier height, $n_t(E_F)$ is the density of states (DOS) at the Fermi

level (E_F) for the tip, R is the effective tip radius, and $\vec{r_0}$ is the center of curvature of the tip. Note that the local density of states (LDOS) at $E_F$at the tip center of curvature $\vec{r_0}$ can be expressed as:

$$n_S(E_F, \vec{r_0}) = \sum_\nu |\psi_\nu(\vec{r_0})|^2 \delta(E_\nu - E_F). \tag{2.8}$$

Therefore the STM images obtained near E_F in constant current mode approximately show contour maps of constant surface LDOS which is evaluated at the center of the tip. The surface wave functions decay exponentially towards the vacuum region, in the z direction normal to the surface, $\psi_\nu(\vec{r}) \propto e^{-\kappa z}$ and $\psi_\nu(\vec{r_0}) \propto e^{-2\kappa(d+R)}$.

For high applied bias voltage, the bias possibly lead a distortion of the tip and sample surface wave functions as well as modification of the energy eigenvalues, making Tersoff Hamann interpretation invalid. Therefore the undistorted zero-voltage wave functions and energy eigenvalues are taken as a first approximation, resulting that the effect of a finite bias V_z only leads to a shift in energy of the undistorted surface wave functions or DOS relative to the tip by an amount of eV_z. With this assumption the tunneling current can be expressed by result of the Tersoff and Hamann theory :

$$I \propto \int_0^{eV_z} n_t(\pm eV_z \mp E) \cdot n_S(E, \vec{r_0})\, \mathrm{d}E \tag{2.9}$$

where $n_t(E)$ is the tip DOS and $n_S(E, \vec{r_0})$ is the surface DOS evaluated at the center of curvature of the tip, and all energies are measured with respect to the E_F. This indicate, the summation of all states contribute to the tunneling current). In addition, generalizing the $n_S(E, \vec{r_0})$ with $\psi_\nu(\vec{r_0})$,

$$n_S(E, \vec{r_0}) \propto n_S(E) \cdot exp\left\{-2(d+R)\left[\frac{2m}{\hbar^2}\left(\frac{\phi_t + \phi_S}{2} + \frac{eV_z}{2} - E\right)\right]^{1/2}\right\} \tag{2.10}$$

when ϕ_t (or ϕ_S) denotes the work function of the tip (or the sample surface). Then, the tunneling current is finally described as:

$$I \propto \int_0^{eV_z} n_t(\pm eV_z \mp E) \cdot n_S(E) \cdot T(E, eV_z)\, dE \tag{2.11}$$

and $T(E, eV_z)$ is defined as

$$T(E, eV_z) = exp\left\{-2(d+R)\left[\frac{2m}{\hbar^2}\left(\frac{\phi_t + \phi_S}{2} + \frac{eV_z}{2} - E\right)\right]^{1/2}\right\}. \tag{2.12}$$

In a similar manner, a lateral resolution of STM can be estimated with the change of current in terms of lateral displacement Δx. If the current-distance relation is brought again with the tip-sample configuration in Figure 2.4, the tunneling current as a function of lateral displacement Δx can be expressed as follows :

$$I(\Delta x) = I(0) \cdot exp\left(-2\kappa \frac{\Delta x^2}{2R}\right) \tag{2.13}$$

The current profile shows a Gaussian-type current distribution with $\sim 0.7(R/\kappa)^{1/2}$. Typical value of κ is $\sim 1\,\text{Å}^{-1}$, resulting in the lateral resolution 6 Å with tip radius R $\sim 5\,\text{Å}$. In general the lateral resolution is higher than the value estimated with *s*-wave approximation, due to the angular distribution of the tip from orbitals other than *s*-orbital with vertically elongated distribution.[7–9]

2.1.3 Scanning Tunneling Spectroscopy(STS)

As described in Equation 2.11, the tunneling current is described as the integration from E_F to the designated energy level eV_z, consequently it reflects the LDOS as described in the previous section. When a bias voltage V_z is applied to the sample, the energy levels shift downward or upward in energy by $|eV_z|$ corresponding to the polarity between a tip

and a sample. Electrons tunnel from the occupied states of the tip into the unoccupied states of the sample for positive sample bias, and vice versa for negative sample bias. Thus which electronic states (i.e. unoccupied or occupied electronic states) of the sample are probed is determined by the bias polarity, and the electronic states contributing the tunneling current can be selected by varying the sample bias.

At a specific position of the tip and the sample, the spectroscopic signal $\mathrm{d}I/\mathrm{d}V_z$ at the point can be directly obtained by a lock-in amplifier technique.[10–13] Assuming $\mathrm{d}n_t/\mathrm{d}V_z \approx 0$, the spectroscopy signal can be derived from Equation 2.11,[14]

$$\begin{aligned}\frac{\mathrm{d}I}{\mathrm{d}V_z} &\propto \frac{\mathrm{d}}{\mathrm{d}V}\int_0^{eV_z} n_t(\pm eV_z \mp E)\cdot n_S(E)\cdot T(E,eV_z)dE \\ &\propto en_t(0)\cdot n_s(eV_z)\cdot T(eV_z,eV_z) + \int_0^{eV_z} n_t(\pm eV_z \mp E)\cdot n_S(E)\cdot \frac{\mathrm{d}T(E,eV_z)}{\mathrm{d}V_z}\mathrm{d}E \end{aligned} \quad (2.14)$$

The first part of Equation 2.14 is proportional to the LDOS of the sample (n_s) at the energy eV. If the second part holds for following assumptions, the whole $\mathrm{d}I/\mathrm{d}V$ can be considered as LDOS of the sample:

- The applied bias should be smaller than the work function of tip and sample.
- The transmission coefficient T should vary slowly (smooth and monotonic) with energy.

If the V_z becomes relatively large, comparable to the work function of tip and sample, then the transmission coefficient depends on the sample bias in an exponential manner (Equation 2.12). This exponential dependence can be rendered to represent improved in terms of LDOS by normalization such as $\mathrm{d}\ln I/\mathrm{d}\ln V = (\mathrm{d}I/\mathrm{d}V)/(I/V)$. In STS at a fixed tip-sample separation, the $1/V_z$ diverges in the low bias limit and the z-dependence of T can be ignored. To remove the singularity near E_F, one can use a filter function.

2.1.4 Inelastic tunneling & action spectroscopy

In the theoretical description of tunneling current, the tunneling process does not take account any energy transfer process, i.e. electrons are elastically tunneling through the tunneling junction. However, when oscillators such as surface phonon or molecular vibration exist at the tunneling junction, the oscillators may interact with tunneling electrons, resulting in energy transfer between the tunneling electrons and the oscillators. This process which involves inelastic energy transfer is called inelastic process at the corresponding tunnel junction.

The theoretical model for inelastic tunneling has been developed by Persson and Baratoff as an adsorbate-induced resonance model.[15] Recall the energy diagram in Figure 2.3, and consider the three components of the system: the tip($|t\rangle$), the surface($|s\rangle$) and adsorbate ($|a\rangle$) states. The adsorbate-induced model is described with a Hamiltonian with the vibrational terms in it:

$$
\begin{aligned}
H &= H_0 + H_{\text{vib}} + H' \qquad (2.15)\\
H_0 &= \varepsilon_a |a\rangle\langle a| + \sum_s \varepsilon_s |s\rangle\langle s| + \sum_t \varepsilon_t |t\rangle\langle t| + \sum_s (V_{sa}|s\rangle\langle a| + \text{H.c.}) + \sum_t (V_{ta}|t\rangle\langle a| + \text{H.c.})\\
H_{\text{vib}} &= \sum_\nu \hbar\Omega_\nu (b_\nu^\dagger b_\nu + 1/2)\\
H' &= \sum_\nu H'_\nu = \sum_\nu \chi_\nu (b_\nu^\dagger + b_\nu)|a\rangle\langle a|
\end{aligned}
$$

The summation takes account of all available vibrational modes of the adsorbate(ν with creation and annihilation operator ($b_\nu, b_\nu^\dagger$), and perturbation term (H') accounts for the coupling (hopping) between the electronic state of the adsorbates and the vibrational modes. If the Hamiltonian is simplified by assuming the tip state constant, and bring the hybridized states $|a\rangle \bigoplus |s\rangle \Rightarrow |\alpha\rangle$ and $|b\rangle \bigoplus |t\rangle \Rightarrow |\beta\rangle$, the tunneling current is expressed as a simple form[16]:

$$
I(V) = 2e \int \mathrm{d}\varepsilon \frac{\Gamma_s \Gamma_t}{(\Gamma_s + \Gamma_t)^2} [n_t(\varepsilon) - n_s(\varepsilon)] \rho_a(\varepsilon), \qquad (2.16)
$$

where Γ_s and Γ_t are the substrate-adsorbate and tip-adsorbate tunneling constants, and $\rho_a(\varepsilon)$ is the adsorbate density of state. This tunneling current includes both of the elastic current and inelastic current. The fraction between elastic current and inelastic current is given near $|eV| = \hbar\Omega$, and assuming the inelastic current is approximated by $I_{\text{in}}^{(2)} \simeq e\Gamma_{\text{in}}$:

$$f_{\text{in}} \simeq \pi \frac{eV - \hbar\Omega}{eV} \frac{\Gamma_{\text{eh}}}{\hbar\Omega} \left[1 + \frac{(\varepsilon_{\text{F}} - \varepsilon_{\text{a}})^2}{\Gamma_s^2}\right] \theta(eV - \hbar\Omega) \tag{2.17}$$

where $I_{\text{in}}^{(2)} = f_{\text{in}} I_{\text{el}}^{(0)}$, and in practice f_{in} is about 1 %.

Series-expansion of $I(V)$ results in not only the elastic current with zeroth order, but also the second-order components with elastic and inelastic currents, and they are given by:

$$I_{\text{el}}^{(2)} = (-2\pi) 2e \frac{\Gamma_s \Gamma_t}{\Gamma_{st}^2} \int \mathrm{d}\varepsilon [\rho_a^{(0)}(\varepsilon)]^2 \Gamma_{\text{a,ph}}(\varepsilon) [n_s(\varepsilon) - n_t(\varepsilon)] \tag{2.18}$$

$$I_{\text{in}}^{(2)} = \frac{2e}{\hbar} \frac{\Gamma_s \Gamma_t}{\Gamma_{st}^2} \int \mathrm{d}\varepsilon \rho_a^{(0)}(\varepsilon) \Gamma_{\text{a,ph}}(\varepsilon) [n_s(\varepsilon) - n_t(\varepsilon)] \tag{2.19}$$

where $\Gamma_{st} = \Gamma_s + \Gamma_t$ and $\Gamma_{\text{a,ph}}$ is the energy dissipation to the vibrational excitation. The elastic component is due to the backscattering with an intermediate virtual state, and inelastic current corresponds to the real emission or absorption over a vibrational excitation. The inelastic tunneling spectroscopy (IETS) deals with the second derivative of tunneling current $\mathrm{d}I^2/\mathrm{d}^2V$, and generally considered as to detect the surface vibrational modes with tunneling electrons. However, in practice it is known that vibrational modes which are detectable in electron excitation as EELS, due to the contribution of elastic components in the correction.

In contrast to IETS which also includes the effect of the elastic correction, the action spectroscopy, the other single-molecule spectroscopy available with STM is known to account for only inelastic currents. In the next subsection I will describe the action spectroscopy and the theoretical model briefly.

Action spectroscopy

If the tunneling current triggers any event to the adsorbate, such as lateral diffusion, rotation, desorption or chemical reaction, the tunneling process is considered as inelastic process because of the energy transfer involved with the specific event. The term "Action spectroscopy" takes account of the rate (or yield, probability) of the event as a function of sample bias voltage(energy). The rate(yield) of the event shows thresholds which correspond to the energy state involved with the reaction coordinate mode of the event.

The event accounted for action spectroscopy purely originates from the inelastic currents, consequently the theoretical model involves the vibrational density of state in its theoretical model. According to the theoretical model assuming the over-barrier reaction via inter-mode coupling. [17] According to the model, the reaction rate $R^{\mathrm{OB\_IM}}(V)$ by inter-mode coupling is expressed by:

$$R^{\mathrm{OB\_IM}}(V) = \frac{\gamma_{\nu,\mathrm{RC}}}{\gamma^{\nu}_{\mathrm{eh}} + \gamma_{\nu,\mathrm{RC}}}\Gamma^{\nu}_{\mathrm{iet}}(V) \simeq \frac{\gamma_{\nu,\mathrm{RC}}}{\gamma^{\nu}_{\mathrm{eh}}}\Gamma^{\nu}_{\mathrm{iet}}(V) \equiv K\,\Gamma^{\nu}_{\mathrm{iet}}(V) \tag{2.20}$$

where $\gamma_{\nu,\mathrm{RC}}$ is ν–RC coupling rate, $\gamma^{\nu}_{\mathrm{eh}}$ is a damping rate via electron-hole pair generation. The inelastic current(I_{iet}) which exert the event is modeled with vibrational generation rate Γ_{iet}, as follows:

$$I_{\mathrm{iet}} = e\Gamma^{\nu}_{\mathrm{iet}}(V) = e\int_0^{\infty} \mathrm{d}\omega\, \rho^{\nu}_{\mathrm{ph}}(\omega)\Gamma^{\nu}_{\mathrm{in}}(\omega, V) \tag{2.21}$$

where $\Gamma^{\nu}_{\mathrm{in}}(\omega, V)$ is a spectral generation rate corresponding to an excitation of energy $\hbar\omega$. Here the ρ_{ph} accounts for vibrational density of states with characteristic frequency Ω, which is high-energy mode. The spectral generation rate is given as follows at low temperature $k_{\mathrm{B}}T \ll \hbar\Omega$, at tunneling condition $\Gamma_t \ll \Gamma_s$ and in the extended wide-band limit:

$$\Gamma^{\nu}_{\mathrm{in}}(\omega, V) \approx \gamma^{\nu}_{\mathrm{eh}}\frac{\Gamma_t}{\Gamma_s}\frac{|eV| - \hbar\omega}{\hbar\omega}\theta(|eV| - \hbar\omega). \tag{2.22}$$

Accordingly the reaction yield is given by:

$$Y(V) = \frac{R(V)}{V} = K_{\text{eff}} \frac{1}{V} \int_0^{|eV|} \mathrm{d}\,\omega \rho_{\text{ph}}(\omega)(|eV| - \hbar\omega), \tag{2.23}$$

where the effective prefactor $K_{\text{eff}} = \frac{\gamma_{\text{eh}}(\Omega)}{\hbar\Omega\sigma_0} \frac{\Gamma_t}{\Gamma_s} K$. The effective prefactor determines the order of the reaction yield, including the effect of the inter-mode coupling, the height of diffusion barrier and damping constant of high-energy mode. The prefactor will be described in Chapter 5 again.

2.2 Experimental: sample preparation & measurements

2.2.1 Low-temperature STM(LT-STM)

All STM measurements were performed with low-temperature STM (LT-STM, Omicron GmbH) equipped with a load-lock, and a sample preparation chamber with a sample transfer system. The sample preparation chamber and the STM chamber were kept in ultra-high vacuum (UHV) with the base pressure 2×10^{-7} Pa and 2.7×10^{-9} Pa, respectively. Temperature of the sample stage during STM measurement is kept as 4.7 K with the liquid helium cryostat.

The detailed configuration of vacuum system for STM chambers is as follows: the load lock chamber, the preparation chamber for cleaning of the sample substrate, and the STM chamber for STM measurement and the introduction of molecules. All the chambers are equipped with rotary pumps and turbo molecular pumps for making high vacuum. Load lock chamber was used to introduce samples into the system. UHV condition of the preparation and the STM chamber was achieved by pumping with rotary pumps and turbomolecular pumps, followed by baking the chamber for 3 or 4 days at $\sim$ 450 K. The UHV condition was maintained with ion pumps and titanium sublimation pumps. Transfer of samples and STM tips between the chambers (STM–preparation, preparation–load lock)

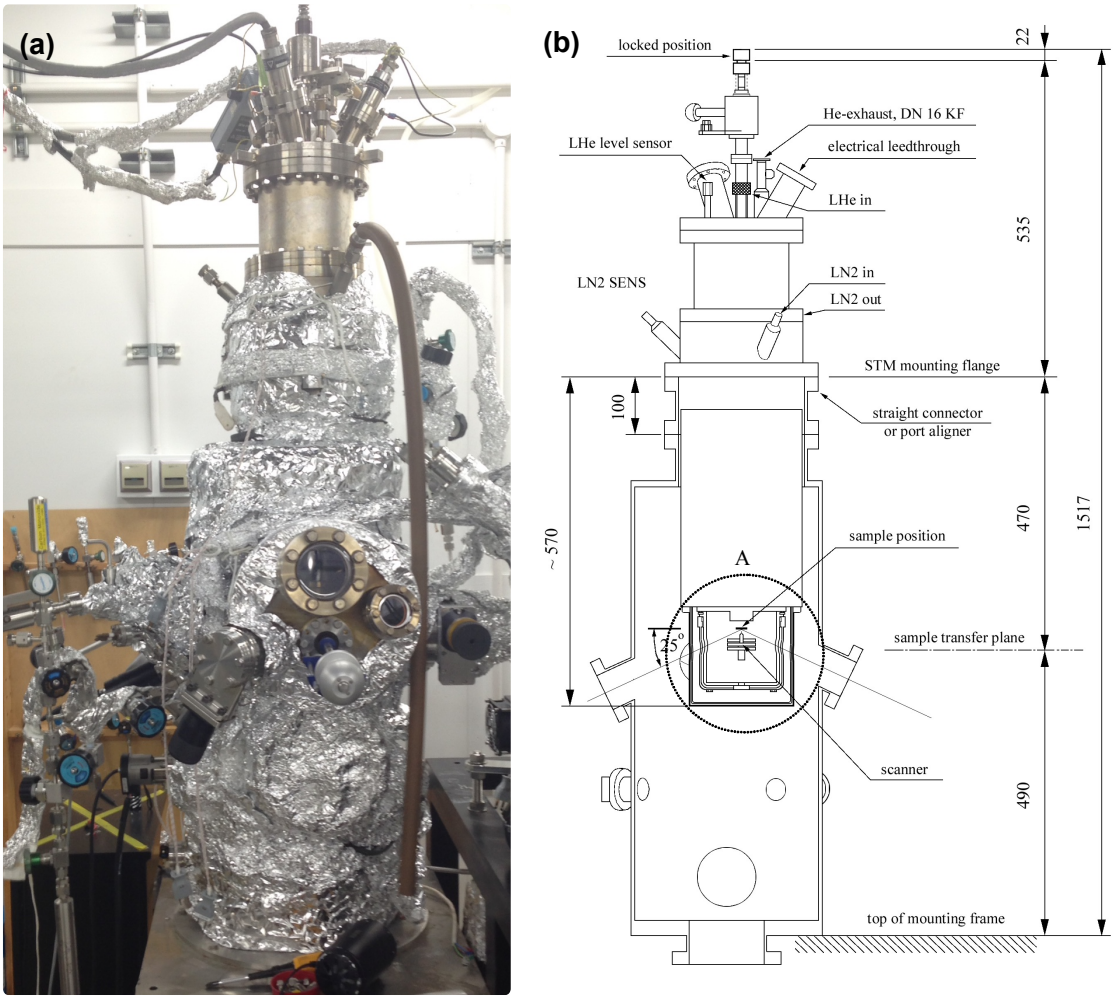

FIGURE 2.5: (a) A photo of Omicron LT-STM used in this dissertation and (b) the configuration of LT-STM chamber. (b) adapted from [18]

was achieved with a magnetically coupled transfer rod. The transfer between the transfer rod and the sample stage (in the preparation chamber), and between STM head and transfer rod (in STM chamber) were carried out by using wobble sticks in each chamber. The introduction of molecules to the STM chamber is through a small pipe connected to a leak valve. At the end of gas-introducing pipe, a small box which is made using Ta foil is adopted to increase the local pressure, achieving high-efficiency in adsorption.

The STM head is cooled down to 4.7 K by double cryostat system equipped in the STM chamber. The outer cryostat is cooled with liquid N_2, and the inner cryostat is cooled with liquid helium, leading to the cooling-down to 4.7 K of STM head and the tip which

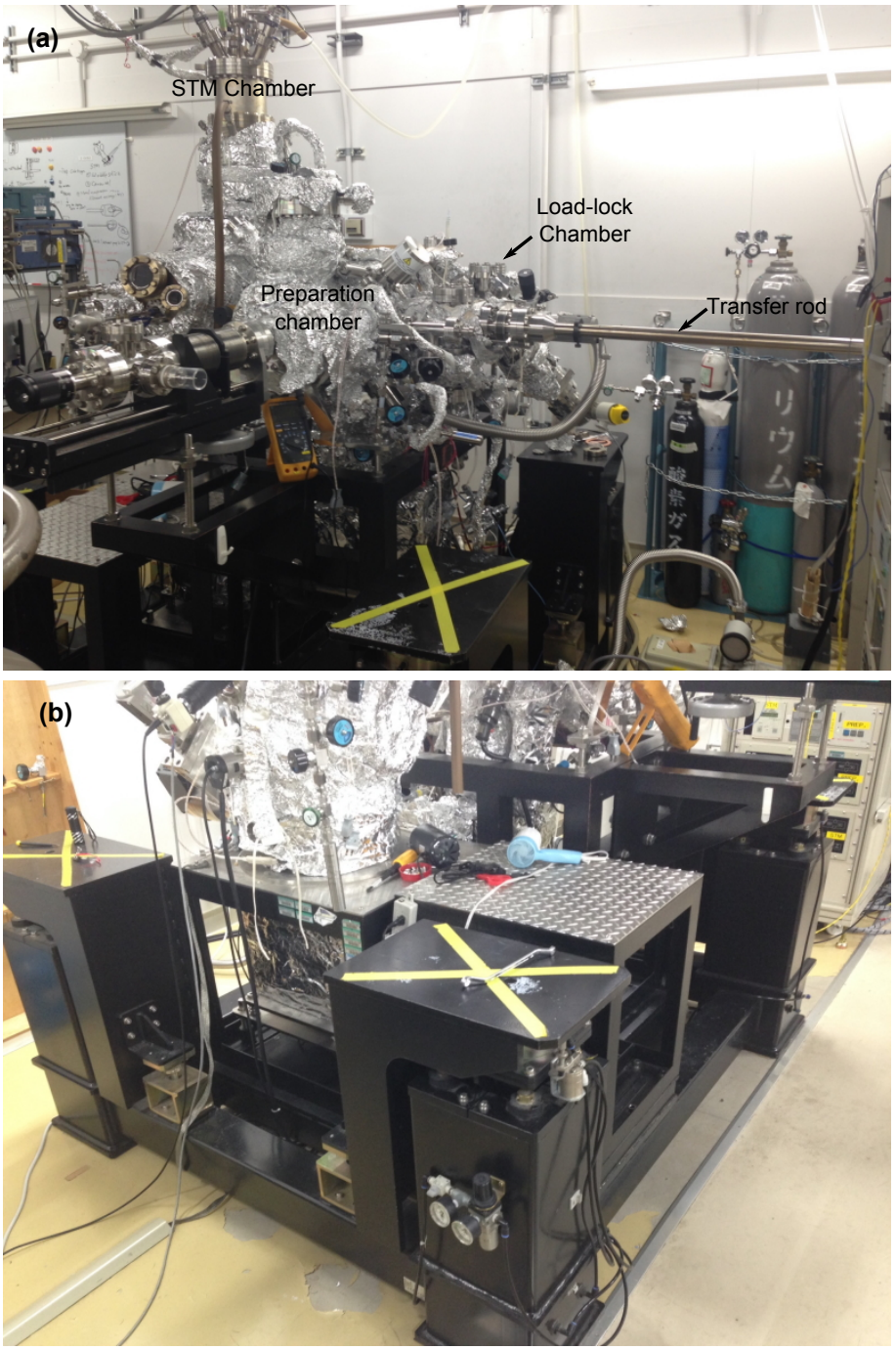

FIGURE 2.6: (a) Photo of chamber configuration and (b) air-damping support.

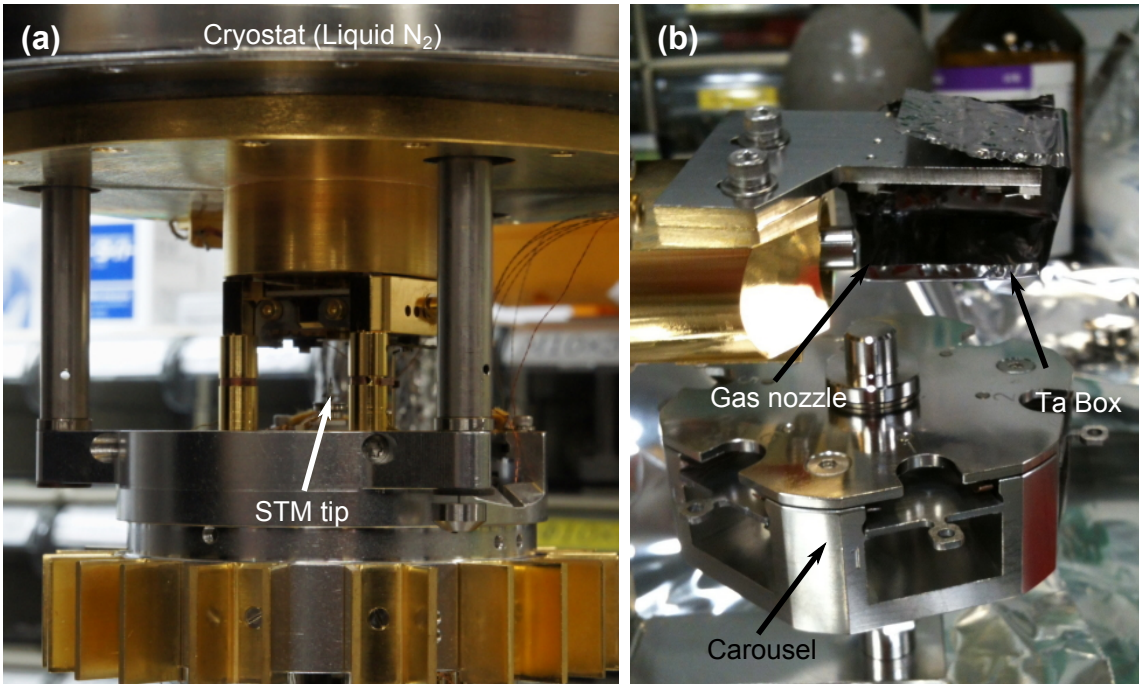

FIGURE 2.7: (a) Photo of STM head and (b) gas-dosing unit

is thermally connected to the bottom of inner cryostat by copper blocks. The temperature of STM head is monitored using Si diode sensor which is connected to the temperature controller. The temperature controller also allows the temperature control in the range of liquid helium temperature to $\sim$ 50 K. The outer cryostat insulates the inner cryostat so as to reduce the evaporation rate of liquid helium, elongating the duration time. Liquid N_2 and liquid He were periodically refilled every 12 and 24 hours respectively, to maintain the 4.7 K of head temperature. To protect the low temperature against radiative heat from the chamber wall as well as viewing ports, the STM stage is covered with two cylindrical Cu shields. These rotatable shields have small hole(approximately 2×2 cm in size) in different direction, which are in different direction when they are in shielding position. The shields are rotated to the transfer position to align the holes onto the direction of wobble stick, allowing the transfer of samples and tips.

To protect the STM system from any noise, two noise-preventing systems are adopted: one is vibration-isolation, and another is electricity-isolation. The isolation of whole STM system from the mechanical vibration, an air-damping support using pressurized N_2(Figure 2.6b)

is adapted. More effective vibration-isolation during the STM measurement is done by hanging the STM head, connecting the STM to the chamber by using only three strings. The electric isolation is achieved by grounding the whole system to the earth. To prevent any electrical interference, most of electric cables are disconnected during the measurements.

2.2.2 Electronic setup: for scanning & measurement of spectroscopy

The STM controller system is "SCALA" provided by Omicron. The system is connected to a PC and the SCALA software is used to user-control of tunneling current, sample bias and the feedback parameters as well as image acquisition. The tunneling current measured at the tip-sample junction is converted to a voltage by a preamp, and the signal is sent to the SCALA and an oscilloscope (Waverunner, NF). Sample bias voltage is controlled by SCALA during scanning, and by function generator (Wavefactory WF1945, NF) during spectroscopy. $\mathrm{d}I/\mathrm{d}V$ and $\mathrm{d}^2I/\mathrm{d}V^2$ are measured with two lock-in amplifiers (LI5640, NF), and recorded using the oscilloscope. The schematics of whole measurement system is shown in Figure 2.8.

2.2.3 Preparation of Pt(111) clean surface & CO exposure

The preparation of clean Pt(111) surface was carried out in the preparation chamber. The crystal was annealed to 1220 K via electron bombardment for 10 min, followed by room-temperature argon ion sputtering for 10 min (Ar pressure, 2×10^{-4} Pa; energy, 1000 eV). After 5 to 8 repeated cycles of annealing and sputtering, the sample was exposed to O_2 (1×10^{-5} Pa) at 750 K for 10 min, and flash-annealed to 1220 K to remove remained oxygen. Prepared sample was transferred to the STM chamber mainly in 5 min, and scanned to confirm the cleanness. Most cases the defect density was lower than 0.003 ML (five defects per 10×10 nm^2).

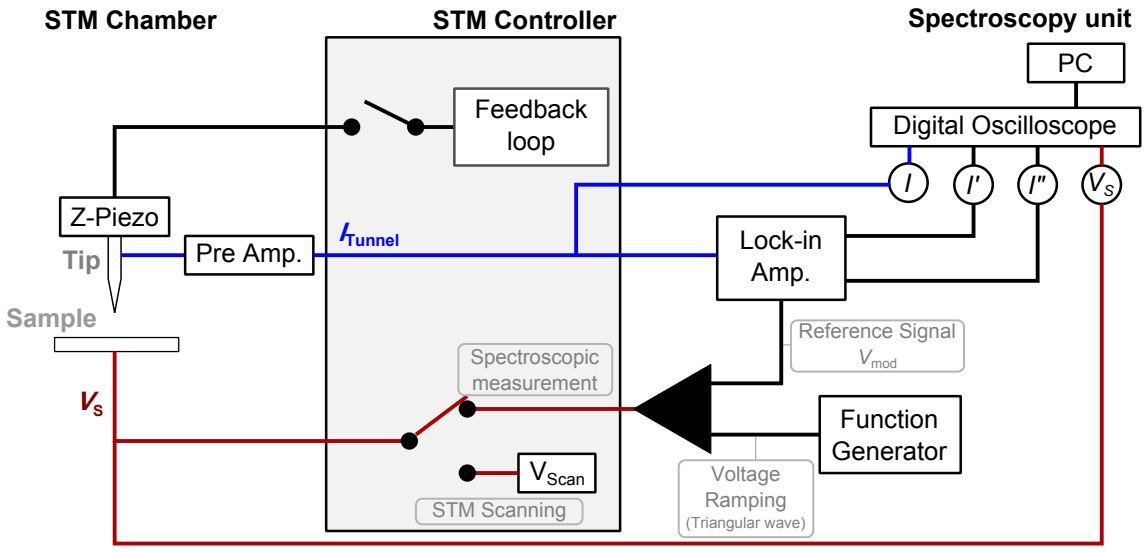

FIGURE 2.8: Schematic configuration of imaging & spectroscopic measurement system. The situation of spectroscopic I-V measurement is shown in the configuration of two switches: feedback loop off, voltage is connected to the lock-in amp and the function generator.

The cleaned surface of Pt(111) was exposed to CO, and the temperature of CO gas was 300 K and the surface temperature of the surface is estimated to be $\sim$ 50 K. The temperature of 50 K reflects the temperature rise during the exposure using the wobble stick, (a) removal of the crystal from the STM sample holder, (b) approaching the crystal to the gas nozzle and waiting for certain time, and (c) inserting the crystal back to the STM head. The surface temperature according to the time taken for the exposure process was estimated from the calibration data measured with a thermocouple attached to the sample. The amount of gas exposure is controlled by the exposing pressure, ranging from $P_{\text{Base}} \times 2$ to $P_{\text{Base}} \times 10$, and the exposing time, ranging from 3 seconds to 30 seconds, according to the intended surface coverage(θ). Note that the pressure was read at the ion gauge, and the gas dosing unit was equipped with a small Ta box to increase local pressure, the actual pressure near the sample surface would be higher than the read value.

2.3 Measurement of spectroscopic information: STS and STM-AS

2.3.1 Spectroscopic measurement: STS

Measurement of STS involves the measurement of $I - V$ curve with specific sample bias range, where the triangular wave is provided by the function generator, with modulation from a lock-in amplifier to obtain differential value $\mathrm{d}I/\mathrm{d}V$. The measurement configuration is schematically represented in Figure 2.8, controlled by STM control unit (SCALA), function generator and lock-in amplifier. Whole control of measurement was done by a Macro, simple language provided from Omicron. The basic experimental step is like below:

- Set the junction resistance by setting I_T and V_S
- Feedback loop open
- Apply measurement wave(triangular wave) modulated by the lock-in amp.

The function generator and oscilloscope is synced by an extra channel provided in the SCALA system. The oscilloscope records whole $I - V$ curve as well as $\mathrm{d}I/\mathrm{d}V$ curve by receiving $\mathrm{d}I/\mathrm{d}V$ signal from the lock-in amplifier. The recorded data is transferred into a PC using ActiveDSO interface, saved into EXCEL file. Typically 797 MHz of modulation frequency and 50 mV of modulation amplitude were used for the lock-in amp. parameters. The initial junction resistance is, (a) first the V_S is determined approximately $25 \sim 30$ % of voltage range (for example, if the measurement range is 3 V, the initial V_S can be set in 1 V), and (2) the I_T is determined by testing the resultant current, which should be in the range of detection limit (typically $\pm 50\,\mathrm{nA}$).

Measurement of STM-IETS basically employs similar configuration and measurement processes to STM measurement, with the adjusted energy range for the wavefunction and more repeated measurements due to low signal-to-noise ratio. For STM-IETS

measurements, the $\mathrm{d}I/\mathrm{d}V$ signal is used as a reference signal to the lock-in amp., and the phase between the reference signal and measured $\mathrm{d}^2I/\mathrm{d}V^2$ kept orthogonal (90°).

2.3.2 Spectroscopic measurement: Action spectroscopy

As previously described in the theory section, the action spectroscopy measures the 'yield', i.e. probability of any specific event in terms of the number of electrons. Here the event can be any surface processes with *change in conductance*, for instance lateral hopping, desorption or chemical reaction.

Experimental measurements

The first step is counting the number of electrons with a specific energy (bias voltage) required for triggering the event. Measurement of single event is done with following processes :

- Fix the position of the tip to the point of measurement
  (for example. on the target molecule).
- Set the junction resistance by setting I_T and V_S with the feedback loop closed.
- Feedback loop open
- Set the energy V_S to the target value, and retain the energy during designated time (t_Pulse).

Here, the initial setting of junction resistance should be adjusted to get wanted I_set when the energy(V_S) is set to target value, and the time ($t_\mathrm{Pulse} = t_\mathrm{Pulse\_End} - t_\mathrm{Pulse\_Start}$ in Figure 2.9) need to be adjusted long enough to detect the event by the current change. With a single measurement of $I - t$, one can get the amount of charges to trigger a single event : $I_\mathrm{set} \times t_\mathrm{event}$. In the real experimental $I - t$ curve shown in Figure 2.10a, each blue line corresponds to each time event. This measurement should be repeated with the designated energy (sample bias V_S) for several times to estimate the representative amount of

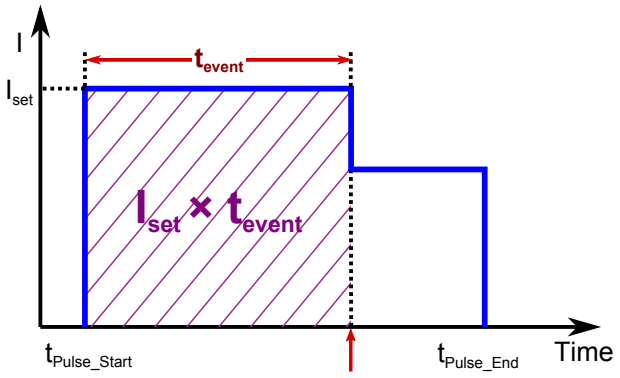

FIGURE 2.9: Schematic $I - t$ curve for a single bias pulse to detect an event.

charge (or mean time, rate) required to trigger one event at corresponding energy(V_S). This repeated measurements should be done at every specified energy (V_S) in the energy range of interest. Note that the set current during the $I - t$ measurement need to be constant over the bias range of interest, because the order of reaction may change according to the sample bias. To obtain the reaction order, the repeated measurements at the specified energy with different I_{set} is also necessary. Another point to note is, the tip condition should be kept stable during the measurements over the energy range. The stability of resultant I_{set} can be one measure of tip stability.

Statistical interval estimation from experimental data: theory

The next step is the interval estimation of mean value of the time (or number of the electron obtained by $I_{set} \times t_{event}$) at the specified energy (sample bias V_S). The repeated measurement at each specified V_S satisfies the Poisson experiment condition, i.e. experiments yielding numerical values of a random variable X, the number of outcomes (events) occurring during a given time interval[19], and having following properties:

- The number of outcomes occurring in one time interval is independent of the number that occurs in any other disjoint time interval : independent trials, no memory

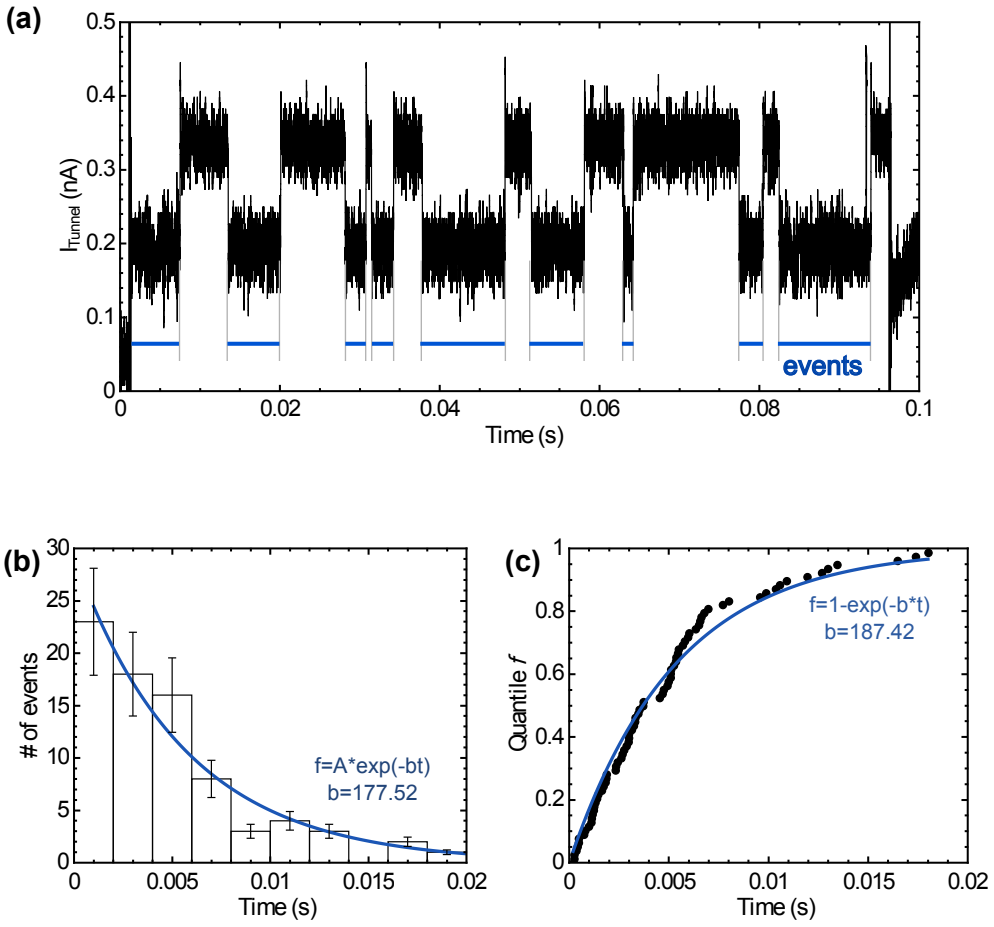

FIGURE 2.10: (a) Experimentally obtained I-t curve for bridge-ontop* shuttling, which will be discussed in Chapter 5. Each blue line indicates each event, and the statistical representations of whole measured time-events are shown in (b) time-bin histogram and (c) inverse of the quantile plot and corresponding results of exponential fitting, from measured 78 time events at 240 mV.

- The probability that a single outcome will occur during a very short time interval or in a small region is proportional to the length of the time interval or size of the region, does not depend on the number of outcomes occurring outside this time interval
- The probability that more than one outcome will occur in such a short time interval is negligible.

However in the action spectrum, the random variable (sample) is not the frequency with specified time interval, but the time (or $I \times t$) taken for having one events. The discrete Poisson distribution can be converted to the exponential distribution, which has the time period as the random variable(X), having the probability distribution function and cumulative distribution function :

$$\begin{aligned} f(x) &= \lambda e^{-\lambda x} \\ F(x) &= 1 - e^{-\lambda x} \end{aligned}$$

with mean and standard deviation $1/\lambda$. λ is considered as rate constant.

Here what should be done is (a) to confirm whether the sampled data follows exponential distribution or not, and (b) to estimate the interval with confidence level. Experimental approach for the estimation of λ has been done by calculating the histogram of time events with arbitrarily chosen time bin to show the exponential-type histogram, and fit the distribution with arbitrary exponential function $A\,e^{-\lambda t}$ to estimate λ, the rate constant(Figure 2.10b).[20] However this process requires many data at a specific energy (sample bias) to estimate the time constant, because at least five time bins should include at least 15 events for the appropriate fitting, then total number of required measurements reaches ~ 100. Furthermore the nonlinear fitting with arbitrarily set time bin is asymptotic in a mathematically strict point of view.

Therefore, to estimate the time constant at a specific sample bias (a) I employed a quantile plot, by ordering all the sampled time (or charge) data in descending order, to check the exponential distribution as well as to remove outliers and (b) estimated the time constant based on maximum likelyhood estimate.[19] A quantile plot, the data values plotted on the vertical axis against an empirical fraction of observations exceed by the data value, is used to diagnose the sampling distribution, to show the inverse of cumulative distribution function.

$$F^{-1}(f;\lambda) = \frac{\ln(1-f)}{\lambda}, \qquad 0 \leq f < 1 \tag{2.24}$$

The assumption of Poisson process leads to the exponential distribution of experimental data, so the resulting quantile plot should show the form given in Equation 2.24. In Figure 2.10c, one experimental data with inverse of the quantile function is given. Note that the quantile function is the inverse of cumulative distribution function, i.e. the inverse of the quantile function (switching the x and y axis of the quantile function) results in the cumulative distribution function, $1 - e^{\lambda t}$, as Figure 2.10c shows.

If sampled data satisfies the exponential distribution without outliers, the interval estimation can be done based on the maximum likelyhood estimate.[19] The likelyhood function $L(\lambda)$ given sample $t = (t_1, t_2, \cdots, t_n)$ is given as :

$$\begin{aligned} L(\lambda) &= \prod_{i=1}^{n} \lambda e^{\lambda t_i} = \lambda^n exp\left(\lambda \sum_{i=1}^{n} t_i\right) \\ &= \lambda^n e^{-\lambda n \bar{t}} \end{aligned} \tag{2.25}$$

where $\bar{t}$ is arithmetic mean (average) of data, $\bar{t} = \frac{1}{n}\sum_{i=1}^{n} t_i$. To get the maximum likelyhood, derivative of likelyhood function's logarithm is taken, resulting in 0 where $\lambda = \frac{1}{\bar{t}}$. Consequently the maximum likelyhood of the rate constant should be inferred by the arithmetic mean of measured data:

$$\hat{\lambda} = \frac{1}{\bar{t}} \tag{2.26}$$

With strict assumption of exponential distribution of measured sample, the standard deviation of sample distribution is known to be equal to the sample mean, therefore the $(1-\alpha)100\%$ confidence interval is given by

$$\frac{2n}{\hat{\lambda}\chi^2_{1-\frac{\alpha}{2},2n}} < \frac{1}{\lambda} < \frac{2n}{\hat{\lambda}\chi^2_{1-\frac{\alpha}{2},2n}} \tag{2.27}$$

, where the $\chi^2_{p,\nu}$ is the $100(1-p)$ percentile of the chi-squared distribution with ν degrees of freedom, n is the number of observation. Therefore, 95% confidence interval is given by

$$\begin{aligned} \lambda_{low} &= \frac{1}{\bar{t}}\left(1 - \frac{1.96}{\sqrt{n}}\right) \\ \lambda_{upp} &= \frac{1}{\bar{t}}\left(1 + \frac{1.96}{\sqrt{n}}\right). \end{aligned} \tag{2.28}$$

This interval estimate holds regardless of the size of n, the number of repeated measurements, if the strict assumption of the exponential distribution is satisfied. Still the sample size n larger than 15 is recommended for acceptance.

In the experimental data shown in Figure 2.10 gives the rate constant 177.52 and 187.42 from the asymptotic exponential fitting from the time-bin histogram(Figure 2.10b) and the inverse of the quantile function(Figure 2.10c). The maximum likelyhood estimation of the 95% confidence interval gives the range of λ as $169.4 < \lambda < 266.1$, which is consistent to the asymptotically fitted estimation.

References

[1] Stroscio, J. A. & Kaiser, W. J. *Scanning Tunneling Microscopy: Volume 27* (Academic Press, 1993).

[2] Binnig, G., Rohrer, H., Gerber, C. & Weibel, E. Surface studies by scanning tunneling microscopy. *Phys. Rev. Lett.* **49**, 57–61 (1982). URL http://link.aps.org/doi/10.1103/PhysRevLett.49.57.

[3] Binnig, G., Rohrer, H., Gerber, C. & Weibel, E. 7×7 reconstruction on Si(111) resolved in real space. *Phys. Rev. Lett.* **50**, 120–123 (1983). URL http://link.aps.org/doi/10.1103/PhysRevLett.50.120.

[4] Bardeen, J. Tunnelling from a many-particle point of view. *Phys. Rev. Lett.* **6**, 57–59 (1961). URL http://link.aps.org/doi/10.1103/PhysRevLett.6.57.

[5] Tersoff, J. & Hamann, D. R. Theory and application for the scanning tunneling microscope. *Phys. Rev. Lett.* **50**, 1998–2001 (1983). URL http://link.aps.org/doi/10.1103/PhysRevLett.50.1998. 01834.

[6] Tersoff, J. & Hamann, D. R. Theory of the scanning tunneling microscope. *Phys. Rev. B* **31**, 805–813 (1985). URL http://link.aps.org/doi/10.1103/PhysRevB.31.805. 00000.

[7] Ohnishi, S. & Tsukada, M. Molecular orbital theory for the scanning tunneling microscopy. *Solid State Commun.* **71**, 391 – 394 (1989). URL http://www.sciencedirect.com/science/article/pii/0038109889907771.

[8] Tsukada, M., Kobayashi, K. & Ohnishi, S. First-principles theory of the scanning tunneling microscopy simulation. *J. Vac. Sci. Technol. A* **8**, 160–165 (1990). URL http://scitation.aip.org/content/avs/journal/jvsta/8/1/10.1116/1.577055. 00042.

[9] Ohnishi, S. & Tsukada, M. Effect of the microscopic electronic states of the tip on the scanning tunneling microscopy image. *J. Vac. Sci. Technol. A* **8**, 174–176 (1990). URL http://scitation.aip.org/content/avs/journal/jvsta/8/1/10.1116/1.577058. 00008.

[10] Binnig, G., Frank, K. H., Fuchs, H., Garcia, N., Reihl, B., Rohrer, H., Salvan, F. & Williams, A. R. Tunneling spectroscopy and inverse photoemission: Image and field states. *Phys. Rev. Lett.* **55**, 991–994 (1985). URL http://link.aps.org/doi/10.1103/PhysRevLett.55.991. 00000.

[11] Binnig, G., Garcia, N. & Rohrer, H. Conductivity sensitivity of inelastic scanning tunneling microscopy. *Phys. Rev. B* **32**, 1336–1338 (1985). URL http://link.aps.org/doi/10.1103/PhysRevB.32.1336. 00072.

[12] Becker, R. S., Golovchenko, J. A., Hamann, D. R. & Swartzentruber, B. S. Real-space observation of surface states on Si(111) 7×7 with the tunneling microscope. *Phys. Rev. Lett.* **55**, 2032–2034 (1985). URL http://link.aps.org/doi/10.1103/PhysRevLett.55.2032. 00236.

[13] Baratoff, A., Binnig, G., Fuchs, H., Salvan, F. & Stoll, E. Tunneling microscopy and spectroscopy of semiconductor surfaces and interfaces. *Surf. Sci.* **168**, 734 – 743 (1986). URL http://www.sciencedirect.com/science/article/pii/0039602886909052.

[14] Hamers, R. J. Atomic-resolution surface spectroscopy with the scanning tunneling microscope. *Annu. Rev. Phys. Chem.* **40**, 531–559 (1989). URL http://www.annualreviews.org/doi/abs/10.1146/annurev.pc.40.100189.002531. 00197.

[15] Persson, B. N. J. & Baratoff, A. Inelastic electron tunneling from a metal tip: The contribution from resonant processes. *Phys. Rev. Lett.* **59**, 339–342 (1987). URL http://link.aps.org/doi/10.1103/PhysRevLett.59.339.

[16] Seideman, T. *Current-Driven Phenomena in Nanoelectronics* (Pan Stanford Publishing, 2011).

[17] Frederiksen, T., Paulsson, M. & Ueba, H. Theory of action spectroscopy for single-molecule reactions induced by vibrational excitations with STM. *Phys. Rev. B* **89** (2014). URL http://link.aps.org/doi/10.1103/PhysRevB.89.035427. 00000.

[18] *LT-STM User's Guide* (Omicron). 00000.

[19] Walpole, R. E. *Probability & statistics for engineers & scientists* (Prentice Hall, Upper Saddle River, NJ, 2002). 00000.

[20] Stipe, B. C., Rezaei, M. A. & Ho, W. Inducing and viewing the rotational motion of a single molecule. *Science* **279**, 1907 –1909 (1998). URL http://www.sciencemag.org/content/279/5358/1907.abstract.

Chapter 3

Adsorbate-substrate interaction of an isolated CO at low coverage

3.1 Introduction

In the frame of total energy composed up of the adsorbate-adsorbent, adsorbate-adsorbate interaction energy, the adsorbate-adsorbent interaction need to be studied in an environment with negligible adsorbate-adsorbate interaction. The adsorbate-adsorbate interaction, i.e. intermolecular interaction, depends on the intermolecular distance, which can be approximated to be the reciprocal of the square root coverage($1/\sqrt{\theta}$). Therefore, to accomplish the intermolecular interaction-free environment to investigate the adsorbate-substrate interaction, isolated adsorbate molecules with low surface coverage is required, such as 0.01 ML of surface coverage to have $\sim$ 10 atoms - apart each other, enough to ignore intermolecular interaction. *

In this chapter, I describe the STM observation of isolated CO molecules on Pt(111) at the coverage range of $\theta < 0.005$ ML, and interpret the observations in terms of substrate-adsorbate interaction. Confirmation of the adsorption site in atomic resolution and the analysis of relative population between two adsorption sites (ontop & bridge) present indirect information on the potential energy surface upon CO adsorption on Pt(111) surface

*This chapter includes some text and figures partly reproduced from my research paper [1] with a permission. Copyright 2013 American Chemical Society.

and the dynamics of initial adsorption at low temperature. Also the substrate-adsorbate interaction is described in terms of electronic structure, including the spatially resolved structures and action spectrum of lateral hopping via electron injection into the unoccupied states.

Detailed experimental procedure and the configuration of experimental equipments are described in the methods & techniques section. The clean surface of Pt(111) was prepared with conventional annealing-sputtering cycles, with the annealing temperature up to $\sim$ 830 °C and Ar^+ sputtering (2 keV, emission current $\sim$ 10 μA). Cleaned surface was exposed to CO gas through a dosing tube located near the surface, and the surface temperature at the exposure was estimated to be 50 K. STM images and spectroscopic data (STS) were acquired at liquid helium temperature (4.7 K) under ultra-high vacuum (UHV) environment (2.7×10^{-9} Pa).

3.2 Adsorption site of isolated molecules & potential energy surface

3.2.1 Appearance and the adsorption site of isolated molecules

Individual CO molecules adsorbed on Pt(111) surface appears as a symmetric, bright protrusion at sample bias near Fermi energy(E_F), as shown in Figure 3.1. The detailed view of an isolated molecule is provided in Figure 3.2a, and the dimension of the protrusion at 0.1 V of sample bias is reproducibly measured to be $\sim$ 8 Å in diameter and $\sim$ 40 pm in height. The measured dimension and the general shape is consistent with so-called ”bump-type” protrusions in Stroscio and Eigler’s observation between two different type of protrusions, ”bump-type” and ”sombrero-type” (Figure 3.2, (b) & (c), [2]). According to their description, the bump-type protrusion shows highly symmetric, 40 pm-high

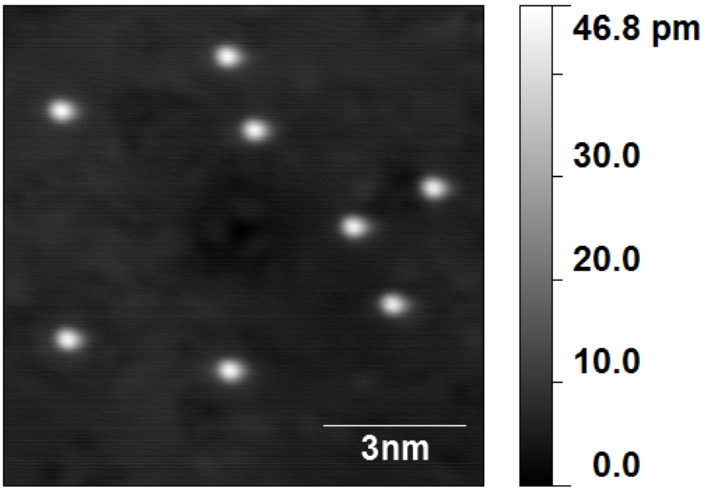

FIGURE 3.1: General appearance of CO molecules at low coverage. V_S= 0.3V and I_T = 1.0 nA.

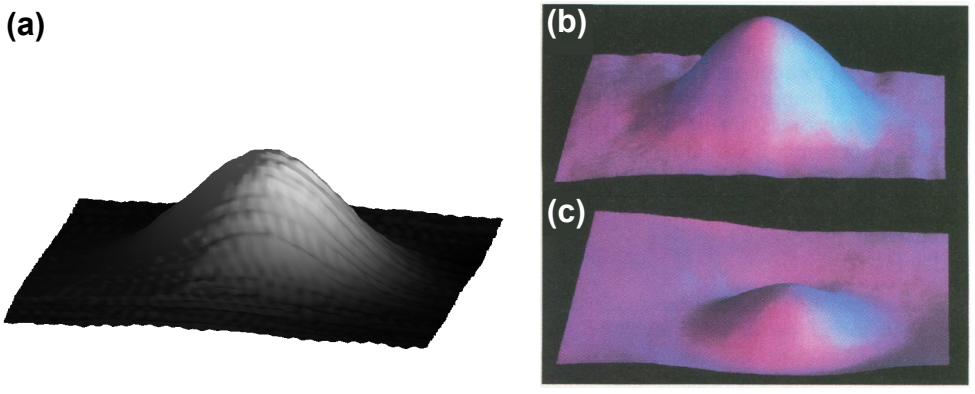

FIGURE 3.2: (a) 3D representation of an isolated CO molecule which was observed in this study(V_S = 20 mV and I_T = 1 nA). (b) and (c) are 3D representations of bump-type and sombrero-type protrusions respectively, adapted from [2], under reprint permission from AAAS.

protrusion, while the sombrero-type shows lower in height (14 pm) than bump-type and surrounded by a dip structure.

The ontop adsorption of the 40 pm-high protrusion was confirmed in atomic resolution by imaging the substrate atoms and the molecule simultaneously by means of modulation of the junction resistance.[3] The atomic-resolution STM image Figure 3.3 was obtained with intentional modulation of junction resistance to get both the atomic position of the substrate (regions marked as A and C, V_S = 2 mV and I_T = 1.6 nA) and the position of the molecule (region marked as B, V_S = 20 mV and I_T = 1.6 nA) within a single image. The objective of the junction resistance modulation is to avoid the dragging of the target molecule due to the close tip-sample distance which is required to achieve atomic-scale high resolution. Due to the larger tip-sample distance in region B, the underlying Pt atoms are not seen the images but the underlying lattice of Pt atoms of region B can be indirectly deduced from superimposed grid (solid line) which connects the top of each Pt atom in region A and region C. In this specific case, the very end of tungsten tip was modified with CO molecules, to show the center-dip protrusion of adsorbed CO molecules at 20 mV. The

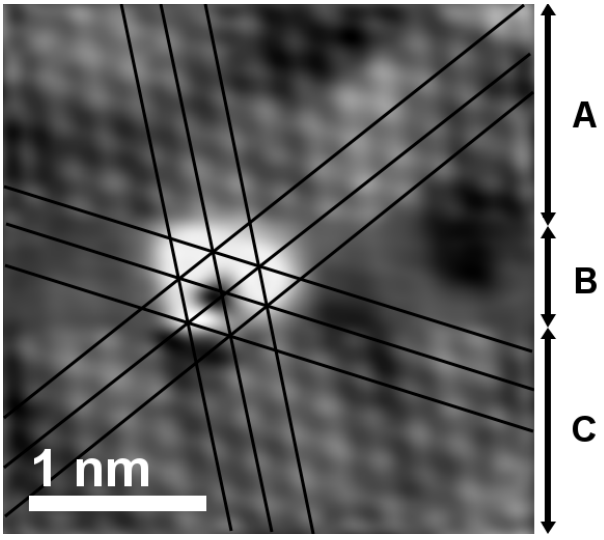

FIGURE 3.3: Determination of CO adsorption site in atomic resolution.
Region marked as A and C: V_S = 2 mV and I_T = 1.6 nA,
and the region marked as B: V_S= 20 mV and I_T = 1.6 nA. See text for more details.

dip-like center of CO protrusion exactly locates at the cross-point of Pt grid lines in region B, clearly showing the ontop adsorption.

The ontop-site adsorption of CO on Pt(111) surface at low-coverage limit has been one of established expectation from the vibrational frequency of C–O stretch mode($\sim$ 2100 cm^{-1}) measured from HREELS[4] and IRAS[5]. Stroscio and Eigler proposed the bump-type and sombrero-type protrusions as ontop CO and bridge CO molecules, respectively, based on the observations through manipulation experiments of adsorbate molecules. The observations are: (a) the manipulation distance between two different protrusions, (b) relative instability of sombrero-type protrusion which readily converts to the bump-type protrusion, and (c) the number of binding sites in a unit cell. Nevertheless, they could not determine the atomically resolved adsorption site due to the required small junction resistance which resulted in the manipulation of CO molecules.[2] Since Stroscio and Eigler's report there has been no other high-resolution real-space observation of isolated CO chemisorbed on Pt(111) surface. The atom-resolved adsorption site determined here provides an exclusive evidence to the ontop adsorption at low surface coverage.

3.2.2 Potential energy surface of isolated CO molecules: bridge-adsorbed CO in low surface coverage

As introduced in the first section, CO on Pt(111) surface has two available adsorption sites namely ontop and bridge sites. Also it is well known that the ontop site is preferentially occupied at low coverage, and the bridge-adsorbed CO appears from certain threshold coverage, e.g. 0.19 ML with adsorption at 100 K by Steininger et al.[6] To understand this multi-site adsorption system, many preceding studies have been performed to provide the adsorption energy difference between two adsorption sites, the energy barrier for lateral diffusion, vibrational mode energies and temperature-dependent properties.

These parameters have been summed up to construct potential energy surface (PES) of individual CO molecules adsorbed on Pt(111) surface, to explain the relative occupation ratio and dynamic motion according to the adsorption sites.

In this subsection, I will describe my trial to find the relative population of bridge CO at low coverage and the relative arrangement of bridge CO, and discuss the result in terms of PES. According to Stroscio and Eigler [2], they successfully observed the isolated bridge CO, but Nekrylova and Harrison [7] showed the quadratic growth of partial coverage for bridge-adsorbed CO at low coverage and low-temperature adsorption, suggesting collision-driven occupation of bridge site, i.e. bridge CO with adjacent ontop COs. Thus, real-space observation of bridge CO and relevant environment near the bridge CO would provide new knowledge on the initial surface processes and the adsorption dynamics, solving the ambiguous points of preceding results. For this purpose, the CO molecules were adsorbed at $\sim$ 35 K, and the surface was scanned with V_S = 20 mV and I_T = 50 pA to avoid any manipulation by tunneling electrons. I tried not only to find the sombrero-type protrusion as Stroscio and Eigler observed[2], but also to confirm the bridge-to-ontop conversion by applying a bias pulse (300 mV, 1 nA, duration 2 s). The number of CO molecules according to the adsorption site was counted for all the scanned images to estimate the population of bridge CO. The surface coverage was restricted to be less than 0.01 ML.

In my observation, only two bridge CO molecules were observed with approximately 9200 ontop CO molecules, at surface coverage θ = 0.01 ML. All observed bridge COs are shown in the Figure 3.4. Unfortunately the tip condition was not good enough to show the sombrero-type protrusion clearly, however the bridge CO molecules which is marked with yellow arrows show definitely lower height in the topographic images, as shown in Figure 3.4a and c. The bridge CO molecules were easily converted to the ontop CO(Figure 3.4b and d), even during the scanning with 400 MΩ of tunneling resistance

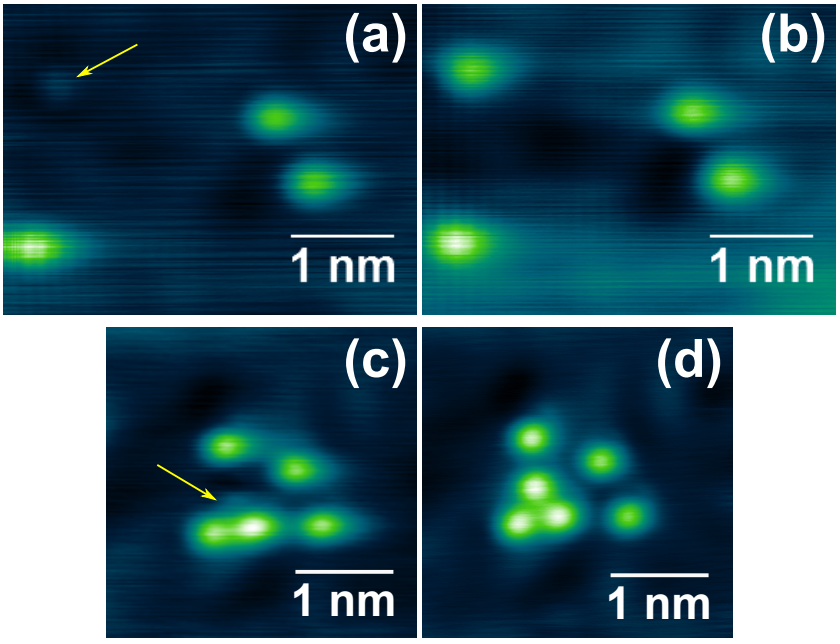

FIGURE 3.4: All two bridge COs at θ = 0.01 ML found in (a) and (c), marked with yellow arrows. (b) and (d) show the result of bridge-to-ontop conversion from (a) and (c), respectively. For all images, V_S = 20 mV and I_T = 50 pA.

(Figure 3.4c→d), which also implies that the ontop site of Pt(111) is more favorable for CO adsorption compared to the bridge sites.

Regarding the local adsorption geometry of bridge CO to the neighboring ontop CO molecules, whereas Figure 3.4a shows one isolated bridge CO, Figure 3.4c shows a bridge CO near two ontop COs which are in distance of $\sqrt{3}a_0$ (a_0 as the Pt-Pt lattice distance). The later geometry can support the collision-induced occupation of bridge site as Nekrylova and Harrison suggested, if the strong repulsive interaction between ontop COs in short-range which only allows inter-adsorbate distance $\geq \sqrt{3}a_0$ between ontop COs. Even though the number of sample is very limited to explain the collision-induced bridge occupation at current observation, it is also indirectly supported by Stroscio and Eigler's observation that the bridge CO is relatively stable when the bridge CO locates near other ontop COs, as well as by my observation with higher surface coverage($\sim$ 0.1 ML) in the following subsection. It is noteworthy that the adsorption temperature of this observation is low enough to suppress the surface dynamic processes to result in the bridge

occupation, which is not in equilibrium.

To quantitatively describe the bridge-site occupation, the population ratio of bridge CO was estimated from my STM images. As stated in the beginning of this subsection, two bridge CO molecules were found during observing $\sim$ 9200 ontop CO molecules. Accordingly the resultant probability to find a bridge CO (P_{B}) is approximately 2×10^{-4} at $\theta \sim 0.01\,\mathrm{ML}$, when the CO molecules were exposed at low temperature ($\sim$ 4.7 K), with maximum temperature of $\sim$ 35 K. In preceding studies, the population ratio between the ontop and the bridge sites has been an important parameter to determine the adsorption energy difference between the adsorption sites ΔE_{ads}, leading to the construction of PES. To compare this P_{B} with previously deduced values, simple lattice gas model is considered as follows.

The approach to derive the PES of CO on Pt(111)[8] begins with the estimation of relative population of molecules at each adsorption site, which leads to the difference in adsorption energy $\Delta E = E_{\mathrm{ads,ontop}} - E_{\mathrm{ads,bridge}}$ from the temperature-dependent C–O stretching intensity. The first factor is the number ratio of available adsorption site, i.e. entropy factor: In the unit cell of (111) surface, the ratio between ontop:bridge:hollow site is 1:3:2. Based on the preceding vibrational information, any possibility of hollow site occupation can be excluded. The second factor is the adsorption energy of two adsorption sites. According to [8], the probabilities to find COs adsorbed on ontop and bridge sites(P_{T} and P_{B}, respectively) can be described with the adsorption energies, E_{T} and E_{B} respectively:

$$P_{\mathrm{T}} = A\, e^{\beta E_{\mathrm{T}}} \tag{3.1}$$

$$P_{\mathrm{B}} = 3A\, e^{\beta E_{\mathrm{B}}} \tag{3.2}$$

where $\beta = 1/k_B T$. The constant A is determined by the normalization condition $P_T + P_B = 1$.

$$P_T + P_B = A\, e^{\beta E_T} + 3A\, e^{\beta E_B} = 1$$

$$A(e^{\beta E_T} + 3e^{\beta E_B}) = 1$$

$$A = \frac{1}{e^{\beta E_T} + 3e^{\beta E_B}}$$

By substituting this A to the equation for P_B gives:

$$P_B = 3 \cdot \frac{1}{e^{\beta E_T} + 3e^{\beta E_B}} \cdot e^{\beta E_B} = \frac{3}{3 + e^{\beta \Delta E}}. \tag{3.3}$$

The difference of potential depth (the difference of adsorption energy E_{ads}) between two adsorption site $\Delta E = E_T - E_B$ has been estimated to be 65 $\pm$ 10 meV at the zero coverage limit, with the intensity analysis of C–O stretch mode in coverage-dependent IRAS spectra.[8] Other studies have reported similar value of ΔE, such as 39 meV from temperature-programmed EELS[9] and 45 meV from in-situ high-resolution XPS[10]. With these adsorption energy differences, P_B is estimated to be 1.3×10^{-9}, 7.3×10^{-6} and 3.7×10^{-6}, respectively, which is roughly comparable to my experimental result, approximately 2×10^{-4}.

In reality, Equation 3.3 cannot properly predict the population of bridge-adsorbed CO at higher temperature, e.g. room temperature, where the equation predicts $P_B \approx 0.21$ at 0.1 ML of low surface coverage while experimental result indicates negligible P_B at the coverage. To account for this discrepancy, the vibrational energy of the reaction coordinate mode for the lateral hopping motion, corresponding to the potential stiffness (Figure 3.5) according to the adsorption site, has been suggested as the third factor to describe the adsorbate population. Regarding the lateral distribution, the hindered translation mode (HT mode) is the reaction coordinate mode (RC mode) for the lateral motion. Under simple

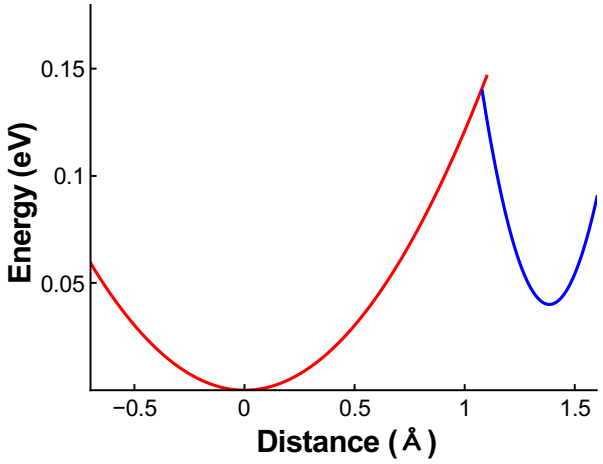

FIGURE 3.5: Potential energy surface with harmonic approximation for both ontop and bridge sites, redrawn with parameters from [11]. Ontop position at $x = 0$.

harmonic-approximation, the potential steepness can be described as following.

When the lateral diffusion of adsorbate (CO) is considered, the vibrational frequency of HT mode can represent the stiffness of PES under harmonic approximation. In particular, HT mode frequency of ontop-adsorbed CO is well known to be small, less than 10 meV for various metals, 7 meV for ontop CO on Pt(111) deduced from HAS study by Toennies and coworkers[12]. This small vibrational energy of CO HT mode involves the dispersed distribution of vibrational state upon thermal excitation. In contrast, the HT mode frequency of bridge site-adsorbed CO has been expected to be higher than the ontop CO,[8] implying steeper potential as shown in Figure 3.5. With the steep potential, the most CO molecules would stay in the ground state of vibrational quantum well, so the simple model in Equation 3.3 is relatively good approximation for bridge-adsorbed CO. If one considers the thermal distribution of vibrational energy state of ontop CO, the probability to find ontop CO is expressed as the ensemble of vibrational states,

$$P_{\mathrm{T}} = A \sum_{n_1=0}^{\infty} \sum_{n_2=0}^{\infty} e^{-\beta(n_1+n_2)\omega_{\mathrm{T}}} e^{\beta E_{\mathrm{T}}} = \frac{A}{(1-e^{-\beta\omega_{\mathrm{T}}})^2} e^{\beta E_{\mathrm{T}}} \tag{3.4}$$

where n_1 and n_2 are the vibrational quantum numbers for HT mode in two orthogonal direction. Again, the normalization condition $P_{\mathrm{T}} + P_{\mathrm{B}} = 1$ gives the P_{B} :

$$P_{\mathrm{B}} = \frac{3}{3 + (1 - e^{-\beta\omega_{\mathrm{T}}})^{-2}\, e^{\beta\Delta E}}. \tag{3.5}$$

The newly estimated P_{B} values using Equation 3.5 in the same manner I did with Equation 3.3 are, $\omega_{\mathrm{T}} = 7\,\mathrm{meV}$[12] and 35 K of adsorption temperature (in $\beta = 1/k_{\mathrm{B}}T$), P_{B} is estimated to be : 3.1×10^{-10} with $\Delta E = 65\,\mathrm{meV}$[6], 1.7×10^{-6} with $\Delta E = 39\,\mathrm{meV}$[9], and 8.9×10^{-7} with $\Delta E = 41\,\mathrm{meV}$[10]. P_{B} values deduced from Equation 3.3 and Equation 3.5 is approximately similar order with the experimentally obtained $P_{\mathrm{B}} \sim 2.0 \times 10^{-4}$.

3.2.3 Bridge-site occupation at relatively low-coverage regime ($\theta \sim 0.1$ ML)

The 0.1 ML of surface coverage is slightly out of the scope of this chapter(Chapter 3), but it is notable how the bridge-adsorbed CO appears with low-temperature adsorption, as an associated discussion from previous section. As discussed in the previous section, the low-temperature adsorption allows the adsorption at bridge sites from relatively low coverage such as 0.04 ML, by collision-induced inequilibrium site occupation, against the direct-occupation of bridge site. This was suggested from the quadratic growth of bridge site CO population with adsorption at 20 K, in contrast to the linearly growing ontop CO population[7]. As a similar system, a study of isotope CO on Ni(100) with low-temperature adsorption also indicated that the interaction between incoming and pre-existing CO molecules contributes to the occupation of relatively unstable adsorption site.[13]

These results are reasonable when one considers the surface dynamic processes at initial adsorption at low coverage, with the adsorption energy gain. The adsorption isotherm of CO on Pt(111) at zero coverage limit is $\sim$ 1 eV, which is $\sim$ 20 times-higher than the adsorption energy difference between ontop and bridge CO. Accordingly, when

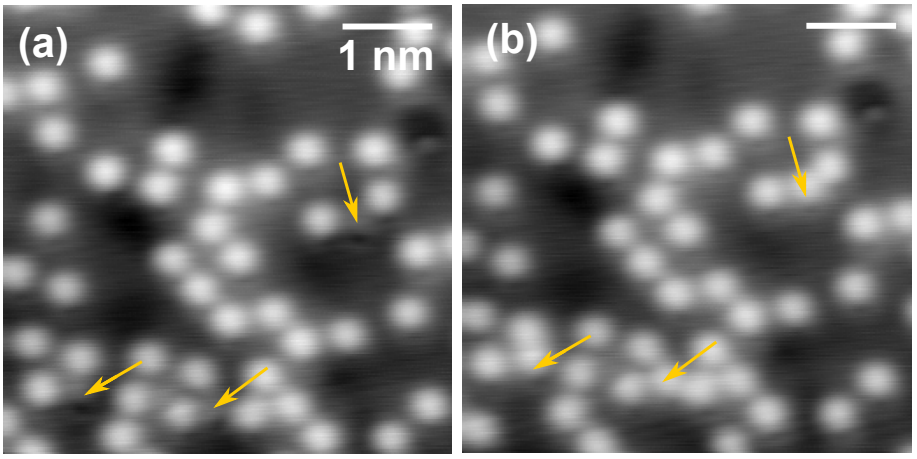

FIGURE 3.6: An STM image of adsorbed CO molecules, $\theta \sim 0.14$ ML. Yellow arrows show the position of bridge-adsorbed COs in (a). (b) shows the position of identical ontop CO molecules in (a), with additional ontop COs which appear by the result of bridge-to-ontop conversion with tunneling electrons. For both images, V_S = 20 mV, I_T = 50 pA.

a CO molecule collides with the surface, the molecule would travel on the surface with dissipating kinetic energy until the kinetic energy becomes less than the diffusion barrier. Due to $\sim$ 60 meV of potential depth difference as well as the difference of diffusion barrier between the ontop and bridge site, the ontop site exhibits higher probability to be occupied than the bridge site. Nonetheless, the bridge site occupation is also available via indirect adsorption by collision and resultant trapping. This elementary process should result in a specific adsorption structure, which the bridge CO resides adjacent to ontop-adsorbed CO molecules.

As an extended observation from previous section, Figure 3.6 shows CO molecules adsorbed at maximum substrate temperature $\sim$ 35 K. Compared to Figure 3.4, the increase surface coverage allowed various local geometries of bridge COs with adjacent ontop COs. Two bridge COs in left-bottom part of Figure 3.6a is adjacent to two ontop COs respectively, where the two ontop COs are $\sqrt{3}a_0$ apart each other. These two bridge CO molecules and corresponding geometry are similar to the geometry found in Figure 3.4c. Even the other bridge CO on the right-top part of Figure 3.6a is also adjacent to two ontop CO molecules, although the intermolecular distance of two ontop COs is larger($\sqrt{7}a_0$ than other two cases. The number density of isolated bridge CO, which has intermolecular distance larger than

$2a_0$, is negligibly small than the number density of bridge CO adjacent to ontop COs. The bridge CO positioned near ontop COs were also readily hopped to nearby ontop site by tunneling electrons, as indicated in Figure 3.6b.

One interesting point is the appearance of rectangular units, at the center of the image, and in-between the two arrows. I found that bridge CO can exist at the center of rectangular units, even when the adsorption temperature is increased to 50 K.

Indeed the bridge CO molecules were appeared adjacent to ontop-adsorbed molecules with $\sim$ 50 K of surface adsorption temperature. In contrast to Figure 3.6 (adsorption at 35 K) where the bridge CO appears as a form both not completely enclosed with ontop COs and completely enclosed in rectangular units, the bridge COs (adsorption at 50 K) show specific geometry which is completely enclosed by four ontop COs. This rectangular geometry is the unit cell of the bulk overlayer structure namely $c(4 \times 2)$ domain, which appears generally at increased coverage $\theta > 0.35\,\mathrm{ML}$ (see detailed descriptions for the coverage-dependent overlayer structures in the next chapter).

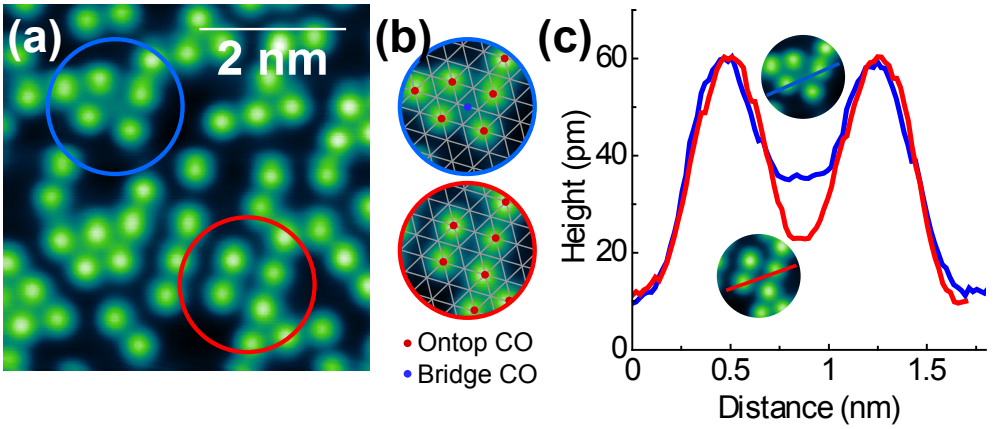

FIGURE 3.7: (a) An STM image of adsorbed CO molecules at 50 K of adsorption temperature, with rectangular units marked with blue, and red circles. The rectangular unit in blue circle have bridge-adsorbed CO at the center of unit, and the unit in red circle do not have one. (b) shows the schematic models superimposed to the STM image for the rectangular unit ($c(\sqrt{3} \times 2)$rect) with bridge CO inside the blue circle, and the rectangular unit ($(\sqrt{3} \times 2)$rect) without bridge CO inside the red circle. (c) Line profiles along the diagonal direction of rectangular unit, to show the difference between two units clearly. The red line corresponds to the line profile of the rectangular units in red circle of the image, the blue line corresponds to the line profile of the rectangular units in the blue circle of the image (a).

Figure 3.7a shows an STM image at $\sim$ 0.14 ML of surface coverage, where the CO molecules were adsorbed on the surface at $\sim$ 50 K. With $\sim$ 50 K adsorption, most of the bridge COs are entirely surrounded by ontop COs, forming a rectangular unit(c($\sqrt{3} \times 2$)rect) which is unit cell structure of c(4×2) domain, as depicted in the c($\sqrt{3} \times 2$)rect unit top circle(blue) in Figure 3.7b. As discussed in previous sections, the topographic height of bridge CO in STM images is $\sim$ 20 pm. which is about half of the topographic height for the ontop CO. Complete enclosure of bridge CO with surrounding ontop CO hinders the recognition of bridge CO at the center. In Figure 3.7b, the rectangular unit without bridge CO at the center is indicated by the bottom red circle. Comparison of height profile (Figure 3.7c) clearly shows a certain protrusion at the center of the rectangular unit, indicating the existence of bridge CO. These rectangular units with bridge CO at the center, namely c($\sqrt{3} \times 2$)rect units, were the main geometry accompanied with the bridge-site occupation. It is noteworthy that the probability to find the rectangular unit without bridge CO (($\sqrt{3} \times 2$)rect) is significantly lower than that for the rectangular unit with bridge CO (c($\sqrt{3} \times 2$)rect).

It is interesting to note that bridge-site occupation in this coverage range ($\theta < 0.15$ ML) is a non-equilibrium state, i.e. not in the minimum of total energy. Not only 35 K, but also 50 K of adsorption temperature is low enough to suppress the dynamic process such as diffusion to minimize the total energy. If the temperature exceeds the thermal threshold to allow ontop to ontop diffusion, bridge CO molecules are repositioned to ontop site to achieve equilibrium state, according to Nekrylova and Harrison [7], and Yoshinobu and Kawai [14]. Indeed, STM images acquired after room-temperature annealing do not show any rectangular units with bridge CO, All CO molecules appear identical in shape and height in the STM image, confirming the existence of only one adsorption species. In addition, triangular units with an intermolecular distance of 4.6 Å often appeared as shown in Figure 3.8, corresponding to the partial ($\sqrt{3} \times \sqrt{3}$)R30° arrangement. It is notable that 4.6 Å, the second nearest neighbor distance between ontop-adsorbed CO

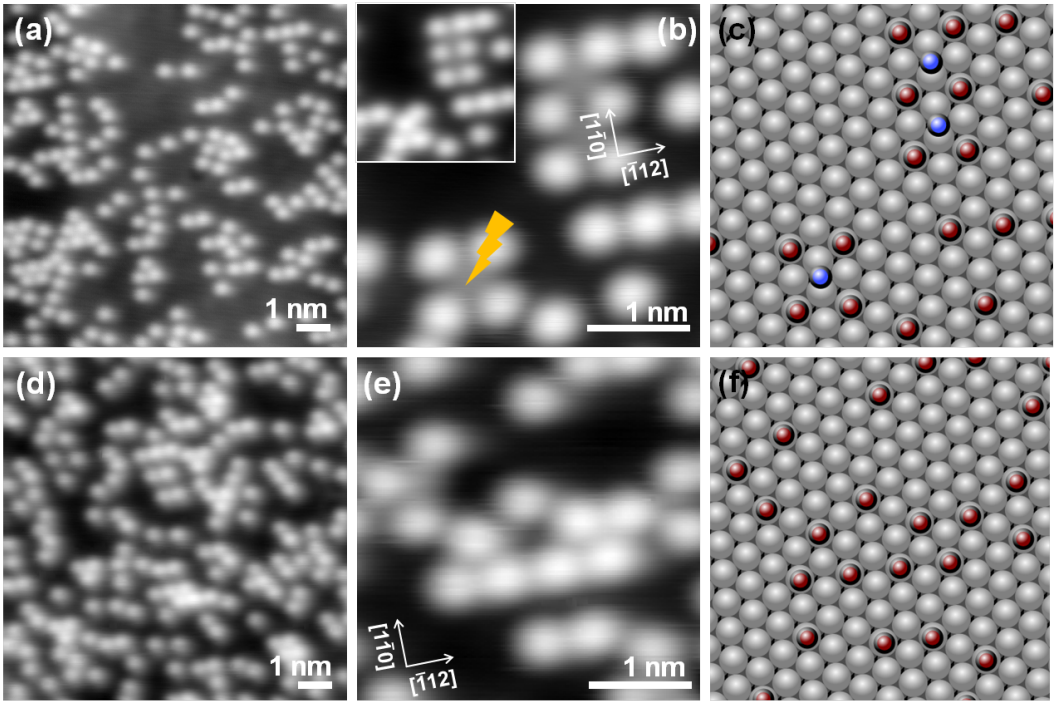

FIGURE 3.8: Topographic image of CO molecules with $\sim$ 0.1 ML coverage with $\sim$ 50 K adsorption(a) and after annealing (d). (b) and (e) are zoomed-in image of (a) and (d) respectively. (b) shows bridge COs at the center of rectangular units. Bias pulse leads to the lateral hopping of bridge CO to change the relative geometry as shown in the inset of (b). (c) is the schematic model of (b) (ontop CO: red, bridge CO: blue, Pt atom: gray). (f) is schematic model of (e), showing the disappearance of bridge CO. Scanning condition: (a) V_S = 0.1 V and I_T = 3 nA, (b) V_S = 0.1 V and I_T = 0.5 nA, (d) V_S = 0.1 V and I_T = 0.5 nA, (e) V_S = 0.1 V and I_T = 1 nA.

molecules, is the minimum ontop-to-ontop distance up to 0.5 ML of coverage, implying that the 1×1 arrangement is prohibited due to strong repulsive intermolecular interaction.

3.3 Adsorbate-substrate interaction: electronic structure in unoccupied energy region

Different from CO adsorbed on Pd(110) surface[15], the isolated CO molecules on Pt(111) surface are not mobile in sample bias range ± 3 eV. Thus the isolated molecule allows stable investigation of bias-dependence of the STM images to visualize the charge density at the specific sample bias. Interestingly the bias-dependent topographic images

of isolated CO molecules under constant current mode show gradual change of the protrusion in the positive $V_S$region, i.e. unoccupied energy region. Section 3.3.1 describes the evolution of topographic images under various sample bias voltages(V_S).

On the other hand, if the sample bias is further increased, for example over 4 eV, the adsorbate molecule starts to hop laterally. Quantified hopping behavior in unoccupied energy region ($3 \sim 5\,\mathrm{eV}$) will be discussed in Section 3.3.2. Additionally, I will compare isolated CO on Pt(111) and Pd(110) to discuss the mechanism of vibration-induced lateral hopping via inelastic tunneling electrons in Section 3.3.3.

3.3.1 Spatial distribution of electronic structures in unoccupied energy region

One of the prominent advantages of STM is the ability to monitor not only the structural but also electronic properties. Topographic image obtained in STM image contains both geometric and electronic information with high spatial resolution, in which dI/dV curves and dI/dV mapping provide robust information on electronic structure of adsorbates. One of representative example would be the imaging of phthalocyanine molecules which demonstrate very different orbital shape according to the polarity of tip–sample bias (V_S), such as the shape of HOMO in negative V_S and LUMO in positive V_S.

In the case of small molecules like CO, the molecular orbital itself is simple, thus appears as a spherical protrusion near the Fermi level (E_F). Interestingly, I found that the bias-dependent images of CO on Pt(111) show evolution of a donut-shape protrusion in unoccupied energy region, and furthermore, the molecule begins to hop laterally from certain threshold bias voltage. In this subsection, the bias-dependent evolution of CO protrusion will be discussed.

Figure 3.9 shows a series of images obtained at a range of energy in unoccupied states with positive V_S, and Figure 3.10 shows the height profile corresponding to the energy level. The symmetric protrusion which was described in Section 3.2 retains from

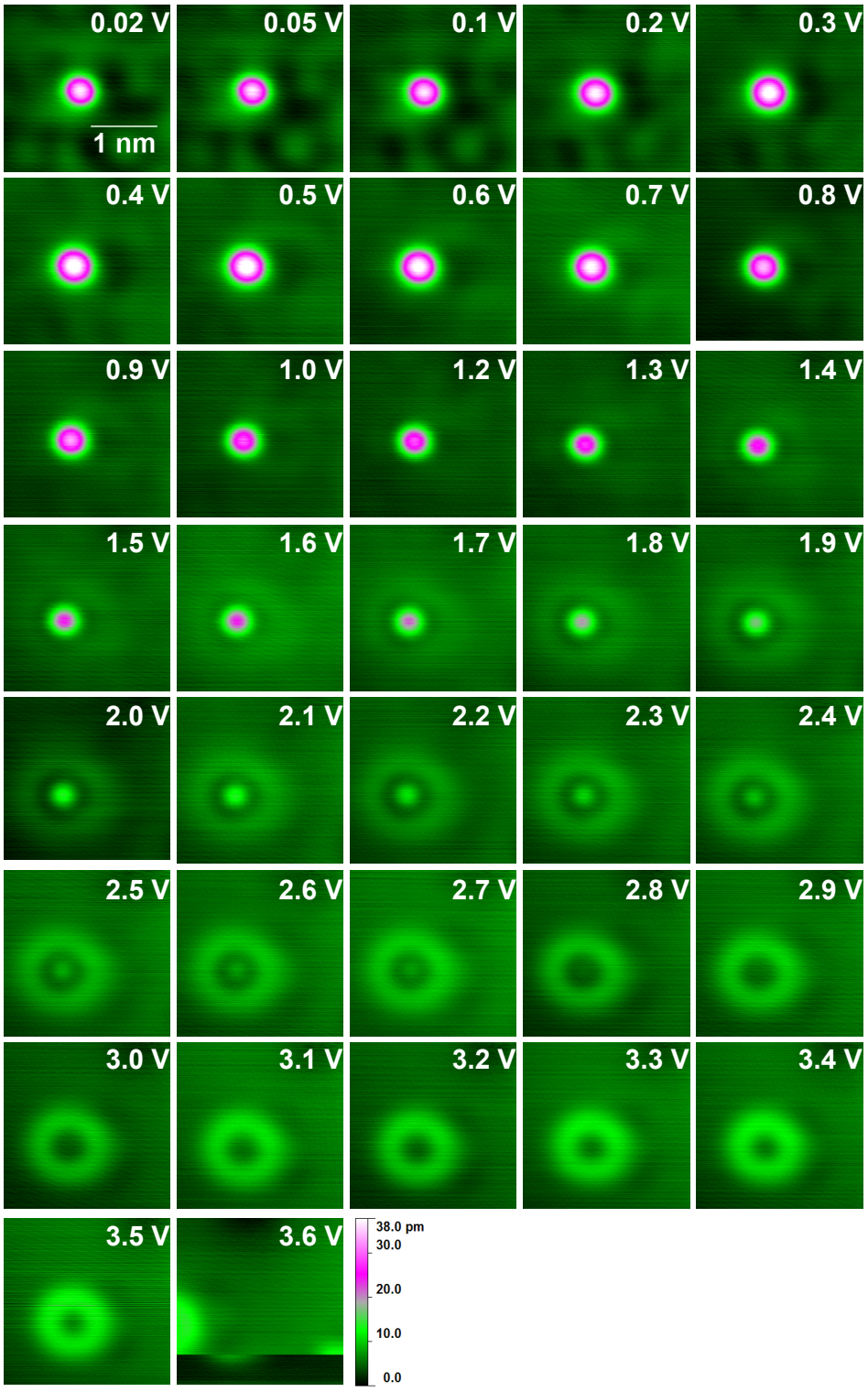

FIGURE 3.9: Scanning bias-dependent images in unoccupied energy region. All the images are 2.5 nm× 2.5 nm in size. V_S is specified in each image, and I_T is 0.5 nA for all images. The identical false color scale was applied in a whole.

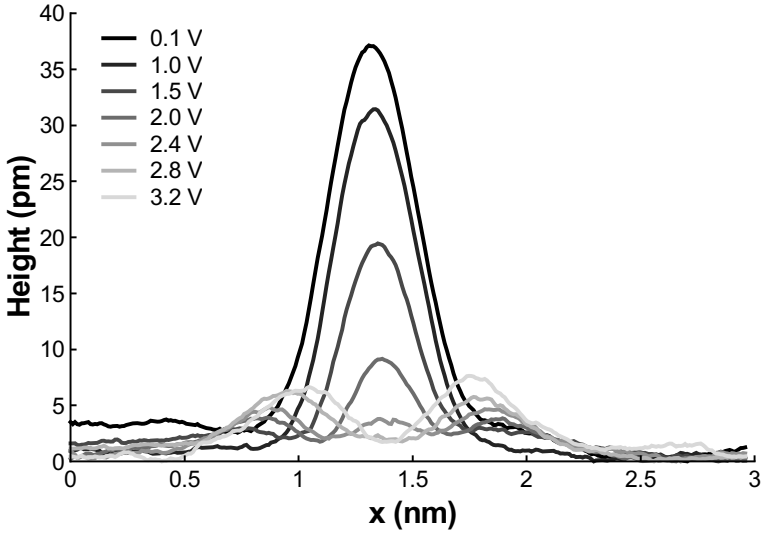

FIGURE 3.10: Selected height profiles from images in Figure 3.9.

the Fermi level to $\sim$ 0.9 eV, as well as negative sample bias region down to $\sim -5\,\mathrm{V}$. When the scanning bias increases to the unoccupied region further, the lateral size and the topographic height of molecule starts to decrease and a rim shape appeared near the edge of the protrusion. The evolution of protrusion with increasing the sample bias (V_S) shows with complete disappearance of central protrusion and increase of the rim height at $\sim$ 3.5 V. More increase of V_S leads to the lateral hopping of the molecule, as shown in Figure 3.9.

Because the size of the molecule (bond length of CO) does not change according to the sample bias, it strongly implies that the above-described change in CO protrusion originates from the change of spatial electronic structure. This explanation is also supported from the fact that such geometry evolution was not observed in occupied energy region down to ~ -5 V scan, in which the symmetric protrusion and height were maintained to be similar to those near E_F.

The topographic STM image exhibits the relative amount of integrated density of state of both sample and the tip, consequently it contains complex information other than pure density of state originated from the adsorbate. To get precise information on lateral distribution of density of state, spatially resolved $\mathrm{d}I/\mathrm{d}V$ spectra were obtained as shown in Figure 3.11. Because the protrusion of CO molecule is concentric, the $\mathrm{d}I/\mathrm{d}V$ spectra

were measured from the center of the molecule to outside, along a line with specified distance from the center.

In contrast to clear change in the protrusion, the spatially resolved STS (Figure 3.11) do not show very significant bias-dependent feature at a glance. However, there are subtle changes in the unoccupied energy region as follows. In Figure 3.11a, the energy region where $V_S \leq 1.2$ V shows the typical protrusion-like DOS distribution as shown in the 3D plot (Figure 3.11b), maximum DOS at the molecular center. In contrast to the left part, the right region($V_S \geq 1.2$ V) shows the inversion of $\mathrm{d}I/\mathrm{d}V$ signal tendency according to the distance from the molecule, showing lower signal at the molecular center. The $\mathrm{d}I/\mathrm{d}V$ tendency changes with larger $V_S(\geq 3$ V), showing complex spatial distribution. Figure 3.11c more apparently visualizes the subtle change in spatial DOS, by projecting at designated, representative sample bias. At 0.1 V, the DOS distribution represents a spherical protrusion similar to the topographic image taken near the E_F. But at 2.0 V, the molecular center shows lower density of state than adjacent region. Moreover, at 3.0 V, off-center region (2 Å) shows higher DOS than the molecular center as well as the outer region (> 10 Å), supporting the rim-shape topographic images in Figure 3.9.

Thus, it is evident that rim-shape DOS exists in unoccupied energy region, still the precise origin of the rim-shape DOS is veiled. One possible explanation is that LUMO of CO, $2\pi^*$, which has a node in the C-O bonding axis, resultantly can show rim (or donut) shape distribution. However, the dimension of rim-shape is larger than the size of molecule when the atomic diameter of C and O are considered. Diameters of the rim-shape in the topographic image and the diameter of the rim-shape in $\mathrm{d}I/\mathrm{d}V$ curve are about $\sim$ 18 Å and $\sim$ 14 Å, respectively. If the maximum heights in Z and maximum $\mathrm{d}I/\mathrm{d}V$ signal are considered, the diameters of rim-shape correspond to 7 $\sim$ 9 Å and 5 Å, respectively. In contrast, the atomic diameter of carbon and oxygen is 3.4 Å and 3.0 Å in terms of van der Waals radii.[16] CO molecule adsorbs on Pt(111) in perpendicular direction to the surface, and consequently the lateral dimension approximately corresponds to the atomic diameter

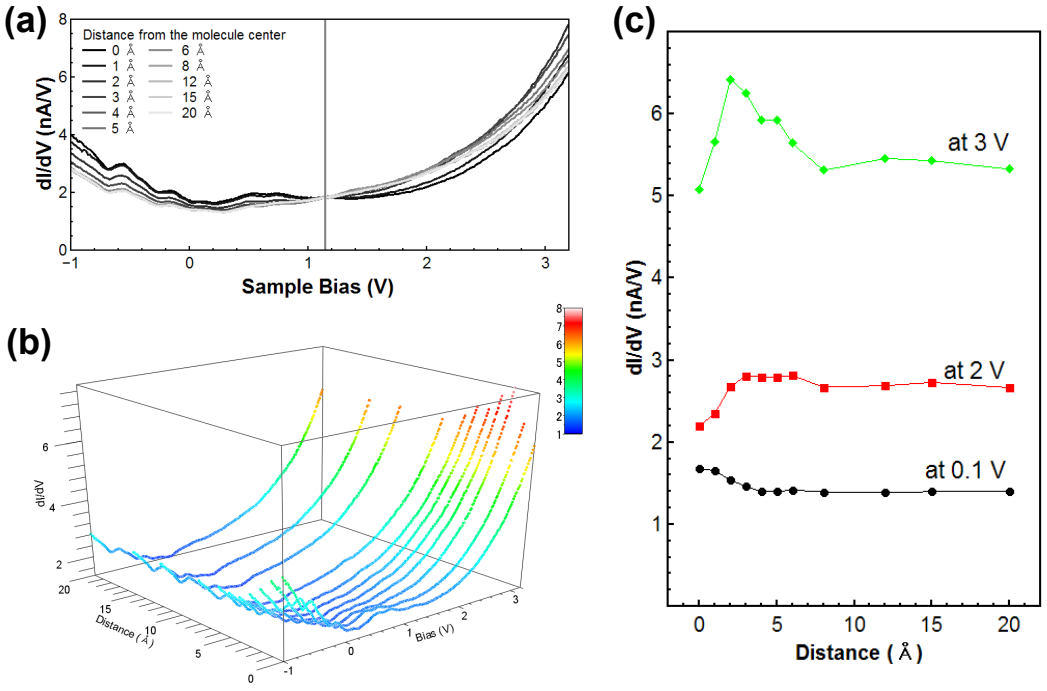

FIGURE 3.11: Spatially resolved STS data with different representations. (a) Whole data in a same layer, (b) 3D representation of whole data and (c) cross-section along the distance from the molecular center, at sample bias of 0.1, 2.0 and 3.0 V, respectively. At all measurement points, the junction resistance was kept constant : $4.2 \times 10^9\ \Omega$ (V_S= 2.1 V, I_T= 0.5 nA).

of C and O, which is the cross section of MO perpendicular to the bonding axis of CO. The dimension of $2\pi^*$ orbital of CO molecule cannot be precisely determined experimentally, nonetheless the van der Waals radius that accounts for induced charge-derived attractive interaction would be considered as practical upper limit of molecular orbital dimension. Thus, it is not reasonable to explain the rim shape with the direct and pure contribution of $2\pi^*$ MO. It is also noteworthy that the energy level for the $2\pi^*$ orbital of CO adsorbed on Pt(111) has been reported to be 4.3 eV and 4.5 eV with regard to E_F from inverse photoemission (IPE) and two-photon photoemission(2PPE), respectively.[17, 18]

Instead of the direct contribution of $2\pi^*$ MO localized in the molecule, another possible explanation would be hybridized electronic state from MO of CO and metallic state, which exist off-center of the molecule. Considering the atomic diameter of Pt (2.7 Å), the relative position of rim shape is the neighboring Pt atoms, not the Pt atom which is directly bonded to the adsorbate molecule. In energetic aspect, the rim shape which appears from 2.5 eV in spatially resolved STS (Figure 3.11), and this energy region overlap to *sp* band of Pt(111) substrate. According to Wiebe et al.[19], the *sp*-derived surface band of Pt(111) has onset in 0.3 eV and parabolic dispersion near $\bar{\Gamma}$ from STS result as well as *ab initio* calculation. In Figure 3.11, STS data taken at 20 Å apart from the CO molecule also show onset near 0.3 eV which is consistent with preceding result. Considering relative energy position of wide-range *sp* band and $2\pi^*$ state, the main electronic contribution to the rim shape would mainly originate from the *sp* band-derived state that is modulated by CO adsorption.

In the aspect of relative spatial distribution of DOS, the spectra in Figure 3.11a can be sectioned into three regions and described like below:

(a) $V_S < 1.2$ V, protrusion-type with maximum DOS at the center of CO molecule,

(b) $1.2\ \text{V} < V_S < 2.1$ V, dip-type distribution with minimum DOS at the center of CO,

(c) $V_S > 2.1$ V, minimum DOS at the center of CO ($d = 0$ Å) as well as maximum DOS at off-center of CO ($d \sim 2$ Å), which shows rise of rim-shape DOS distribution.

As indicated in the previous paragraph, the relative position of rim shape lies in neighboring Pt atoms which are not directly bonded to CO molecule. From this point of view, the rim shape can be interpreted as the reconstructed electronic structure mainly from metallic states upon CO adsorption, even the corresponding metal atoms are not in contact with adsorbed CO molecule. This kind of re-distribution of DOS is predicted in the Nilsson model about CO adsorbed on Cu(100) and Ni(100), in which the substrates are assumed by the cluster model using Ni_{13} and Cu_{26}, respectively. Nilsson model proposed the DOS composed of molecular $2\pi^*$ state and metallic d_π states as well as metallic d_σ states can be appeared at the neighboring substrate atoms. There is one report which deals with the electronic reconstruction on Pt atom due to adsorption symmetry, using *ab initio* calculation with numerical basis sets with all electron calculations with scalar relativistic corrections(AER).[20] According to this calculation using Pt(111) slab model, CO adsorption on Pt(111) changes the LDOS at the Pt atoms which are not bonded with CO molecule, shifting the LDOS to the direction of lower energy, and it differs according to the distance to the Pt atom bonded to CO molecule. In Figure 3.12a at 0.11 ML (1/9 ML) of surface coverage, all the Pt atoms on the surface are categorized as (a) CO-bonded Pt atoms, (b) Pt atoms which have one CO-bonded Pt atom in its neighbor(marked as Pt-close (atop 1/9 ML) in Figure 3.12b), and (c) Pt atoms which have no direct contact with CO-bonded Pt atoms (marked as Pt-far (atop 1/9 ML) in Figure 3.12 a and b). The energy region of electronic reconstruction in Figure 3.12 is different from my experimental results shown in Figure 3.11, which might be originated from the self-interaction error in density functional method employed in the calculation. However, the computational results indicate the possibility of the reconstruction of metallic electronic states due to CO adsorption which has an influence on the DOS position not only for CO-bonded Pt atoms but also for other Pt atoms not directly bonded to CO molecules. The rim-shape distribution observed in my

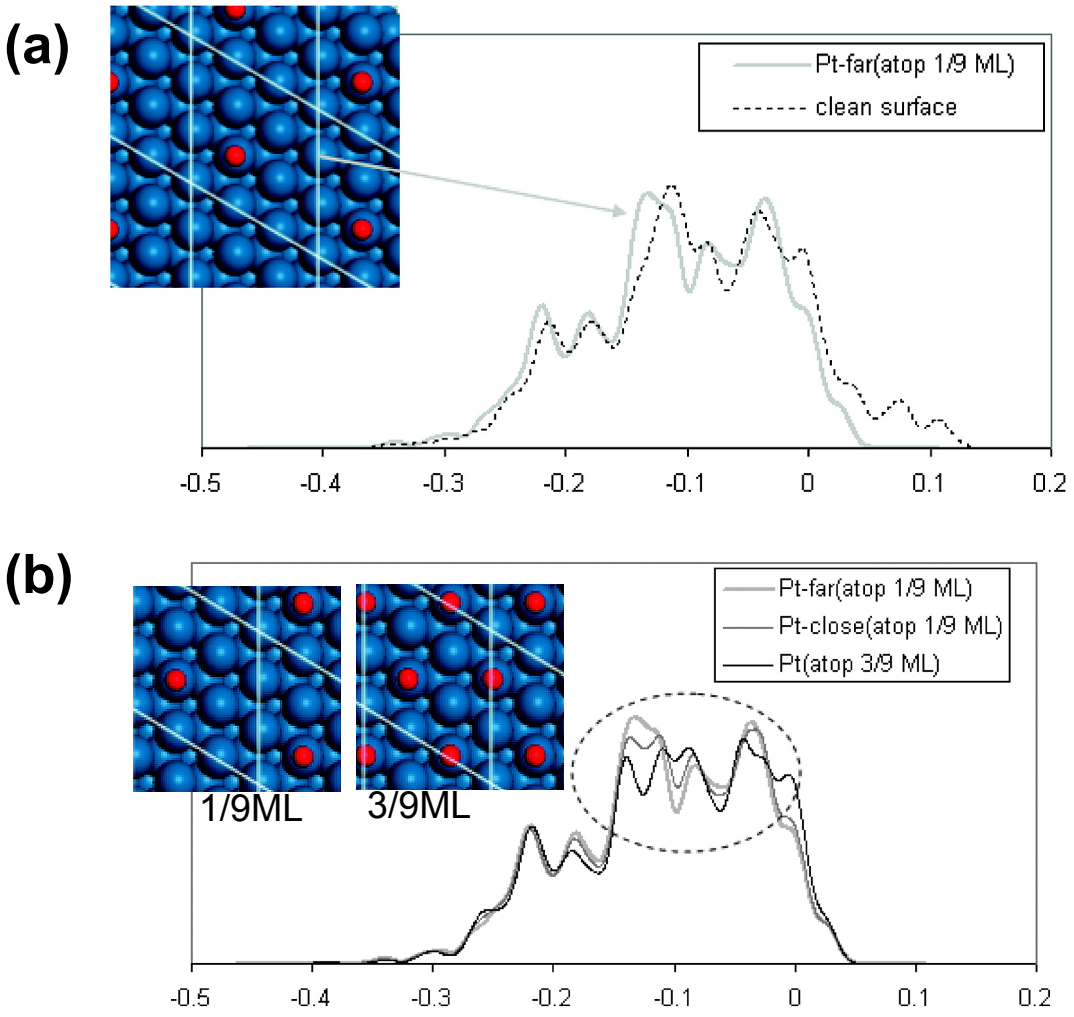

FIGURE 3.12: Change in metal LDOS upon CO adsorption, adapted with permission from [20]. Copyright 2009 American Chemical Society.

bias-dependent images(Figure 3.9) of a CO molecule on Pt(111) can therefore be explained by the repositioning of DOS states from metal substrate upon CO adsorption.

Note that the reconstruction of electronic structure on Pt(111) may explain the origin of intermolecular interaction in overlayer structures, which will be described in the next chapter.

3.3.2 Unoccupied state detected with tunneling electron-induced lateral hopping

Isolated CO molecules were immobile upon scanning up to $\sim$ 3.5 V as shown in previous subsection. However, as the last image in Figure 3.9, higher bias scans caused lateral hopping of the molecules. This lateral hopping could be triggered with electron injection with bias pulse. Figure 3.13a exhibits the lateral hopping of a CO molecule, before dosing tunneling electrons (left), the disappearance of the target molecule during electron injection (4 V) (middle) and the subsequently repositioned target molecule (right).

The topographic height of the individual CO molecules did not change before and after the hopping event, indicating that the adsorption geometry (ontop) was retained. The detection of hopping event was by monitoring the step-like current change during the bias pulse with previously set junction resistance. Monitoring the time taken for the lateral hopping under injection of tunneling electrons, the number of electrons required for each hopping event was estimated, and the results of repeated measurements were statistically treated under the assumption of Poisson event. Estimated probability of lateral hopping (yield) per electron as a function of the sample bias voltage is shown in Figure 3.13b. Figure 3.13b shows two sets of hopping probability data for two different CO molecules with the same tip, and the two sets were in agreement with each other, showing a rapid increase of hopping probability at 4.5 V. Figure 3.13c shows the wide-range $\mathrm{d}I/\mathrm{d}V$ spectra measured on a CO molecule and on the Pt bare surface, where the signal from CO stiffly

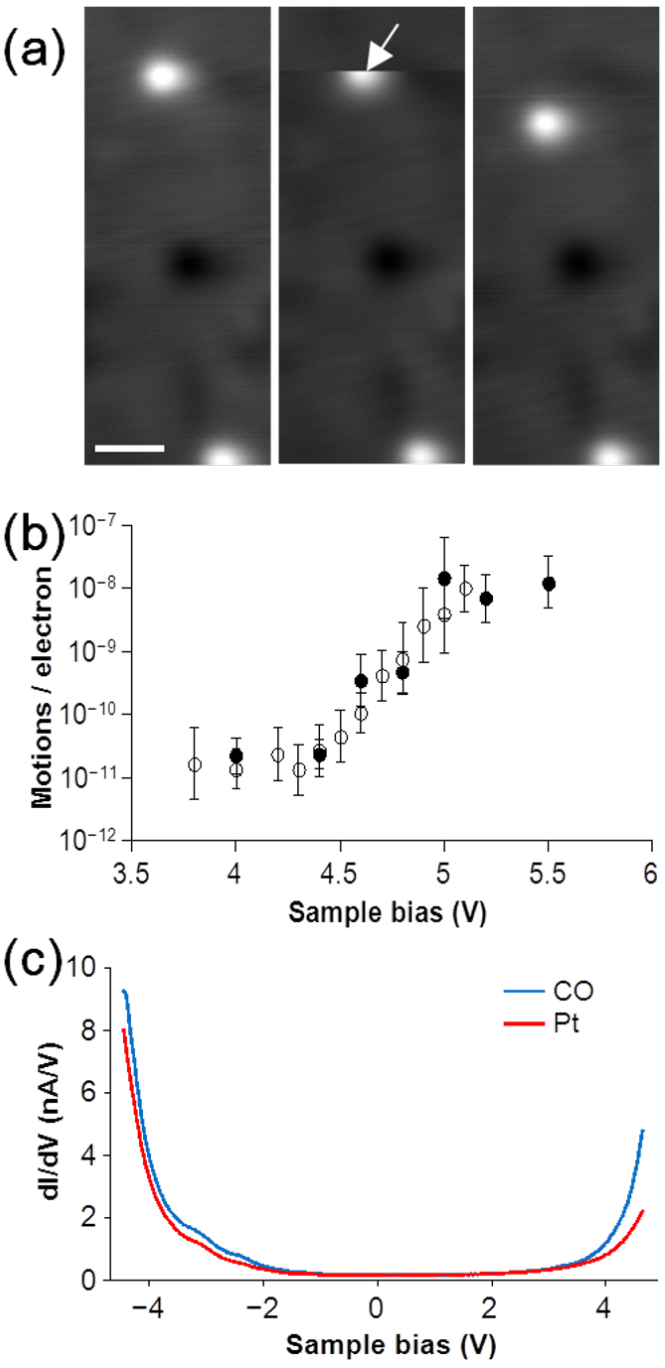

FIGURE 3.13: Lateral motion of an isolated CO molecule by electron injection on the top of the protrusion. (a) STM images before dosing electron (left), during the electron injection and consequent disappearance of the target molecule(middle) and resultantly repositioned molecule (right). (All three images are 2 nm$\times$ 6 nm in size. $V_S = 0.1$ V, $I_T = 0.5$ nA). (b) Two sets of action spectra, measured with the same tip. (c) Wide range STS measured on the protrusion.

increased at $\sim$ 4 V, compared to the signal from Pt. Therefore the DOS from 4 eV can be considered as an adsorbate-induced electronic state. Because the energy region covered in Figure 3.13 is not enough to show the peak position of corresponding state, the 4 eV should be considered as the onset of the electronic state.

Regarding the origin of corresponding electronic state, previous results from two-photon photo-emission (2PPE)[18] and inverse photoemission[17] reported the unoccupied $2\pi^*$ state of ontop CO on Pt(111) at 4.5 eV. Thus, the threshold near 4.5 V in the action spectrum for lateral hopping of CO corresponds to the tail of the $2\pi^*$ state of ontop CO on Pt(111), where the electrons tunnel into. The hopping mechanism may be similar to the pathway of energy transfer in CO hopping on Cu(110) by $2\pi^*$ excitation, as shown by Bartels et al.[21].

3.3.3 No lateral hopping of ontop CO by inelastic tunneling electron

Though isolated molecules exhibited hopping motion with electronic excitation, lateral hopping of an isolated ontop CO was never observed near the vibrational energy level of CO internal stretch (260 meV) during scanning as well as bias pulse applied with high current density(> 40 nA), in contrast to the CO on Pd(110)[15] which exhibits the drastic increase of lateral hopping yield at the energy of C–O internal stretch mode (230 meV). There are three parameters for vibration-induced CO hopping via tunneling electron on metal substrate, for which the system of CO/Pt(111) cannot simultaneously fulfill the requirements.[22–24] One parameter is the amount of density of state at the corresponding energy level, from the aspect of resonant excitation regime. which is negligible amount of DOS near E_F supported from both DFT calculation[25, 26] and my STS results(Figure 3.11 and Figure 3.13c). Another parameter is the diffusion barrier and the stiffness of potential energy surface, represented by the vibrational mode frequency of hindered translation mode. Finally the other parameter is the degree of anharmonic coupling between IS mode

and HT mode; which has been revealed to be very low, similar to CO on Cu(110), according to the dephasing analysis of $c(4 \times 2)$ with IRAS[8] as well as the pump-probe study of ontop CO on Pt(111). The mechanism of hopping motion induced by tunneling electron, and its adsorption site-dependence will be discussed in detail in Chapter 5.

3.4 Conclusion

In this chapter I described the adsorbate-substrate interaction by investigating isolated CO molecules at low coverage by means of real-space observation in a variety of circumstances. At low coverage, the protrusion-type appearance of ontop was described, and the adsorption site of protrusion was determined to be ontop site in an atom-resolved image which was obtained with modulation technique of tip-sample junction resistance to avoid dragging-out of adsorbate molecules. Bridge-adsorbed CO, which is known to be available on Pt(111) surface at increased surface coverage, could be observed by low-temperature adsorption, but the ratio of bridge CO over ontop CO was low as 10^{-4} order at $\sim$ 0.005 ML coverage. More bridge CO molecules could be observed with increasing the surface coverage up to $\sim$ 0.1 ML at 50 K adsorption, and most of bridge CO molecules were adjacent to ontop COs, supporting the collision-induced occupation of bridge site, if the lateral diffusion and resultant adsorption site conversion was suppressed by low temperature. Bridge CO mainly appeared at the center of rectangular unit c$(\sqrt{3} \times 2)$rect, implying the stabilization of bridge-site occupation due to the intermolecular interaction between ontop and bridge CO. The bridge CO changes the adsorption site to ontop site upon applied energy (scanning as well as bias pulse), different from the ontop CO.

Isolated ontop CO exhibited bias-dependent change in topographic images, from simple protrusion to donut(rim)-shape in unoccupied energy region (> 1.5 V). The rim-shape distribution of DOS may originate from the reconstruction of metallic state of Pt(111) upon the CO adsorption. Further increase of sample bias induced the lateral hopping of

adsorbed CO molecules, and the threshold energy for the lateral hopping was estimated to be $\sim$ 4.5 eV. The energy level of 4.5 eV is consistent with IPS and 2PPE-reported value of $2\pi^*$ state of CO on Pt(111). My results provide deeper insights into a long-standing issue on electronic and geometric structures of CO molecules adsorbed on Pt(111) substrate.

References

[1] Yang, H. J., Minato, T., Kawai, M. & Kim, Y. STM investigation of CO ordering on Pt(111): From an isolated molecule to high-coverage superstructures. *J. Phys. Chem. C* **117**, 16429–16437 (2013). URL http://dx.doi.org/10.1021/jp404231t.

[2] Stroscio, J. A. & Eigler, D. M. Atomic and molecular manipulation with the scanning tunneling microscope. *Science* **254**, 1319 –1326 (1991). URL http://www.sciencemag.org/content/254/5036/1319.abstract.

[3] Doering, M., Buisset, J., Rust, H.-P., Briner, B. G. & Bradshaw, A. M. Adsorption site determination with scanning tunnelling microscopy. *Faraday Discuss.* **105**, 163–175 (1996). URL http://pubs.rsc.org/en/content/articlelanding/1996/fd/fd9960500163.

[4] Froitzheim, H., Hopster, H., Ibach, H. & Lehwald, S. Adsorption sites of CO on Pt(111). *Appl. Phys.* **13**, 147–151 (1977). URL http://rd.springer.com/article/10.1007%2FBF00882473.

[5] Shigeishi, R. & King, D. A. Chemisorption of carbon monoxide on platinum {111}: Reflection-absorption infrared spectroscopy. *Surf. Sci.* **58**, 379–396 (1976). URL http://www.sciencedirect.com/science/article/pii/0039602876904775.

[6] Steininger, H., Lehwald, S. & Ibach, H. On the adsorption of CO on Pt(111). *Surf. Sci.* **123**, 264–282 (1982). URL http://www.sciencedirect.com/science/article/pii/0039602882903284.

[7] Nekrylova, J. & Harrison, I. Site resolved adsorption dynamics of CO on Pt(111). *Chem. Phys.* **205**, 37–46 (1996). URL http://www.sciencedirect.com/science/article/pii/0301010495003045.

[8] Schweizer, E., Persson, B., Tüshaus, M., Hoge, D. & Bradshaw, A. The potential energy surface, vibrational phase relaxation and the order-disorder transition in the adsorption system Pt{111}-CO. *Surf. Sci.* **213**, 49–89 (1989). URL http://www.sciencedirect.com/science/article/pii/0039602889902525.

[9] Mieher, W. D., Whitman, L. J. & Ho, W. A time resolved electron energy loss spectroscopy study of CO on Pt(111): Adsorption site occupations versus coverage and temperature. *J. Chem. Phys.* **91**, 3228–3239 (1989). URL http://jcp.aip.org/resource/1/jcpsa6/v91/i5/p3228_s1.

[10] Kinne, M., Fuhrmann, T., Whelan, C. M., Zhu, J. F., Pantförder, J., Probst, M., Held, G., Denecke, R. & Steinrück, H.-P. Kinetic parameters of CO adsorbed on Pt(111) studied by in situ high resolution x-ray photoelectron spectroscopy. *J. Chem. Phys.* **117**, 10852 (2002). URL http://link.aip.org/link/JCPSA6/v117/i23/p10852/s1&Agg=doi.

[11] Hähner, G., Toennies, J. P. & Wöll, C. Normal modes of CO adsorbed on metal surfaces. *Appl. Phys. A* **51**, 208–215 (1990). URL http://www.springerlink.com/content/ru0324463453u104/.

[12] Lahee, A., Toennies, J. & Wöll, C. Low energy adsorbate vibrational modes observed with inelastic helium atom scattering: CO on Pt(111). *Surf. Sci.* **177**, 371–388 (1986). URL http://www.sciencedirect.com/science/article/pii/0039602886901469.

[13] Kawai, M. & Yoshinobu, J. Direct and indirect mechanisms in site occupation of CO molecules on Ni(100) and Pt(111). *Surf. Sci.* **368**, 239–246 (1996). URL http://www.sciencedirect.com/science/article/pii/S0039602897800271.

[14] Yoshinobu, J. & Kawai, M. Initial adsorption sites of CO on Pt(111) and Ni(100) at low temperature. *Surf. Sci.* **363**, 105–111 (1996). URL http://www.sciencedirect.com/science/article/pii/0039602896001173.

[15] Komeda, T., Kim, Y., Kawai, M., Persson, B. N. J. & Ueba, H. Lateral hopping of molecules induced by excitation of internal vibration mode. *Science* **295**, 2055–2058 (2002). URL http://www.sciencemag.org/content/295/5562/2055.abstract.

[16] Bondi, A. van der Waals volumes and radii. *J. Phys. Chem.* **68**, 441–451 (1964). URL http://pubs.acs.org/doi/abs/10.1021/j100785a001. http://pubs.acs.org/doi/pdf/10.1021/j100785a001.

[17] Dose, V., Rogozik, J., Bradshaw, A. & Prince, K. Inverse photoemission from CO co-adsorbed with K on Pt(111). *Surf. Sci.* **179**, 90–100 (1987). URL http://www.sciencedirect.com/science/article/pii/003960288790121X.

[18] Anazawa, T., Kinoshita, I. & Matsumoto, Y. Two-photon photoemission study of CO/Pt(111). *J. Electron Spectrosc. Relat. Phenom.* **88-91**, 585–590 (1998). URL http://www.sciencedirect.com/science/article/pii/S036820489700131X.

[19] Wiebe, J., Meier, F., Hashimoto, K., Bihlmayer, G., Blügel, S., Ferriani, P., Heinze, S. & Wiesendanger, R. Unoccupied surface state on Pt(111) revealed by scanning tunneling spectroscopy. *Phys. Rev. B* **72**, 193406 (2005). URL http://link.aps.org/doi/10.1103/PhysRevB.72.193406.

[20] Sumer, A. & Aksoylu, A. E. Adsorption-induced surface electronic reconstruction of pt and Pt–Sn alloys during CO adsorption. *J. Phys. Chem. C* **113**, 14329–14334 (2009). URL http://dx.doi.org/10.1021/jp9021079.

[21] Bartels, L., Meyer, G., Rieder, K.-H., Velic, D., Knoesel, E., Hotzel, A., Wolf, M. & Ertl, G. Dynamics of electron-induced manipulation of individual CO molecules on Cu(111). *Phys. Rev. Lett.* **80**, 2004–2007 (1998). URL http://link.aps.org/doi/10.1103/PhysRevLett.80.2004.

[22] Persson, B. & Ueba, H. Theory of inelastic tunneling induced motion of adsorbates on metal surfaces. *Surf. Sci.* **502-503**, 18–25 (2002). URL http://www.sciencedirect.com/science/article/pii/S0039602801018933.

[23] Motobayashi, K., Kim, Y., Ueba, H. & Kawai, M. Insight into action spectroscopy for single molecule motion and reactions through inelastic electron tunneling. *Phys. Rev. Lett.* **105**, 076101 (2010). URL http://link.aps.org/doi/10.1103/PhysRevLett.105.076101.

[24] Ueba, H. Analysis of lateral hopping of a single CO molecule on Pd(110). *Phys. Rev. B* **86**, 035440 (2012). URL http://link.aps.org/doi/10.1103/PhysRevB.86.035440.

[25] Forsblom, M. & Persson, M. Vibrational lifetimes of cyanide and carbon monoxide on noble and transition metal surfaces. *J. Chem. Phys.* **127** (2007). WOS:000250295900021.

[26] Schimka, L., Harl, J., Stroppa, A., Grüneis, A., Marsman, M., Mittendorfer, F. & Kresse, G. Accurate surface and adsorption energies from many-body perturbation theory. *Nat. Mater.* **9**, 741–744 (2010). URL http://dx.doi.org/10.1038/nmat2806.

Chapter 4

Intermolecular interaction in coverage-dependent overlayer structures

In the previous chapter, I discussed mainly on isolated CO molecules chemisorbed on Pt(111) surface, which is considered free of intermolecular interaction due to sufficiently low surface coverage. In this chapter the coverage is increased to observe the overlayer structures, and the intermolecular interaction regarding the overlayer structures will be discussed. *

4.1 Introduction

4.1.1 Intermolecular interaction and overlayer structures

If one observe overlayer structure on a surface, the factors which affect to the overlayer structures would be the intermolecular interaction, and the temperature which allows thermal diffusion of the adsorbate. The intermolecular interaction can be categorized into two, one is attractive interaction and another is repulsive interaction. The amplitude of the

*Part of this chapter are based on/reproduced from my research paper with permission from [1]. Copyright 2013 American Chemical Society.

interaction, the effective distance in other word, with the surface coverage (number density of the adsorbates) determines the phase of overlayer structure. For example, an adsorbate strong attractive intermolecular interaction with long-range interaction will form localized, compact islands on a surface. On the other hand, an adsorbate which repulsively interacts with long effective distance will form well-organized overlayer structure over whole the surface of the substrate, and the intermolecular distance will decrease with increasing the surface coverage. Adsorbates with weak/intermediate intermolecular interaction would show different overlayer structure according to the surface coverage, from randomly scattered (or islands with a few molecules) to form a specific island structures over the whole surface.

In this aspect, the observation of overlayer structures according to the surface coverage provides many information on the intermolecular interaction. To get the information of overlayer structures, various techniques have been developed with diffraction such as low-energy electron diffraction, or a special form of scattering (molecular beam) such as ^{3}He spin echo.[2] With the development of scanning probe microscopy, the direct and real-space observation has become available, for example, Co adatom on Cu(111) surfaces. For the quantitative analysis of intermolecular interaction, pair distribution function is adopted in this case. [3]

4.1.2 Ambiguities beyond the overlayer structures of CO on Pt(111)

A brief summary of previous results concerning the adsorption geometry at a temperature range between 100 K and 150 K is as follows: (1) atop sites are primarily occupied by CO, followed by bridge-site occupation at increased coverage of 0.2 ML,[4–7] (2) ontop-dominant $(\sqrt{3}\times\sqrt{3})$R30° structures appear up to coverage of $\sim$ 0.3 ML,[4, 8, 9] and ontop-bridge mixed c(4×2) [4, 8–10] appears at higher coverage (see Figure 4.1).

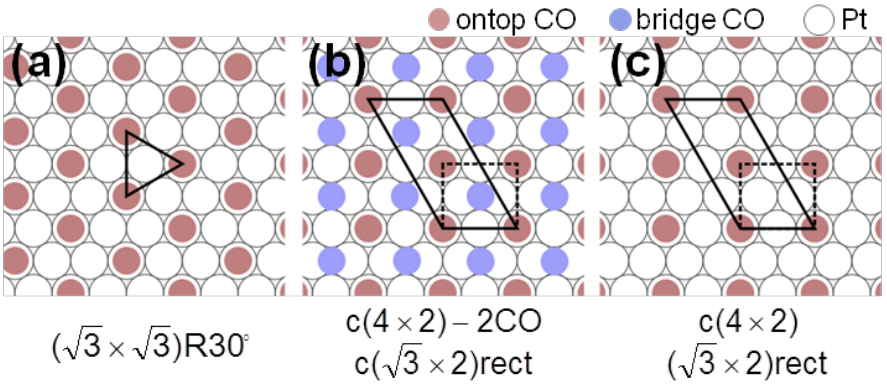

FIGURE 4.1: Representative overlayer structures of CO adsorbed on Pt(111) surface.

Low energy electron diffraction (LEED) experiments have shown that $(\sqrt{3} \times \sqrt{3})$R30°-derived structures appear at 0.17 ML, 0.25 ML and 0.33 ML,[4] and Tüshaus et al. suggested real space models of 4×4 and 8×8 islands with $(\sqrt{3} \times \sqrt{3})$R30° local structure having all molecules in the atop position for 0.17 and 0.33 ML, respectively.[11] However, they did not mention the location of bridge CO molecules and their contribution to the formation of the overlayer structure, although bridge CO must be involved in surface coverage higher than 0.2 ML. Indeed, both infra-red absorption-reflection spectroscopy (IRAS)[11–13] and electron energy loss spectroscopy (EELS)[4, 6, 7, 9, 10] confirmed that the vibrational peak corresponding to the C-O internal stretch mode of bridge CO appears from 0.2 ML. So far, there has been no report that precisely describes where the bridge CO is located inside superstructures. The most reasonable space for bridge-CO occupation is between islands, but still there has been no direct evidence to prove it.

Another issue to be discussed is the detailed phase evolution of overlayer structures from $(\sqrt{3} \times \sqrt{3})$R30° to c$(4 \times 2)$ in the coverage range from 0.3 to 0.5 ML. According to the LEED pattern, the c(4×2) structure starts appearing above 0.33 ML.[14] The line width of M-C stretch mode ($\nu(M-C)$) of ontop CO measured by IRAS is sensitive to the structural homogeneity of the adsorbate layer,[14, 15] providing precise information on structural changes. Ryberg observed a distinct minimum and a sharp increase in line width at 0.3 ML, which revealed a change in the overlayer structure from 8×8 islands with $(\sqrt{3} \times \sqrt{3})$R30°

local structure to a c(4×2) domain.[14] Interestingly, they observed that the line width rapidly increased to a maximum value at 0.38 ML and decreased to a constant value, which was kept up to 0.5 ML. Malik and Trenary also observed a similar feature.[12] However, no detailed explanation for this has been provided in terms of overlayer structure.

4.1.3 Scope of this section & methods

In previous chapter, I described isolated molecules with surface coverage less than 0.01 ML, which is in a regime with negligible intermolecular interaction due to the long intermolecular distances. This chapter deals with the intermolecular interaction by observing the overlayer structures at increased coverage, from 0.10 ML to 0.55 ML.

With gradual increase of the surface coverage, well-known overlayer structures, e.g. $(\sqrt{3} \times \sqrt{3})$R30° and c$(4 \times 2)$ (Figure 4.1) were observed with previously unveiled details. Also the unveiled detailed structures suggest new type of intermolecular interactions, other than the simple repulsive interaction.

The experimental procedure is like below: The clean surface of Pt(111) was prepared with repeated cycles of annealing up to 800 °C and Ar^+ sputtering, followed by oxygen treatment (1.0×10^{-5} Pa, ∼450 °C) and flash annealing up to 800 °C to remove remaining oxygen. CO gas was leaked from a leak valve, and the metal substrate was brought to near the nozzle to achieve exposure in UHV environment, and the substrate temperature at the exposure was estimated to be 50 K. Unless stated, CO-exposed surfaces were annealed room temperature (300 K) prior to scanning at 4.8 Kto get overlayer structures in thermodynamically ground state. The surface coverages were estimated from the number of molecules in the unit area.

4.2 Formation of $(\sqrt{3} \times \sqrt{3})$R30°slands: Intermolecular interaction between ontop CO molecules

Up to $\theta \approx 0.35$ ML, the most of adsorbates preferentially occupy the ontop sites of Pt(111) surface. Therefore the overlayer structures in these surface coverages are reflecting the intermolecular interaction between ontop-adsorbed molecules. [†]

Mostly accepted interaction model of CO adsorbed on metal surface is simple short-range repulsive model from dipole-dipole interaction, which is wholly depending on the intermolecular distance. In previous model [16] and following studies assumed the simple repulsive model whole depending on the intermolecular distance, and the effective distance which the adsorbate feels the repulsive interaction significantly was $\frac{\sqrt{7}}{2}a_0$($a_0 = 2.7$ Å, unit lattice of Pt(111) surface), the distance between ontop and bridge CO in c(4×2)domain at 0.5 ML. Consequently the shortest ontop-ontop distance is $\sqrt{3}a_0$, which is the unit distance of $(\sqrt{3} \times \sqrt{3})$R30° structure. Note that, if the effective distance of repulsive interaction is limited to be less than $\sqrt{3}a_0$, the probability to have intermolecular distance longer than $\sqrt{3}a_0$ should be identical for all distance. With a simple calculation, the average intermolecular distance at a specific surface coverage θ is $\frac{1}{\sqrt{\theta}}a_0$ because the definition of coverage unit "monolayer" is simple number ratio of adsorbate over the surface atom.

4.2.1 Formation of $(\sqrt{3} \times \sqrt{3})$R30° islands with antiphase boundary

A gradual increase in CO exposure from the low coverage with isolated molecules brought forth the ordering of molecular layers, as shown in Figure 4.2.

Figure 4.2 shows the evolution of $(\sqrt{3} \times \sqrt{3})$R30°islands from a randomly distributed molecular arrangement (Figure 4.2a) with increasing surface coverage. In Figure 4.2b-d, all

[†]Additional analysis on the geometry of $(\sqrt{3} \times \sqrt{3})$R30° islands and the size distribution is provided in Appendix A.

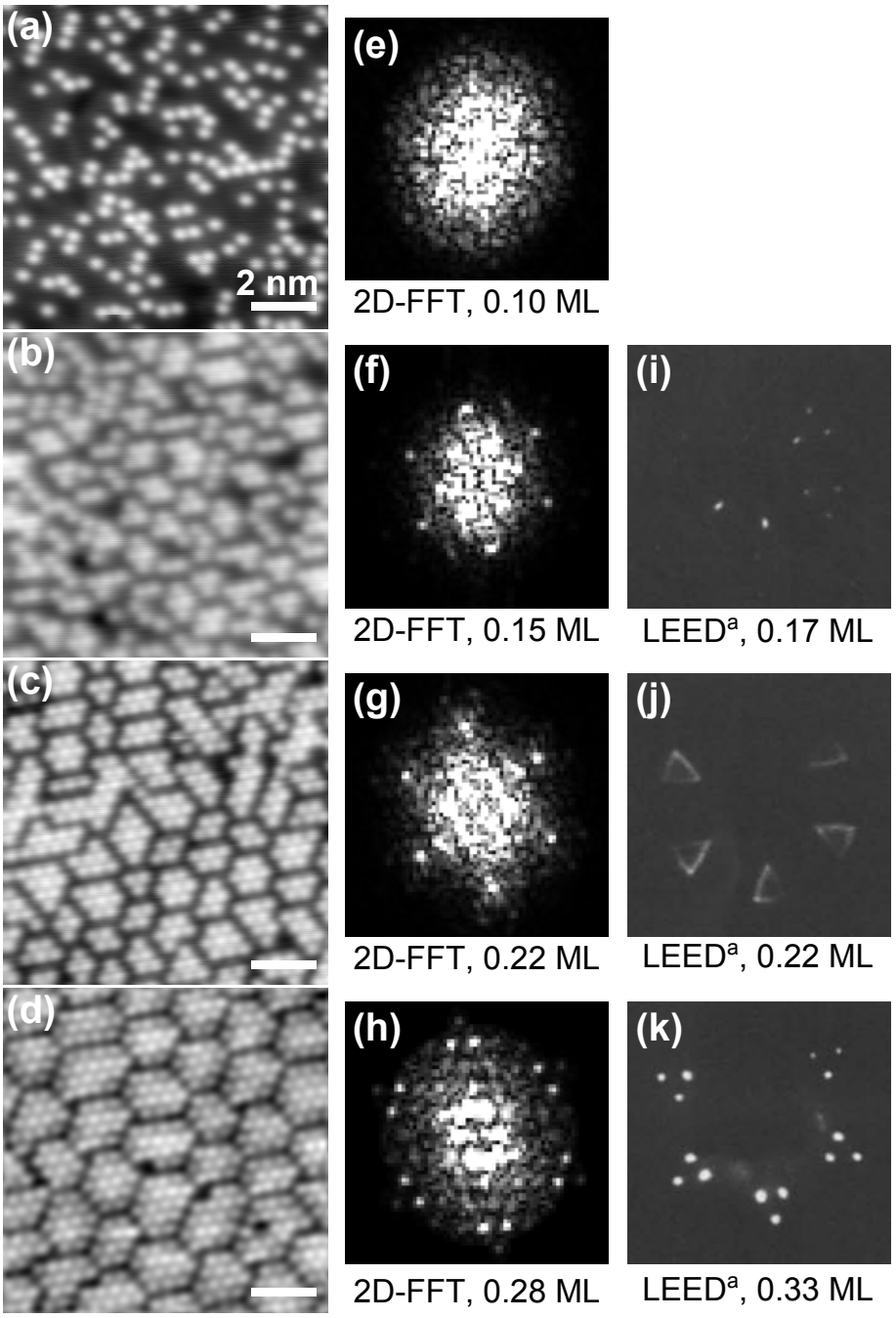

FIGURE 4.2: (a)-(d) are STM images with increasing surface coverage, and (e)-(h) are two-dimensional Fourier transform of corresponding STM images, respectively. Scanning condition: (a) V_S = 0.1 V and I_T = 1 nA, (b) V_S = 0.1 V and I_T = 1 nA, (c) V_S = 0.1 V and I_T = 0.5 nA, and (d) V_S = 0.1 V and I_T = 0.5 nA.

[a](i)-(k) are LEED pattern observed in preceding study, adapted from [4]. Copyright 1982, with permission from Elsevier.

molecules inside the islands show the $(\sqrt{3} \times \sqrt{3})$R30° arrangement, and the average number of molecules in the island at each coverage was measured to be 3.09 ± 1.37 molecules (0.15 ML, Figure 4.2b), 5.47 ± 2.66 molecules (0.22 ML, Figure 4.2c), and 13.04 ± 2.31 molecules (0.28 ML, Figure 4.2d). Although small-sized (10 nm×10 nm) STM images are presented in Figure 4.2, the homogeneity of island size and structures was confirmed by wide-area scanning at various positions. ‡

The results of two-dimensional Fourier transform (2D-FFT)(Figure 4.2e-h) and the LEED patterns reported by Steininger *et al.*[4](Figure 4.2i-k) are shown in Figure 4.2. 2D-FFT images greatly reproduce the split pattern of $(\sqrt{3} \times \sqrt{3})$R30° arrangement observed by LEED. In Figure 4.2f, outer spots of split pattern is very faint but surely exist. In Figure 4.2g also, outer split patterns are fainter than the most inner spot, but clearly shows the split pattern. For Figure 4.2j, LEED pattern shows triangles which connect the split spots with continuous line. This is different from the clear spots shown in 2D-FFT pattern(Figure 4.2g), and the reason of difference may be originated from the observation temperature, 4.7 K in this study and 100 K in [4]. 100 K of observation temperature may result in the thermally activated diffusion among the islands, blurring the diffraction spots. Irregular intensity of split spots are due to the limited image size. In our best observation, no large-area domains with the $(\sqrt{3} \times \sqrt{3})$R30° arrangement were found, which implies the existence of intermolecular interactions limiting the size of islands. Though all observations in Figure 4.2 were made after room-temperature annealing, additional low-temperature adsorption onto the 0.22 ML (Figure 4.2c) without room-temperature annealing resulted the similar island formation as Figure 4.2d, no large-area domain with $(\sqrt{3} \times \sqrt{3})$R30° arrangement .

In order to find detail information about the molecular arrangement in c and d of Figure 4.2, cropped images from Figure 4.2c and d are depicted with the corresponding

‡The coverages in the paper published in Journal of Physical Chemistry C[1] are corrected to the values written in this dissertation (0.16 ML, 0.24 ML and 0.32 ML → 0.15ML, 0.22 ML and 0.28 ML for Figure 4.2b, c and d, respectively), after the calibration of scan size with the atomic resolution images of Pt(111) surface.

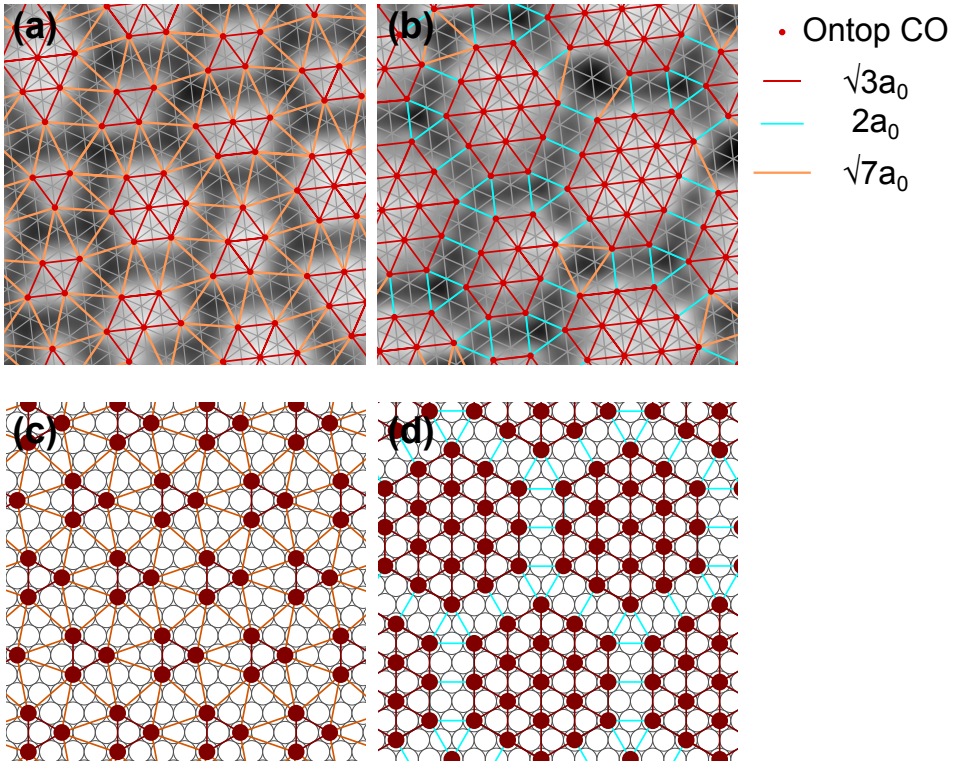

FIGURE 4.3: (a) and (b) are schematic models superimposed to the zoomed-in STM images from Figure 4.2 c and d. (c) and (d) are schematic model suggested from $(\sqrt{3} \times \sqrt{3})$R30° split patterns from LEED observation [11]

schematic models as shown in a and b of Figure 4.3, respectively. Although the internal arrangement of each island is $(\sqrt{3} \times \sqrt{3})$R30°, neighboring islands are laterally shifted relative to each other by a unit lattice of the Pt(111) surface at both surface coverages. This lateral shift results in the formation of an anti-phase boundary between neighboring islands. However, despite of the same magnitude of shift, the island structures in Figure 4.3a and b are different from each other in terms of the inter-island distance. The inter-island distance is defined as the shortest intermolecular distance between two neighboring islands, which corresponds to $\sqrt{7}a_0$ in Figure 4.3a and $2a_0$ in Figure 4.3b, and is represented by orange lines and light blue lines, respectively. The inter-island distances are remarkably homogeneous in both coverages.

Compared to the suggested models in Figure 4.3c and d, the experimental results

Figure 4.3a and b are very consistent in terms of inter-island distance, $\sqrt{7}a_0$ and $2a_0$ respectively.

4.2.2 Bridge-adsorbed CO in $(\sqrt{3} \times \sqrt{3})$R30° - structures

8×8 islands form the boundaries with rectangular geometry, which is the unit structure of c(4×2) domain. In Figure 4.2 and corresponding model in Figure 4.3b, it is notable that $2a_0$ of the inter-island distance leads to the formation of the c$(\sqrt{3} \times 2)$rect arrangement between neighboring islands, consistent with the suggested (8×8) real space model from LEED observations.

The c$(\sqrt{3} \times 2)$rect arrangement is identical to the structure of the rectangular units observed in Chapter 3, which provides the possibility of locating a bridge CO (marked with light blue dots in Figure 4.4f) in the center of each rectangular unit(c$(\sqrt{3} \times 2)$rect). This would imply that bridge-adsorbed COs can coexist with ontop-dominating $(\sqrt{3} \times \sqrt{3})$R30° islands by forming a local boundary with a c$(\sqrt{3} \times 2)$rect structure. Note that some CO molecules at the rim of each island show a lower protrusion than COs inside the island, which will be discussed in the next section as the evidence of bridge occupation with c$(\sqrt{3} \times 2)$rect arrangement. If every available center of the rectangular units is occupied

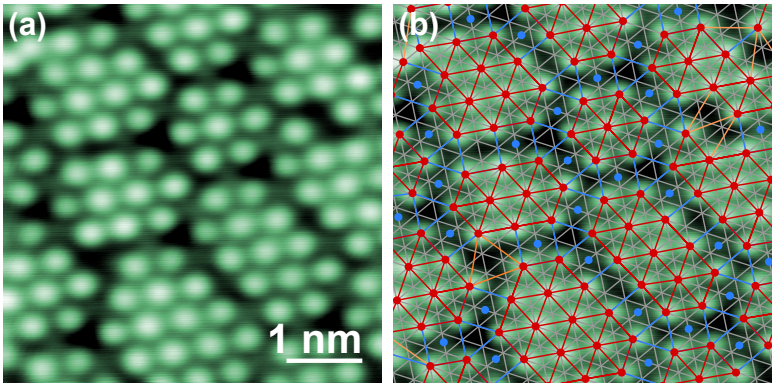

FIGURE 4.4: 8x8 islands with inter-island distance of $2a_0$ and model for bridge-occupation at the boundaries. V_S = 2 mV and I_T = 2 nA

by a bridge CO, the coverage of this surface (Figure 4.2d) could reach to 0.41 ML while it was previously estimated to be 0.315 ML when only ontop CO molecules were counted.

4.3 Phase transition from $(\sqrt{3} \times \sqrt{3})$R30° to c$(4 \times 2)$

An additional dose of CO molecules on the surface of Figure 4.4 induced the emergence of a rectangular superlattice (Figure 4.5) on the surface covered with hexagonally arranged $(\sqrt{3} \times \sqrt{3})$R30° islands. At the early stage of rectangular lattice formation, three regions are observed (Figure 4.5a); the $(\sqrt{3} \times \sqrt{3})$R30° islands that already existed, an inhomogeneous mixture of $(\sqrt{3} \times \sqrt{3})$R30° and c$(4 \times 2)$ domains (Figure 4.5b), and a well-developed rectangular superlattice (Figure 4.5c). The size of most domains in the mixture region (Figure 4.5b) does not exceed the size of $(\sqrt{3} \times \sqrt{3})$R30° islands (Figure 4.2d), so that the mixture region can be understood as an intermediate of the phase transition from hexagonal to rectangular superlattices which results from the compression of the $(\sqrt{3} \times \sqrt{3})$R30° islands accompanied with widening of c$(\sqrt{3} \times 2)$rect (c(4×2)) boundary.

4.4 c(4×2) domains & intermolecular interaction between bridge CO and ontop CO

Inside the rectangular superlattice in Figure 4.5, ontop COs are clearly recognizable, whereas individual bridge COs are not clearly resolved in the STM image due to their low protrusion ($\sim$ 20 pm). Dip structures are also observed at the center of the rectangular units, which corresponds to the vacancies of bridge CO. The bridge vacancies provide contrast to recognize individual bridge CO molecules. A detailed STM image (Figure 4.6a) and the line profile (Figure 4.6f) along the blue solid line apparently indicate that bridge vacancies appear as dip structures at the position where bridge CO are supposed to occupy.

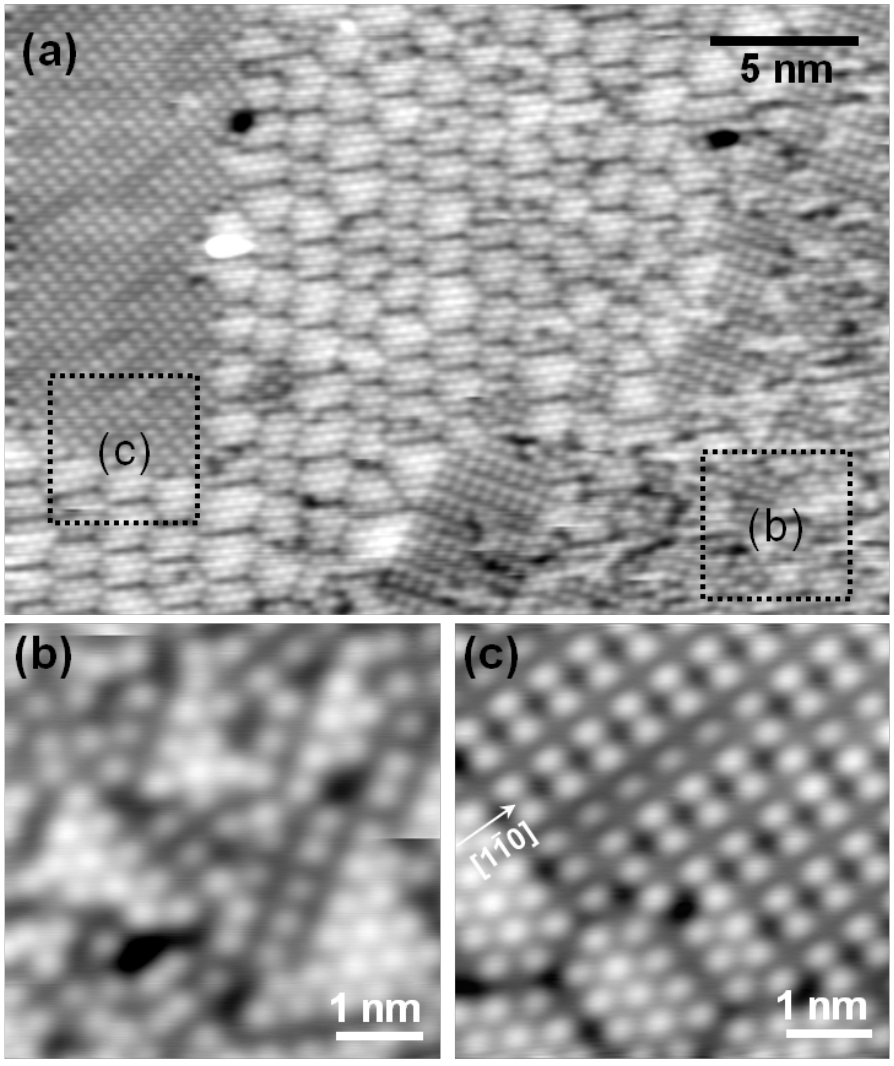

FIGURE 4.5: Phase transition from $(\sqrt{3} \times \sqrt{3})$R30° to c$(4 \times 2)$. (a) Coexistence of hexagonal and rectangular lattice of CO molecules, appearing in the middle of phase transition (image size $30 \times 20\,\mathrm{nm}^2$, V_S = 0.1 V, I_T = 0.5 nA), (b) and (c) are zoomed-in images from marked regions in (a). (b) Irregularly mixed phase with small domain of $(\sqrt{3} \times \sqrt{3})$R30° phase and c$(4 \times 2)$ phase. (image size $5 \times 5\,\mathrm{nm}^2$, V_S = 0.1 V, I_T = 1 nA). (c) Boundary region between the $(\sqrt{3} \times \sqrt{3})$R30° phase and bridge-vacant c(4×2) phase (image size $5 \times 5\,\mathrm{nm}^2$, V_S = 0.1 V, I_T = 0.5 nA).

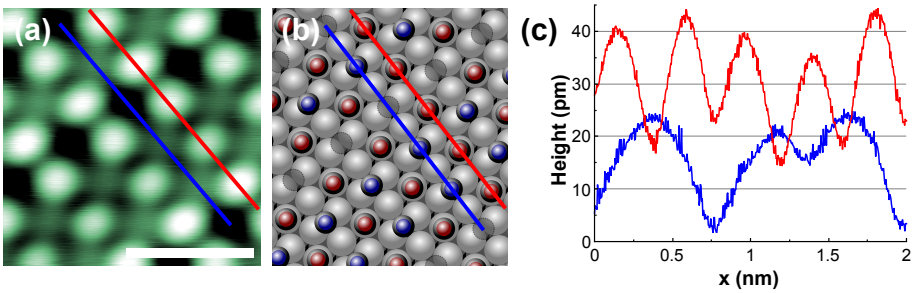

FIGURE 4.6: Bridge-vacant $c(4 \times 2)$ domain. (a) Detailed image of c(4×2) domain (the scale bar is 1 nm, V_S = 20 mV and I_T = 50 pA), (b) corresponding model for the image, and (c) the line profile along the red line (ontop CO molecules) and blue line (bridge CO molecules)

As a consequence, the rectangular units are classified into two types according to whether it has a bridge CO or not; one is c$(\sqrt{3} \times 2)$rect with a bridge CO, and the other is $(\sqrt{3} \times 2)$rect without any bridge CO. Note that both c$(\sqrt{3} \times 2)$rect and $(\sqrt{3} \times 2)$rect can be commonly considered as c(4×2) in the conventional Wood notation, as depicted in b and c of Figure 4.1, respectively. The bridge vacancies lie along the $[1\bar{1}0]$ direction of the Pt surface in Figure 4.5c. The surface coverage of the rectangular domain region in Figure 4.5a was estimated to be 0.375 ML. This number lies in the coverage range of $(\sqrt{3} \times \sqrt{3})$R30° islands region between 0.315 and 0.41 ML, according to the number of boundary rectangular units filled with bridge CO as mentioned in section 3-3. Thus, the hexagonal-rectangular phase transition might occur at the observed surface coverage of 0.375 ML, which is consistent with the LEED studies observing that the c(4×2) structure appeared from 0.35 ML.

Interestingly, Figure 4.5c shows ontop CO molecules with various heights. A magnified image of a rectangular domain (Figure 4.6a), a schematic model of Figure 4.6a (Figure 4.6b), and the corresponding line profile along the red dashed line (Figure 4.6c) indicate that the CO molecule marked with an arrow is apparently dimmer and lower than the other ontop CO molecules. Considering the arrangement of brighter and dimmer ontop molecules, the height difference reveals strong correlation with the number of neighboring

bridge CO molecules. Each ontop CO has four available sites for adjacent bridge occupation in a c($\sqrt{3} \times 2$)rect arrangement. In Figure 4.6b, the brighter ontop CO have only two neighboring bridge CO molecules while the dimmer ontop CO are fully surrounded by four bridge COs.

In order to examine this observation quantitatively, another STM image of bridge-vacant $c(\sqrt{3} \times 2)$ domain was obtained as shown in Figure 4.7a, and the height of all ontop CO was measured.

Figure 4.7b represents one of the line profiles used for measuring the height of ontop COs, with each ontop CO marked with the number of neighboring bridge CO (N_{nbCO}) using black circles ($N_{\mathrm{nbCO}} = 2$), red squares ($N_{\mathrm{nbCO}} = 3$), and green triangles ($N_{\mathrm{nbCO}} = 4$). There are 98 ontop CO molecules in Figure 4.7a; 63 ontop COs with two neighboring bridge COs ($N_{\mathrm{nbCO}} = 2$), eight ontop COs with three neighboring bridge COs ($N_{\mathrm{nbCO}} = 3$), and 27 ontop COs with four neighboring bridge COs ($N_{\mathrm{nbCO}} = 4$). The average height of ontop CO according to N_{nbCO} are 26.1 $\pm$ 1.2, 21.6 $\pm$ 0.9, and 17.8 $\pm$ 1.0 pmfor N_{nbCO} = 2, 3, and 4, respectively (Figure 4.7c). Therefore, our observation clearly indicates that

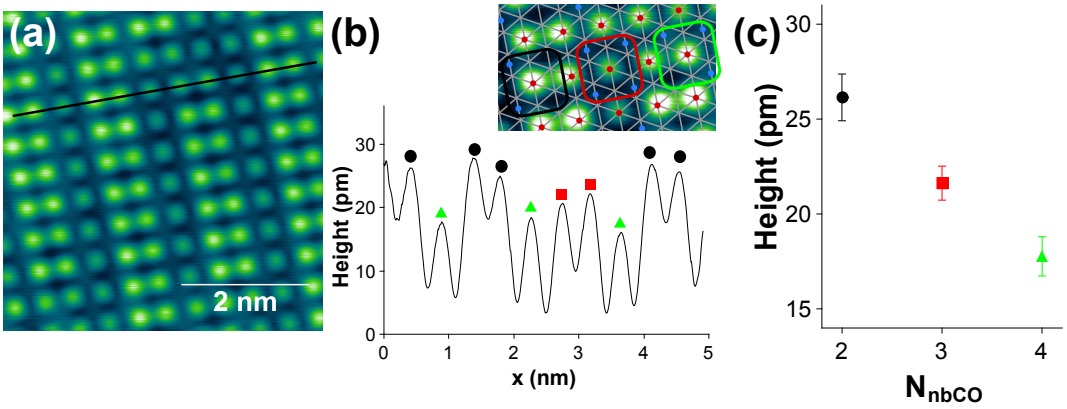

FIGURE 4.7: Bridge - ontop CO interaction in bridge-vacant c(4×2) domain. (a) An STM image of bridge-vacant domain, (b) the line profile along the black line in (a), the position of each ontop CO is marked with black circle ($N_{\mathrm{nbCO}} = 2$), red square($N_{\mathrm{nbCO}} = 3$), and green triangle($N_{\mathrm{nbCO}} = 4$). Inset: magnified part of STM image indicating the ontop COs according to N_{nbCO}. (c) Resultant historgram to show the height of ontop CO depending on N_{nbCO}.

the protrusion of ontop CO is significantly dimmed as the number of adjacent bridge CO increases.

One of the possible explanations accounting for the height modulation of ontop CO would be a change in real topographic height, by altering the M–C or C–O bond length. However, the relative position of each atom in ontop CO at 0.3 ML of surface coverage coincides well within error bars of $\pm$ 0.1 Å with that at 0.5 ML of surface coverage, according to the analysis of LEED intensity. Another possibility might be tilting of ontop CO resulting from a repulsive intermolecular interaction that forces the ontop CO to lean toward the bridge vacancy. However, this explanation does not seem reasonable, as the ontop CO at this coverage are known to stand upright from electron-stimulated desorption ion angular distribution (ESDIAD), near edge x-ray absorption fine structure (NEXAFS), and LEED studies. Another possible explanation would be a change in the charge density distribution of ontop CO by the surrounding bridge CO, considering that the topographic STM image provides information not only about geometry but also about the charge density distribution based on the local density of state.

The charge density distribution of each adsorption species is dependent on (1) the amount and direction of charge transfer between the metal and CO and (2) the internal charge distribution of the CO molecule itself. On one hand, regarding the charge transfer between CO and the Pt surface, several groups have reported a work function decrease upon CO adsorption up to certain coverage and a subsequent increase with additional dose, with the minimum work function at the onset coverage for bridge occupation. This work function change has been interpreted as showing the opposite direction of charge transfer between ontop CO and bridge CO, i.e. the direction of ontop CO-to-metal and metal-to-bridge CO charge transfer, respectively. At surface coverage exceeding the work function minimum, bridge CO depolarize the metal surface, which had been polarized by charge transfer from the ontop CO. This depolarizing scheme may apply to the height modulation of ontop COs in the bridge-vacant c(4×2) domain on the microscopic scale,

such that the charge density of ontop CO decreases upon adjacent bridge-CO adsorption due to charge re-distribution through the metal substrate. The typical Blyholder model and further modified models of CO adsorption also support this explanation, since bridge CO have been considered to accept the charges from the Pt substrate from its lower C-O stretch frequency, which is evidence of stronger back-bonding to the $2\pi^*$ orbital[17], while the ontop CO have been considered to provide charges to the Pt substrate.

On the other hand, regarding the internal charge distribution of each CO adsorbate, Norton et al. insisted that the dipole moment of each adsorption species must be opposite, as ontop CO have the positive end outwards ($C^{\delta-} - O^{\delta+}$), while bridge CO have the negative end outwards ($C^{\delta+} - O^{\delta-}$) by simultaneously measuring the work function change and temperature-programmed desorption.[18] In this point of view, various height of ontop CO in bridge-vacant $c(4 \times 2)$ domain can be understood as the different degree of dipole-dipole interaction according to the number of neighboring bridge CO in local environment. Additionally, the dimmer ontop CO with fully occupied bridge CO may result from the lateral broadening of the charge density distribution due to the attractive electrostatic interaction between two opposite direction of dipoles. Our observation provides the microscopic evidence for the previous discussions about the inter-adsorbate interactions.

The opposite direction of charge transfer can provide additional explanations to our observations. One aspect regarding the attractive interaction between ontop and bridge COs is the existence of rectangular $c(\sqrt{3} \times 2)$rect units with low-temperature adsorption. As an extended discussion following section 3.2, the electrostatic interaction between the ontop CO dipole and the bridge CO dipole may provide significant stabilization of $c(\sqrt{3} \times 2)$rect units over the $(\sqrt{3} \times 2)$rect structure without a bridge CO. Also the alignment of the bridge vacancy along the $[1\bar{1}0]$ direction can be understood with the electrostatic dipolar interaction. The ontop COs in the $(\sqrt{3} \times 2)$rect unit will repulsively interact with each other due to the same direction of their dipole moments, resulting in preference

for the $[1\bar{1}0]$ direction, which provides a longer ontop-ontop distance ($2a_0$) than the $[1\bar{1}2]$ direction ($3a_0$).

Observation of bridge-vacant c(4×2) domain and the inter-adsorbate interaction can provide plausible explanation about the maximum line width of M-C stretch mode at 0.38 ML of surface coverage. As mentioned in the Introduction section, the line width has been interpreted as a measure of the ordering of overlayer structure, so that the maximum line width at 0.38 ML with well developed c(4×2) pattern was explained as indicating c(4×2) island in very disordered matrix.[19] However our observation revealed that the overlayer structure at 0.38 ML is well ordered c(4×2) domain accompanied with bridge vacancies, without any disordered matrix. Moreover ontop COs with various height according to the number of neighboring bridge CO indicates the ontop COs are in locally inhomogeneous environment due to the inter-adsorbate interaction, possibly resulting in the broadening of the line width.

The height difference of ontop CO according to the number of neighboring bridge CO (N_{nbCO}) consistently appears with increased surface coverage, as shown in Figure 4.8.

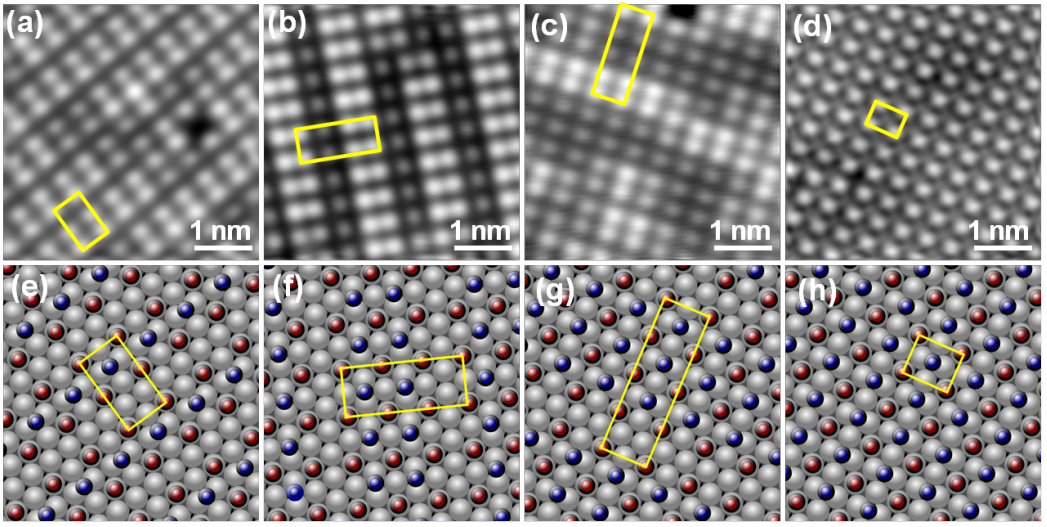

FIGURE 4.8: Bridge-vacant c(4×2) domains at various surface coverages. (a) $\sim$ 3/8 ML (V_S = 0.1 V, I_T= 1 nA), (b) $\sim$ 5/12 ML (V_S = 0.1 V, I_T= 0.5 nA), (c) $\sim$ 7/16 ML (V_S = 0.1 V, I_T= 1 nA), and (d) $\sim$ 1/2 ML (V_S = 0.1 V, I_T= 0.5 nA)

As more CO molecules were dosed, the number of brighter ontop species gradually decreased, resulting in a complete c(4×2) structure with homogeneous height of ontop CO (Figure 4.8d). The unit cells in Figure 4.8 are simple combinations of the c$(\sqrt{3} \times 2)$rectunit and $(\sqrt{3} \times 2)$rect, and we can find the position of bridge CO vacancies from the relative height of ontop COs in the rectangular unit. The number ratio of bridge vacancies over all the available bridge sites was modeled to be $1/2$ for 0.375 ML (Figure 4.8a and e), $1/3$ for 0.4175 ML (Figure 4.8b and f), $1/4$ for 0.4375 ML (Figure 4.8c and g), and eventually zero for 0.5 ML (Figure 4.8d and h). In our STM images, the minimum surface coverage to form rectangular domains was estimated to be 0.375 ML, as shown in Figure 4.8a and the rectangular domain in Figure 4.5, also described in the previous section, for which the minimum required number ratio of bridge CO over all available bridge sites to stabilize the c(4×2) domain is $1/2$. As the surface coverage increased, i.e. filling the bridge vacancy, the arrangement of bridge CO vacancies along the $[1\bar{1}0]$ direction of the Pt crystal lattice became irregular.

Figure 4.9 describes the adsorption structure when the coverage was higher than 0.5 ML. As suggested in previous studies as the "fault-line model", a higher dose of CO to the c(4×2) domain causes the compression of the c(4×2) structure to form a 1×1 domain boundary, resolved at the individual molecular level (Figure 4.9a and b). The intermolecular interaction between neighboring ontop CO molecules in the 1×1 domain appears repulsive, deduced from the intermolecular distance (3.0 Å) and the angle (close to 90°), significantly larger than the Pt-Pt distance and smaller than the Pt-Pt angle (120°), respectively. Consequently, the CO molecules at the 1×1 boundary may be tilted with respect to the surface normal direction by repulsive interactions, as suggested in an ESDIAD study[20].

It is generally known that achieving coverage greater than 0.5 ML is difficult in a UHV environment, and we found that this is true especially when the coverage is gradually increased with room temperature annealing. To increase the coverage up to approximately

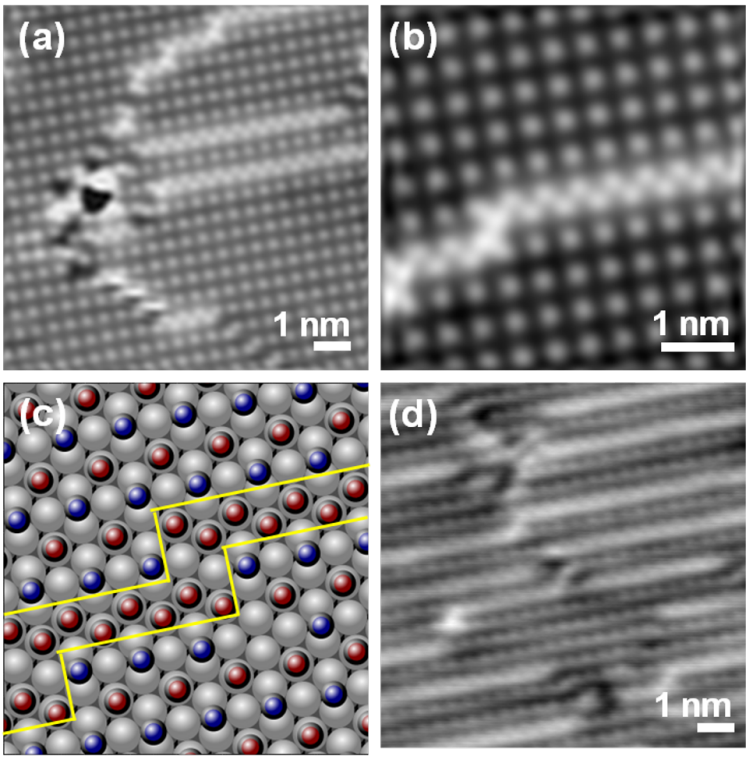

FIGURE 4.9: STM images of surface coverage over 0.5 ML V_S = 20 mV and I_T = 50 pA.

0.55 ML, a higher dose of CO at low temperature is mandatory prior to the annealing step. The resulting structure is presented in Figure 4.9d, consistent with previous predictions of a reduction in the c$(\sqrt{3} \times 2)$rect domain size as well as an increase in the relative area of 1×1 boundaries.[16]

4.5 Conclusion

In conclusion, we presented the adsorption behavior of CO on Pt(111) from a single-molecule limit to high coverage superstructures. The adsorption geometry and the formation of overlayer structures were observed in molecular resolution from coverage of 0.1 ML to approximately 0.56 ML, to show the evolution of $(\sqrt{3} \times \sqrt{3})$R30° islands and phase transition to a c(4×2) rectangular lattice, and further 1×1 boundary formation in the c(4×2) domain. CO adsorption on the bridge site in the range of our observations involves the rectangular unit structure, c$(\sqrt{3} \times 2)$rect, from the appearance of bridge CO

at 0.1 ML by low-temperature adsorption to the boundary structure in $(\sqrt{3} \times \sqrt{3})$R30° islands and bridge-vacant c(4×2) domains. Bridge-vacant c(4×2) domain exhibit height modulation of atop CO by adjacent bridge CO, indicating the existence of inter-adsorbate interactions between the atop and bridge CO. As the origin of the interaction, the directions of charge transfer and the dipole according to the adsorption site were discussed. The present study may clear up the ambiguities in the overlayer structure of CO on Pt(111) as well as provide insight into inter-adsorbate interactions.

References

[1] Yang, H. J., Minato, T., Kawai, M. & Kim, Y. STM investigation of CO ordering on Pt(111): From an isolated molecule to high-coverage superstructures. *J. Phys. Chem. C* **117**, 16429–16437 (2013). URL http://dx.doi.org/10.1021/jp404231t.

[2] Jardine, A. P., Hedgeland, H., Alexandrowicz, G., Allison, W. & Ellis, J. Helium-3 spin-echo: Principles and application to dynamics at surfaces. *Prog. Surf. Sci.* **84**, 323–379 (2009). WOS:000272587600001.

[3] Knorr, N., Brune, H., Epple, M., Hirstein, A., Schneider, M. A. & Kern, K. Long-range adsorbate interactions mediated by a two-dimensional electron gas. *Phys. Rev. B* **65**, 115420 (2002). URL http://link.aps.org/doi/10.1103/PhysRevB.65.115420.

[4] Steininger, H., Lehwald, S. & Ibach, H. On the adsorption of CO on Pt(111). *Surf. Sci.* **123**, 264–282 (1982). URL http://www.sciencedirect.com/science/article/pii/0039602882903284.

[5] Kinne, M., Fuhrmann, T., Whelan, C. M., Zhu, J. F., Pantförder, J., Probst, M., Held, G., Denecke, R. & Steinrück, H.-P. Kinetic parameters of CO adsorbed on Pt(111) studied by in situ high resolution x-ray photoelectron spectroscopy. *J. Chem. Phys.* **117**, 10852 (2002). URL http://link.aip.org/link/JCPSA6/v117/i23/p10852/s1&Agg=doi.

[6] Cudok, A., Froitzheim, H. & Schulze, M. Low-temperature adsorption kinetics of CO on Pt(111) derived from nonequilibrium time-resolved electron-energy-loss spectroscopy measurements. *Phys. Rev. B* **47**, 13682–13686 (1993). URL http://link.aps.org/doi/10.1103/PhysRevB.47.13682.

[7] Mieher, W. D., Whitman, L. J. & Ho, W. A time resolved electron energy loss spectroscopy study of CO on Pt(111): Adsorption site occupations versus coverage and temperature. *J. Chem. Phys.* **91**, 3228–3239 (1989). URL http://jcp.aip.org/resource/1/jcpsa6/v91/i5/p3228_s1.

[8] Ertl, G., Neumann, M. & Streit, K. M. Chemisorption of CO on the Pt(111) surface. *Surf. Sci.* **64**, 393–410 (1977). URL http://www.sciencedirect.com/science/article/pii/0039602877900528.

[9] Hopster, H. & Ibach, H. Adsorption of CO on Pt(111) and Pt 6(111) $\times$ (111) studied by high resolution electron energy loss spectroscopy and thermal desorption spectroscopy. *Surf. Sci.* **77**, 109–117 (1978). URL http://www.sciencedirect.com/science/article/pii/0039602878901644.

[10] Froitzheim, H., Hopster, H., Ibach, H. & Lehwald, S. Adsorption sites of CO on Pt(111). *Appl. Phys.* **13**, 147–151 (1977). URL http://rd.springer.com/article/10.1007%2FBF00882473.

[11] Tüshaus, M., Schweizer, E., Hollins, P. & Bradshaw, A. Yet another vibrational study of the adsorption system Pt{111}-CO. *J. Electron Spectrosc. Relat. Phenom.* **44**, 305–316 (1987). URL http://www.sciencedirect.com/science/article/pii/0368204887870317.

[12] Malik, I. J. & Trenary, M. Infrared reflection-absorption study of the adsorbate-substrate stretch of CO on Pt(111). *Surf. Sci. Lett.* **214**, L237–L245 (1989). URL http://www.sciencedirect.com/science/article/pii/0167258489900327.

[13] Hayden, B. & Bradshaw, A. The adsorption of CO on Pt(111) studied by infrared reflection-absortion spectroscopy. *Surf. Sci.* **125**, 787–802 (1983). URL http://www.sciencedirect.com/science/article/pii/S0039602883800600.

[14] Ryberg, R. Phase transitions in a chemisorbed overlayer studied by infrared spectroscopy: CO on Pt(111). *Phys. Rev. B* **40**, 865–868 (1989). URL http://link.aps.org/doi/10.1103/PhysRevB.40.865.

[15] Kuhl, D., Lin, K., Chung, C., Luo, J., Wang, H. & Tobin, R. Coverage-, temperature-, and frequency-dependent broadband infrared reflectance change induced by CO adsorption on Pt(111). *Chem. Phys.* **205**, 1–10 (1996). URL http://www.sciencedirect.com/science/article/pii/0301010495002642.

[16] Schweizer, E., Persson, B., Tüshaus, M., Hoge, D. & Bradshaw, A. The potential energy surface, vibrational phase relaxation and the order-disorder transition in the adsorption system Pt{111}-CO. *Surf. Sci.* **213**, 49–89 (1989). URL http://www.sciencedirect.com/science/article/pii/0039602889902525.

[17] Blyholder, G. Molecular orbital view of chemisorbed carbon monoxide. *J. Phys. Chem.* **68**, 2772–2777 (1964). URL http://dx.doi.org/10.1021/j100792a006.

[18] Norton, P., Goodale, J. & Selkirk, E. Adsorption of CO on Pt(111) studied by photoemission, thermal desorption spectroscopy and high resolution dynamic measurements of work function. *Surf. Sci.* **83**, 189–227 (1979). URL http://www.sciencedirect.com/science/article/pii/0039602879904886.

[19] Ryberg, R. The metal-molecule stretch vibrational mode studied by infrared spectroscopy; CO on Pt(111). *J. Electron Spectrosc. Relat. Phenom.* **54–55**, 65–80 (1990). URL http://www.sciencedirect.com/science/article/pii/036820489080200T.

[20] Kiskinova, M., Szab, A. & Yates Jr., J. Compressed CO overlayers on Pt(111) — evidence for tilted CO species at high coverages by digital ESDIAD. *Surf. Sci.* **205**, 215–229 (1988). URL http://www.sciencedirect.com/science/article/pii/0039602888901732.

Chapter 5

Bridge-adsorbed CO and the dynamics of the overlayer structure in high coverage

In preceding chapter (Chapter 4), bridge-site occupation of CO on Pt(111) at increased coverage ($\theta > 0.3$ ML) has been discussed in terms of the specific geometry c($\sqrt{3} \times 2$)rect which is the unit cell of c(4×2) domain. Also in Chapter 3 as well, I discussed about the bridge CO at the center of c($\sqrt{3} \times 2$)rect units and the bridge-to-ontop (B-T) conversion upon applying bias pulse from the tip of STM. From these two facts, bridge site of Pt(111) for CO adsorption can be considered as a meta-stabilized state through intermolecular interaction under a specific geometry, and the degree of meta-stabilization can be deduced by constructing potential energy surface. The construction of potential energy surface may allow the discussion of the bridge-CO dynamics depending on the surface coverage, and extended discussion on the intermolecular interaction. In this chapter, the dynamics of bridge CO inside overlayer structures including bridge-ontop conversion (B-T conversion) and bridge-ontop* shuttling (B-T* shuttling) will be discussed with observation of STM images as well as STM action spectroscopy.

5.1 Introduction

5.1.1 Preliminaries: bridge CO & c$(\sqrt{3} \times 2)$rect units in overlayer structures

The bridge-adsorbed CO on Pt(111) demonstrated a very curious and important role in its coverage dependent overlayer structures as shown in the previous chapter. The most well-ordered overlayer structure among $(\sqrt{3} \times \sqrt{3})$R30°-derived structures is characterized by $2a_0$ of inter-island distance (Figure 4.3, Section 4.2.1), and the specific ontop-ontop intermolecular distance($2a_0$) involves the occupation of the bridge site. The $2a_0$ of inter-island distance and the bridge occupation exhibit the formation of c$(\sqrt{3} \times 2)$rect unit, which is the unit cell of c(4×2) domain. The correlation between the bridge CO and c$(\sqrt{3} \times 2)$rect unit is also supported from the significantly smaller probability to find the rectangular unit without bridge CO over probability to find a c$(\sqrt{3} \times 2)$rect unit with bridge CO at low-temperature adsorption, as described in Section 3.2.3.

The evidence $(\sqrt{3} \times \sqrt{3})$R30° island formation with $2a_0$ of inter-island distance has been reproducibly observed by LEED[1–3], while most of Monte-Carlo simulation studies failed to reproduce the island formation.[4–9] Considering that these simulation results successfully demonstrated c(4×2) structures under assumption of exponentially decaying repulsive interaction, another form of intermolecular interaction should be accounted for the formation of antiphase islands. This may reflect the subtle nature of lateral interaction residing in the CO chemisorption system on Pt(111), regarding the intermolecular interaction and correlation of adsorption sites. The intermolecular interaction would also affect to the surface processes involved in lateral motion.

The high resolution of STM to resolve individual molecules enables to investigate very subtle interaction, as demonstrated with the detailed overlayer structures in Chapter 4. In addition to the interactions found from the overlayer structures, the dynamic motion of the bridge-adsorbed CO chemisorbed on Pt(111) will be described in this chapter, in

terms of intermolecular interaction. The bridge-adsorbed CO, which is laterally confined in a specific geometry (c($\sqrt{3} \times 2$)rect), shows unique dynamic conversion of adsorption site by vibrational excitation with inelastic tunneling electrons, as briefly described with Figure 3.8b. It is noteworthy that the ontop CO which does not show any site conversion with tunneling electrons in the energy range of vibrational excitation, in contrast to the bridge CO (Section 3.3.3).

5.1.2 Bridge site occupation and potential energy surface derived from c(4×2) structure

Schweizer *et al.* have described the potential energy surface of CO chemisorbed on Pt(111) at two different surface coverages, very low coverage and 0.5 ML.[10] As briefly described in Chapter 3 (Figure 3.5), the potential energy surface(PES) at the very low surface coverage has been constructed with $\sim$ 60 meV of the adsorption energy difference (ΔE_{ads}) between ontop CO and bridge CO, and the vibrational mode energies of hindered translation(HT) for ontop and bridge CO (Figure 5.1b, green dashed curve). The HT mode is considered as a reaction coordinate for lateral diffusion for both COs, and determines the potential stiffness according to the adsorption site($m\omega_T^2$ and $m\omega_B^2$ for force constants of ontop and bridge CO, respectively). Resultant PES gives $\sim$ 190 meV of ontop-to-bridge diffusion barrier.

Based on the PES at low coverage(dashed green curve in Figure 5.1b), they calculated the potential energy surface at 0.5 ML of surface coverage with c(4×2) overlayer structure, under an assumption of repulsive intermolecular interaction with a short effective range(intermolecular distance). According to their calculation, displacing the bridge CO from the equilibrium position (c(4×2)) towards the nearest neighboring ontop site (v) results in local minimum of PES which is called as T* state as an excited state of bridge CO, at the off-center position of the nearest neighboring ontop site (Figure 5.1b, orange

solid curve). In the following parts, I will reproduce* their procedure to construct the PES with the displaced bridge CO, and find the position of T* state. †

The beginning point is considering one c($\sqrt{3} \times 2$)rect unit in a complete c(4×2) domain (Figure 5.1a), and setting the position of bridge CO (blue circle in Figure 5.1) at the origin. If the bridge CO is displaced a distance v in $[1\bar{1}0]$ direction, the surrounding ontop COs(filled red circles) at the frame of c($\sqrt{3} \times 2$)rect will slightly move(empty red circles) to adjust the force field by the repulsive interaction, as modeled in Figure 5.1a. The calculation of modified PES Figure 5.1b is fulfilled under two assumptions:

(a) Only the nearest-neighbor, i.e. the ontop CO and bridge CO inside c($\sqrt{3} \times 2$)rect unit with $\sqrt{7}a_0/2$ of intermolecular distance, experiences significant intermolecular interaction each other,

(b) Every ontop CO in c(4×2) domain is coupled to four bridge CO, and every bridge CO is also coupled with four ontop CO molecules. If one bridge CO is taken as one of interest, each of surrounding four ontop CO molecules are also coupled to three other bridge CO molecules, respectively.

The two assumptions are parameterized as follows:

(a) Intermolecular interaction: each CO molecule is connected to its four nearest neighbors by harmonic spring with spring constants $m\omega_S^2$ where $m = 28u$ is the mass of CO molecule,

(b) Potential energy surface at the equilibrium position: ontop and bridge CO molecules are confined to their respective lattice sites by harmonic and isotropic springs with force constants $m\omega_T^2$ and $m\omega_B^2$, respectively.

*Reproduced parts are from Appendix A of [10], with permission from Elsevier. Copyright 1989.
†In Appendix B, simplified derivation of modified PES for an isolated c($\sqrt{3} \times 2$)rect unit is provided.

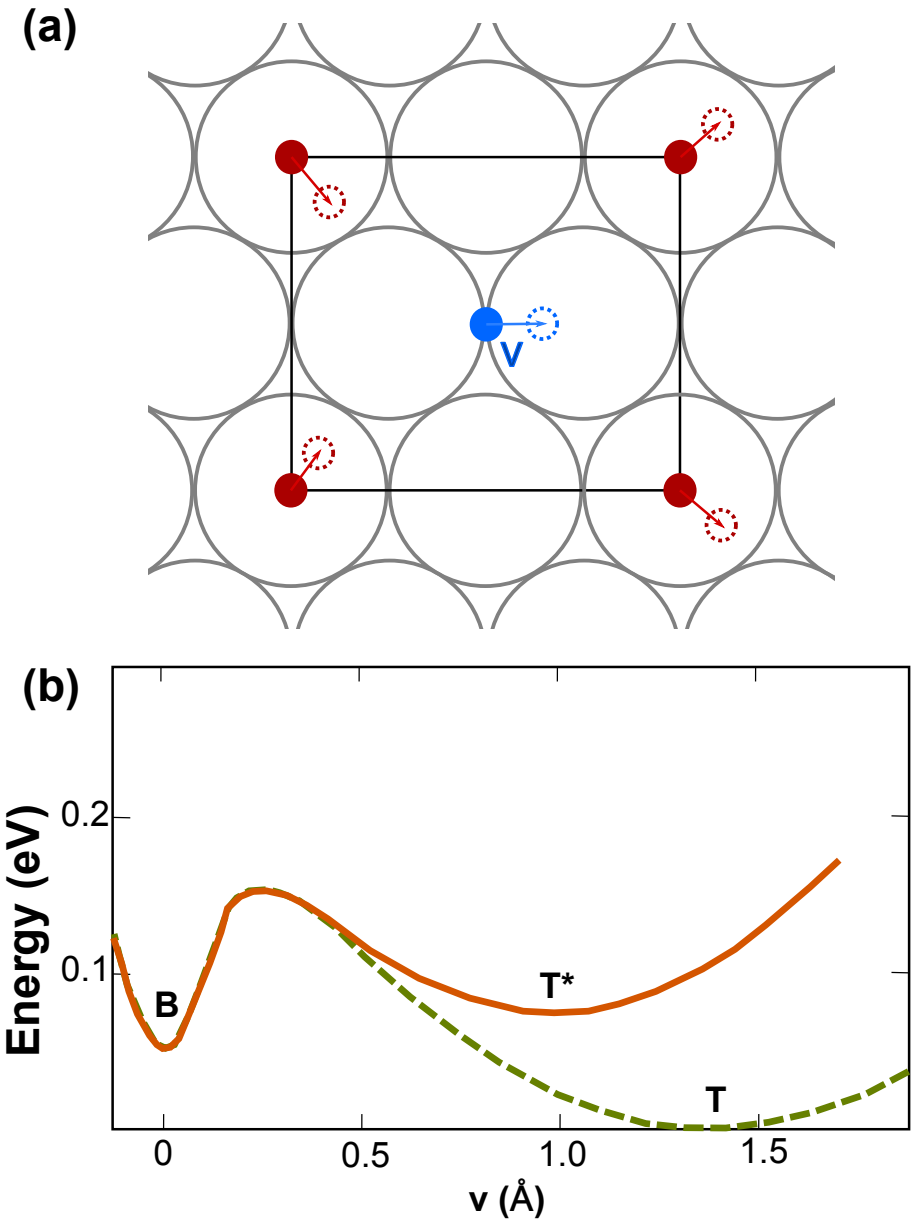

FIGURE 5.1: (a) Schematic model to derive semi-quantitative PES of c(4×2) domain, the bridge CO at the origin is displaced a distance v towards a nearby ontop site. (b) calculated variation of total energy (PES) as a function of v(solid line) from the bridge CO at the origin is occupied (Dashed line). T* denotes the local minimum corresponding to the excited state. Adapted from [10]. Copyright 1989, with permission from Elsevier

With one additional approximation that replacing the rectangular unit cell into a square by taking a geometric average of the rectangular dimension, the equations of motion upon the displacement of a bridge CO by v are described with two unit vectors

$$\boldsymbol{e} = \frac{1}{\sqrt{2}}(\hat{x} + \hat{y}), \qquad \boldsymbol{e'} = \frac{1}{\sqrt{2}}(-\hat{x} + \hat{y}),$$

and two displace vectors $\boldsymbol{u_n}$ and $\boldsymbol{v_n}$ for ontop and bridge COs in the unit cell $\boldsymbol{n} = (n_x, n_y)$:

$$\begin{aligned} m\ddot{\boldsymbol{u}}_{\boldsymbol{n}} &= -m\omega_T^2 \boldsymbol{u_n} - m\omega_S^2[(\boldsymbol{u_n} - \boldsymbol{v_n}) \cdot \boldsymbol{ee} + (\boldsymbol{u_n} - \boldsymbol{v}_{\boldsymbol{n}-\hat{x}-\hat{y}}) \cdot \boldsymbol{ee} \\ &\quad + (\boldsymbol{u_n} - \boldsymbol{v}_{\boldsymbol{n}-\hat{x}}) \cdot \boldsymbol{e'e'} + (\boldsymbol{u_n} - \boldsymbol{v}_{\boldsymbol{n}-\hat{y}}) \cdot \boldsymbol{e'e'}] \qquad (5.1) \\ m\ddot{\boldsymbol{v}}_{\boldsymbol{n}} &= -m\omega_B^2 \boldsymbol{v_n} - m\omega_S^2[(\boldsymbol{v_n} - \boldsymbol{u_n}) \cdot \boldsymbol{ee} + (\boldsymbol{v_n} - \boldsymbol{u}_{\boldsymbol{n}+\hat{x}+\hat{y}}) \cdot \boldsymbol{ee} \\ &\quad + (\boldsymbol{v_n} - \boldsymbol{u}_{\boldsymbol{n}+\hat{x}}) \cdot \boldsymbol{e'e'} + (\boldsymbol{v_n} - \boldsymbol{u}_{\boldsymbol{n}+\hat{y}}) \cdot \boldsymbol{e'e'}]. \qquad (5.2) \end{aligned}$$

By substitution $\boldsymbol{u_n} = \boldsymbol{u_q} e^{i(\boldsymbol{q} \cdot \boldsymbol{n}c - \omega t)}$, $\boldsymbol{v_n} = \boldsymbol{v_q} e^{i(\boldsymbol{q} \cdot \boldsymbol{n}c - \omega t)}$ and elimination of $\boldsymbol{v_q}$, the equations of motion give eigenvalue problem with eigenvectors $\boldsymbol{e}_+ = \boldsymbol{e}$ and $\boldsymbol{e}_- = \boldsymbol{e'}$, and eigenvalues $\omega = \omega_\pm$ which satisfy

$$\left(\omega^2 - \omega_T^2 - 2\omega_S^2\right)\left(\omega^2 - \omega_B^2 - 2\omega_S^2\right) = 2\omega_S^4\left[1 + cos(q_x \pm q_y)c\right],$$

resultantly ω_S can be estimated from ω_T and ω_B.

Return to the calculation of the potential energy variation as the bridge CO in one unit of c(4×2) domain is displaced a distance v towards a nearby ontop site, denoting $\boldsymbol{u} = (\xi, \eta)$ as the resulting displacement of ontop CO marked as 1 in Figure 5.1a results in the displacement vectors of other ontop CO molecules 2, 3 and 4 to be $(\xi, -\eta)$, (ξ, η), and $(\xi, -\eta)$. Then the total elastic energy can be written as

$$U = 2m\omega_{\mathrm{T}}^2(\xi^2 + \eta^2) + \tfrac{1}{2}m\omega_{\mathrm{T}}^2(R_0 - v)^2 + m\omega_{\mathrm{S}}^2[(\xi - \eta - v)^2 + (\xi - \eta)^2 + 2(\xi + \eta)^2]. \quad (5.3)$$

Here large v is assumed, which the displacement v is large enough to find the original bridge CO at the off-center of ontop site, close to $v = R_0$. Hence the force constant of ontop site ω_T applies for the displaced molecule. By introducing $\alpha = \omega_S^2/\omega_T^2$ and equilibrium condition

$$\frac{\partial U}{\partial \xi} = \frac{\partial U}{\partial \eta} = 0$$

, the total energy as a function of v (solid curve in Figure 5.1) can be written as follows after some simplifications:

$$U(v) = m\omega_T^2 \left(\frac{1}{2}(R_0 - v)^2 + v^2 \frac{\alpha^2(1+\alpha^2)}{1+2\alpha^2} \right). \tag{5.4}$$

The minimum of $U(v)$ occurs when

$$\frac{\partial U}{\partial v} = 0, \qquad \text{i.e.} \quad v = \frac{R_0(1+2\alpha^2)}{1+4\alpha^2+2\alpha^4}, \tag{5.5}$$

consequently $v \approx 1$ Å with $\alpha = \omega_S/\omega_T \approx 0.49$ and $R_0 \approx 1.4$ Å. This position is about 0.4 Å away from the ontop site, so this site should be considered as an off-center ontop site, referred as T* site. If the bridge CO is displaced to T* state, the surrounding ontop CO molecules are also displaced and the magnitude of the displacement is about 0.08 Å, and the energy required to B $\rightarrow$ T* is about 20 meV here. More precise calculation with beyond the harmonic approximation gives $\Delta E^* \approx 56$ meV. The resultant PES is shown in Figure 5.1b, orange solid curve.

According to the authors, the B $\rightarrow$ T* is an excitation process for bridge CO and T* state can be utilized to explain the temperature-dependent IR band intensity with estimation of relative population of bridge and T* site. The temperature dependent IRAS spectrum shows the intensity increase of ontop band as well as decrease of bridge band, with increasing temperature. The temperature is lower than the order-disorder transition, i.e. the overlayer structure retains its $c(4 \times 2)$ domain. They interpreted this result as the increased population of ontop CO due to occupation of T* site by thermal excitation of

bridge CO. Still there is no direct evidence of T* state such as resolved IRAS band or resolved low-energy mode energies, due to the difficulty to separate the signal of CO at T* from other ontop CO.

5.1.3 Scope of this chapter

In the previous chapter, I described that the occupation of the bridge site inside an overlayer structure involves rectangular arrangement of neighboring ontop CO, i.e. formation of c($\sqrt{3} \times 2$)rect units. This chapter deals with the dynamic behavior(lateral hopping and shuttling) of bridge-adsorbed CO at the center of c($\sqrt{3} \times 2$)rect units, triggered by tunneling electrons, describing the phenomena in a quantitative way with STM-action spectroscopy.

5.2 Lateral hopping of bridge CO & rearrangement of c($\sqrt{3} \times 2$)rect units

5.2.1 Bridge CO at low surface coverage: PES of a c($\sqrt{3} \times 2$)rect unit

Regarding the occupation of bridge sites at low coverage ($\theta \leq$ 0.1ML) which is achieved by low-temperature ($\sim$ 50 K) adsorption, the bridge-site occupation mainly accompanies the formation of rectangular units(c($\sqrt{3} \times 2$)rect units) as described in Chapter 3(Section 3.2.3). The c($\sqrt{3} \times 2$)rect unit is not a structure in energetic equilibrium, due to the energetic instability of bridge CO over ontop-site occupation at low coverage. Nonetheless, the formation of c($\sqrt{3} \times 2$)rect unit is available with low-temperature adsorption, by collision-induced bridge site occupation followed by the suppression of thermal diffusion from bridge to ontop site. Not only isolated c($\sqrt{3} \times 2$)rect units, but also high-coverage overlayer structures also prefer the bridge occupation with c($\sqrt{3} \times 2$)rect geometry. One plausible explanation for preference of c($\sqrt{3} \times 2$)rect units, no other different

geometry, in terms of bridge-site occupation may be achieved from the relative height of diffusion barrier. Due to the adsorption energy difference, the diffusion barrier of ontop CO to ontop CO is $\sim$ 50 mV higher than bridge-to-ontop diffusion barrier (Figure 3.5). The diffusion barrier of bridge CO at the center of rectangular unit is higher than the not-enclosed bridge CO, because the bridge-to-ontop-conversion of bridge CO inside the completely enclosed rectangular unit resulting in the 1×1 arrangement of ontop COs, which is significantly repulsive. Another possible explanation is the existence of inter-adsorbate interaction depending on the adsorption site. As described in the Chapter 4, there exist the inter-adsorbate interaction between the ontop CO and bridge CO. Even though the amplitude and the polarity (repulsive vs. attractive) are currently not clear, significance of observing rectangular units with bridge CO implies the existence of intermolecular interaction, which affects on the formation of the specific geometry.

The appearance of c($\sqrt{3} \times 2$)rect units is evident from the experimental results described in Chapter 3 and Chapter 4. To consider the potential energy surface of the c($\sqrt{3} \times 2$)rect unit in a semi-quantitative way similar to Section 5.1.2, assume an isolated c($\sqrt{3} \times 2$)rect unit, with displacement v of center bridge CO. The difference of an isolated c($\sqrt{3} \times 2$)rect unit and c(4×2) domain is that the existence of intermolecular interaction for ontop COs at the boundary of the rectangular unit. In Section 5.1.2, every ontop CO is connected to four bridge CO to result in isotropic intermolecular interaction. However, the ontop COs in an isolated c($\sqrt{3} \times 2$)rect unit are under influence of intermolecular interaction from the center bridge CO, which is outward repulsive interaction if the same assumption(only the nearest neighbor interaction is significant, between the bridge CO at the center and the surrounding ontop COs) in Section 5.1.2 applies.

The absence of intermolecular interaction from outside of the c($\sqrt{3} \times 2$)rect unit will greatly modify the motion of equation and total energy.

5.2.2 Conversion of adsorption site & the rearrangement of c($\sqrt{3} \times 2$)rect units

The bridge CO molecules at the center of c($\sqrt{3} \times 2$)rect units are stable upon scanning up to $\sim$ 200 meV, compared to not-completely-enclosed bridge COs which easily converts to ontop CO even at 20 meV. However, even a bridge CO in a c($\sqrt{3} \times 2$)rect unit also undergoes an irreversible conversion of the adsorption-site (B$\rightarrow$T conversion) if the scanning bias exceeds approximately 200 meV, or if a bias pulse with $\sim$ 230 meV of energy is applied to the units. The conversion of adsorption site involves the rearrangement of the c($\sqrt{3} \times 2$)rect unit, repositioning one surrounding ontop CO to outward, one Pt lattice. This phenomenon has been described briefly in Section 3.2.3(Figure 3.8), which was utilized to confirm the existence of bridge CO at the center of unit. The comparison of before and after the rearrangement could clearly demonstrate the existence of bridge CO in spite of poor resolution for bridge CO at the center of a c($\sqrt{3} \times 2$)rect unit. Figure 5.2 shows

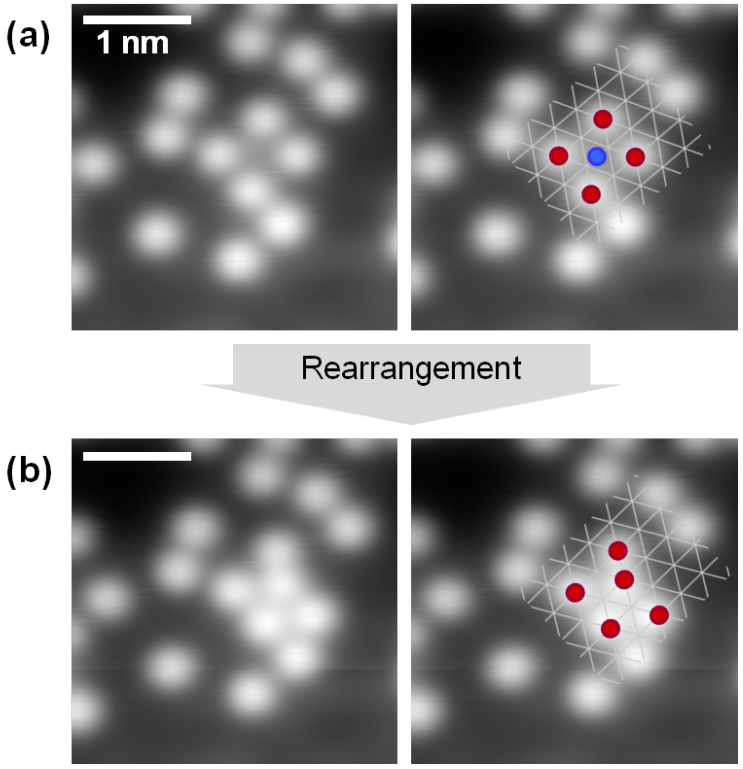

FIGURE 5.2: STM images showing (a) a c($\sqrt{3} \times 2$)rect unit before rearrangement, and (b) after rearranged c($\sqrt{3} \times 2$)rect unit via B-T hopping. Left ones are original images, and right ones are superimposed with schematic models.

more detailed STM image before (a) and after (b) the rearrangement of c($\sqrt{3} \times 2$)rect with a schematic model.

The rearrangement of a c($\sqrt{3} \times 2$)rect unit is achieved in two process: (a) the conversion of adsorption site for bridge CO to neighboring ontop CO, in $[1\bar{1}0]$ direction, (b) followed by pushing one ontop CO outward from the c($\sqrt{3} \times 2$)rect unit (Figure 5.2). There are two parameters to describe the rearrangement of c($\sqrt{3} \times 2$)rect unit by injecting tunneling electron. One is the threshold energy to trigger the bridge-to-ontop conversion. As described in Chapter 3, isolated ontop CO never changes the adsorption site in the energy range less than 1 eV. Another is the the amplitude of intermolecular interaction exerted by bridge-to-ontop conversion inside the c($\sqrt{3} \times 2$)rect unit, relative to the energy of ontop-ontop diffusion. Due to the limited number of c($\sqrt{3} \times 2$)rect units observed in the coverage range $\sim$ 0.1 ML, the quantitative description for the two parameters are not available in this section. Instead of the quantitative description, I will focus on the discussion of the resultant structures to describe qualitative change involved with the rearrangement. Thus, the c($\sqrt{3} \times 2$)rect units and the bridge-to-ontop conversion of bridge COs described here is limited to the c($\sqrt{3} \times 2$)rect units which appear in relatively lower coverage(less than 0.2 ML).

The process of rearrangement, the conversion of adsorption site from the bridge to ontop inside the c($\sqrt{3} \times 2$)rect unit and the followed rearrangement of neighboring ontop CO are modeled in Figure 5.3. Inside the rectangular frame composed up of four ontop COs, the bridge-to-ontop conversion at the center results in a 1×1 arrangement with two ontop COs among four surrounding ontop COs(Figure 5.3b). The direction of bridge-to-ontop hopping is $[1\bar{1}0]$, i.e. the bridge CO directly moves to the adjacent ontop site, without crossing the hollow sites($[1\bar{2}1]$ direction). Inside the c($\sqrt{3} \times 2$)rect unit, the adsorption site conversion from bridge-to-top site is available in both directions ($[1\bar{1}0]$ & $[\bar{1}10]$), and they are identical in terms of resultant 1×1 arrangement. The converted ontop CO faces two surrounding ontop COs, so that three ontop COs to be aligned in

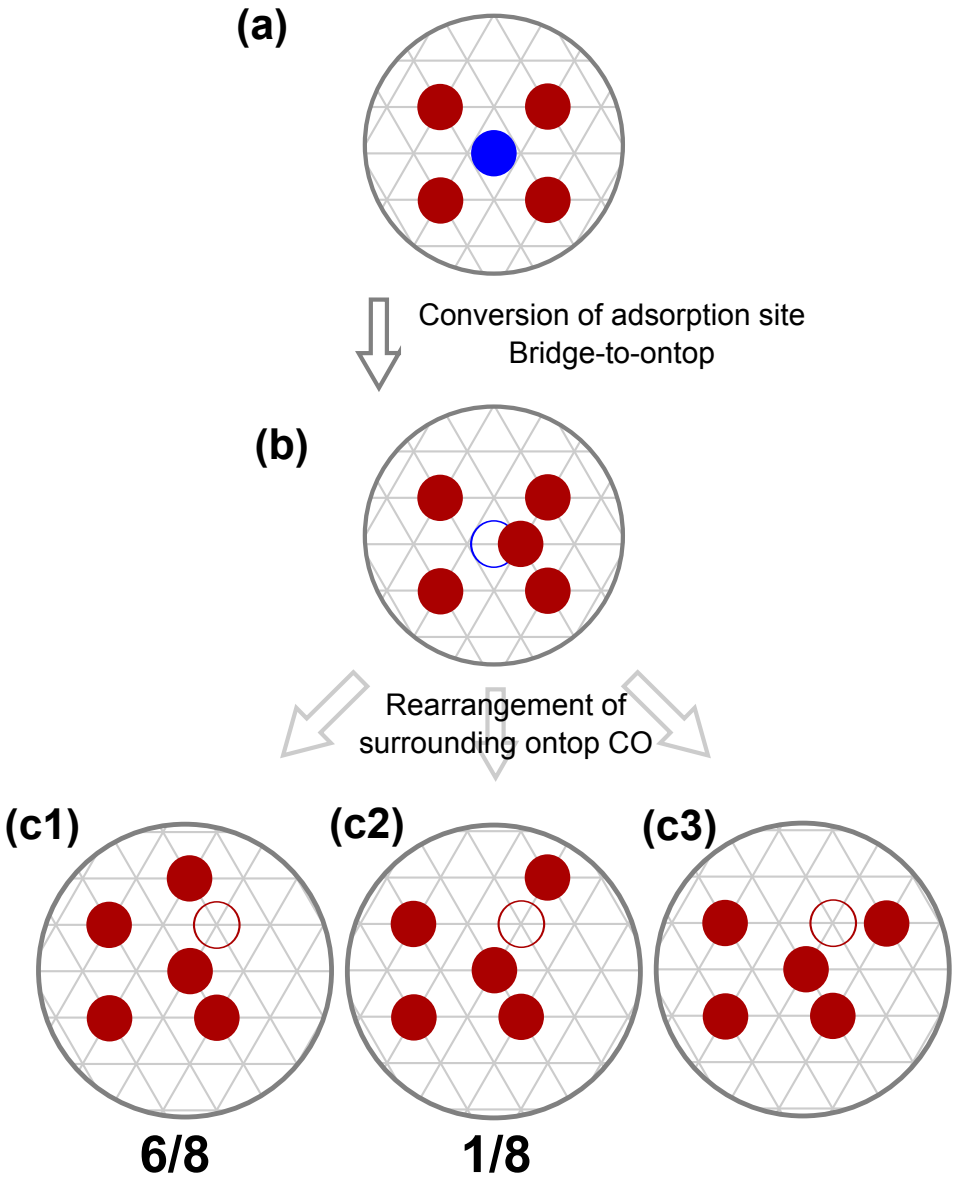

FIGURE 5.3: Schematic model of rearrangement following the bridge-to-ontop conversion in a c($\sqrt{3} \times 2$)rect unit, according to the direction of ontop repositioning.

1×1 geometry. Consequently those ontop COs inside 1×1 arrangement will repulsively interact each other. The repulsive interaction leads the re-positioning of one ontop CO at the frame, pushing the ontop CO to outside of the rectangular unit, one Pt-atom shift (Figure 5.3c).

One interesting point in the rearranged structure Figure 5.3c is that two ontop CO remain as 1×1 geometry, only one ontop CO undergoes the rearrangement among three ontop COs in 1×1 arrangement in Figure 5.3b. The remaining of 1×1 arrangement was reproducibly observed. This indicates the relative amplitude of intermolecular interaction in 1×1 geometry, that three-body interaction in 1×1 arrangement is enough to overcome ontop-ontop diffusion barrier ($\sim$ 150 meV) while two-body interaction in 1×1 arrangement does not. Repeated scan after rearrangement of the c($\sqrt{3} \times 2$)rect unit or additional injection of electrons onto the remained 1×1 ontop COs could exert the repositioning of ontop CO to remove 1×1 geometry.

The re-positioning of ontop CO accompanied with the B-T conversion is dependent on the environment of c($\sqrt{3} \times 2$)rect units, neighboring COs outside the c($\sqrt{3} \times 2$)rect units. The re-positioning of ontop CO at the frame of rectangular unit requires an available vacant Pt site outside c($\sqrt{3} \times 2$)rect units, and the vacant Pt site should be apart from other neighboring COs enough to avoid the repulsive intermolecular interaction, for example, 1×1 arrangement. This condition decides which ontop CO among four at the frame would be re-positioned upon tunneling electron, one which does not have nearby CO forming 1×1 arrangement.

Repositioning of ontop CO involves shift of the corresponding ontop CO by one lattice of Pt, towards three available directions as modeled in Figure 5.3c1-3. The mostly observed arrangement was Figure 5.3c1, ($\sqrt{3} \times \sqrt{3}$)R30° structure with four ontop CO as a result of rearrangement (6 cases among 8 observations). Comparison of three structures in Figure 5.3c indicates that Figure 5.3c1, the most frequently observed case has maximized

number of ontop COs in $(\sqrt{3} \times \sqrt{3})$R30° geometry (four ontop COs in $(\sqrt{3} \times \sqrt{3})$R30° arrangement) contacting each other forming a rhombus-type arrangement, while Figure 5.3b and c have three ontop COs in $(\sqrt{3} \times \sqrt{3})$R30° arrangement. Though the difference in the environment for each c$(\sqrt{3} \times 2)$rect unit should be considered for the rearrangement upon B-T conversion, still this type of preference in resultant rearrangement indicates the existence of intermolecular interaction which preferring $(\sqrt{3} \times \sqrt{3})$R30° arrangement, consistent with the intermolecular interaction suggested in Chapter 4.

5.3 Modified potential energy surface & Bridge-Ontop* shuttling: approach with action spectroscopy

In the previous section I described the B-T conversion which involves the rearrangement of c$(\sqrt{3} \times 2)$rect units at low surface coverage, with available Pt atoms near the c$(\sqrt{3} \times 2)$rect units. If the coverage is increased to populate more ontop COs near the c$(\sqrt{3} \times 2)$rect units, the neighboring ontop COs near the c$(\sqrt{3} \times 2)$rect units prevent the rearrangement of surrounding ontop CO of the c$(\sqrt{3} \times 2)$rect. The immobile, surrounding ontop COs in the c$(\sqrt{3} \times 2)$rect unit will provide local minimum in the potential energy surface for bridge CO upon lateral displacement, namely T* state similar to the state calculated in the Section 5.1.2. In this section I describe the reversible bridge-to-ontop* (B-T*) shuttling upon injection of the tunneling electrons, where the c$(\sqrt{3} \times 2)$rect unit is under influence of neighboring molecules.

5.3.1 Bridge-to-Ontop shuttling

When a c$(\sqrt{3} \times 2)$rect unit is confined by neighboring ontop COs as shown in the left image of Figure 5.4, STM scanning with V_S= 0.23 V resulted in a noisy image as shown in the right image of Figure 5.4. The STM image is noisy only at the position of

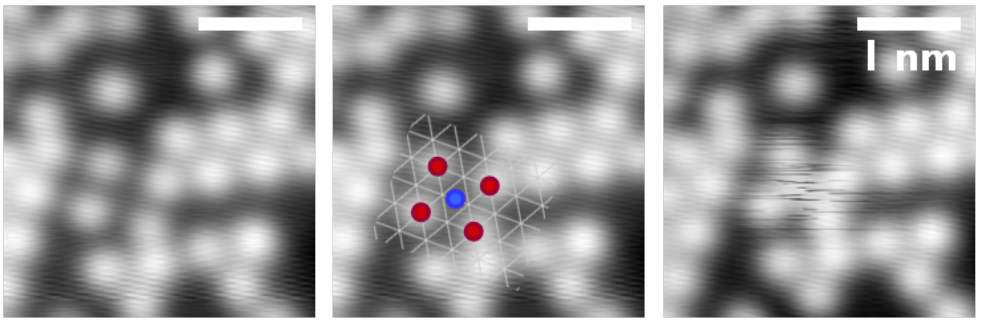

FIGURE 5.4: STM images taken at the identical position. Left, middle: V_S = 0.1 V, I_T = 0.5 nA. Middle : a schematic model is superimposed to the STM image. Right image is during high bias scanning (V_S = 0.23 V), showing noisy at the position of c($\sqrt{3} \times 2$)rect units.

c($\sqrt{3} \times 2$)rect unit with bridge CO at the center, without any change in the position of ontop CO molecules, both the ontop COs consisting the c($\sqrt{3} \times 2$)rect unit and ontop COs outside the c($\sqrt{3} \times 2$)rect unit. Considering the B-T conversion-induced rearrangement which is described in the previous section, the origin of the noise may be deduced as the conversion of adsorption site from bridge-adsorbed CO.

For a quantitative description for B-T* shuttling, $I - t$ curves at various V_S were obtained by applying the bias pulse at the bridge CO at the center of the c($\sqrt{3} \times 2$)rect unit. One $I - t$ curve obtained with V_S = 240 mV is shown in Figure 5.5 with superimposed schematic models and corresponding STM images. The $I - t$ curve shows clear two-step

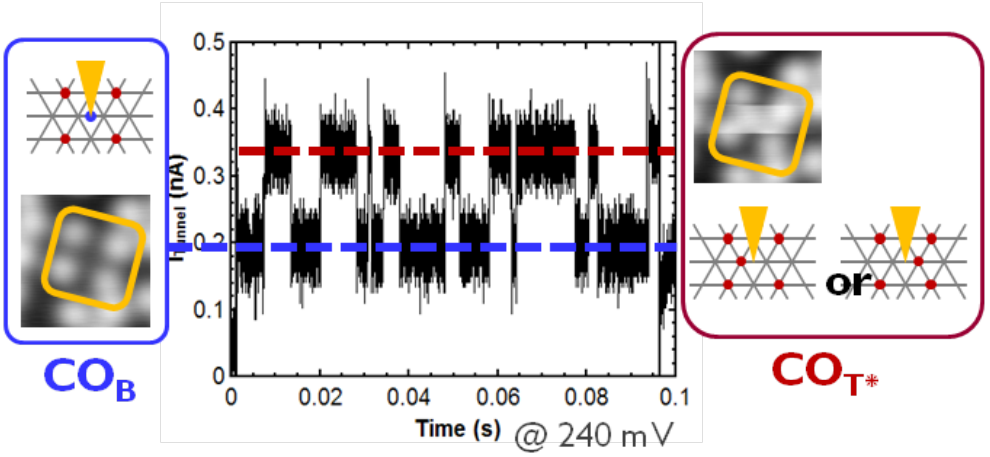

FIGURE 5.5: A representative $I_T - t$ curve which shows bridge-to-ontop* shuttling, when the bias pulse was applied to the bridge CO at the center of c($\sqrt{3} \times 2$)rect unit.

telegraph noise signal, and the low current mode is designated as bridge CO (CO_B, blue dashed line) and the high current mode is designated as ontop* CO(CO_{T^*}, red dashed line). As described in Chapter 3, the bridge CO at the center of c($\sqrt{3} \times 2$)rect unit shows ~ 20 pm of height which is about half of ontop CO. If the bridge CO is repositioned to neighboring ontop CO (the scheme in right side of Figure 5.5), the repositioned CO shows the height of ontop CO (~ 40 pm). Accordingly the T* state should be the high-current state, which is also supported by the height profile in Figure 5.6 before and after the rearrangement followed by the B-T conversion. Even rearranged structure in Figure 5.6b, the position which was corresponding to the center of c($\sqrt{3} \times 2$)rect unit (beneath the tip, marked with the yellow arrow) shows significantly higher height than the bridge CO, even though the height of ontop CO was measured in an off-center position.

Note that one bridge CO at the center of c($\sqrt{3} \times 2$)rect unit has two adjacent T* states, and the current measured by the tip positioned at the center of c($\sqrt{3} \times 2$)rect unit is identical for both T* states, consequently the $I_T - t$ curve shows only one high-current state. This B-to-T* shuttling and resultant $I_T - t$ curves were treated in a similar manner to the rotation of acetylene molecule adsorbed on Cu(100) surface[11] as well as the rotation of oxygen molecule[12], to extract the parameters regarding the switching action. The time spent for each B$\rightarrow$T* event can be estimated from the $I_T - t$ curve, by counting the time that the molecule stays at low-current state. The distribution characteristic of the event at a specific V_S is estimated to be Poisson by plotting the inverse of quantile. Detailed process is described in Chapter 2.

The yield Y at each V_S in the range of interest is estimated from the repeated measurement of each event (B-T conversion), and statistical interval estimation from the measured (sampled) time and current. The resultant action spectrum, $Y(V)$ is shown in Figure 5.7. The action spectrum clearly shows sharp increase of shuttling yield at the threshold energy of 230 meV, and the 230 meV corresponds to the C–O stretch mode energy

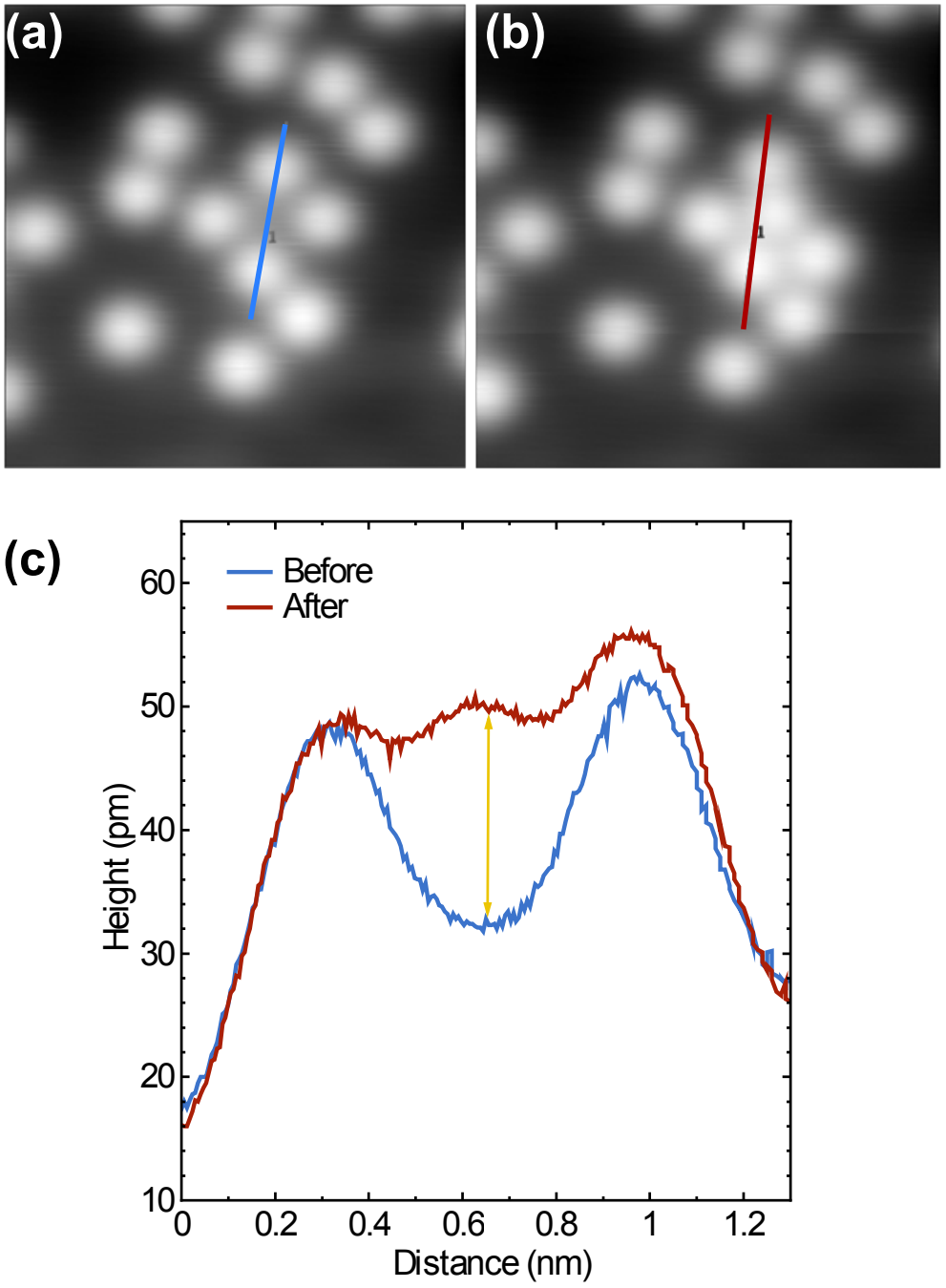

FIGURE 5.6: Approximately estimated height change upon B-T* shuttling

of bridge-adsorbed CO.[1] Accordingly the action spectrum in Figure 5.7 is considered to describe vibration-induced lateral shuttling of CO. [13]

To estimate the reaction order of the shuttling process by injecting electrons, the rate of B-to-T* shuttling was measured with various I_T, and plotted as log-log plot in Figure 5.8. The current-dependence was measured at 220 mV and 240 mV, for the before and after the excitation of C–O stretch mode, respectively.

The least-square fit of measured current dependence at 220 mV and 240 mV are shown in solid line in Figure 5.8. The reaction order N, the number of necessary electrons during the shuttling process, can be deduced from the power-law relation between the rate(R) and the tunneling current (I_T), $R \propto I^N$. The result of least-square fit was N 1.0 and 1.1 for 220 and 240 mV, respectively, implying that the reaction order of shuttling is one (single-electron process) at both 220 and 240 meV.

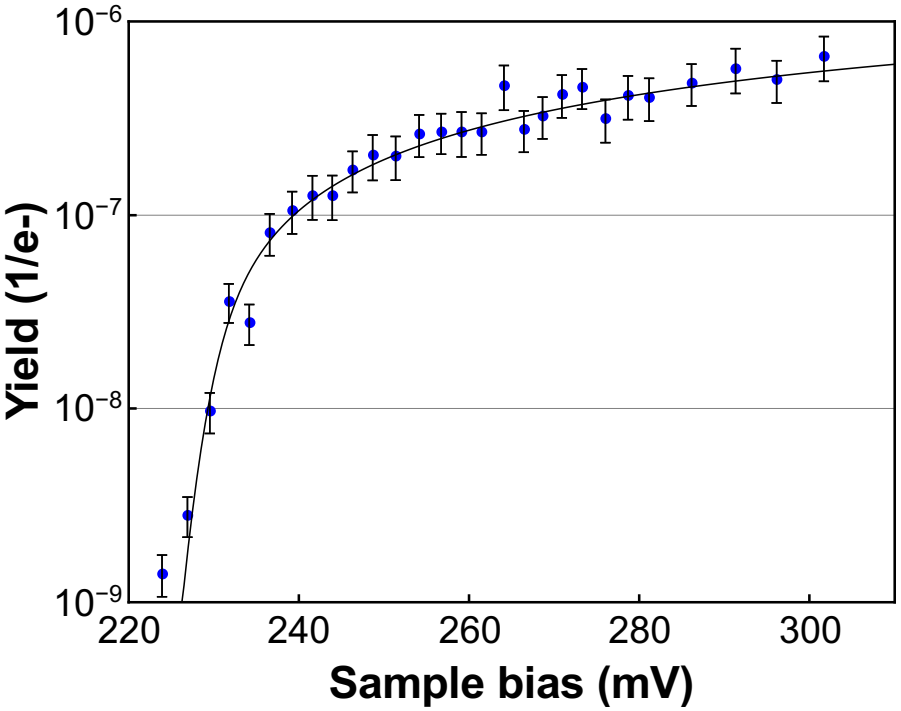

FIGURE 5.7: One representative action spectrum from bridge-ontop* (B-T*) hopping. Solid line is result of theoretical fitting, with high energy mode energy $\hbar\Omega = 229$ meV and linewidth $\sigma = 2.1$

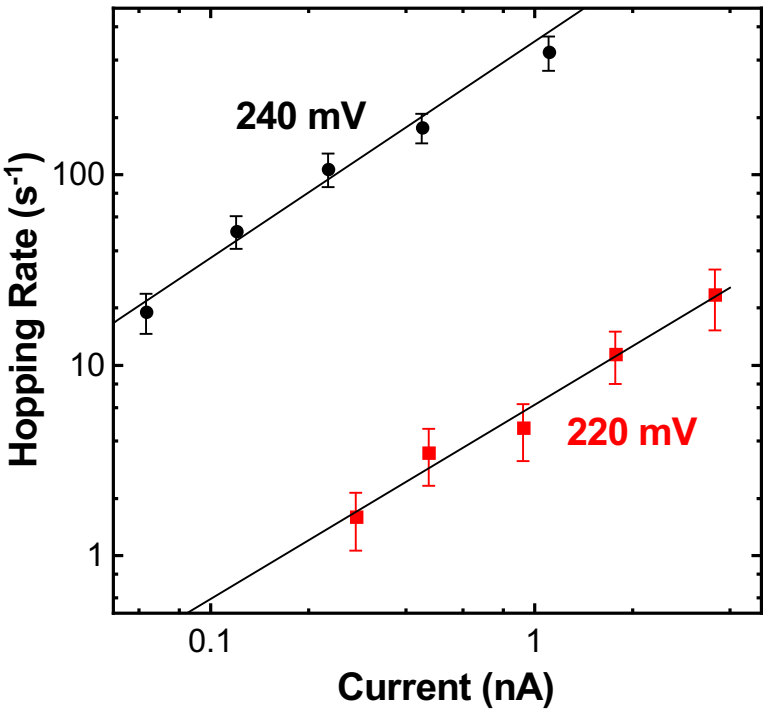

FIGURE 5.8: Current dependence of bridge-ontop* (B-T*) hopping measured at 220 mV (red square) and 240 mV(black circle). Solid lines are the result from the least square fit.

The event which occurs during B-T* shuttling is displacement in lateral direction, accordingly the reaction coordinate is hindered translation (HT) mode. In Figure 5.7, the threshold of shuttling yield appeared at 230 mV which corresponds to the C–O stretch mode of bridge CO. Hindered translation mode and C–O stretch mode is orthogonal each other, and the energy transfer between two modes requires the anharmonic mode coupling. Considering this case similar to the vibration-induced lateral hopping of CO on Pd(110) surface [13], the energy transfer mechanism should be similar, the energy transfer from inelastic tunneling electron to the high frequency C–O stretch mode, and anharmonic mode coupling between C–O stretch mode and low-frequency reaction coordinate mode, in this case hindered translation mode of bridge CO.

With the reaction order obtained from current dependence(Figure 5.8, $N = 1$), the action spectrum in Figure 5.7 was fitted into theoretical model suggested by Motobayashi

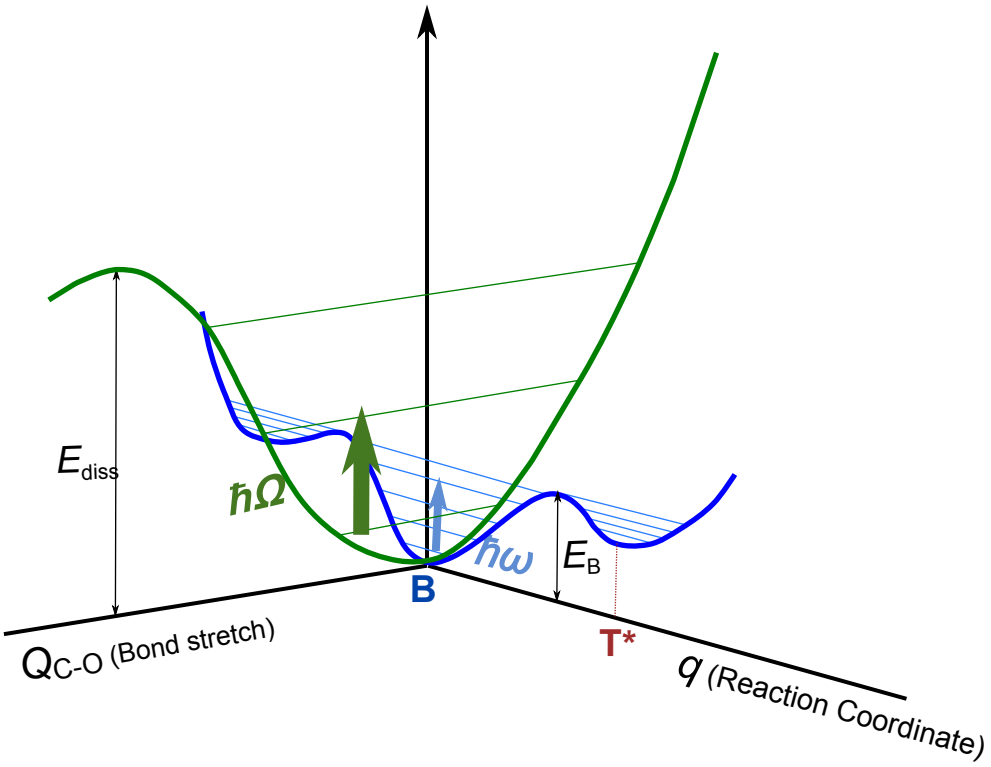

FIGURE 5.9: Schematic diagram of anharmonic mode coupling.

et al.[14] and modified by Ueba[15], as solid line in Figure 5.7 indicates.

$$Y(V) = K_{\text{eff}} \frac{F(V, \Omega, \sigma_{\text{ph}})}{V} \tag{5.6}$$

with Gaussian form of $F(V, \Omega, \sigma_{\text{ph}})$:

$$\begin{aligned} F(V) =& \sqrt{\frac{2}{\pi}} \sigma_{\text{ph}} \left[e^{-(V-\Omega)^2/(2\sigma_{\text{ph}}^2)} - e^{-\Omega^2/(2\sigma_{\text{ph}}^2)} \right] \\ &+ (V - \Omega) \left[\text{Erf}\left(\frac{V-\Omega}{\sqrt{2}\sigma_{\text{ph}}} \right) + \text{Erf}\left(\frac{\Omega}{\sqrt{2}\sigma_{\text{ph}}} \right) \right], \end{aligned} \tag{5.7}$$

and effective prefactor is given by

$$K_{\text{eff}} = \frac{\gamma_{v,\text{RC}}}{\sigma_0 \hbar \Omega} \frac{\Gamma_t}{\Gamma_s}, \tag{5.8}$$

where Γ_s and Γ_t are tunneling couplings to substrate and the tip site, $\gamma_{v,\text{RC}}$ is the activation

rate of the reaction coordinate (RC) mode over a barrier via an inter-mode coupling between a vibrational mode v(high energy mode). The fitting to this theoretical model gives, $K_{\mathrm{eff}} = 2.3 \times 10^{-6}$, $\hbar\Omega = 229\,\mathrm{meV}$ and $\sigma_{\mathrm{ph}} = 2.1$ meV.

The B-T* shuttling by electron injection is available for both positive and negative V_S. There exists only negligible difference in yield obtained from each polarity. According to STS result described in Chapter 3, the amount of DOS in each polarity does not differ each other. Similar level of DOS allows the similar amount of inelastic electron to trigger the B-T* shuttling.

5.3.2 Adsorption site-dependent dynamic motion

As discussed in Section 3.3.3, isolated ontop molecules never showed lateral hopping with tunneling electron at vibrational energy level. In contrast, bridge CO easily changes its position to ontop site (Section 5.2 and Section 5.3). The experimental result clearly demonstrates that the dynamic behavior (conversion of adsorption site) upon electron injection differs according to the initial adsorption site, even on the surface of identical metal. To compare the dynamic property according to the adsorption site in terms of anharmonic mode coupling, one useful estimate is "branching ratio" derived by Persson and Ueba.[16]:

$$P = \frac{w}{w_{\mathrm{eh}}} \approx \frac{8\eta^2}{(2\pi)^{1/2}} \frac{(1 - \epsilon_{\mathrm{B}}/\hbar\Omega)}{(2 - \epsilon_{\mathrm{B}}/\hbar\Omega)^2} \left(\frac{\hbar\delta\omega}{\epsilon_{\mathrm{B}}}\right)^2 n^{3/2} e^{-2n} \tag{5.9}$$

where $n = \epsilon_{\mathrm{B}}/\hbar\omega_0$, the ratio between the barrier height and the energy of low-frequency mode, η is a damping constant, $\hbar\delta\omega$ is anharmonic coupling constant. When high-energy vibrational mode with energy $\hbar\Omega$ is excited, the dominant relaxation channel is excitation of electron-hole pair (w_{eh}), so the ratio $P = w/w_{\mathrm{eh}}$ can be interpreted as the fraction of electrons consumed for vibrational excitation of molecules which transfers the energy to the reaction coordinate to overcome the hopping barrier ϵ_{B}, over whole inelastic electrons.

TABLE 5.1: Parameters to calculate the branching ratio, and estimated branching ratio according to the adsorption site.

	Ontop CO	Bridge CO
$\hbar\delta\omega$	-0.25 meV [1]	-5.0 meV [1]
$\hbar\Omega$	260 meV [2]	230 meV [2]
$\hbar\omega$	7.4 meV [1]	38.4 meV [1]
η	1.2 meV [1]	3.1 meV [1]
ϵ_B	190 meV [3]	135 meV [3]
$P = \frac{w}{w_{eh}}$	$\mathbf{8.6 \times 10^{-27}}$	$\mathbf{5.1 \times 10^{-5}}$

[1] from [10] [2] from [1] [3] from [17]

To compare the branching ratio of ontop CO and bridge CO, the necessary parameters from preceding results are listed in Table 5.1. The anharmonic coupling constant ($\hbar\delta\omega$), damping parameter(η) and low-energy mode energy ($\hbar\omega$) are estimated from the dephasing analysis of temperature-dependent IRAS spectrum from 0.5ML of surface coverage[10]. The identical hopping barrier is assumed between B→T* and B→T hopping, with the barrier value deduced from the dynamics of low-temperature, low-coverage IRAS by Nekrylova and Harrison.[17]

According to the estimated branching ratio according to the adsorption site, bridge CO shows $\sim$ 20 order higher branching ratio than ontop-adsorbed CO. Thus, bridge CO is more efficiently transfer C–O stretch mode energy to the low-energy reaction coordinate mode, than ontop-adsorbed CO.

5.3.3 B-T* shuttling triggered by electron injection onto ontop CO

In the previous chapter (Chapter 4), I described the interaction between ontop and bridge CO in bridge-vacant c(4×2) domain as shown in Figure 4.7. The height of ontop CO at the frame of c$(\sqrt{3} \times 2)$rect units are under influence of bridge CO, where the

existence of bridge CO lowers the height of ontop CO. On the other hand, the interaction between ontop COs increases the height of ontop CO, especially with decreasing the ontop-ontop intermolecular distance. This could be observed with $(\sqrt{3} \times \sqrt{3})$R30° islands, that $(\sqrt{3} \times \sqrt{3})$R30° islands with interisland distance $\sqrt{7}a_0$ showed relatively darker protrusions than the $(\sqrt{3} \times \sqrt{3})$R30° islands with interisland distance $2a_0$. Also in compressed domain of c(4×2) as shown in Figure 4.9, ontop COs which are in 1×1 boundary shows significantly brighter protrusion than other ontop COs inside c(4×2) units.[18]

If one combines the result of all observations, the order of height protrusion may be expressed with the intermolecular distance and the number of neighboring molecules at the specified intermolecular distance. In most cases, the main position of bridge CO is at the center of c$(\sqrt{3} \times 2)$rect units, resulting in the intermolecular distance $\sqrt{7}/2$.

In the preceding section I described the bridge-to-ontop* transition by injection of tunneling electrons onto the bridge CO. If the tip position is fixed on bridge CO, the B-T* transition shows the increase of tunneling current approximately 180 % of I_T as Figure 5.5 demonstrated. Then, what would be the effect of B-T* transition for the neighboring ontop COs which are at the frame of c$(\sqrt{3} \times 2)$rect units? In a view point of ontop CO, B-T* transition is disappearance of bridge CO which lowers the height of ontop CO. Accordingly the height of the ontop CO will increases with B-T* transition of bridge CO, though the magnitude of height change would be significantly smaller than the magnitude of change for bridge CO.

In Figure 5.10a, the tip is positioned at the ontop CO as designated with yellow arrow. The interesting point is that the injection of electron is onto the ontop CO at the frame of c$(\sqrt{3} \times 2)$rect unit while the bridge CO is pushed to the neighboring T* site. Moreover, the $I - t$ curve demonstrates two deliberately separated high-current states, which is marked with red and orange dashed line in Figure 5.10b. The B-T* transition is available in two opposite directions along $[1\bar{1}0]$, and the ontop CO feels different intermolecular interaction due to the resultant intermolecular distance. If the bridge CO at the

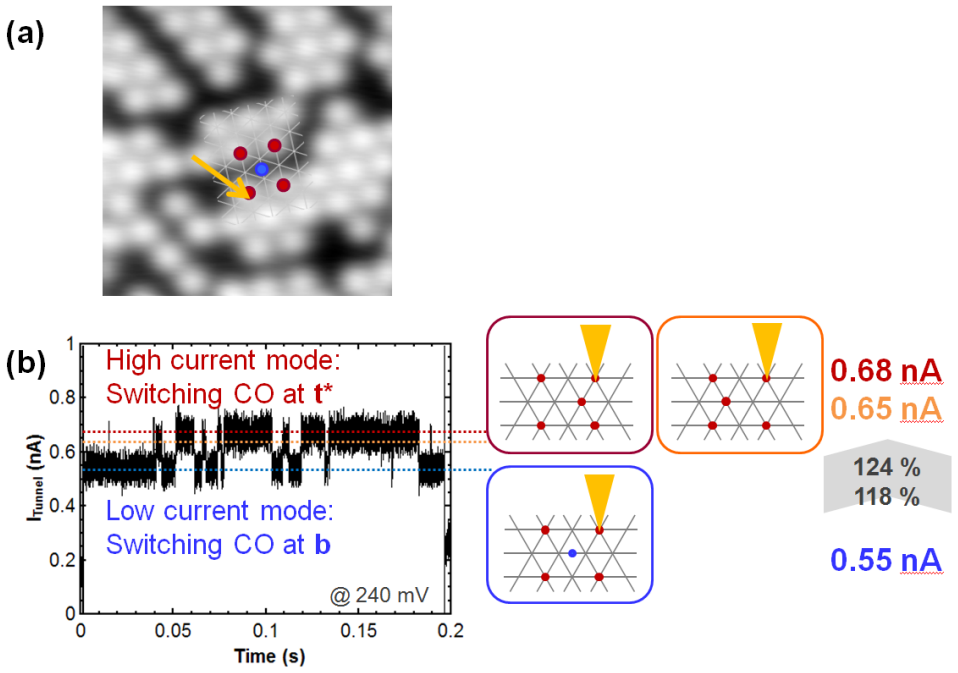

FIGURE 5.10: $I-t$ measured on ontop CO at the frame: B-T* shuttling is indirectly detected at the ontop CO by current change. (a) A STM image with the target c($\sqrt{3}\times 2$)rect unit, yellow arrow designates the target ontop CO, where the tip is positioned. (b) $I-t$ curve measured on the ontop CO.

center moves toward the ontop CO where the electrons are injected, the ontop CO beneath the tip will be under influence of 1×1 arrangement of three ontop COs, in addition to the loss of bridge CO to lower the height. Consequently the ontop CO would show higher height than the ontop CO in the opposite site as designated in the yellow rectangle, which is represented by higher tunneling current in $I-t$ curve. In the opposite case, which the bridge CO moves toward the opposite direction from the ontop CO beneath the tip, the resultant arrangement will be close to $(\sqrt{3}\times\sqrt{3})$R30° triangular arrangement, with less intermolecular interaction than previous case, resulting in slightly smaller current as designated in orange rectangle. Note that the magnitude of current change is about 20 % of low-current mode current, significantly different from the magnitude of change for bridge CO.

The injection of electron is on to the ontop CO, and the neighboring bridge CO hops to the neighboring position. Considering the lateral resolution and stability of STM tip,

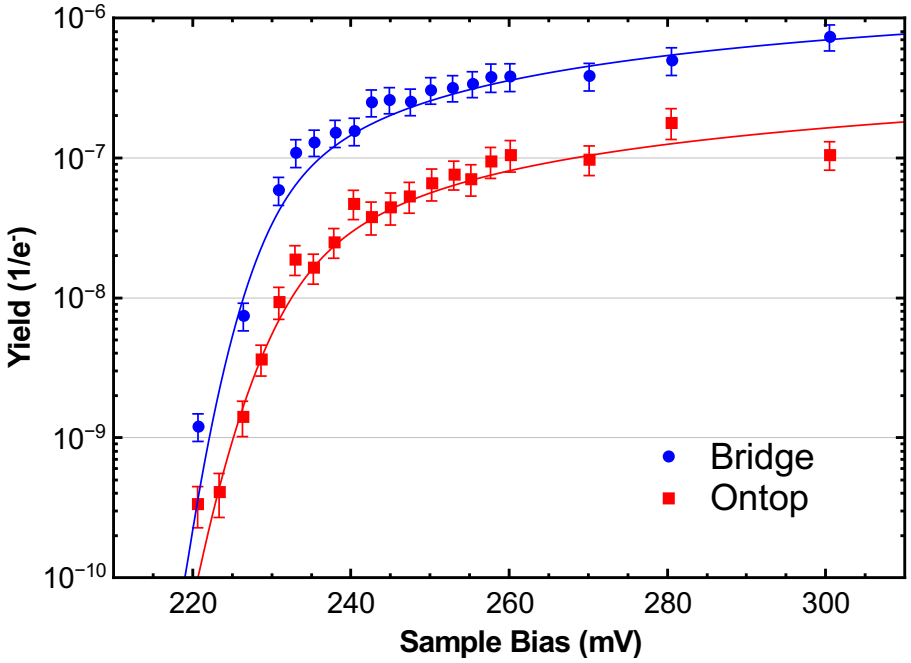

FIGURE 5.11: Action spectrum measured on ontop and bridge CO taken with a same tip, in a c($\sqrt{3} \times 2$)rect unit. The solid lines are theoretical fitting using Ueba's equation with Gaussian peak.[15].

the current fluctuation to result in direct injection onto bridge CO is not likely. Thus B-T* shuttling triggered by electron injection to ontop CO can be considered as one of indirect excitation of the reaction coordinate mode for B-T* shuttling. To find out the energetic origin of this indirect excitation, action spectrum was obtained as shown in Figure 5.11.

One may expect that tunneling electron excites the vibrational mode of ontop CO, and transferring the energy to the bridge CO to trigger B-T* transition. However, the threshold energy for B-T* transition with electron injection to ontop CO is identical to the one with electron injection to bridge CO, estimated from the theoretical fitting[15] to be 230 meV and 229 meV for injection onto bridge CO and injection onto ontop CO, respectively. This result discards the possibility of energy transfer from the excitation of ontop C–O stretch mode. Available explanation is the hybridization of the electronic states between the ontop and bridge CO, where the injected electron is shared inside the ontop CO electronic states, and the overlap of ontop and bridge CO electronic states results in

the electron injection to the state of bridge CO.

5.4 Further investigation: Long-range interaction

5.4.1 Ontop*-to-Bridge hopping: Influence of COs outside c(4×2) units

In previous section, I discussed only B→T* direction in the shuttling event. However the $I - t$ curve also allows the estimation of time event for high-current mode, i.e. T*→B hopping. When the bridge CO is excited to T* state (in accordance to the description of Schweizer et al.), the time that the CO molecule stays at the T* state may reflect the energy difference between B and T* sites as well as the hopping barrier in the direction from T* to B.

Figure 5.12a - c show three STM images with different surface coverage, approximately 0.14 ML, 0.23 ML and 0.35 ML, respectively. Each image bears one c$(\sqrt{3} \times 2)$rect units in the center, and action spectrum is acquired for each c$(\sqrt{3} \times 2)$rect units, with positioning the tip at the position of bridge CO. From obtained $I - t$ curve, B→T* and T*→B events are separately estimated as in Figure 5.12d and e, respectively. In the action spectrum for B→T* hopping, all three action spectra are consistent each other, for the position of threshold energy (230 mV) as well as the order of yield. However, action spectra of T*→B direction differ each other significantly, as shown in Figure 5.12e. The blue diamond curve (from 0.14 ML) shows weak threshold near 260 mV, while the red square(0.23 ML) and green triangle(0.35 ML) curve do not. Even the order of hopping yield differs as one order of magnitude each other.

As discussed in the previous subsection about the branching ratio $P = w/w_{eh}$ (Equation 5.9), the main parameter which determine the hopping probability through anharmonic mode coupling is $n = \epsilon_B/\hbar\omega_0$. In addition to that, because the B – T* shuttling involves the energy difference (ΔE^*), thermodynamic population ratio also should be taken

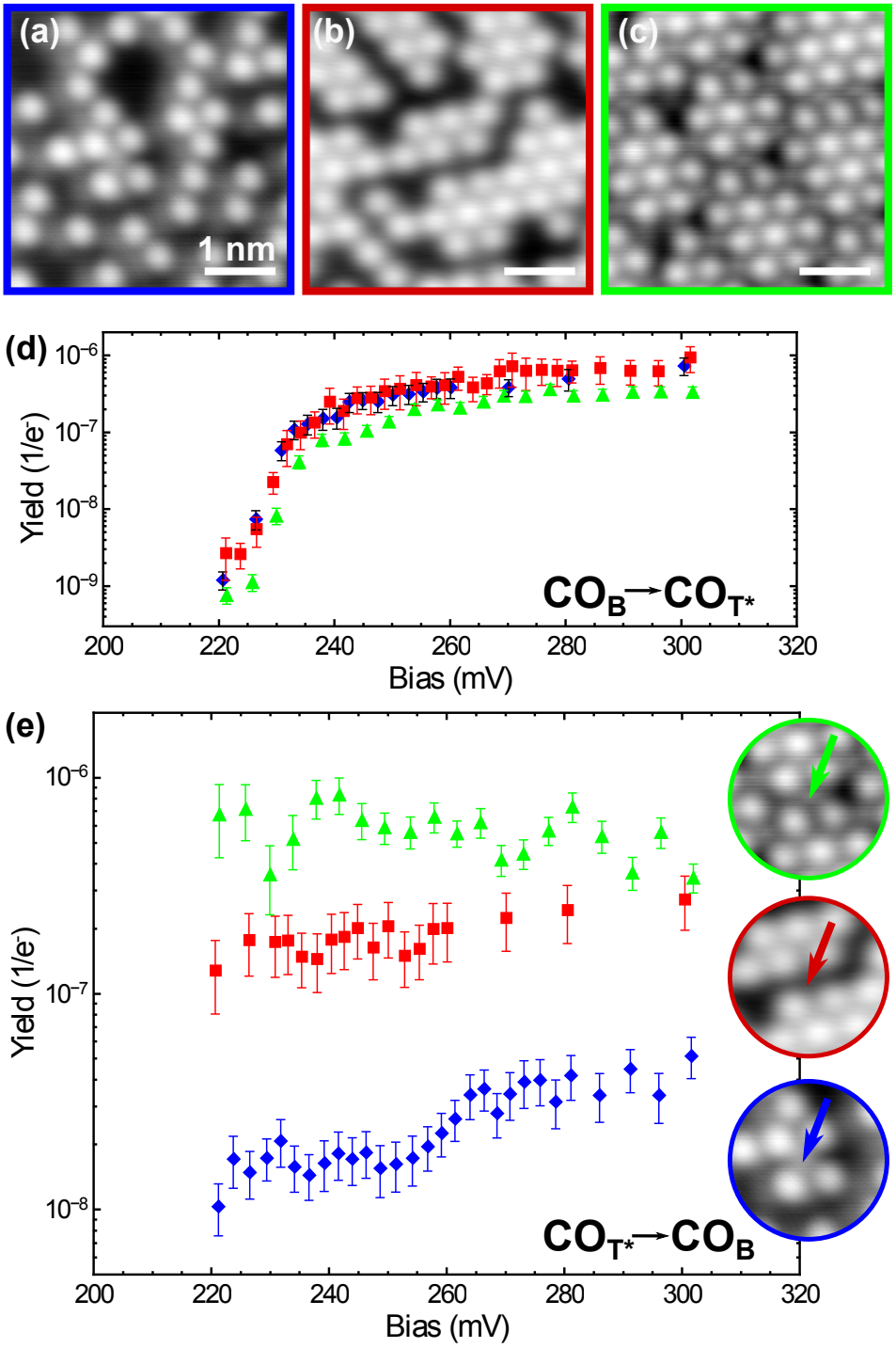

FIGURE 5.12: Action spectrum of ontop*-to-bridge hopping with various θ.

into account. If the CO in T* state shows similar low-energy mode frequency $\hbar\omega_0$ and anharmonic coupling $\hbar\delta\omega$ to the one of T (ontop) state, Only two parameters which affects to the hopping yield remain, diffusion barrier height ϵ_B in T*→B direction and the energy difference between B and T* state ΔE^*. If one consider the potential energy surface regarding the hopping event as shown in Figure 5.13 and ϵ_B for B→T* direction is assumed to be known, the diffusion barrier height in T*→B direction (denoted as ϵ_B^* as shown in Figure 5.13b) becomes $\epsilon_B^* = \epsilon_B - \Delta E^*$, a function of ΔE^*. Therefore, the hopping yield of T*→B is determined by only ΔE^*, under assumption (a) all the parameters for B→T* hopping is known, and (b) the low energy mode frequency of T* states($\hbar\omega_{T^*}$) is known (or at least, similar to the value of ontop state low energy mode frequency $\hbar\omega_B$).

Accordingly the coverage-dependent difference in the hopping yield of T*→B transition (Figure 5.12e) indicates that the ΔE^* at each coverage differs each other. The factor which determines ΔE^* is the intermolecular interaction, which is modeled by spring constants $m\omega_S^2$ in the Section 5.1.2. In the model calculation in Section 5.1.2, the overlayer structure is assumed to be complete c(4×2) structure, i.e. the intermolecular interaction which is taken account is *isotropic* and *uniform in amplitude* over all the CO molecules with identical spring constant $m\omega_S^2$. However, the c$(\sqrt{3} \times 2)$rect units in Figure 5.12a - c are all in different environment so that the net interaction of each ontop CO at the frame of

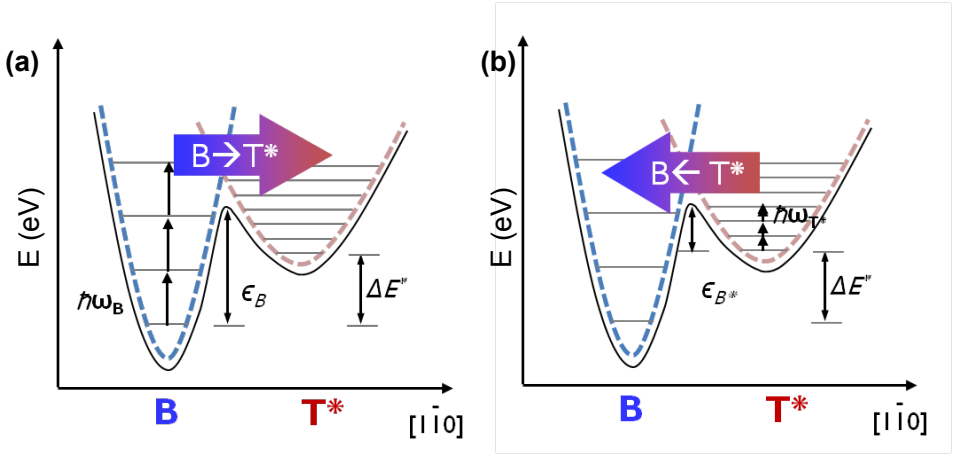

FIGURE 5.13: Schematic model potential energy surface with hopping parameters, (a) B→T* and (b) T*→B direction.

c($\sqrt{3} \times 2$)rect unit becomes *anisotropic* and *different in amplitude* due to various ontop-ontop distances between the ontop CO and other ontop COs in the environment. The differences lead the different amount of displacement of each ontop CO $u = (\xi, \eta)$, resulting in complicated total energy equation than Equation 5.3, changing the position of T* state (amplitude of v) as well as the total energy at T*.

5.4.2 Long-range momentum transfer: Multi-level current change in c(4×2) domain

The coverage-dependence, precisely the influence of neighboring ontop COs around the corresponding c($\sqrt{3} \times 2$)rect unit, of B-T* shuttling indicates that, the intermolecular interaction onto the bridge CO and the excited state of it (T* state) is long range, not limited to the nearest-neighbor interaction. The existence of long-range interaction other than

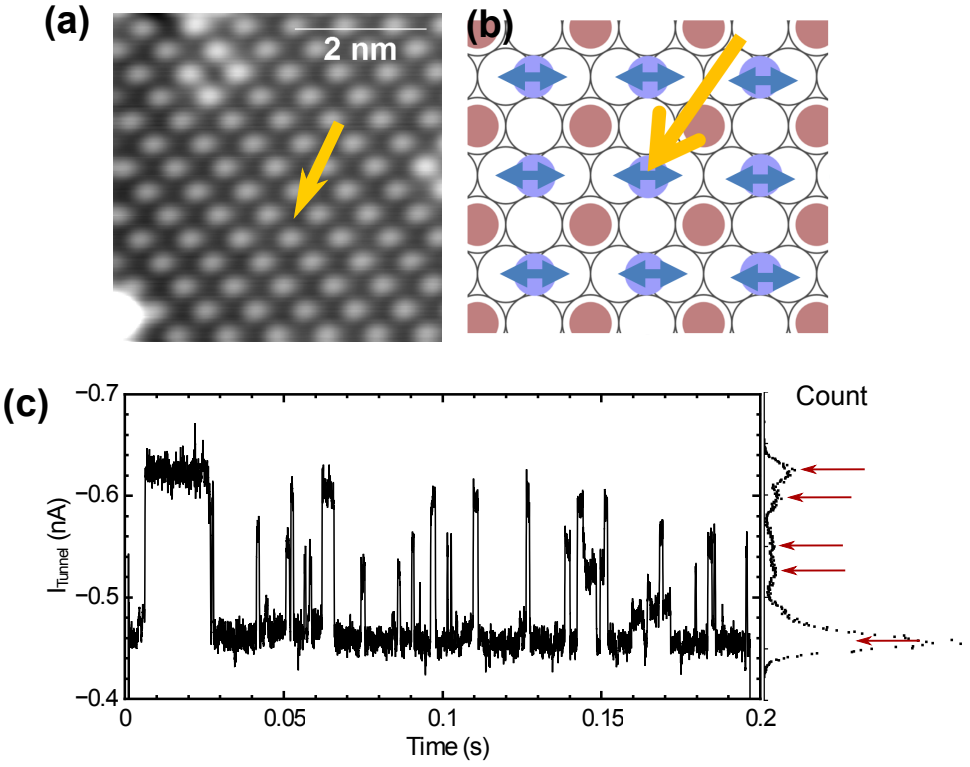

FIGURE 5.14: Multi-level current change in c(4×2) domain

the nearest-neighbor interaction is also confirmed from the $I - t$ curve measured in complete c(4×2) domains, showing multi-step current change. The multi-step current change implies that the tunneling electron injected to the bridge CO under the tip triggers the B-T shuttling of other bridge COs in neighboring c$(\sqrt{3} \times 2)$rect units. The energy transfer mechanism and precise intermolecular interaction are remained as a future discussion.

5.5 Conclusion

In this chapter, I described on the dynamic behavior upon excitation by injection of tunneling electrons in CO overlayer structures. Between ontop and bridge CO, only bridge CO at the center of c$(\sqrt{3} \times 2)$rect unit shows the vibration-induced lateral hopping by injection of tunneling electron. The B-T conversion-induced rearrangement of c$(\sqrt{3} \times 2)$rect unit implies the preference of specific geometry as well as the relative energy difference between the T* state and the diffusion barrier between ontop sites. Confined c$(\sqrt{3} \times 2)$rect units by surrounding ontop COs exhibit the B-T* shuttling behavior and described with action spectroscopy, and the energy transfer by anharmonic mode coupling is suggested as the mechanism. The mobility difference of ontop and bridge CO is also explained based on the anharmonic coupling-induced motion. Interesting coverage dependence of lateral hopping with the direction of T* to B is discussed in terms of the intermolecular interaction modeled as springs, that various intermolecular distances between the ontop CO at the frame and the ontop COs outside c$(\sqrt{3} \times 2)$rect units indicate different spring constants.

References

[1] Steininger, H., Lehwald, S. & Ibach, H. On the adsorption of CO on Pt(111). *Surf. Sci.* **123**, 264–282 (1982). URL http://www.sciencedirect.com/science/article/pii/0039602882903284.

[2] Hayden, B. & Bradshaw, A. The adsorption of CO on Pt(111) studied by infrared reflection-absortion spectroscopy. *Surf. Sci.* **125**, 787–802 (1983). URL http://www.sciencedirect.com/science/article/pii/S0039602883800600.

[3] Tüshaus, M., Schweizer, E., Hollins, P. & Bradshaw, A. Yet another vibrational study of the adsorption system Pt{111}-CO. *J. Electron Spectrosc. Relat. Phenom.* **44**, 305–316 (1987). URL http://www.sciencedirect.com/science/article/pii/0368204887870317.

[4] Persson, B. Monte-carlo calculations of adsorbate structures. *Solid State Commun.* **70**, 211–214 (1989). URL http://www.sciencedirect.com/science/article/pii/0038109889909769.

[5] Persson, B. N. J. & Ryberg, R. Vibrational line shapes of low-frequency adsorbate modes: CO on Pt(111). *Phys. Rev. B* **40**, 10273–10281 (1989). URL http://link.aps.org/doi/10.1103/PhysRevB.40.10273.

[6] FICHTHORN, K., GULARI, E. & ZIFF, R. Monte-carlo simulation of the adsorption of CO on Pt(111) - thermodynamic consideration s for the surface configuration of adsorbed species. *Surf. Sci.* **243**, 273–294 (1991). WOS:A1991FD22500037.

[7] Yeo, Y. Y., Vattuone, L. & King, D. A. Calorimetric heats for CO and oxygen adsorption and for the catalytic CO oxidation reaction on Pt(111). *J. Chem. Phys.* **106**, 392–401 (1997). URL http://jcp.aip.org/resource/1/jcpsa6/v106/i1/p392_s1.

[8] Zasada, I., Hansali, G., Le Bossé, J. & Lopez, J. Determination of site-occupancy pair correlation functions of CO adsorbed on Pt(111) adapted for DLEED intensity calculations. *Surf. Sci.* **383**, 241–247 (1997). URL http://www.sciencedirect.com/science/article/pii/S0039602897001787.

[9] Petrova, N. & Yakovkin, I. Lateral interaction and CO adlayer structures on the Pt(111) surface. *Surf. Sci.* **519**, 90–100 (2002). URL http://www.sciencedirect.com/science/article/pii/S0039602802021994.

[10] Schweizer, E., Persson, B., Tüshaus, M., Hoge, D. & Bradshaw, A. The potential energy surface, vibrational phase relaxation and the order-disorder transition in the adsorption system Pt{111}-CO. *Surf. Sci.* **213**, 49–89 (1989). URL http://www.sciencedirect.com/science/article/pii/0039602889902525.

[11] Stipe, B., Rezaei, M. & Ho, W. Coupling of vibrational excitation to the rotational motion of a single adsorbed molecule. *Phys. Rev. Lett.* **81**, 1263–1266 (1998). WOS:000075303600032.

[12] Stipe, B. C., Rezaei, M. A. & Ho, W. Inducing and viewing the rotational motion of a single molecule. *Science* **279**, 1907 –1909 (1998). URL http://www.sciencemag.org/content/279/5358/1907.abstract.

[13] Komeda, T., Kim, Y., Kawai, M., Persson, B. N. J. & Ueba, H. Lateral hopping of molecules induced by excitation of internal vibration mode. *Science* **295**, 2055–2058 (2002). URL http://www.sciencemag.org/content/295/5562/2055.abstract.

[14] Motobayashi, K., Kim, Y., Ueba, H. & Kawai, M. Insight into action spectroscopy for single molecule motion and reactions through inelastic electron tunneling. *Phys. Rev. Lett.* **105**, 076101 (2010). URL http://link.aps.org/doi/10.1103/PhysRevLett.105.076101.

[15] Ueba, H. Analysis of lateral hopping of a single CO molecule on Pd(110). *Phys. Rev. B* **86**, 035440 (2012). URL http://link.aps.org/doi/10.1103/PhysRevB.86.035440.

[16] Persson, B. & Ueba, H. Theory of inelastic tunneling induced motion of adsorbates on metal surfaces. *Surf. Sci.* **502-503**, 18–25 (2002). URL http://www.sciencedirect.com/science/article/pii/S0039602801018933.

[17] Nekrylova, J. & Harrison, I. Site resolved adsorption dynamics of CO on Pt(111). *Chem. Phys.* **205**, 37–46 (1996). URL http://www.sciencedirect.com/science/article/pii/0301010495003045.

[18] Yang, H. J., Minato, T., Kawai, M. & Kim, Y. STM investigation of CO ordering on Pt(111): From an isolated molecule to high-coverage superstructures. *J. Phys. Chem. C* **117**, 16429–16437 (2013). URL http://dx.doi.org/10.1021/jp404231t.

Chapter 6

Conclusion and outlook

In this dissertation I described various interactions existing inside an adsorption system, with adapting CO chemisorbed on Pt(111) surface as the model system, by means of scanning tunneling microscopy(STM). I tried to understand the CO chemisorbed on Pt(111) surface in the frame of total energy, which is the total sum of adsorbate-adsorbent interaction and adsorbate-adsorbate interaction, with a range of surface coverage from isolated molecules (0.005 ML) to highly ordered overlayer structures up to 0.55 ML. Scanning tunneling microscopy (STM), the powerful tool for microscopic, real-space investigation, allowed the observation of isolated molecules, overlayer structures, and even the dynamics (motion) of the molecules. CO chemisorbed on Pt(111) is the model system which is one of most extensively studied system with full of information. I could find additional insights on the electronic structure of isolated molecules, subtle intermolecular interaction, and the dynamics inside the overlayer structures.

For the isolated CO molecules on Pt(111) surfaces at very low coverage, I focused on various aspects of isolated CO molecules in appearance, as well as the electronic structure which reflects the adsorbate-substrate interaction. Precise adsorption site of isolated CO molecule was determined to be ontop site, in atomic resolution. The primary ontop-site occupation is also confirmed with the population ratio with low-temperature adsorption. Regarding the bridge site occupation, microscopic observation supports the collision-driven

occupation of the bridge site at low temperature. Bias-dependent images as well as spatially resolved STS revealed unveiled spatial electronic structure in unoccupied energy region. Injection of the tunneling electrons could induce the lateral motion of CO at the energy level corresponds to the $2\pi^*$ state of CO on Pt(111), providing another experimental evidence on the unoccupied state of CO on Pt(111).

The intermolecular interaction among adsorbate CO molecules was investigated with the observation of coverage-dependent overlayer structures. Previously unknown detailed overlayer structures at intermediate surface coverage ($0.1 \sim 0.5$ ML) were successfully visualized, from $(\sqrt{3} \times \sqrt{3})$R30° islands to c$(4 \times 2)$ domain. Constant inter-island distance ($\sqrt{7}/2a_0$ and $2a_0$, a_0 for Pt-Pt atomic distance 2.7 Å) indicate the existence of the intermolecular interaction between the same adsorption species. Inside the overlayer structures, bridge CO appears at the boundary of islands, especially with the inter-island distance to be $2a_0$, forming the unit of c(4×2) domain, namely c$(\sqrt{3} \times 2)$rect units at the boundary. Well known c(4×2) domain developed on the whole surface from 0.38 ML which embracing bridge-site vacancies. The relative population between ontop and bridge CO at the threshold of phase transition ($(\sqrt{3} \times \sqrt{3})$R30° $\rightarrow$ c(4×2)) is $2:1$, and every ontop CO inside c(4×2) possessed at least one neighboring bridge CO inside the c(4×2) domain. Inter-species interaction between ontop and bridge CO could be found inside the bridge-vacant c(4×2) domains, which the height of ontop CO decreases with increasing the number of neighboring bridge CO. At the coverage exceed 0.5 ML, formation of 1×1 boundary inside c(4×2) domain was observed with evident repulsive interaction in 1×1 boundary.

The dynamic behavior, lateral hopping, of CO on Pt(111) dominates only for the bridge CO that appears only at certain increased coverage. While the ontop CO never moves with injection of the tunneling electrons with vibrational energy level, the bridge CO easily convert its adsorption site to ontop site upon electron injection with a few hundred electronvolt. The analysis of the bridge-to-ontop (B-T) conversion also implies a

specific form of intermolecular interaction which avoids the ontop-ontop distance $2a_0$. If the c($\sqrt{3} \times 2$)rect units containing bridge CO is confined inside neighboring ontop CO, the bridge CO exhibit shuttling behavior with the adjacent ontop sites, and it is considered to be T* state which has been suggested previously. The hopping of bridge CO shows the threshold of hopping yield at 230 mV which corresponds to the C–O stretching mode energy, implying the energy transfer by anharmonic coupling. According to the local environment of c($\sqrt{3} \times 2$)rect unit which is determined by the surface coverage, the shuttling behavior differs in terms of T*→B hopping, implies that the potential energy surface which stabilize the bridge occupation as well as the energetic position of T* state strongly depends on the environment, implying the existence of long range intermolecular interaction other than the nearest neighbor interaction.

I believe that my doctoral study established a small, but interesting piece of information onto large sea of previously accumulated knowledge about CO chemisorption on Pt(111) surface, especially about very subtle interactions which were not previously available. To extend the understanding of intermolecular interaction, a few of available research topics are suggested as follows:

- Isolated COs in various transition metals: Spatial distribution of electronic structure of isolated molecules, especially in the unoccupied energy region.
- Bridge-vacant c(4×2) domains of CO on Pt(111): Investigation on the mechanism of inter-species interaction, namely intermolecular interaction between ontop and bridge CO in c($\sqrt{3} \times 2$)rect unit, possibly by local work function measurement.
- CO on Pt(111): Statistical analysis of intermolecular distance of various overlayer structures, to clarify the distance-dependence of intermolecular interaction.
- CO on Pt(111): Manipulation of CO molecules to control the neighboring environment of c($\sqrt{3} \times 2$)rect to find systematic origin of B-T* shuffling and relevant energetics.

Besides these suggested future works, there may remain far more interesting works to extend the understanding of intermolecular interaction. I hope my dissertation work contributes to extend the fundamental understanding of intermolecular interaction as well as to trigger interesting science in the field of surface science.

Appendix A

$(\sqrt{3} \times \sqrt{3})$R30° islands revisited

In Chapter 4, I described the gradual change of overlayer structures depending on the surface coverage, from $(\sqrt{3} \times \sqrt{3})$R30° islands, through bridge-vacant c(4×2), eventually to complete c(4×2) domains and 1×1 boundaries inside c(4×2) structures. Especially, the details in $(\sqrt{3} \times \sqrt{3})$R30° islands including the size of the islands, the inter-island distance and the bridge-site occupation at the boundary of islands with c$(\sqrt{3} \times 2)$rect arrangement were described(Section 4.2.1 and Figure A.1), which has not been experimentally demonstrated prior to this work[1]. However, the interpretation of the detailed overlayer structures into intermolecular interaction was not fully discussed. In this appendix, I will describe the detail of $(\sqrt{3} \times \sqrt{3})$R30° islands in a quantitative way, and discuss the intermolecular interaction which is deduced from the detail of $(\sqrt{3} \times \sqrt{3})$R30° islands.*

Prior to the discussion of this appendix, short summary of Chapter 4 regarding the $(\sqrt{3} \times \sqrt{3})$R30° islands is as following. From randomly scattered molecules at low surface coverage(θ), the $(\sqrt{3} \times \sqrt{3})$R30° islands appear with the coverage range of 0.16 ML $< \theta <$ 0.38 ML, and the size of islands in terms of the number of molecules increases with increase of the surface coverage. As shown in Figure A.1, experimentally observed $(\sqrt{3} \times \sqrt{3})$R30° islands are categorized into two sub-structures, one structure is $(\sqrt{3} \times \sqrt{3})$R30° islands with inter-island distance $\sqrt{7}a_0$(a_0 for Pt-Pt lattice constant, 2.7 Å) (Figure A.1a and b)

*This appendix deals with $(\sqrt{3} \times \sqrt{3})$R30° islands which is the main contents of Section 4.2, with more detailed analysis. The contents of this appendix was presented in the final defense, and added to this dissertation according to the suggestion of the committee members.

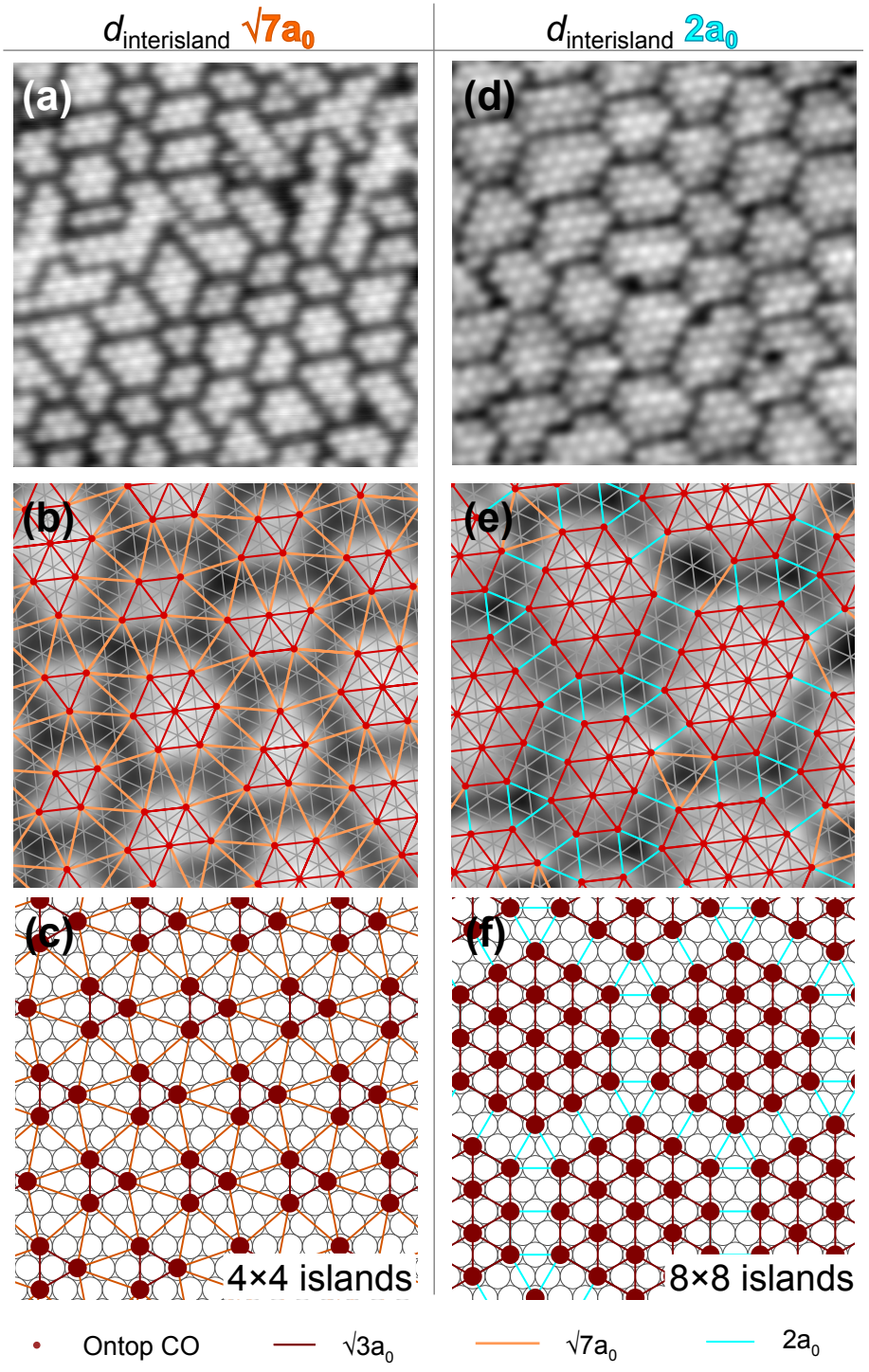

FIGURE A.1: STM images of $(\sqrt{3} \times \sqrt{3})$R30° islands (10 × 10 nm, V_S = 0.1 V, , superimposed models & previously suggested island models from LEED result, from Chapter 4(Figure 4.2, Figure 4.3).

which is similar to the 4×4 island structure(Figure A.1c) suggested by Tüshaus et al[2], and the other is $(\sqrt{3} \times \sqrt{3})$R30° islands with inter-island distance $2a_0$ (Figure A.1d and e) which is similar to 8×8 island(Figure A.1f) in the same reference. The surface coverage of (a) and (c) were estimated to be 0.22 ML and 0.28 ML respectively, with island size of 5.5 ± 2.7 and 13.0 ± 2.3 molecules, respectively.

A.1 Detailed observation of $(\sqrt{3} \times \sqrt{3})$R30° islands

Figure A.2 and Figure A.3 show the representative STM images with bigger dimension (30 nm $\times$ 30 nm) than the previously shown images (Figure A.1) for the $(\sqrt{3} \times \sqrt{3})$R30° islands, two dimensional fast Fourier transformation (2D FFT) of each image and its model, and corresponding histograms for the size distribution of islands for $d_{\text{intersland}} = \sqrt{7}a_0$ and $d_{\text{intersland}} = 2a_0$, respectively. As a whole, the detailed descriptions on the characteristics of $(\sqrt{3} \times \sqrt{3})$R30° islands are consistent to the contents of Section 4.2.1.

A.1.1 General appearance of $(\sqrt{3} \times \sqrt{3})$R30° islands

The appearance of $(\sqrt{3} \times \sqrt{3})$R30° islands are shown the STM images in Figure A.2a and Figure A.3a. As discussed in Section 4.2.1, very uniform interisland distances for two distinct island phases are confirmed in the STM images. The exceptions in $d_{\text{interisland}}$ mainly come from the perturbation of island structure due to the surface defects. In the $(\sqrt{3} \times \sqrt{3})$R30° islands with $d_{\text{interisland}} = \sqrt{7}a_0$, few $2a_0$-long interisland units were observed with c$(\sqrt{3} \times 2)$rect arrangement, but the number ratio is less than 2 %.

Both 2D FFT patterns(Figure A.2 and Figure A.3) show the triangular split patterns from each hexagonal position representing $(\sqrt{3} \times \sqrt{3})$R30° structure, with different direction of split according to the overlayer structure according to $d_{\text{interisland}}$. These patterns are consistent to the LEED observation[3] as well as the suggested model[2]. The 2D FFT images from the STM images show one additional feature than the previous LEED observation, which is a blur hexagon inside the split $(\sqrt{3} \times \sqrt{3})$R30° patterns. This blur pattern in each 2D FFT indicates that the $(\sqrt{3} \times \sqrt{3})$R30° islands are aligned periodically.

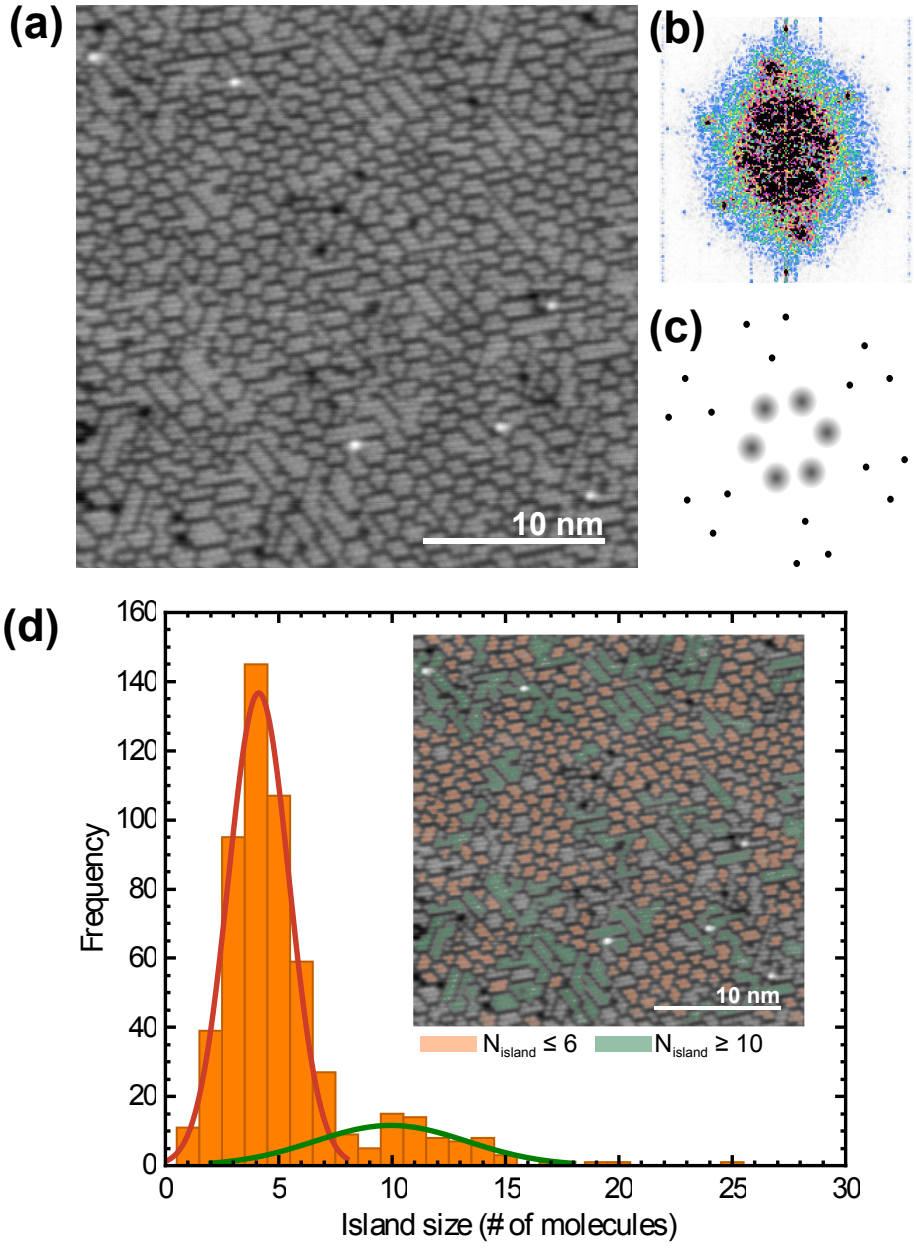

FIGURE A.2: (a) An STM image of $d_{\text{intersland}} = \sqrt{7}a_0$ (4×4) overlayer structure, with the image size 30 × 30 nm, V_S 0.1 V, I_T 0.5 nA. (b) the 2D FFT image of (a), (c) a model of (b), and (d) the histogram of island size distribution extracted from (a), with total average size of islands(N_{island}) 5.2 ± 3.0 molecules. The solid lines in the histogram represent the two Gaussian fit. (Orange line : mean size 4.1, standard deviation 2.0, green line : mean 9.9, standard deviation 6.7.) Inset : Color-mapped image of (a), orange region represents the island size with $N_{\text{islands}} \leq 6$, green region represents the islands with size $N_{\text{island}} \geq 10$. Surface coverage $\theta = 0.19$ ML.

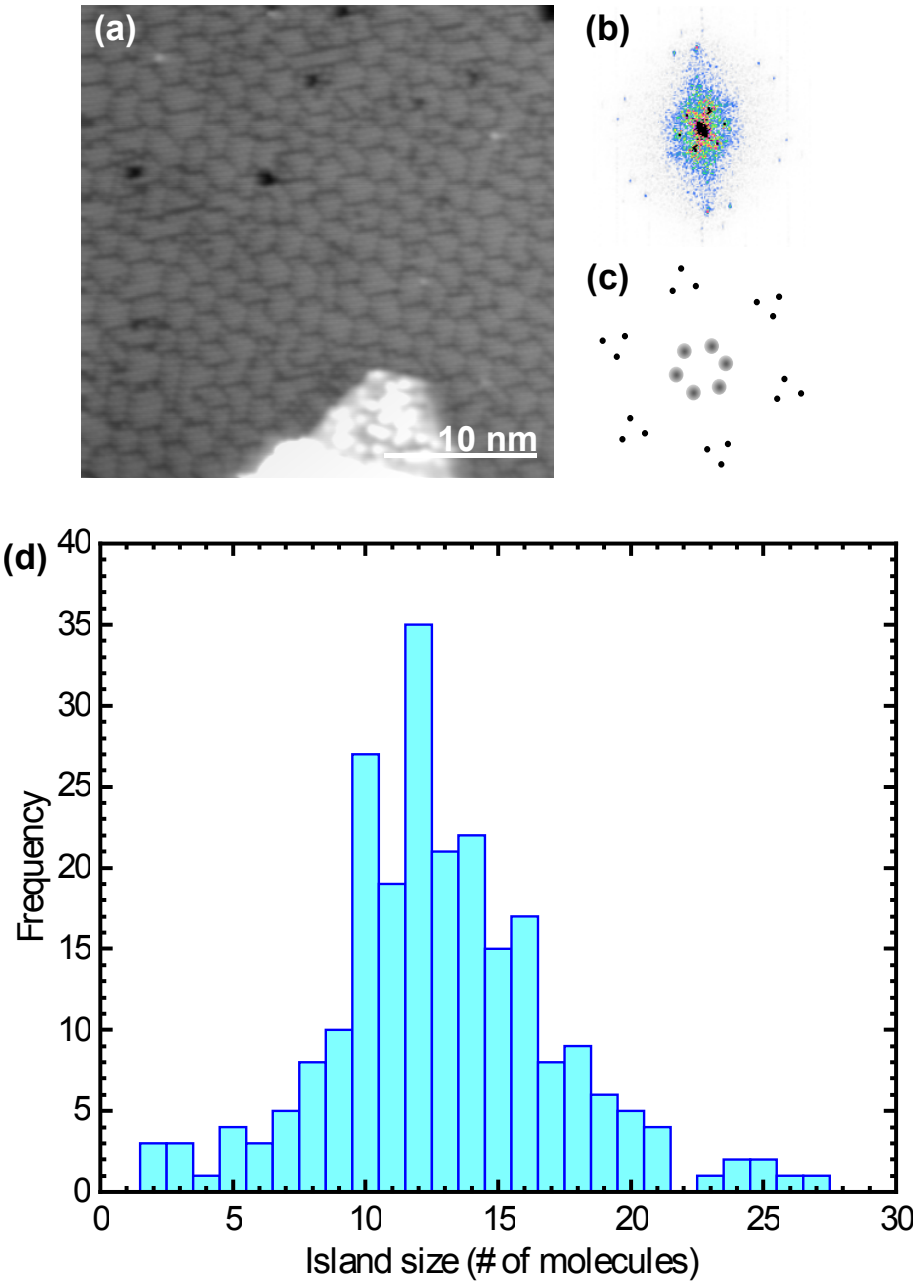

FIGURE A.3: (a) An STM image of $d_{\text{intersland}} = 2a_0$ (8×8) overlayer structure, with the image size 30 × 30 nm, V_S 0.1 V, I_T 0.5 nA. (b) the 2D FFT image of (a), (c) a model of (b), and (d) the histogram of island size distribution extracted from (a), with average island size 12.9 ± 4.3 molecules. Surface coverage $\theta \approx 0.29$ ML.

The relative angle of hexagon in both island structures is identical each other, 30 °rotated from the $(\sqrt{3} \times \sqrt{3})$R30° spots which is corresponding to the crystallographic direction of Pt(111) substrate. The relative angle indicates that all the islands are aligned along the Pt substrate lattice in both island structures ($d_{\text{interisland}} = \sqrt{7}a_0$ & $2a_0$). The size of hexagon, the center-to-apex distance was measured to be 1.0 nm^{-1} and 5.9 nm^{-1} for Figure A.2b and Figure A.3b, respectively. The estimated inter-island arrangement is $4.5a_0$ and $7.5a_0$ for Figure A.2b and Figure A.3b, respectively.

The shape of individual islands depend on the size of islands in terms of the number of molecules, as well as the inter-island distance, i.e. the whole overlayer structures. Small islands with three to six molecules, mainly appears with $d_{\text{interisland}} = \sqrt{7}a_0$, appear as trapezoids and parallelograms. $(\sqrt{3} \times \sqrt{3})$R30° islands composed up of more than seven CO molecules are observed in both island structures ($d_{\text{interisland}} = \sqrt{7}a_0$ & $2a_0$), but the shape of islands is different according to the average $d_{\text{interisland}}$, the phase of $(\sqrt{3} \times \sqrt{3})$R30° islands. In the overlayer structure with $d_{\text{interisland}} = 2a_0$, overall shape of the islands are strictly hexagonal, except the islands near the surface defects (Figure A.3a). The minimum island size with hexagonal arrangement is seven molecules, where at least one CO molecule at the center of the island is completely enclosed with six neighboring CO in $(\sqrt{3} \times \sqrt{3})$R30° arrangement. However, the larger islands ($N_{\text{island}} \geq 10$) in Figure A.2 shows elongated parallelogram shape (or branched parallelogram) rather than hexagonal shape, as shown in the green-colored region in the color-mapped image(inset of Figure A.2c). The elongated parallelogram is mostly two-molecule-wide, i.e. there is only negligible amount of CO molecules which are completely enclosed with neighboring molecules in $(\sqrt{3} \times \sqrt{3})$R30° arrangement. The difference in the shape of islands may originate from the distance- and direction-dependent intermolecular interaction of CO on Pt(111). This will be discussed further in Section A.2.

A.1.2 Size distribution of $(\sqrt{3} \times \sqrt{3})$R30° islands

In order to quantitatively describe the $(\sqrt{3} \times \sqrt{3})$R30° islands, the detailed distribution is given as histograms in Figure A.2c and Figure A.3c for two distinct phase of

$(\sqrt{3} \times \sqrt{3})$R30° islands. The histograms given in Figure A.2 and Figure A.3 is experimentally obtained by counting all the molecules in the STM images. To count the size of islands in terms of the number of molecules, two conditions were checked as following: (a) the molecules inside the islands are apart each other $\sqrt{3}a_0$, (b) the island itself is separated from other islands with a distance longer than $\sqrt{3}a_0$.

The $(\sqrt{3} \times \sqrt{3})$R30° islands with $d_{\text{interisland}} = 2a_0$ (Figure A.3d) shows relatively symmetric distribution in the histogram, as shown that arithmetic average(12.9 ± 4.3) and a fit to the Gaussian distribution (12.4 ± 6.7) are agree well each other. The geometric constraint of hexagonal island formation leads to the preference to specific N_{islands}, for example 7, 10, 12, 14 and 16. However, the $(\sqrt{3} \times \sqrt{3})$R30° islands with $d_{\text{interisland}} = \sqrt{7}a_0$(Figure A.2d) shows asymmetric size distribution, having tails in the right side. The maximum frequency for the island size appears at $N_{\text{island}} = 4$ in Figure A.2d, relatively separated from the arithmetic mean of island size 5.2 ± 3.0. Furthermore, specifically the histogram (Figure A.2c) could be fit into two separated Gaussian distribution as shown in the orange, and green solid lines which are superimposed to the histogram (Figure A.2d). The average $\pm$ standard deviation pairs deduced from the Gaussian fit are 4.1 ± 2.0 and 9.9 ± 6.7 for orange and green solid line, respectively.

To find the island size distribution of $(\sqrt{3} \times \sqrt{3})$R30° islands with $d_{\text{interisland}} = \sqrt{7}a_0$, three STM images at different surface coverages(approximately 0.19 ML, 0.21 ML and 0.22 ML) and corresponding size distributions are shown in Figure A.4. Not every histogram of $(\sqrt{3} \times \sqrt{3})$R30° island size extracted from STM image are separable with two Gaussian distribution as Figure A.2c. However, the evolution of the size distribution indicates that the peak position (the most frequently appearing island size) is maintained regardless of the surface coverage, and the increase of average island size with increasing surface coverage is due to the broadening of the distribution, mainly the increasing portion of large-size ($N_{\text{island}} \approx 10$) islands. It is worth to remind that the general shape of large-size islands in the $(\sqrt{3} \times \sqrt{3})$R30° islands with $d_{\text{interisland}} = \sqrt{7}a_0$ are elongated trapezoid or parallelogram with two-molecule wide.

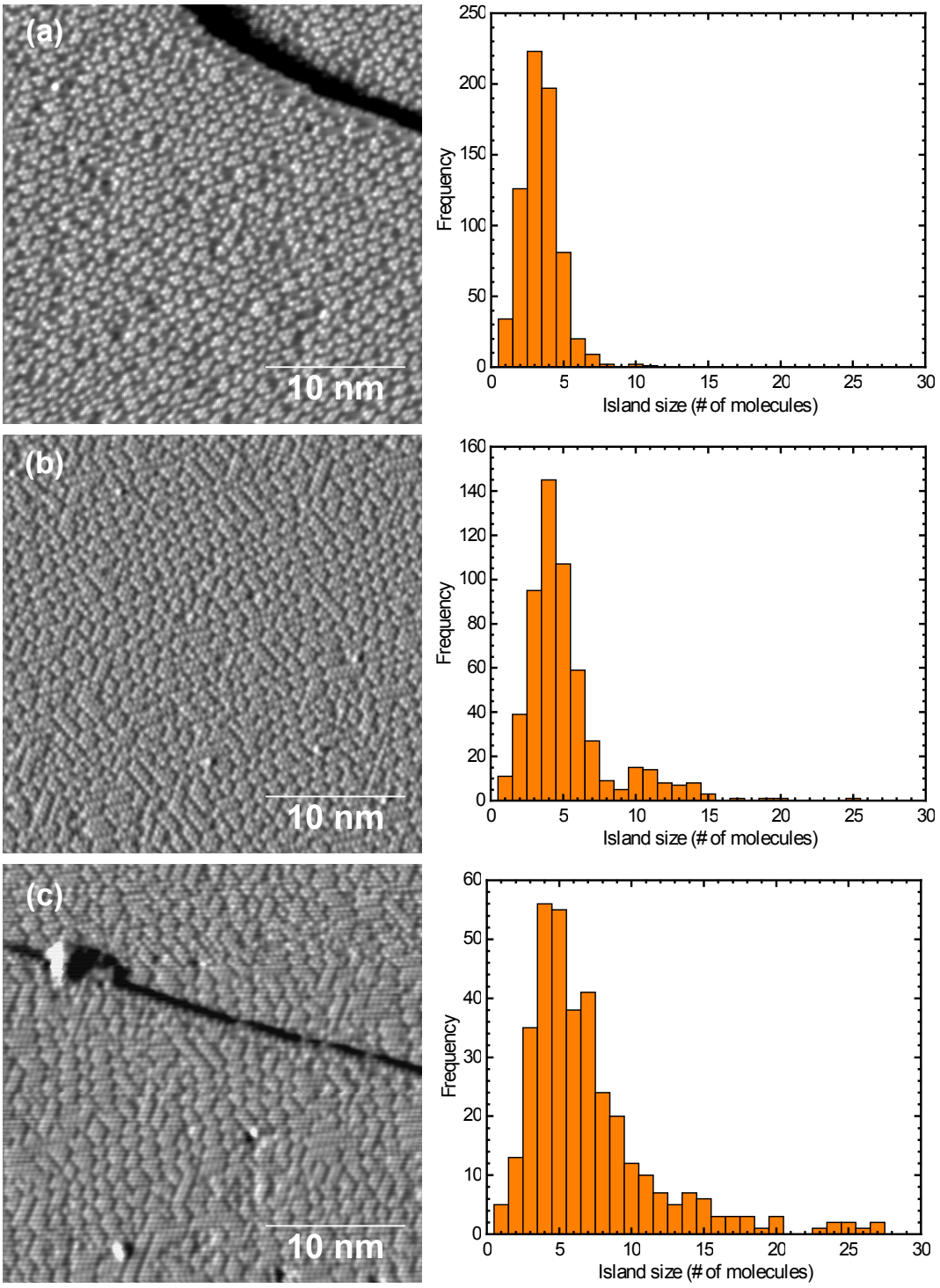

FIGURE A.4: STM images of $(\sqrt{3} \times \sqrt{3})$R30° islands with $d_{\text{interisland}} = \sqrt{7}a_0$ at different surface coverages, and corresponding size distribution. All images are 30×30 nm in size, V_S = 0.1 V and I_T = 1 nA. For recognizability of individual molecules over Pt step, current(I) images are shown. Arithmetic average (μ) and standard deviation(σ) of island size ($\mu \pm \sigma$): (a) 3.4 ± 1.3, (b) 5.2 ± 3.0 and (c) 7.2 ± 5.1.

A.2 Discussion: intermolecular interaction from the island structures

A.2.1 The size of island and phase transition depending on the surface coverage

The distinct difference in two $(\sqrt{3}\times\sqrt{3})$R30° island structures is the portion of bridge CO occupation. $(\sqrt{3}\times\sqrt{3})$R30° islands with $d_{\text{interisland}} = \sqrt{7}a_0$ also incorporate a few bridge CO by forming a few, local c$(\sqrt{3}\times 2)$rect units. However, the major portion of bridge CO occupation is involved with the formation of $d_{\text{interisland}} = 2a_0$ to achieve c$(\sqrt{3}\times 2)$rect boundaries between the $(\sqrt{3}\times\sqrt{3})$R30° islands. Therefore, the threshold surface coverage for the bridge-site occupation becomes the threshold coverage for the phase transition from the $(\sqrt{3}\times\sqrt{3})$R30° islands with $d_{\text{interisland}} = \sqrt{7}a_0$ to the $(\sqrt{3}\times\sqrt{3})$R30° islands with $d_{\text{interisland}} = 2a_0$.

As discussed in previous subsection, the shapes of the large-size islands($N_{\text{island}} \geq 10$) in $(\sqrt{3}\times\sqrt{3})$R30° islands with $d_{\text{interisland}} = \sqrt{7}a_0$ structure are elongated trapezoid or parallelogram, only two-molecule wide. If the elongated trapezoid / parallelogram shape is assumed, the number of substrate atoms can be simply calculated in terms of the N_{island}, as $4\times(N_{\text{island}}+1)$. Then the surface coverage is estimated to be $N_{\text{island}}/\{4\times(N_{\text{island}}+1)\}$. Accordingly, the extreme limit with this island shape model, the maximum coverage which can be achieved with $d_{\text{interisland}} = \sqrt{7}a_0$ is 0.25 ML. The maximum N_{island} so far observed is near 30 ontop molecules in the overlayer structure, thus the realistic threshold coverage for the phase transition $d_{\text{interisland}} = \sqrt{7}a_0 \rightarrow 2a_0$ exist near 0.24 ML.

On the other hand, the minimum coverage which can be achieved with hexagonal islands in the $(\sqrt{3}\times\sqrt{3})$R30° overlayer structures with $d_{\text{interisland}} = 2a_0$ over whole surface is 0.28 ML with $N_{\text{island}} = 7$, if no bridge-site occupation at the inter-island boundary is assumed. Because no bridge-site occupation at the inter-island boundary with $d_{\text{interisland}} = 2a_0$ is not likely, the realistic coverage may be higher than 0.28 ML. Accordingly the intermediate coverage from 0.23 ML to 0.28 ML, the mixed domain of two $(\sqrt{3}\times\sqrt{3})$R30° island phases may exist.

A.2.2 Interisland distance & intermolecular interaction

One interesting point of the $(\sqrt{3} \times \sqrt{3})$R30° islands with $d_{\text{interisland}} = \sqrt{7}a_0$ is the exclusion of a specific intermolecular distance, $2a_0$, while the mean field intermolecular distance $(1/\sqrt{\theta})$ in the coverage range ($0.19\,\text{ML} \leq \theta \leq 0.25\,\text{ML}$) is close to $2a_0$. This is clearly shown in Figure A.5, where the observed frequency of $2a_0$ of intermolecular distance converges to zero, while $\sqrt{3}a_0$ and $\sqrt{7}a_0$ occupy the most population.

According to the general understanding from the adsorption energy decrease with increasing the surface coverage, the CO molecules on Pt(111) surface interact each other repulsively. The amplitude of repulsive interaction decreases as the intermolecular distance (r) increases, as represented by exponential decay by Schweizer et al[4] in the violet line in Figure A.6. However, this simple repulsive interaction is impossible to explain the higher

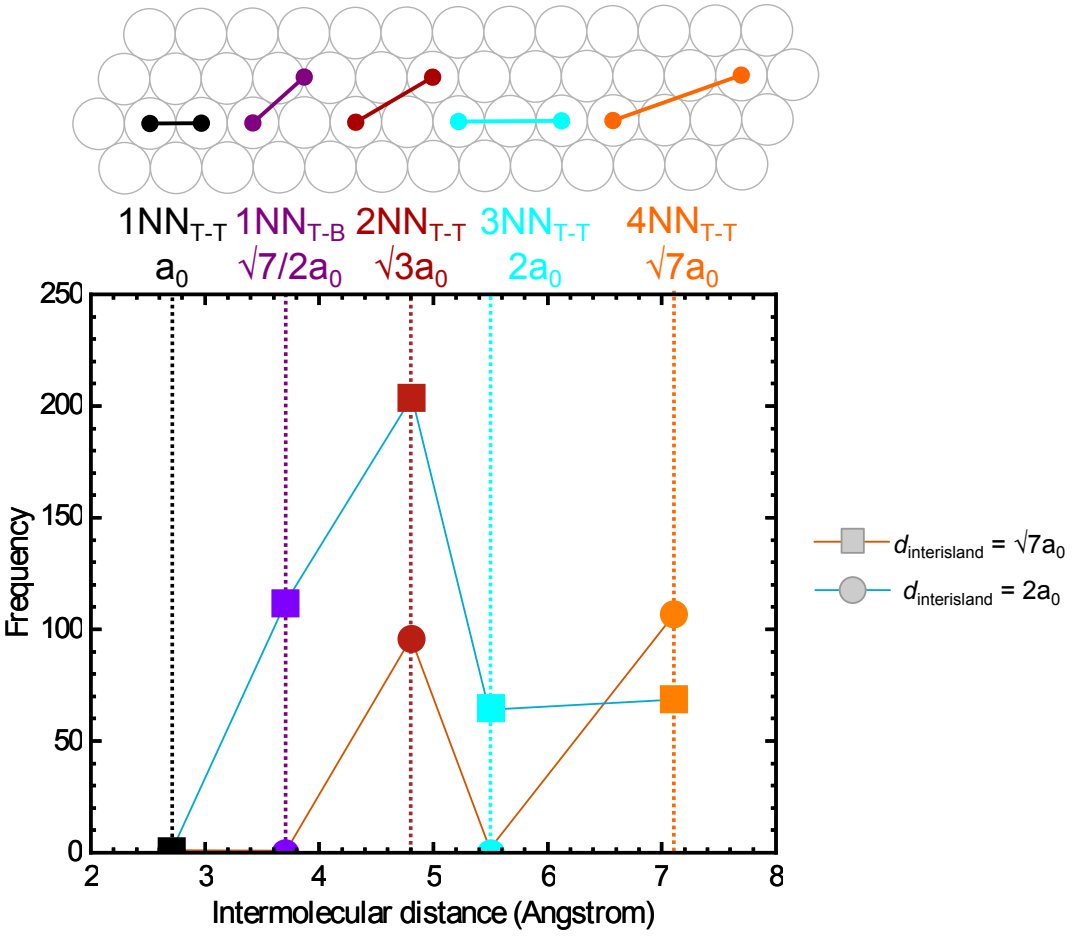

FIGURE A.5: The distributions of intermolecular distance in $(\sqrt{3} \times \sqrt{3})$R30° islands according to the overlayer structures, deduced from 5×5 nm^2 images.

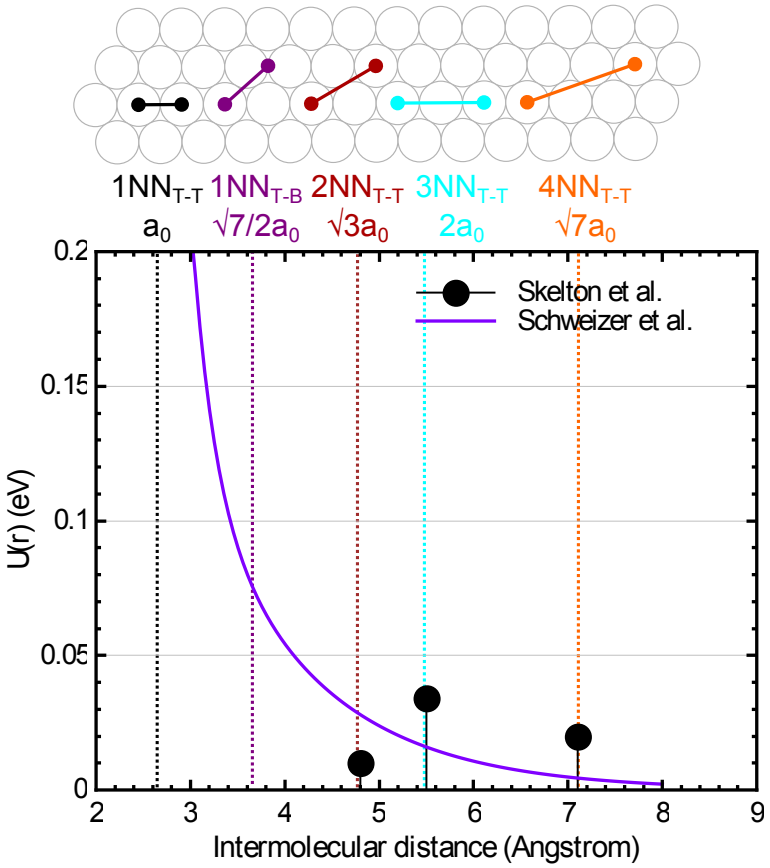

FIGURE A.6: Intermolecular interaction of CO on Pt(111) from previous studies. The solid violet line is from Schweizer et al.[4], and black circle value is from Skelton et al.[5].

frequency of $\sqrt{3}a_0$ than $2a_0$ intermolecular distance, i.e. the $(\sqrt{3} \times \sqrt{3})$R30° island formation. Skelton et al.[5] tried to re-interpret the experimental result of CO isotherm at low coverage done by He scattering technique[6], with employing lattice-gas approach with transfer matrix. Skelton et al.'s re-interpretation was non-monotonic decrease of repulsive interaction upon intermolecular distance (black dots in Figure A.6), the amplitude of repulsive interaction for $r = 2a_0$ is larger than the amplitude of the repulsive interaction for $r = \sqrt{3}a_0$, which is consistent to my experimental result with the $(\sqrt{3} \times \sqrt{3})$R30° islands with $d_{\text{interisland}} = \sqrt{7}a_0$.

My experimental results of $(\sqrt{3} \times \sqrt{3})$R30° islands with $d_{\text{interisland}} = 2a_0$ strongly indicate that the appearance of intermolecular distance $2a_0$ is strongly coupled to the bridge CO occupation, suggesting the relaxation of repulsive interaction for $2a_0$ intermolecular distance by bridge-site occupation. One possible supporting explanation would be the model suggested by Brako et al., which the non-monotonic decrease of intermolecular

interaction is due to the strong anharmonic coupling CO adsorbate vibrational mode to the in-plane displacement of surrounding Pt atoms[7, 8]. Even though Brako et al. have not discussed any influence of bridge-site occupation onto the in-plane displacement of surrounding Pt atoms, my discussion – relaxation of interaction energy for $2a_0$ intermolecular distance by bridge-site occupation through c$(\sqrt{3} \times 2)$rect unit formation – may be reasonable, supported by the stronger anharmonic coupling of bridge CO than ontop CO[4]. I infer that this model would suggest the possible explanation for the limited size of $(\sqrt{3} \times \sqrt{3})$R30° islands as well as the geometric constraints in large-size $(\sqrt{3} \times \sqrt{3})$R30° islands with $d_{\text{interislad}} = \sqrt{7}a_0$.

A.3 Conclusion

This appendix tried to focus on the $(\sqrt{3} \times \sqrt{3})$R30° island structures among all available overlayer structures in CO on Pt(111) system. In addition to the information given in Chapter 4, detailed characteristics of two distinct $(\sqrt{3} \times \sqrt{3})$R30° island structures according to the inter-island distance ($d_{\text{interisland}}$). The detailed observations such as the shape, relative arrangement, and the quantitative size distribution of the $(\sqrt{3} \times \sqrt{3})$R30° islands depending on the surface coverage as well as $d_{\text{interisland}}$, lead to discussion on the subtle nature of intermolecular interaction for CO chemisorbed on Pt(111). I hope this information provide fruitful insight on the fundamental nature of intermolecular interaction of small molecules, as well as enhance the understanding for the practical aspects of overlayer structures.

References

[1] Yang, H. J., Minato, T., Kawai, M. & Kim, Y. STM investigation of CO ordering on Pt(111): From an isolated molecule to high-coverage superstructures. *J. Phys. Chem. C* **117**, 16429–16437 (2013). URL http://dx.doi.org/10.1021/jp404231t.

[2] Tüshaus, M., Schweizer, E., Hollins, P. & Bradshaw, A. Yet another vibrational study of the adsorption system Pt{111}-CO. *J. Electron Spectrosc. Relat. Phenom.* **44**, 305–316 (1987). URL http://www.sciencedirect.com/science/article/pii/0368204887870317.

[3] Steininger, H., Lehwald, S. & Ibach, H. On the adsorption of CO on Pt(111). *Surf. Sci.* **123**, 264–282 (1982). URL http://www.sciencedirect.com/science/article/pii/0039602882903284.

[4] Schweizer, E., Persson, B., Tüshaus, M., Hoge, D. & Bradshaw, A. The potential energy surface, vibrational phase relaxation and the order-disorder transition in the adsorption system Pt{111}-CO. *Surf. Sci.* **213**, 49–89 (1989). URL http://www.sciencedirect.com/science/article/pii/0039602889902525.

[5] Skelton, D., Wei, D. & Kevan, S. Non-monotonic lateral interactions in CO/Pt(111). *Surf. Sci.* **320**, 77–84 (1994). URL http://www.sciencedirect.com/science/article/pii/0039602894004552.

[6] Poelsema, B., Palmer, R. L. & Comsa, G. A thermal he scattering study of CO adsorption on Pt(111). *Surf. Sci.* **136**, 1–14 (1984). URL http://www.sciencedirect.com/science/article/pii/0039602884906514.

[7] Brako, R. & Brenig, W. Vibrational linewidth of CO adsorbed on Pt(111). *Surf. Sci.* **336**, 27–36 (1995). URL http://www.sciencedirect.com/science/article/pii/0039602895005153.

[8] Brako, R. & Šokčević, D. Adsorbate interactions of CO chemisorbed on Pt(111). *Surf. Sci.* **401**, L388–L394 (1998). URL http://www.sciencedirect.com/science/article/pii/S0039602898000740.

Appendix B

Local potential energy surface of bridge CO at the center of a c$(\sqrt{3} \times 2)$rect unit

Regarding the existence of c$(\sqrt{3} \times 2)$rect units and accompanying stabilization of bridge CO, potential energy surface(PES) of c(4×2) domain has been discussed by Schweizer et al. [1] and reproduced in Chapter 5. The potential energy surface is based on the harmonic approximation for the reaction coordinate mode(RC mode) for each adsorption site, and repulsive intermolecular interaction which depends on the intermolecular distance, for c(4×2) domain, $\sqrt{7}a_0$ (a_0 as a Pt-Pt lattice constant). However, the discussion of PES for c(4×2) domain caanot directly explain the PES of isolated c$(\sqrt{3} \times 2)$rect unit, due to the absence (or low degree) of intermolecular interaction in c$(\sqrt{3} \times 2)$rect units.

This appendix aims to describe the PES of a c$(\sqrt{3} \times 2)$rect unit, especially local PES near the center bridge CO with a simplified way. First of all, the basic framewalk to understand the multi-molecule overlayer structure with modified PES, which is based on PES of low surface coverage, modified by intermolecular interaction. The assumptions regarding the relative position of molecules at the c$(\sqrt{3} \times 2)$rect unit and intermolecular interaction will be described, and the resultant PES and the interpretation will be described. Finally, the influence of relaxed assumption and further discussion will be described.

As indicated in the Chapter 1, my approach to the total energy highly covered surface is, having total sum of adsorption energy for each molecule, and eventually adding intermolecular interaction term. The approach to the modified PES is also similar to the total energy, choosing the PES at low surface coverage as the base and the intermolecular interaction as a perturbation to the PES at low surface coverage.

The Figure B.1 shows 3-dimensional PES at low surface coverage limit, based on the PES parameters from Hähner et al.[2]* Every available adsorption site, i. e. high-symmetry point on Pt(111) surface has its own potential well, where the potential stiffness is defined from the reaction coordinate mode (RC mode) energy, which is hindered translation mode for the lateral displacement. The central bridge CO will experience the potential well of bridge CO, with higher vibration quanta ($\sim$ 38 meV) than the ontop CO at the frame of the c($\sqrt{3} \times 2$)rect unit (4 meV or 7 meV).

*For simplicity, the anisotropy of PES at bridge site, i.e. the difference in HT mode energy along [1$\bar{1}$0] direction and [$\bar{2}$10] direction is not considered.

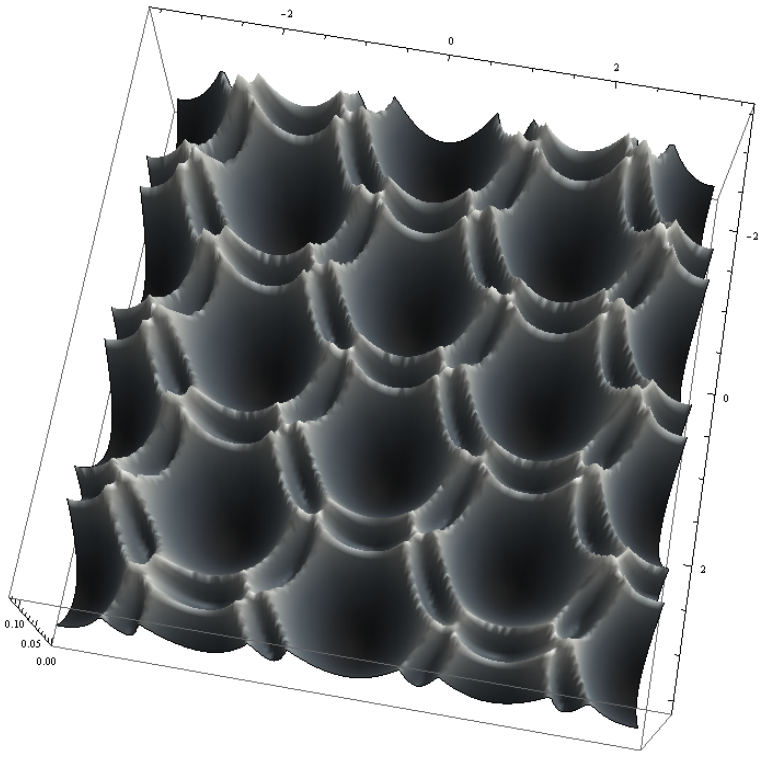

FIGURE B.1: 3D potential energy surface, calculated under harmonic approximation. Potential well depth according to the adsorption site and the potential stiffness parameters are adopted from [2].

Assume there is one c($\sqrt{3} \times 2$)rect unit on Pt(111) surface. If one consider the individual molecules at the unit are in PES at low surface coverage, each molecule is inside the corresponding potential well according to the adsorption site, as shown in the Figure B.2, top image. The cross-section view of PES over the position of ontop CO – bridge CO – ontop CO along the crystallographic direction [$\bar{3}$23] is taken in to visualize the RC mode potential for each CO in the c($\sqrt{3} \times 2$)rect unit(ω_T and ω_B for ontop and bridge CO, respectively) as well as the intermolecular interaction. Figure B.2. In addition to the potential well according to the HT mode, the ontop CO and bridge CO will affect each

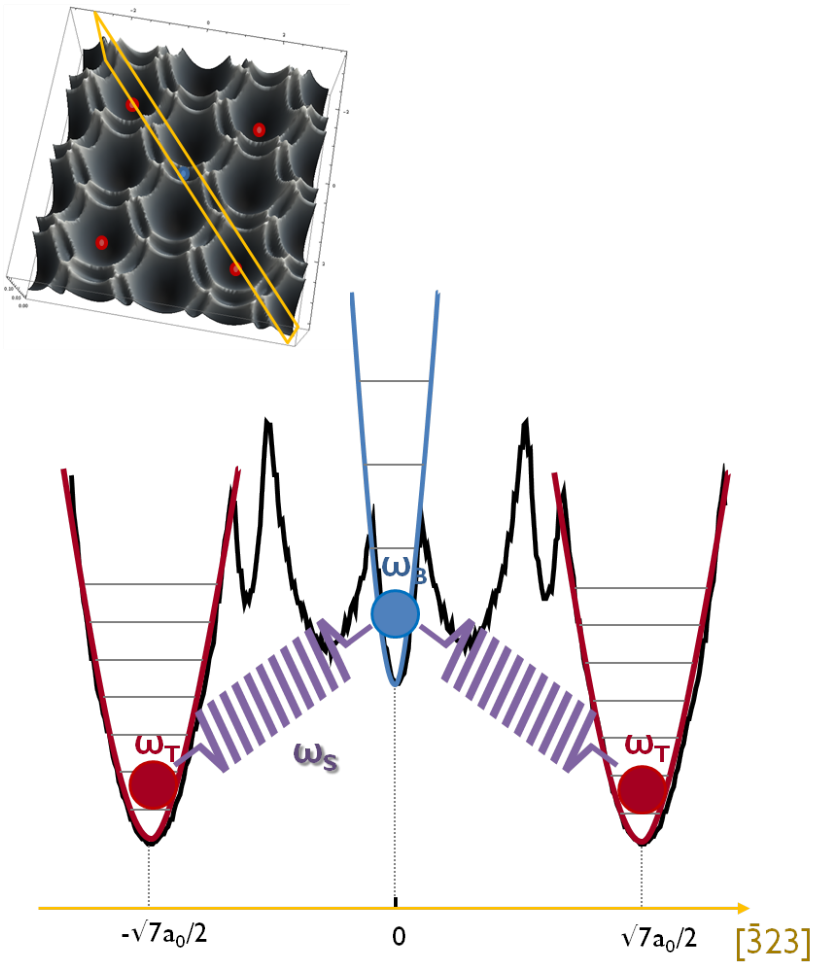

FIGURE B.2: Cross-sectional view of low-coverage PES along [$\bar{3}$23] direction(yellow line over a c($\sqrt{3} \times 2$)rect unit in 3D PES), over ontop CO – bridge CO – ontop CO in a c($\sqrt{3} \times 2$)rect unit, and the intermolecular interaction between ontop CO and bridge CO. Each CO molecule experiences its harmonic potential well defined by HT mode energy, which is represented as red parabola for ontop CO (ω_T) and blue parabola for bridge CO(ω_B), respectively. The intermolecular interaction is expressed as violet spring, with force constant of ω_S.

other by intermolecular interaction, where the intermolecular distance between those two CO is close enough to have significant intermolecular interaction, which is schematically represented as a spring between ontop and bridge CO with force constant ω_S.

The next step is considering the intermolecular interaction according to the relative distance among the molecules. The intermolecular interaction is usually described in terms of intermolecular distance, r. To simply the problem, I adopted the simple repulsive intermolecular interaction model suggested by Schweizer et al[1]. This model only considers the intermolecular distance, not for the adsorption sites of accounted molecule. The intermolecular interaction is composed up of two parts: the Pauli expulsion in short distance (< 0.3 Å) and through-substrate long-range interaction($\tilde{3}$, 4 Å). The detailed equation for the interaction model as a function of intermolecular distance (r) is like below:

$$U(r) = A_1 \cdot e^{-\alpha_1 x} + A_2 \cdot e^{-\alpha_2 x} \tag{B.1}$$

where the parameters are: $A_1 = 3.9 \times 10^4\,\text{eV}$, $\alpha_1 = 4.3\,\text{Å}^{-1}$ for Pauli repulsion and $A_2 = 1.3\,\text{eV}$, $\alpha_2 = 0.8\,\text{Å}^{-1}$ for through-substrate interaction. Figure B.3 shows the the

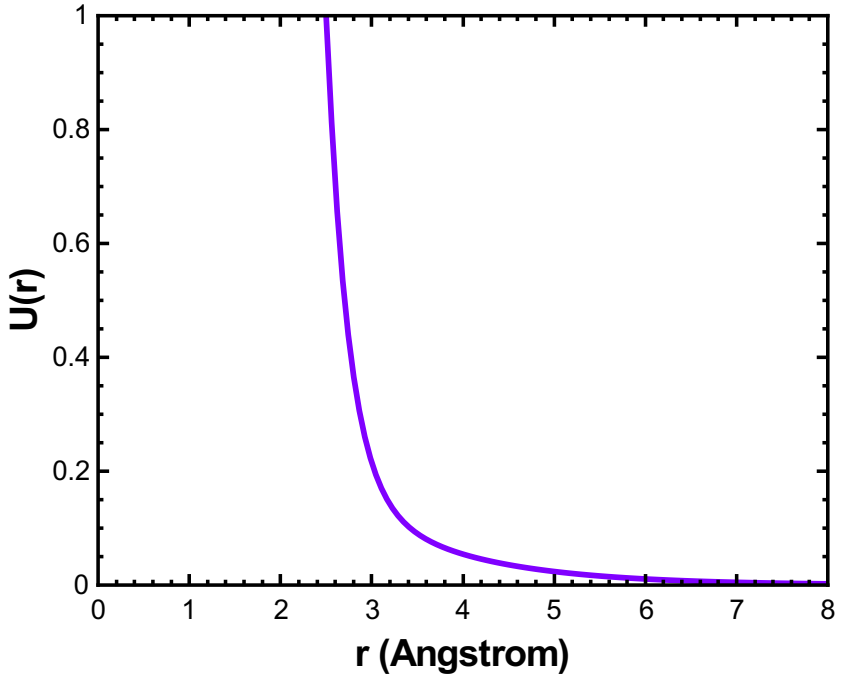

FIGURE B.3: Intermolecular interaction($U(r)$) in electronvolt, estimated by Schweizer et al., in terms of intermolecular distance r.

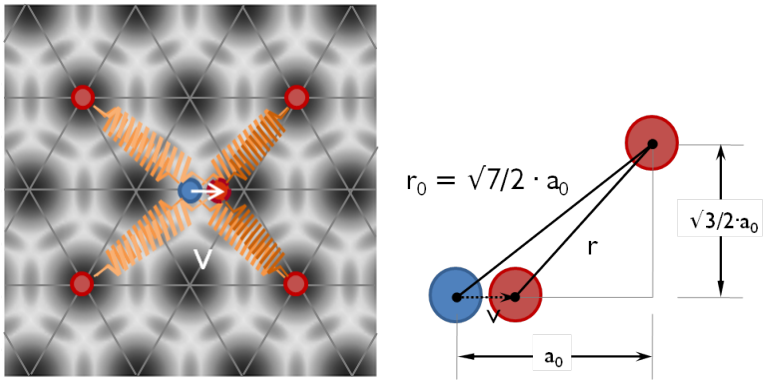

FIGURE B.4: Schematic model for the process to find intermolecular interaction in terms of the displacement of bridge CO (v)(left) and simple correlation between the intermolecular distance between the surrounding ontop CO and the displaced bridge CO r, and the displacement v.

resultant intermolecular interaction, which is exponentially decaying.

If the position of surrounding ontop CO is fixed regardless of intermolecular interaction, the intermolecular distance between ontop and bridge CO in a c($\sqrt{3} \times 2$)rect unit corresponds to $\sqrt{7}/2a_0$, which is approximately 3.7 Å, and the intermolecular interaction energy for the intermolecular distance is $\sim$ 72 meV. In a static c($\sqrt{3} \times 2$)rect unit, the bridge CO stays in the bridge position and the intermolecular interaction applied to the bridge CO is sum of four vectors, from four surrounding ontop COs.

Here the center of interest is the intermolecular interaction-modified local PES near the bridge CO, along the $[1\bar{1}0]$ direction. However, the intermolecular interaction between ontop CO and bridge CO is along the $[\bar{3}23]$ direction. To obtain the target modified PES, two constraints were made as follows:

- Four surrounding ontop COs are fixed at the very top of Pt atoms,
- Only one ontop CO is considered.

For the first constraint, soft potential(small vibrational quanta for HT mode) of ontop CO enables rough approximation of fixed ontop CO. For the second constraint, one isolated c($\sqrt{3} \times 2$)rect unit has two mirror-symmetry plane, allowing simplification to the interaction with only one ontop CO.

Assume that the bridge CO is at the origin, and the ontop CO in the first quadrant is at $(a_0, \sqrt{3}/2a_0)$. If the bridge CO is displaced by v towards to the x direction(along $[1\bar{1}0]$ axis), the resultant intermolecular distance between the ontop CO at $(a_0, \sqrt{3}/2a_0)$ and the displaced bridge CO becomes

$$r(v) = \sqrt{\left(\frac{\sqrt{3}}{2}a_0\right)^2 + (a_0 - v)^2} \tag{B.2}$$

by simple Pythagoras equation, as depicted in Figure B.4. Simple exchange of r in Equation B.1 into Equation B.2 results in the intermolecular interaction in terms of the displacement of bridge CO, v.

The final process to obtain the modified PES is, simple summation of the low-coverage PES (Figure B.5a) and the intermolecular interaction as a function of the displacement ($U(v)$, Figure B.5b). The resultant modified PES is shown in Figure B.5c, providing two insights about the c($\sqrt{3} \times 2$)rect unit, as follows:

- The bridge CO at the center of c($\sqrt{3} \times 2$)rect unit is indeed stabilized relative to the neighboring ontop site, because of the intermolecular interaction between the surrounding ontop CO molecules.
- Appearance of T* state: there exist a local minimum in the modified PES at the off-center position of adjacent Pt atom.

These two points enables the laterally confined dynamics of bridge CO upon injection of energy, namely B-T* shuttling which is described in Chapter 5.

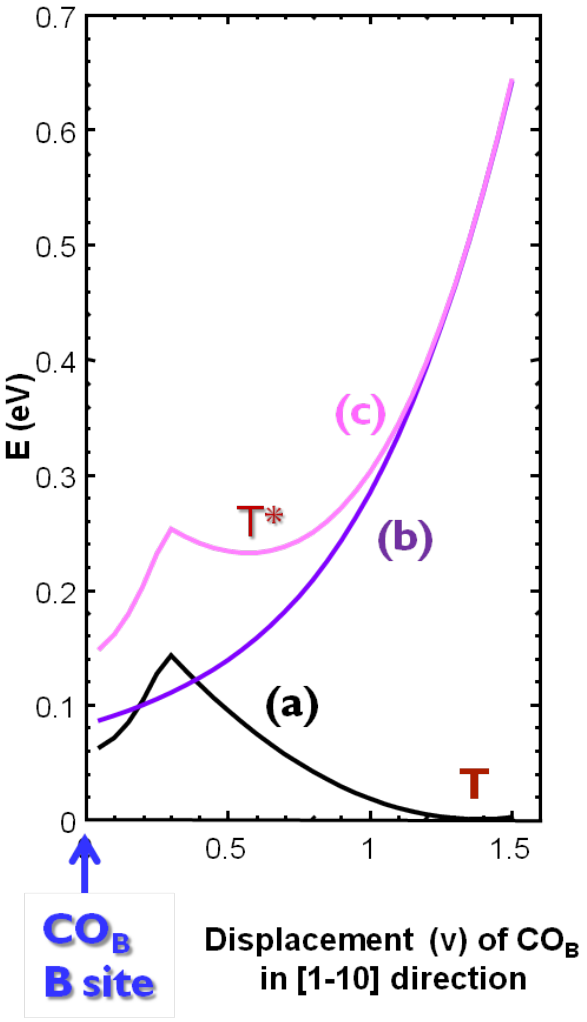

FIGURE B.5: Resultant modified PES by intermolecular interaction, along $[1\bar{1}0]$ direction. (a) the original PES at low surface coverage, (b) the intermolecular interaction U as a function of the displacement of bridge CO v, (c) the resultant modified PES by taking simple sum of (a) and (b).

References

[1] Schweizer, E., Persson, B., Tüshaus, M., Hoge, D. & Bradshaw, A. The potential energy surface, vibrational phase relaxation and the order-disorder transition in the adsorption system Pt{111}-CO. *Surf. Sci.* **213**, 49–89 (1989). URL `http://www.sciencedirect.com/science/article/pii/0039602889902525`.

[2] Hähner, G., Toennies, J. P. & Wöll, C. Normal modes of CO adsorbed on metal surfaces. *Appl. Phys. A* **51**, 208–215 (1990). URL `http://www.springerlink.com/content/ru0324463453u104/`.

Acknowledgements

This unbelievable moment, which I complete my dissertation and write this 'acknowledgement', would not come up without all the supports, advises, encouragements and patience from many people.

I would like to express my sincere gratitude to my supervisors, Prof. Maki Kawai at the University of Tokyo and Dr. Yousoo Kim at RIKEN, for considerate guidance and supports during my doctorate course. With great research environment and enthusiastic atmosphere full of scientific passion they provided, I could step forward for an academic career in the field of surface science. I also deeply appreciate their priceless comments and the model behavior regarding the scientific attitude, which will be the ground for my life as a scientist.

I am grateful for all the dissertation committee members, Prof. Jun Yoshinobu, Prof. Kaoru Kimura and Prof. Tohru Suemoto at the University of Tokyo, for warm comments, keen advices and encouragements throughout the examining process. I want to express my gratefulness to Prof. Noriaki Takagi for his kind help and supports during the program.

To the mentor at the period that I started the first step in scientific research, Prof. Hee Cheul Choi at POSTECH, I would like to thank very much for the guidance and encouragements. I would like to thank to Prof. Hiromu Ueba at Toyama University, for the precious insight on the STM action spectroscopy, and the passionate discussion. Also, I am grateful to Prof. Michael Trenary and Prof. Bo Persson for the discussion and encouraging comments on my work.

I thank all the colleagues I met in Surface and Interface Science Laboratory (SISL) at RIKEN. Thank Dr. Taketoshi Minato and Dr. Hyo Won Kim for guiding me to be familiar with UHV environment and LT-STM experiments at the early stage of my doctor course. I am very grateful particularly to Dr. Jaehoon Jung, for all the scientific discussion as well as warm encouragements and advices throughout my doctor course. Thank you very much, all Korean members, Dr. Ju-Hyung Kim, Dr. Hyunseob Lim and Dr. Junepyo Oh, for the sense of solidarity which has supported me, as well as strong encouragements and scientific discussions in my mother-tongue. I wants to give my thanks to all senior members that I have met here, Prof. Hyung-Joon Shin, Dr. Tomoko K. Shimizu, Dr.

Hiroshi Imada, Dr. Emi Minamitani, Dr. Toshu An, Dr. Emiko Kazuma, for affectionate attitude onto science as well as all the scientific / nonscientific conversations. I also thank all student members who shared their time with me, Dr. Kenta Motobayashi, Dr. Seiji Takemoto, Ms. Miyabi Imai, Mr. Kan Ueji, Mr. Takuma Omiya, Ms. Tika Kusbandiah and Mr. Shota Kawahara. I cannot miss out all the short-term members and the memories with them in SISL, Mr. Tae Soo Kim, Ms. Zhu Liang, Dr. Selena Russell, Ms. Holly Walen and Mr. Inhae Zoh. I sincerely appreciate Ms. Yoshiko Shimizu's assistance for all the administrative processes at RIKEN. I would like to say thanks with my condolence to Mr. David Chapmon, for all conversation that we had.

Also, I thank all members of Kawai-Takagi laboratory at the University of Tokyo. I am grateful to Dr. Noriyuki Tsukahara, Dr. Ryuichi Arafune and Dr. Chun Liang Lin, Ms. Naoka Ohta and Mr. Ryoichi Hiraoka, for the fruitful discussions and encouragements. I thank very much to Ms. Yoshie Izumi, for her care on administrative processes in the university. To all student members who share pleasant memories with me, thank you very much!

I acknowledge the Junior Research Associate program in RIKEN for financial supports throughout the doctor course. Also, I would like to thank Ms. Yunike Shimizu in the Global Relations and Research Coordination Office at RIKEN, for the supports and help.

I would like to thank for all the emotional supports that kept me from any frustration. Thank you all friends from POSTECH, sorry for not mentioning every name due to limited space, but I believe they will understand me that I have no need to add any explanation for my thanks to them. Thank you, Ms. Yoon Hee Kim and Ms. Zae Hee Kim, for our moments of chattering and warm affection. Thanks Ms. Seungwon Lee, for being a friend in a place far from our country. Thank my relatives for warm encouragements every time. Thank you, Lucid Fall (Dr. Yun Suk Jo), *the musician* in my life, for all consolation that I've got from your music.

Lastly, it is very difficult to find appropriate expression for my thanks to my beloved family. My mother's prayer on every morning, my father's warm hug, my sister's wordless patting, and the invaluable faith from them brought me to this point. I would like to send my deepest gratitude to my family, from the bottom of my heart.

From Wako,

Hyun Jin YANG

Bibliography

Publication list (During the doctor course[†])

- Hyun Jin Yang, Taketoshi Minato, Maki Kawai and Yousoo Kim
  STM Investigation of CO Ordering on Pt(111): From an Isolated Molecules to High-Coverage Superstructures. *J. Phys. Chem. C* **117**, 16429 (2013). URL: `http://dx.doi.org/10.1021/jp404231t`
- Hyunseob Lim, Jaehoon Jung, Hyun Jin Yang and Yousoo Kim
  Lattice-Contraction-Induced Moiré patterns in Direction-Controlled Epitaxial Graphene on Cu(111). *Adv. Mater. Interfaces* **1**, 1300080 (2014). URL: `http://dx.doi.org/10.1002/admi.201300080`
- Zhu Liang, Hyun Jin Yang, Yousoo Kim and Michael Trenary
  The Surface Morphology of Atomic Nitrogen on Pt(111). *J. Chem. Phys.* **140**, 114707 (2014). URL: `http://dx.doi.org/10.1063/1.4868141`
- Hyunseob Lim, Hyun Jin Yang, Takeshi Takami and Yousoo Kim
  The Atomic-Scale Identification of Epitaxial Graphene Orientation on Metal (111) Substrates from its Moiré Pattern. *In Preparation* (2014).
- Hyun Jin Yang, Maki Kawai and Yousoo Kim
  $(\sqrt{3} \times \sqrt{3})$R30° Islands for CO Chemisorbed on Pt(111) and Intermolecular Interaction *In preparation* (2014).
- Hyun Jin Yang, Maki Kawai and Yousoo Kim
  Laterally confined dynamics of bridge-adsorbed CO on Pt(111) *In preparation* (2014).

[†]Full list of publications and conference presentations is available on my personal website(`http://sites.google.com/site/hyunjinyang`) or via e-mail(hjyang@riken.jp, hyunjin.yang@gmail.com).